Microhydrodynamics of Droplets and Particles: Applications in Microfluidics and Agglomeration

By

Gesse Roure

A thesis submitted to the Faculty of the
Graduate School of the

University of Colorado

In partial fulfillment of the requirement for
the degree of
Doctor of Philosophy
Department of Chemical and Biological
Engineering
2023

Committee Members:
Robert H. Davis
Alexander Z. Zinchenko
Mark J. Ablowitz
Ankur Gupta
Kristi Anseth

Roure, Gesse A. (Ph.D., Chemical Engineering)

Microhydrodynamics of Droplets and Particles: Applications in Microfluidics and Agglomeration

Dissertation directed by Prof. Dr. Robert H. Davis and Dr. Alexander Z. Zinchenko

Abstract

Low-Reynolds-number flows are present throughout several fields in applied sciences and engineering, such as in the study of colloidal suspensions, cell motility, and other small-scale phenomena. This project concerns the investigation of two distinct systems involving the motion of particles and droplets in such flows. In the first part, we consider the problem of capturing small particles suspended in a fluid by using an emulsion of saltwater droplets covered by a semi-permeable oil layer. This problem is motivated by a recently proposed mineral-recovery technique. A theoretical investigation of binary interactions between droplets and particles provides us insight on how the physical parameters such as permeability and drop expansion due to osmotic swelling may affect particle capture. We observe that drop expansion considerably increases the capture efficiency of particle capture. Expansion limitation due to the diffusion of salt inside the droplets are also considered. In the second part, we investigate the motion of droplets in microchannels. This problem was motivated by the increasing number of applications of drop-based microfluidic systems, ranging from emulsion generation to medical diagnosis. To this end, we have designed a boundary-integral algorithm to simulate the droplet motion through three-dimensional channels with complex geometries. The algorithm also uses a moving frame that follows the droplet throughout its motion in the channel to reduce computational time. Physical parameters such as capillary number, viscosity ratio, and drop size can affect drop motion and breakup conditions. We investigate the effects of channel depth on drop motion. For regular geometries of uniform cross-section, the infinite-depth limit is approached only slowly with increasing depth, though we show much faster convergence by scaling with maximum versus average velocities. For non-regular channel geometries, features such as different branch heights can affect drop partitioning, as the flow rate required to make a droplet go through a smaller branch of a channel is larger than the one required for making the same droplet go through a smaller branch, in contrast to the symmetrical behavior usually found in regular geometries. Moreover, non-regular geometries present further challenges when comparing the results for deep and infinite-depth channels. A simplified approach is also developed to probe inertial effects on drop motion. To this end, the full Navier-Stokes equations are first solved for the entire channel, and the tabulated solution is then used as a boundary condition at the moving-frame surface for

the Stokes flow inside the moving frame. We find that, for moderate Reynolds numbers up to $Re = 5$, inertial effects on the undisturbed flow are small even for a more complex, irregular geometry, meaning that inertial contributions arise only from the transience of drop motion and are likely small. Finally, using our boundary-integral algorithm we also analyze the dynamics of a droplet in a hydrodynamic trap. By changing the fluxes in the different branches, we can manipulate drop shape and position. A linear controller is used to manipulate drop position, and the drop deformation is characterized by a decomposition of the shape into spherical harmonics. For droplets with small deformation (e.g., small radii and/or capillary number), we observe a linear superposition of harmonics that can be used to manipulate drop shape. We also investigate how the different flow modes may be combined to induce mixing inside the droplets. The transient combination of modes produces an effective chaotic mixing inside the droplet, which can be further enhanced by changing parameters such as viscosity ratio and flow frequency.

Acknowledgments

Doing a PhD away from my home country presented various challenges, the most significant being the separation from my family throughout this entire journey. Hence, I want to extend my heartfelt gratitude to my entire family for their unwavering support over the years. Without them, I would not have reached this point. To my dear Mom, Dad, and little brother, I miss you all tremendously. You are always in my thoughts and hold a special place in my heart.

I would like to express my appreciation to Rocío, Jake, and Hillary, who have been by my side me over the past four years. I am very proud of your current pursuits and achievements. Jake, thank you for engaging in numerous discussions with me and for always helping me prepare for my presentations. Congratulations on your new appointment to a faculty position! Rocío, I extend my gratitude for your kindness and for finding me a place to live when I first arrived in Colorado, even though we were strangers at the time. You have been a great friend and I have no doubt that you will excel in your career in industry. Hillary, thank you for being my closest friend during your time in Colorado. I wish you the very best as you start your own PhD journey.

I would also like to acknowledge my officemates: Filipe, Arkava, Ritu, Nathan, Souradeep, and Raj. Sharing an office space with such brilliant minds has made the work environment more enjoyable. A special thanks goes to Filipe, who not only has been a longtime friend and labmate but also, currently, my roommate. Your future is bright, and I appreciate your support. I would also like to thank Arkava for being such a good friend over the past couple of years. Moreover, I want to express my gratitude to my former labmates Igor, Yuri Sinzato, Victor, and Adriano for their friendship and the countless discussions we had throughout these years. Igor, thanks for all the mental support you provided me and for being such a wonderful person. I would also like to thank my friends Tadashi, Lucas, and Breno for interesting general scientific discussions.

I am grateful to the mentors who guided me prior to my PhD journey: Prof. Yuri Sobral, Prof. Gustavo Abade, and my senior thesis and master's advisor, Prof. Francisco Ricardo da Cunha. Yuri, my first undergraduate advisor, not only taught me about granular materials and partial differential equations but also supported me during challenging situations. Gustavo, my second undergraduate advisor, fostered my deep interest in suspension mechanics and statistical physics. He is also one of the most exceptional lecturers I have encountered. Prof. Cunha, thank you for sharing your extensive knowledge of microhydrodynamics, multiphase flows, soft materials, and continuum mechanics through our lengthy discussions and your lectures. Your support and belief in me have been invaluable.

Finally, I would like to express my gratitude to my PhD advisors, Prof. Robert Davis and Dr. Alexander Zinchenko. It has been an absolute honor to work with these two individuals whose research has served as a constant inspiration for my own even before starting my PhD. Prof. Davis, thanks for taking me as your student and for mentoring me throughout these years. I learned a lot from you both as a scientist and as a person. You set an example of remarkable character and intellectual honesty that I often find lacking in the scientific community. I would also like to thank Dr. Zinchenko for the valuable scientific discussions we had over the years. Alex, you are one of the brightest people I have ever known, and I hope to collaborate more with you in the future. Furthermore, I want to thank you for giving me a newfound appreciation for numerical methods and analysis.

CONTENTS

LIST OF FIGURES

LIST OF TABLES

Part I

Introduction and fundamentals

CHAPTER 1

INTRODUCTION

"Motion at low Reynolds number is very majestic, slow, and regular."

E. M. Purcell

1.1 Why do we care?

For a long time, natural philosophy and physical sciences have been guiding the progress of society in various fields of knowledge such as engineering, chemistry, and biomedical sciences. The fundamental understanding of physical phenomena through the development and analysis of model systems gave humankind the capability of understanding and predicting the behavior of complex systems, improving our ability to design them.

In the past few decades, plenty of problems in chemical and biological engineering have been motivated by systems where a large portion of the relevant physical phenomena happens in small but multiple scales: from the quantum-mechanical principles that govern the chemical reactions between molecules to the microscopic behavior of colloidal particles, cells, and soft materials, usually described by classical transport modeling. As

a large portion of these classically-described phenomena is related to small particles, cells, and droplets slowly moving in a fluid medium, the theory of low-Reynolds-number hydrodynamics is a powerful framework to investigate these systems.

As it is probably of common knowledge these days, the dynamics of Newtonian liquids is described by the (in)famous Navier-Stokes equations — a set of non-linear equations governing the dynamics of the velocity and pressure fields in a fluid. In the low-Reynolds-number limit, the non-linear Navier-Stokes equations transform into the linear Stokes equations. This simplification removes the issues regarding existence, uniqueness, and blowup of solutions present in the regular Navier-Stokes equations due to the non-linear convective term. This linearization allowed for substantial theoretical development of the field of low-Reynolds-number hydrodynamics during the past century by researchers such as G.I. Taylor, G. K. Batchelor, A. Acrivos, H. Brenner, and others, who developed analytical, asymptotic, and numerical techniques to deal with particles and droplets moving in low-Reynolds-number flows. Here, it is important to note that, despite the linear nature of the Stokes equations, most of these systems are still too complicated to be solved analytically, often requiring approximation techniques such as asymptotic methods and numerical analysis. In contrast to inertial flows, the complexity of these problems does not come from non-linear equations, but rather from complex geometries, multiple particles, moving interfaces, and intricate boundary conditions. In fact, even for systems where analytical solutions for the flow problem can be found, the resulting particle/droplet dynamics can still be highly non-linear. Low-Reynolds-number hydrodynamics is often combined together with tools from statistical mechanics to describe the behavior of complex soft materials. For these reasons, there is a plethora of open problems in the field, from both fundamental/theoretical and applied standpoints.

In this dissertation, we answer open questions about the motion of particles and droplets in low-Reynolds-number flows motivated by two specific applications: the extraction or capture of small mineral particles suspended in a fluid and the motion and

deformation of droplets in microfluidic channels. The issues that we address concerning these systems include how we can use emulsion binders to improve the efficiency of recovery of small mineral particles in a fluid and how we can use microfluidic devices to manipulate the shape of droplets or to induce active chaotic mixing inside droplets inside microfluidic reactors. On our way to answer these applied questions, we also tackle more fundamental issues such as adapting collision theory for systems with mobile interfaces and understanding the transient microstructure behavior in these suspensions through an analysis of the time-dependent pair-distribution function.

1.2 Particle agglomeration by swelling emulsions

Particle agglomeration is a key phenomenon in colloidal sciences and engineering. In some circumstances, such as designing stable suspensions and emulsions, particle agglomeration can lead to phase separation and destabilization of the suspension and is, thus, undesirable. In contrast, for applications such as particle self assembly (Han et al., 2017) and filtration, particle agglomeration is desirable.

From the practical applications where particle agglomeration is desirable, an important class is the extraction of small particles suspended in fluids. These problems arise in fields such as waste treatment and the recovery of small mineral particles from water. A standard technology for these applications is the process of froth flotation, in which rising air bubbles are used to recover small, hydrophobic particles suspended in a fluid (Kitchener, 1984). As the bubbles rise from the bottom of the flotation cell, they collide with the particles, which attach to the bubble surface often due to an attractive interaction (e.g., hydrophobic and van der Waals forces). The froth formed at the top of the cell is then collected.

Besides the popularity of the froth flotation method in mineral processing and waste treatment, mainly due to its low cost and practicality, the method still has its shortcomings, one of them being its low capture efficiency for small-sized particles (e.g., with diameters

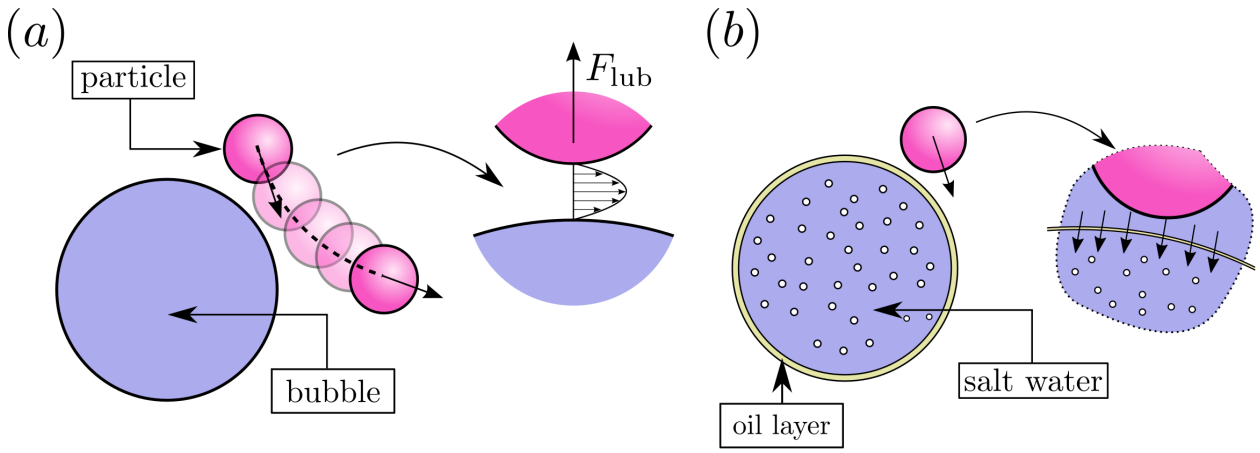

Figure 1.1: Effect of lubrication in particle capture. (a) shows the effect of lubrication in froth flotation, where, for very small particles, the lubrication forces between the particle and the bubble hinder particle capture. In contrast, for emulsion binders (b), the permeation of water through the oil interface makes it easier to squeeze the fluid layer between the particle and the interface, decreasing the axial lubrication force.

of a few microns). In these situations, the hydrophobic forces are not strong enough to overcome the lubrication resistance between the particle and bubble, resulting in the particles not getting captured, and, instead, circling around the bubble (Barnocky and Davis, 1989; Loewenberg and Davis, 1994). This process is illustrated in Figure 1.1(a).

Alternatively, another class of more efficient particle recovery methods is the capture of particles by selective oil agglomeration (Capes and Germain, 1982), where hydrophobic particles attach to oil droplets that are vigorously mixed in the fluid. For larger particles, the oil droplets act as a binder, helping particles to form agglomerates consisting of multiple particles (van Netten et al., 2014). However, these methods can be expensive, and environmentally harmful, due to the large consumption of oil in the process. To reduce the amount of oil consumption in these methods, a new method for particle agglomeration, consisting of a water-in-oil emulsion in place of the single oil droplets, was proposed by van Netten et al. (2014). The new compound binder, composed of water droplets in a surfactant-stabilized oil phase, drastically reduces the amount of oil used. This new method presented similar improvement in collision efficiency as the oil-binder methods. However, due to effects such as Ostwald ripening, the stability of such emulsions was a

limiting factor for practical applications.

To resist Ostwald ripening destabilization of the water-in-oil emulsion, van Netten et al. (2017) introduced salt in the aqueous phase, resulting in a method that required a substantially smaller amount of oil (compared to conventional oil-binder methods) to achieve almost complete recovery of particles ranging from more than 100 μm to less than 500 nm in very fast times. Although the physical mechanisms behind the increase in efficiency were initially unclear, the theoretical work by Davis and Zinchenko (2018) suggested that permeation of water through the thin oil layers could play a role in the increase in capture efficiency for small particles, as the non-zero permeability of the oil layer results in a decrease of the repulsive lubrication forces. Namely, the permeation of water through the oil membrane facilitates the full drainage of the fluid layer between the particle and the drop interfaces, allowing for particles to collide with the droplet even in the absence of attractive forces (see Figure 1.1(b)).

The work by Davis and Zinchenko (2018) investigated the binary interaction between pairs of spherical particles and droplets with a fixed size. In experiments, however, it was observed that the water-in-oil emulsion underwent a swelling process over time. This increase in size is driven by the presence of salt in the water phase of the emulsion. When the emulsion is added to fresh water, where the particles are suspended, the gradient of salt concentration produces an osmotic pressure gradient that causes an influx of water from the fresh water phase to the saltwater phase through the oil interface, resulting in an increase in volume of the saltwater droplets. As the emulsion swelling occurs in a quasi-static manner, the droplets can act as a sieve, capturing small particles. In the first part of this dissertation we aim to better understand the kinetics of drop swelling and to assess its effects on the capture of small particles.

1.3 Droplet-based microfluidics

The term *fluidics* was created as an analogy to the word *electronics* and refers to the use of hydrodynamic circuits to perform operations similar to electronic systems. Indeed, by using physical properties of fluids, it is possible to build fluidic analogs of logic gates, diodes and even complex control systems (Joyce and Gottron, 1979). Not surprisingly, studies and development of fluidic-based analogue computers date back to the same era as the early development of electronic computers. However, it was not until more recently that the field of *microfluidics* (i.e., fluidics performed in small scales) gained more attention due to a wide range of applications such as cell sorting, generation of low-polydispersity emulsions, medical diagnostic systems, particle detection, and lab-on-a-chip devices, among many others relevant applications in biotechnology and engineering.

More specifically, the subfield of droplet-based microfluidics, which refers to microfluidic applications involving the motion of a single or multiple droplets in microfluidic channels, is of particular importance, since it includes many of the main applications of microfluidics. In this context, microfluidics can be used to perform multiple operations with the droplets (Suea-Ngam et al., 2019), such as mixing (Muradoglu and Stone, 2005; Fu et al., 2019), splitting, sorting (Shields IV et al., 2015), droplet generation (Jena et al., 2023), and coalescence. More recently, microfluidic devices have also been used to perform microrheology experiments (Hsiao et al., 2017; Lin et al., 2021). These applications are illustrated in Figure 1.2.

Of course, understanding the physics involved in the motion of droplets, particles, and cells in microchannels is crucial to optimally design such microfluidic systems. To this end, much of the recent work in the literature involves the simulation of droplets inside geometries that commonly appear in microfluidic channels, such as T- and Y-shaped channel branches (Carlson et al., 2010; Navarro et al., 2020) and straight channels with square cross sections (Wang and Dimitrakopoulos, 2012; Horwitz et al., 2014; Luo et al., 2018, 2019).

However, although current multiphase simulation methods are capable of simulating droplets in complex channels, there are still gaps in the literature. For instance, most of the current literature for three-dimensional microfluidic channels is focused on regular geometries (i.e., with uniform branches). However, it is known that the geometry of the channels strongly influences drop motion and splitting (Navarro et al., 2021). Moreover, the effect of the channel depth on the motion of droplets through irregular channel geometries has also not been properly assessed. Also, multiphase Navier-Stokes solvers often have a hard time obtaining precise results at very low Reynolds numbers, where microfluidic devices usually operate, besides often requiring substantially finer meshes to deal with the interaction between drops/particles and the channel walls and corners. Hence, using techniques such as boundary-integral methods, which are formulated for the regime of low Reynolds numbers, can be advantageous. However, to our knowledge, boundary-integral simulations of droplets in bifurcating channels have been focused either on simple geometries, such as straight channels with square cross sections, two-dimensional problems, and deep channels.

In this work, we developed a boundary-integral algorithm capable of simulating drop

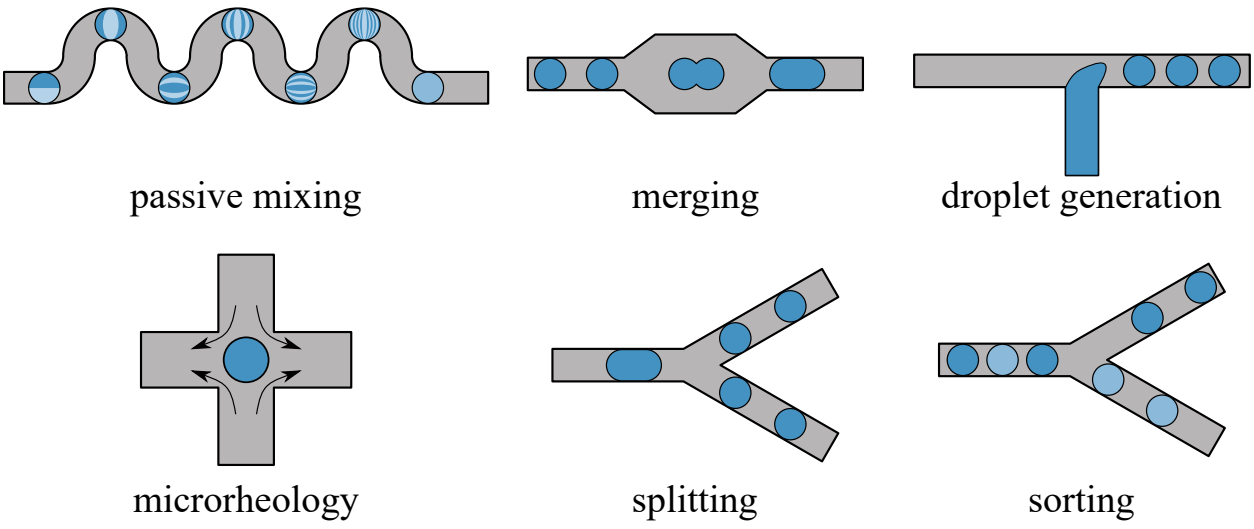

Figure 1.2: Different applications of drop-based microfluidics (diagrams inspired by the representations in Suea-Ngam et al. (2019)).

motion in three-dimensional channels of a wide variety of shapes. We use our algorithm to investigate the motion of droplets in these complex geometries, assessing the effects of the channel depth on drop dynamics. We also use our algorithm to explore the control of shape and position of droplets inside hydrodynamic traps, showing how complex flow modes can be used to induce active mixing inside the droplet, which can be useful for designing active microreactors.

1.4 Dissertation overview

This dissertation consists of nine chapters, plus appendices, divided into six different parts. The chapter structure is outlined in Figure 1.3. In Part I, Introduction, we introduce the problems covered in this work and review the fundamental principles of low-Reynolds-number hydrodynamics used throughout the dissertation. Part II covers the modeling of particle agglomeration by swelling emulsion binders. More specifically, Chapters 3 and 5 refer to the problem of particle capture itself, where we explore the collision efficiency between rigid particles and semi-permeable, swelling droplets. In Chapters 4 and 6, we develop models for swelling of the droplets and emulsions, by considering both a diffusion-limited swelling model and a network model for double emulsions.

In Part III, we shift our focus to the investigation of drop motion in microchannels. In Chapter 7, we describe our boundary-integral method used in the simulations and explore the motion of droplets in channels with irregular geometries, assessing the effects of channel depth on drop motion. In Chapter 8, we investigate the problem of shape control and active mixing of droplets in a hydrodynamic trap. In Part IV, we present some concluding remarks and suggestions for future works. Part V is the bibliography. Part VI includes appendices, which supplement the results presented in the main chapters.

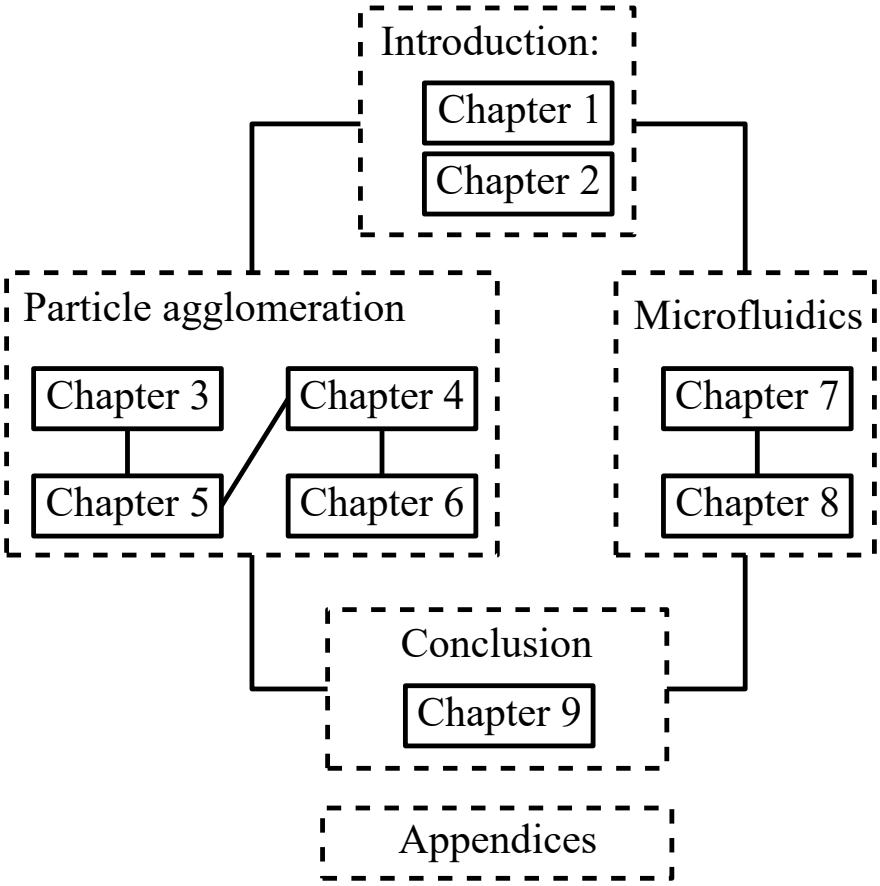

Figure 1.3: Chapter structure for the dissertation. The solid lines connecting chapters represent dependence of a chapter on a previous one.

CHAPTER 2

GENERAL THEORY

2.1 Low-Reynolds-number hydrodynamics

As the focus of our work is an investigation of the motion of droplets and small particles in fluids, below is a brief description of the general theory of fluid mechanics in small scales, which is largely used in this dissertation. The motion of a Newtonian liquid is governed by the incompressible Navier-Stokes equations:

$$\rho\left(\frac{\partial \mathbf{u}}{\partial t} + \mathbf{u}\cdot\nabla\mathbf{u}\right) = \mathbf{f} + \nabla\cdot\mathbf{T}, \tag{2.1}$$

$$\nabla\cdot\mathbf{u} = 0, \tag{2.2}$$

where equation (2.1) comes from the balance of linear momentum and equation (2.2) comes from the mass balance for an incompressible fluid. In this general form, equation (2.1) is known as the Cauchy equation. Moreover, $\mathbf{u}$ is the velocity field of the fluid, $\mathbf{f}$ is a body force (often given by the gravitational force), and $\mathbf{T}$ is the the stress tensor, which, for a Newtonian fluid, is given by the following constitutive equation:

$$\mathbf{T} = -p\mathbf{1} + 2\mu\mathbf{E}, \tag{2.3}$$

where $\mathbf{1}$ is the identity tensor, μ is the dynamical viscosity, and $\mathbf{E} = (\nabla\mathbf{u} + (\nabla\mathbf{u})^T)/2$ is the symmetric part of the velocity gradient tensor. Combining equations (2.1) and (2.3), we can write the momentum balance equation in its more well-known form:

$$\rho\left(\frac{\partial\mathbf{u}}{\partial t} + \mathbf{u}\cdot\nabla\mathbf{u}\right) = \mathbf{f} - \nabla p + \mu\nabla^2\mathbf{u}. \tag{2.4}$$

For the types of systems of interest in this work, most of the motion happens in the low-Reynolds-number (plus moderate to low Strouhal number) regime, meaning that the inertial term at the left hand side of equation (2.4) can be neglected, resulting in the Stokes equations:

$$\mu\nabla^2\mathbf{u} = \nabla p - \mathbf{f}, \quad \nabla\cdot\mathbf{u} = 0. \tag{2.5}$$

2.1.1 The fundamental solution of the Stokes equations

One of the most important concepts in the theory of linear partial differential equations is the Green's function, which is the kernel[1] of the inverse operator for the linear differential problem. For the Stokes equations, the Green's function is associated with the solution of the following fundamental problem:

$$\nabla\cdot\tilde{\mathbf{T}} = \delta(\mathbf{r})\mathbf{F}, \tag{2.6}$$

where $\delta(\mathbf{r})$ is the Dirac delta distribution. The solution for the fundamental Stokes problem is given by $\tilde{\mathbf{u}}(\mathbf{r}) = \mathbf{G}(\mathbf{r})\cdot\mathbf{F}/\mu$ and $\tilde{\mathbf{T}}(\mathbf{r}) = \boldsymbol{\tau}(\mathbf{r})\cdot\mathbf{F}$, where $\mathbf{G}$ is the Oseen tensor, or Stokeslet, and $\boldsymbol{\tau}$ is the fundamental stresslet, given, respectively, by

$$\mathbf{G}(\mathbf{r}) = -\frac{1}{8\pi}\left(\frac{\mathbf{1}}{r} + \frac{\mathbf{rr}}{r^3}\right) \; ; \; \boldsymbol{\tau}(\mathbf{r}) = \frac{3}{4\pi}\frac{\mathbf{rrr}}{r^5}. \tag{2.7}$$

Using the fundamental solution we can write the formal solution for the unbounded, non-homogeneous Stokes problem $\nabla\cdot\mathbf{T} = -\mathbf{f}$ for an arbitrary force density $\mathbf{f}$ as

[1]Here, we are using the term kernel meaning the function defining an integral operator.

$$\mathbf{u}(\mathbf{y}) = -\frac{1}{\mu}\int_{\mathbb{R}^3} \mathbf{G}(\mathbf{x}-\mathbf{y})\cdot\mathbf{f}(\mathbf{x})\mathrm{d}V_{\mathbf{x}}, \tag{2.8}$$

where $\mathbf{y}$ is a given point in space and the convolution integral in $\mathbf{x}$ ranges over the whole space.

2.1.2 The reciprocal theorem

One of the most powerful tools in low-Reynolds-number hydrodynamics is the reciprocal theorem. This theorem, although simple, is fundamental for obtaining several important results, including the boundary-integral representation of the Stokes equations, which is extensively used in this work.

Let us consider two different Stokes flows $(\mathbf{u}_1, p_1)$ and $(\mathbf{u}_2, p_2)$ for a fluid with viscosity μ such that $\nabla\cdot\mathbf{T}_1 = \mathbf{f}_1$ and $\nabla\cdot\mathbf{T}_2 = \mathbf{f}_2$. As both flows are incompressible, the following identity follows:

$$\nabla\cdot(\mathbf{T}_1\cdot\mathbf{u}_2) - \mathbf{f}_1\cdot\mathbf{u}_2 = 2\mu\mathbf{E}_1 : \mathbf{E}_2 = \nabla\cdot(\mathbf{T}_2\cdot\mathbf{u}_1) - \mathbf{f}_2\cdot\mathbf{u}_1. \tag{2.9}$$

The integration of equation (2.9) over the fluid volume Ω, combined with the divergence theorem, results in the following reciprocal relationship:

$$\int_{\partial\Omega} \mathbf{t}_1\cdot\mathbf{u}_2\ \mathrm{dS} - \int_{\Omega}\mathbf{f}_1\cdot\mathbf{u}_2\ \mathrm{dV} = \int_{\partial\Omega}\mathbf{t}_2\cdot\mathbf{u}_1\ \mathrm{dS} - \int_{\Omega}\mathbf{f}_2\cdot\mathbf{u}_1\ \mathrm{dV}, \tag{2.10}$$

which is the most general form of the reciprocal theorem. Here, $\mathbf{t}_i = \mathbf{n}\cdot\mathbf{T}_i$ is the surface traction, $\mathbf{n}$ is the unit normal external to Ω, and $\partial\Omega$ is the boundary of Ω. If both flows satisfy the homogeneous Stokes equations (i.e., in the absence of body forces), the reciprocal theorem reduces to its most well-known form:

$$\int_{\partial\Omega}\mathbf{t}_1\cdot\mathbf{u}_2\ \mathrm{dS} = \int_{\partial\Omega}\mathbf{t}_2\cdot\mathbf{u}_1\ \mathrm{dS}. \tag{2.11}$$

As we shall see in the following section, the reciprocal theorem plays an important role when deriving the boundary-integral equations for a deformable droplet.

2.1.3 The boundary-integral formulation of the Stokes equations

Like other time-independent, elliptic linear differential equations, the homogeneous Stokes equations can be re-written as a set of boundary-integral equations. Let us consider the simple problem of a Stokes flow inside a closed domain Ω. We start from the more general form of the reciprocal theorem in equation (2.10) for the case where one of the flows, $(\mathbf{u}, p)$, is a homogeneous Stokes flow and the second flow is the fundamental solution described in section 2.1.1. In this case, we have

$$\int_\Omega \delta(\mathbf{x}-\mathbf{y})\mathbf{u}\, dV_\mathbf{x} = -\frac{1}{\mu}\int_{\partial\Omega} \mathbf{t}(\mathbf{x})\cdot\mathbf{G}(\mathbf{x}-\mathbf{y})\, dS_\mathbf{x} + \int_{\partial\Omega} \mathbf{n}(\mathbf{x})\cdot\boldsymbol{\tau}(\mathbf{x}-\mathbf{y})\cdot\mathbf{u}(\mathbf{x})\, dS_\mathbf{x} \quad (2.12)$$

From the definition of the Dirac delta distribution, the left hand side of equation (2.12) is zero when $\mathbf{y} \notin \Omega$ and $\mathbf{u}(\mathbf{y})$ when $\mathbf{y} \in \Omega\backslash\partial\Omega$. Hence, the flow velocity at any point of the fluid domain Ω can be represented by a distribution of hydrodynamic monopoles (i.e., single layer) and dipoles (i.e., double layer) on the boundary, with potential densities given by the traction and velocities at the boundary. However, the usual boundary conditions of Stokes flow often determine only one of these quantities at a given boundary point, not both. The additional data can be found by solving the boundary-integral equations that result from taking the limit of equation (2.12) when $\mathbf{y} \to \mathbf{y}^* \in \partial\Omega$, which, for a Lyapunov surface, results in

$$\frac{1}{2}\mathbf{u}(\mathbf{y}) = -\frac{1}{\mu}\int_{\partial\Omega} \mathbf{t}(\mathbf{x})\cdot\mathbf{G}(\mathbf{x}-\mathbf{y})\, dS_\mathbf{x} + \int_{\partial\Omega} \mathbf{n}(\mathbf{x})\cdot\boldsymbol{\tau}(\mathbf{x}-\mathbf{y})\cdot\mathbf{u}(\mathbf{x})\, dS_\mathbf{x} \quad (\mathbf{y}\in\partial\Omega). \quad (2.13)$$

The integrals on the right hand side of equation (2.13) are understood in the sense of Cauchy principal values:

$$\mathscr{PV}\int_S f(\mathbf{x})dS = \lim_{\varepsilon\to 0}\int_{S\backslash S_\varepsilon(\mathbf{y})} f(\mathbf{x})dS, \quad (2.14)$$

where $\mathbf{y}$ is the singular point, and $S_\varepsilon(\mathbf{y}) = S\cap B_\varepsilon(\mathbf{y})$, where $B_\varepsilon(\mathbf{y}) = \{\mathbf{x}\in\mathbb{R}^3 | \quad \|\mathbf{x}-\mathbf{y}\| < \varepsilon\}$ is an open ball in $\mathbb{R}^3$ with radius ε centered at the singular point $\mathbf{y}$.

For problems where either the velocity or stress is defined at the boundary collocation points, equation (2.13) can be discretized into a system of linear algebraic equations that can be solved. This was, in fact, the first application of boundary-integral methods in hydrodynamics (Youngren and Acrivos, 1975) and was used to solve the motion of an arbitrarily-shaped particle in Stokes flow. However, for Dirichlet-type problems, equation (2.13) has the disadvantage of being a Fredholm equation of the first kind for the traction $\mathbf{t}$, which are known for being ill-posed. Alternatively, for force- and torque-free Dirichlet problems, it is possible to represent the flow in terms of the double-layer potential only. Namely,

$$\mathbf{u}(\mathbf{y}) = 2\int_{\partial\Omega} \mathbf{n}(\mathbf{x}) \cdot \boldsymbol{\tau}(\mathbf{x}-\mathbf{y}) \cdot \mathbf{q}(\mathbf{x}) \mathrm{d}S_{\mathbf{x}} \tag{2.15}$$

for $\mathbf{y} \in \Omega \backslash \partial\Omega$. Here, $\mathbf{q}$ is a generalized potential density to be determined. By taking the limit of $\mathbf{y}$ approaching the surface, we obtain a Fredholm boundary-integral equation of the second-kind for $\mathbf{q}$, given by

$$\mathbf{u}(\mathbf{y}) = 2\int_{\partial\Omega} \mathbf{n}(\mathbf{x}) \cdot \boldsymbol{\tau}(\mathbf{x}-\mathbf{y}) \cdot \mathbf{q}(\mathbf{x}) \mathrm{d}S_{\mathbf{x}} + \mathbf{q}(\mathbf{y}) \quad (\mathbf{x} \in \partial\Omega). \tag{2.16}$$

This double-layer representation will be extensively used in chapters 7 and 8 to calculate the flow inside simply-connected microfluidic channels and inside droplets for a given interfacial velocity distribution. The boundary-integral equation 2.16 constitutes a well-posed problem[2] but has multiple solutions due to the spectrum of the double-layer operator, an issue that is fixed by partial deflation of the double-layer operator (see chapter 7).

For problems such as the motion of a droplet in Stokes flow, which involves a jump condition at the interface, a combination of the boundary-integral equations for the flow inside and outside the droplet is needed to find the boundary-integral equation for the

[2]Although the integral kernels defined by the single- and double-layer operators are singular, this singularity is weak, meaning that a slightly modified version of Fredholm theory can be used to guarantee existence, uniqueness, and well-posedness of solutions (Kim, 1992; Kim and Karrila, 2013).

interface velocity of the droplet. This combination is done in Appendix A for a droplet in a microfluidic channel.

2.2 Osmotic pressure and permeation through an interface

One of the main concepts used in the first part of this dissertation is the permeation of water through an interface driven by a difference in osmotic pressure. In this section we provide an brief overview of osmotic flux in the context of our problem. The results in this section will come into play when investigating the swelling of a saltwater droplet and double emulsions. To begin, let us consider a two-component system consisting of a fresh water phase and a saltwater phase. The phases are separated by a semi-permeable membrane that allows for the passage of solvent (water) but not solute (salt). This simple setup is shown in Figure 2.1(a).

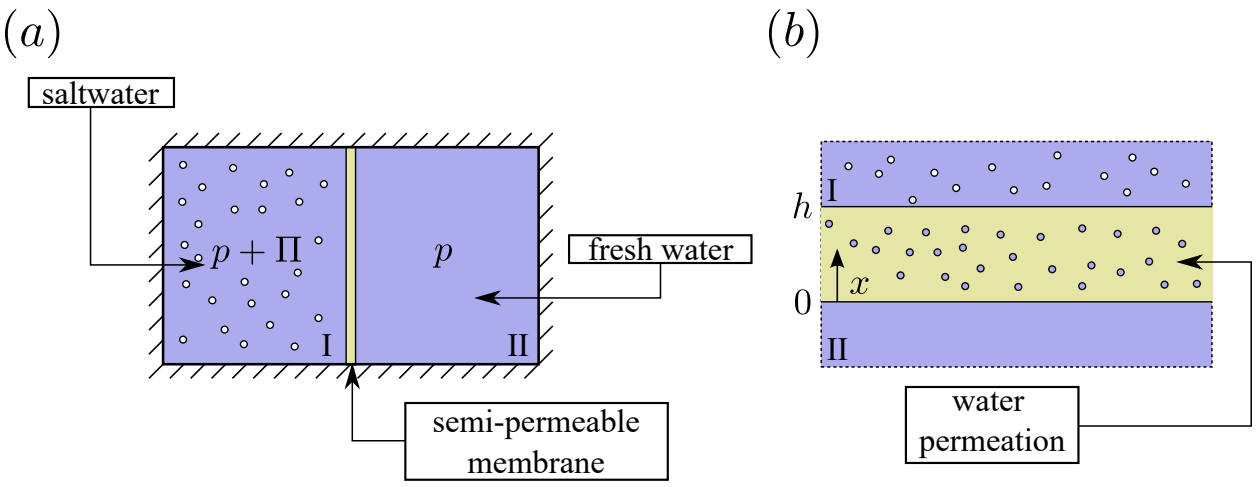

Figure 2.1: Osmotic permeation of water through a semi-permeable layer. The diagrams illustrate (a) the osmotic pressure produced by the presence of salt in one side of the system and (b) the transport of water through a semi-permeable oil layer. Blue represents water, yellow represents oil or a membrane, and small white circles are salt.

If the two volumes are fixed, the condition for thermodynamic equilibrium is that the chemical potential of water in both phases is the same. That is:

$$\mu_{\mathrm{I}}^{w} = \mu_{\mathrm{II}}^{w} \tag{2.17}$$

The chemical potential of the solvent in a binary mixture is a function of temperature, pressure, and the solvent mass fraction, i.e., $\mu_w(T, p, x_s)$. As we are working in a constant temperature regime, we will neglect the temperature dependency and re-write the equilibrium condition as

$$\mu_w(p + \Pi, x_w) = \mu_w^0(p), \tag{2.18}$$

where x_w is the molar fraction of water, μ_w^0 is the chemical potential for a pure-water solution (i.e., $x_w = 1$), and the extra pressure Π in the saltwater region is called the osmotic pressure. From classical thermodynamics, we can write the LHS of equation (2.18) as:

$$\mu_w(p + \Pi, x_w) = \mu_w^0(p + \Pi) + RT \log(\gamma_w x_w), \tag{2.19}$$

where $\gamma_w(T, p+\Pi)$ is the activity coefficient of water. From the Gibbs-Duhem relationship for a single-phase fluid, we have

$$\mu_w^0(p + \Pi) - \mu_w^0(p) = \int_p^{p+\Pi} \nu dp, \tag{2.20}$$

where $\nu = V/N$ is the molar volume. Considering water to be an incompressible liquid results in:

$$\nu\Pi + RT \log(\gamma_w x_w) = 0 \tag{2.21}$$

As, for a dilute suspension of salt in water, $\gamma_w \approx 1$, and $x_s = 1 - x_w \ll 1$, we have:

$$\Pi = cRT, \tag{2.22}$$

where $c = N_s/V$ is the molar density of salt. Equation (2.22) is known as Van't Hoff law. This pressure imbalance means that, if the membrane was suddenly allowed to move, it would move towards the fresh water phase, in order to reach mechanical equilibrium. If the interface motion happens quasi-statically and the membrane is considered to be a Darcy porous medium with permeability K, the velocity of the porous medium (which coincides with the velocity of water in the membrane frame of reference) is given by:

$$u_s = K\Pi = cKRT. \tag{2.23}$$

Of course, an oil layer is not a porous medium. Instead, the water transport through the oil layer happens because of diffusion, as represented in Figure 2.1(b). Considering local thermodynamic equilibrium at the saltwater and oil+water interfaces, the concentration of water at the top of the oil layer is given by Henry's law:

$$c_w(h) = H_s p_{sw} = H_s(p + \Pi), \tag{2.24}$$

where H_s is the solubility of water in oil. Applying the same reasoning to the oil and fresh water interface results in the dissolved water concentration at the bottom of the oil layer:

$$c_w(0) = H_s p_w = H_s p. \tag{2.25}$$

Considering that water diffuses through the oil layer with diffusivity D_{wo}, at steady-state, the diffusive flux of water through the oil layer is given by:

$$J_w = \frac{D_{wo} H_s \Pi}{h}. \tag{2.26}$$

Hence, the osmotic transport of water through an oil layer is similar to the transport of water through a porous membrane with permeability $K = D_{wo} H_s / h$. Note that we are assuming here that water is transported across the oil layer by dissolution and molecular diffusion. Since the water/oil/water emulsions employed by van Netten et al. (2017) are surfactant stabilized , another possibility is that reverse micelles form and provide a vehicle for water transport.

Part II

Particle capture by permeable droplets

CHAPTER 3

PARTICLE CAPTURE BY EXPANDING DROPLETS

This work was originally published in the *Journal of Fluid Mechanics* 912 (2021) A11 with co-author Robert H. Davis

Synopsis

This chapter investigates the two-particle dynamics of a solid particle and a semi-permeable spherical drop that expands due to osmosis in an external, pure-extensional flow field. A dimensionless engulfment parameter measures the relative effects of droplet growth and convective flow. The computational results from numerical integration determine a transient collision efficiency, which describes the influence of hydrodynamic interactions and osmotic flow on particle capture. The results show that drop expansion, which decays slowly with time, greatly increases particle capture rates, especially for small particles. Moreover, as the engulfment parameter increases, there is a transition from flow-dominated capture to expansion-dominated capture. For the case of a non-expanding droplet, we provide a numerical solution for the transient pair distribution function, which enables us to explain the transient particle capture rate in terms of the microstructure of the suspension. Furthermore, we derive an analytical expression for the initial collision efficiency at zero times, which agrees with our numerical data. The numerical results for non-expanding droplets at long times show increasing collision efficiency as the permeability increases and when the size ratio is near unity, in agreement with previous steady-state calculations.

3.1 Introduction

Froth flotation, in which rising air bubbles are used for recovering hydrophobic particles, has been traditionally used in industry (Kitchener, 1984; Wills and Napier-

Munn, 2006). However, this method is not efficient for particles smaller than about 20 μm, which, instead of being captured by the bubble, move around it (Barnocky and Davis, 1989; Loewenberg and Davis, 1994; Mehrotra et al., 1983; Miettinen et al., 2010). An alternative to froth flotation is provided by the more efficient hydrophobic oil-binder techniques (Mehrotra et al., 1983; Sirianni et al., 1969; van Netten et al., 2014, 2016). These methods, however, can be expensive due to the amount of oil required. The present project is motivated by a more recent particle-capture technique, which circumvents the limitations of froth flotation and oil-binder techniques (van Netten et al., 2017; Galvin and van Netten, 2017). This method consists of using a binder containing droplets filled with salt water and covered by thin, surfactant-stabilized, semi-permeable oil layers. The presence of salt inside the droplet results in an osmotic flow that increases particle capture.

Several works have used two-particle dynamics to characterize aggregation phenomena (*e.g.*, Zeichner and Schowalter (1977); Davis (1984); Rother and Davis (2001); Phan et al. (2003); Roure and Cunha (2018)). In a recent work, Davis and Zinchenko (2018) found both semi-analytical and asymptotic solutions (*i.e.*, far-field and near-field) for the translational mobility functions (Batchelor and Green, 1972b) for the relative motion of a solid particle and a semi-permeable drop interacting in creeping flow for linear external flows. In the work of Davis and Zinchenko (2018), the collision rates were found in the absence of osmotic flow. However, it should be noted that their results regarding the collision rates, as well as the ones in the aforementioned studies, were obtained in a quasi-steady context, in the sense that they assume a steady-state pair distribution function.

The goal of the present work is to investigate the two-particle dynamics of a solid particle and an expanding semi-permeable drop in the presence of both osmotic flow and an external, extensional flow field. The numerical integration of the relative particle motion is performed using the mobility functions found in Davis and Zinchenko (2018). The computational results from the numerical integration are used for calculating the particle-drop collision efficiency. Rather than making a quasi-steady assumption, we

consider both the short-term dynamics, as the particle-drop pair distribution function is being established, and the long-term dynamics, as the drop expands. We compare our results with an analytical result for the collision efficiency at time zero and with the steady-state solution (in the case of non-expanding droplets) by Davis and Zinchenko (2018).

The equivalence between our approach and the standard quasi-steady one relies on the expectation that, in the context of non-expanding droplets, an initially uniform probability distribution will eventually approach a steady state, as calculated by Batchelor and Green (1972a). There are several works concerning the steady-state pair distribution function for shear and pure strain flows (*e.g.*, Morris and Katyal (2002); Brady and Morris (1997); Blanc et al. (2013); Wilson (2005)). These works use distinct approaches, ranging from experimental to theoretical. However, all of them focus on steady-state distributions. Although works such as Gadala-Maria and Acrivos (1980) present some transient experiments, the transient regime of microstructure is rarely explored in the literature. Hence, in the present work, we provide a numerical solution of the transient pair distribution function for the case of a non-expanding droplet, which enables us to better explain the transient particle capture rate in terms of the suspension microstructure. This solution, besides justifying the assumptions made in the work, provides an estimation of the time it takes to reach the steady state.

3.1.1 Problem description and drop growth

We consider the creeping motion of a solid spherical particle relative to a semi-permeable spherical droplet filled with saltwater in the presence of a linear flow at infinity. At the surface of the rigid particle, we consider both impenetrability and no-slip boundary conditions. At the drop interface, although we still consider a no-slip boundary condition, with the membrane allowed to rotate to remain torque-free, we allow the existence of a normal component of the fluid velocity, as the drop is semi-permeable. The relative

velocity through the interface is described by Darcy's law as being proportional to the hydrodynamic pressure jump. We also assume continuity of velocity at the drop's interface and that changes in the viscosity and density of the fluid inside the drop due to the presence of salt are negligible. Details concerning analytical and asymptotic solutions for the hydrodynamic problem are provided by Davis and Zinchenko (2018).

The normal component of the fluid velocity relative to the semi-permeable interface is given by Darcy's law:

$$-(\mathbf{u}-\mathbf{u}_s)\cdot\hat{\mathbf{n}}|_S = K(\Pi+\Delta p), \tag{3.1}$$

where S represents the drop surface, $\hat{\mathbf{n}}$ is the outward unit normal vector, K is the oil-layer or membrane permeability, Π is the osmotic pressure, Δp is the jump in dynamic pressure across the thin oil layer at the drop interface, $\mathbf{u}_s$ is the velocity of the interface and $\mathbf{u}$ is the fluid velocity. The osmotic pressure for dilute solutions may be estimated by Van't Hoff's law:

$$\Pi \approx RTc_s, \tag{3.2}$$

where c_s is the salt concentration near the drop's interior surface, R is the ideal gas constant, and T is the absolute temperature. The pressure jump Δp is of order $\sim \mu\dot{\gamma}$, which is much smaller than the osmotic pressure jump Π in typical cases. Here, μ is the fluid viscosity and $\dot{\gamma}$ is the intensity of the far-field extensional flow, whose undisturbed velocity field is given by $(\dot{\gamma}x, \dot{\gamma}y, -2\dot{\gamma}z)$.

As we are assuming flow of an incompressible liquid, the osmotic flow will result in an increase of the drop's size. To find the expansion rate of the drop, we note that the terms $\mathbf{u}\cdot\hat{\mathbf{n}}|_S$ and Δp in equation (3.1) cancel out due to the boundary conditions of the hydrodynamic problem. It is noted that the term Π does not contribute to the velocity of the fluid at the boundary, as this extra source term would result in a violation of continuity, as the integral $\int_S \mathbf{u}\cdot\hat{\mathbf{n}}\, dS$ at the drop's interface would be nonzero. Thus, as we consider the

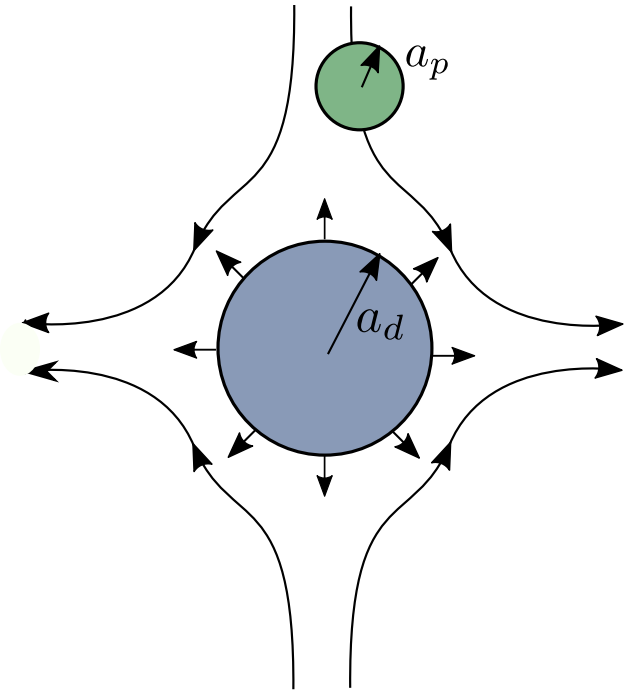

Figure 3.1: Schematic of a solid particle interacting with an expanding drop in an external extensional flow field.

fluid motion to be quasi-stationary, as drop expansion happens slowly, the hydrodynamic problem at each time is reduced to the same one investigated by Davis and Zinchenko (2018), with the same boundary conditions. Again, we refer to the aforementioned paper for the full analysis and solution of the hydrodynamic problem both outside and inside the drop. Considering that the interface velocity $\mathbf{u}_s = u_s \hat{\boldsymbol{e}}_r$ is purely radial, as the drop keeps its spherical shape, so $\hat{\mathbf{n}} = \hat{\boldsymbol{e}}_r$, the velocity of the interface is given by:

$$u_s = KRTc_s. \tag{3.3}$$

As the drop expands, its interface moves outward through the surrounding suspension, with velocity $\mathbf{u}_s$, without modifying the fluid velocity $\mathbf{u}$, and it acts as a passive sieve that captures or engulfs the particles that it encounters in the suspension. Particles are also swept to this interface by the external flow, as shown in Figure 5.1.

From this point on, quantities are nondimensional unless noted otherwise. For the nondimensionalization of the problem, we use a_{d0} as the length scale and $\dot{\gamma}^{-1}$ as the time

scale, where a_{d0} is the initial drop radius. Considering a small spherical drop with instant relaxation (*i.e.*, in a regime of low Péclet numbers for the salt molecules), conservation of mass yields a differential equation for the non-dimensional drop radius:

$$da_d/dt = Eg\ a_d^{-3}, \tag{3.4}$$

where

$$Eg = KRTc_0/(\dot{\gamma} a_{d0}) \tag{3.5}$$

is the engulfment parameter, which represents the ratio between osmotic permeate flow and external convective flow and c_0 is the initial salt concentration in the drop. The word engulfment here is used in analogy to the phenomenon in solidification where particles are engulfed by a solidifying or freezing moving interface (*e.g.*, Omenyi and Neumann (1976); Asthana and Tewari (1993); Stefanescu et al. (1998); Mukherjee and Stefanescu (2004)). This parameter can also be thought as a ratio between the characteristic dimensional flow time $\tau_{fl} = \dot{\gamma}^{-1}$ and the characteristic dimensional drop expansion time $\tau_{eng} = a_{d0}/(KRTc_0)$. The engulfment parameter can be decomposed as $Eg = K^* c_0 RT/\mu\dot{\gamma}$, in which the first term is the nondimensional permeability $K^* = K\mu/a_{d0}$, which is usually small (Davis and Zinchenko, 2018), and the second term is the ratio between osmotic and viscous pressures, which is usually large. Thus, Eg can take on a broad range of values. In particular, Davis and Zinchenko (2018) noted that $\mu K \approx 10^{-4}$ μm for microfiltration membranes, yielding $K^* = \mu K/a_{d0} \approx 10^{-6} - 10^{-4}$ for $a_{d0} = 1 - 100$ μm. Then, for $\mu = 0.01$ g/cm-s, $RTc_0 = 10^6$ g/cm-s^2 (*i.e.*, $c_0 \approx 0.04$ M at room temperature), and $\dot{\gamma} = 10^3$ s^{-1}, Eg $= 0.1 - 10$. As another example, Matsumoto et al. (1980) examined the swelling of small, oil-covered water drops and globules with $a_{d0} = 2 - 10$ μm, $c_0 = 0.06 - 0.6$ M, and corresponding initial swelling rates of $KRTc_0 = \mathcal{O}(10^{-4} - 10^{-3}$ cm/s), from which $\mu K = \mathcal{O}(10^{-8}$ μm), $K^* = \mathcal{O}(10^{-9} - 10^{-8})$ and $Eg \approx 0.1 - 10$ for very low shearing of $\dot{\gamma} = 1 s^{-1}$. Corresponding permeabilities for the experiments of van Netten et al. (2017) are thought

to be somewhat higher, due to active water transport by micelles, but quantitative values are not available because swelling experiments with much larger binder fragments for their system exhibited diffusion limitations (DeIuliis et al., 2021).

For constant membrane permeabilities, equation (3.4) can be solved analytically, yielding

$$a_d(t) = (1 + 4\,Eg\,t)^{1/4}. \tag{3.6}$$

From equation (3.6), the drop expands with time due to the osmotic flow. The flux across the drop interface, however, decreases with time due to dilution of the internal salt water, resulting in a decrease of expansion effects at large times. The time it takes for expansion effects to become negligible can be estimated by a scaling argument. As pointed out before, the ratio between the osmotic and hydrodynamic pressure differences is of order $Eg/(K^* a_d^3(t))$. Hence, for this ratio to be small, we should have $a_d(t) \gg (Eg/K^*)^{1/3}$. For rapid diffusion, $a(t) \sim (4Eg\,t)^{1/4}$ at large times. Thus, for the hydrodynamic effects to dominate over osmotic ones, we should have $t \gg K^{*-4/3} Eg^{1/3}$, which can be quite large for $K^* \ll 1$ and $Eg = \mathcal{O}(1)$.

3.2 Two-particle dynamics

3.2.1 Kinematic equations

Following Batchelor and Green (1972b), the general expression for the relative velocity between two smooth, spherical particles freely suspended in a linear flow field at small Reynolds number is

$$\mathbf{V} = \boldsymbol{\Omega}^\infty \wedge \mathbf{r} + \mathbf{E}^\infty \cdot \mathbf{r} - \left[A(r)\frac{\mathbf{rr}}{r^2} + B(r)\left(\mathbf{1} - \frac{\mathbf{rr}}{r^2}\right)\right] \cdot \mathbf{E}^\infty \cdot \mathbf{r}, \tag{3.7}$$

where $A(r)$ and $B(r)$ are the so-called *mobility functions*, $\mathbf{r}$ is the vector from the center of the drop to the center of the particle, $r = \|\mathbf{r}\|$, and $\boldsymbol{\Omega}^\infty$ and $\mathbf{E}^\infty$ are the undisturbed rotation

vector and rate-of-strain tensor, respectively, for the far-field flow. These mobility functions arise in the solution of the hydrodynamic problem at low Reynolds number and are related to the intensity of hydrodynamic interaction between the particles, which cause them to deviate from the undisturbed flow streamlines. Both functions A and B vanish when the distance between the particle and the drop goes to infinity, as hydrodynamic interactions become weaker. For non-permeable surfaces, the quantity $1-A$ goes to zero as the particle approaches the drop, which prevents contact in finite time, unless additional attractive forces are present. In contrast, the presence of a semi-permeable interface mitigates this lubrication resistance, allowing the particle and the drop to collide. In the context of the present problem, these functions depend on the non-dimensional permeability and the ratio between particle and drop radii (Davis and Zinchenko, 2018). Although there is an implicit dependence of the mobility functions on the engulfment parameter and time (due to the changing radii ratio), there is no explicit dependence of the mobility functions on the expansion rate, as we are assuming the motion to be quasi-stationary for small Reynolds numbers (*i.e.*, the diffusion of vorticity is much faster than the motion of the particles or the expansion rate). By definition of a pure extensional flow, the rotation vector is $\boldsymbol{\Omega}^{\infty} = \mathbf{0}$ and the nondimensional strain rate tensor at infinity is given by

$$\mathbf{E}^{\infty} = \begin{bmatrix} 1 & 0 & 0 \\ 0 & 1 & 0 \\ 0 & 0 & -2 \end{bmatrix}. \tag{3.8}$$

Thus, in Cartesian components, the equations of motion are

$$dx/dt = \quad (1-B)x + E\,x, \tag{3.9}$$

$$dy/dt = \quad (1-B)y + E\,y, \tag{3.10}$$

$$dz/dt = -2(1-B)z + E\,z, \tag{3.11}$$

where

$$E = (B - A)(x^2 + y^2 - 2z^2)/r^2. \tag{3.12}$$

Note that the present set of differential equations is not autonomous for the case of an expanding drop, as the mobility functions depend on the decreasing ratio between the radii of the particle and drop, and, consequently, on time.

3.2.2 Particle trajectories

The numerical integration of the relative particle trajectories was performed using a 4^{th}-order Runge-Kutta scheme. The exact solution of the hydrodynamic problem by Davis and Zinchenko (2018) in terms of bi-spherical harmonics was used to evaluate the mobility functions. We also employed an adaptive time step at small gaps, to avoid particle-drop overlap in the intermediate Runge-Kutta steps. The drop-size evolution was described analytically by equation (3.6). As illustrated in Figure 3.2, there are some initial conditions that lead to collision between the particle and the drop and others that do not. Hence, we perform several simulations for trajectories starting at varied initial positions to determine starting locations that lead to particle-drop collision within a certain time.

3.3 Collision efficiency

In this section, we start by showing the equivalence of the multiple definitions of the pair collision rate used in this work. Furthermore, we proceed to derive an analytical expression of the ideal pair collision rate between a particle with an expanding drop at time zero. This initial collision rate is used in latter sections to validate the numerical results for the collision efficiency.

3.3.1 Pair collision rates

The problem of calculating the rates at which two different species collide with one another is present in many branches of science, such as chemistry and colloidal sciences. In a

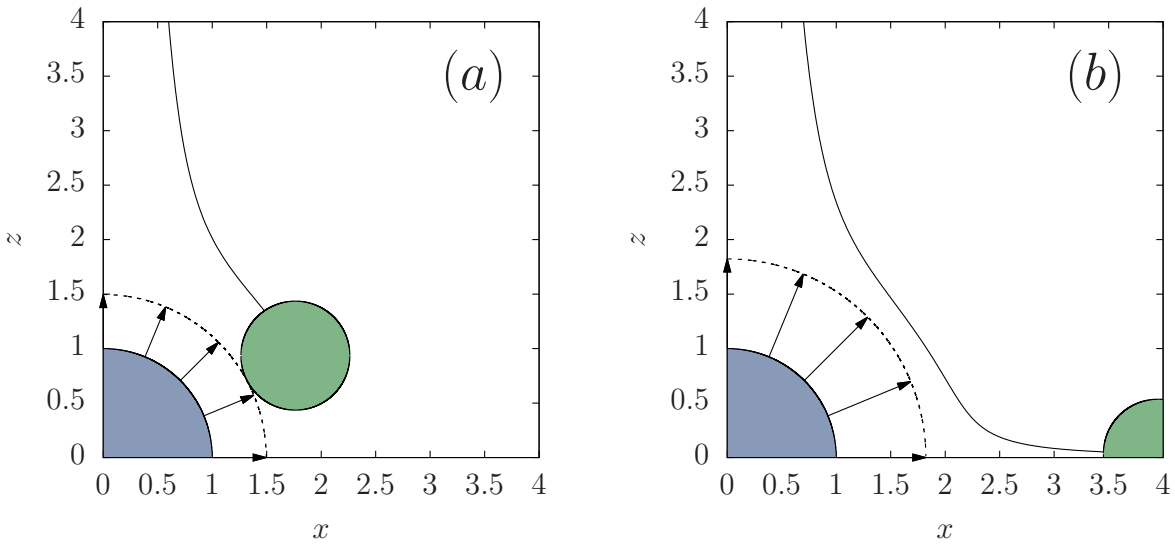

Figure 3.2: Trajectory simulation for $Eg = 1.0$, $K^* = 10^{-4}$, $a_p = 0.5$, and $z_0 = 4.0$, with (a) $x_0 = 0.6$ and (b) $x_0 = 0.7$. The dashed line represents the final interface of the drop at the end of the trajectory. In (a), the solid particle is captured by the expanding drop, whereas trajectory (b) does not result in aggregation.

classical point of view, this problem is closely related to the scenario of particles colliding with a surface. Namely, a particle will collide with another one when the surfaces make contact.

For a given surface S and given particle dynamics, we define $V_{col}(t; S)$ (the S here will be usually omitted, reading $V_{col}(t)$) as the collisional volume of the surface S in a time t. It is the volume in which every trajectory starting within this volume will result in a collision in a time smaller than t. By using this notation, the probability $\mathcal{P}_{col}(t)$ of a particle colliding with a surface S in a time less than t is given by the probability measure of a particle to be inside $V_{col}(t)$ at time equal zero. For two different species, we can compute the (average) total number of collisions between two species by multiplying the collisional probability $\mathcal{P}_{col}(t)$ by $N_1 N_2$, with N_i being the total number of particles of species i, or, in the case of two particles of the same species, by $N(N-1)/2$. Hence, the general rate of pairwise collision between two species per unit volume is given by

$$J_{12} = n_1 n_2 \frac{d}{dt} \int_{V_{col}(t)} \tilde{f}(\mathbf{x}) dV, \tag{3.13}$$

where n_i is the number density of species i, and $\tilde{f}(\mathbf{x}) \equiv f(\mathbf{x}, 0)$ is the pair distribution function evaluated at $t = 0$. The unsteady state for $f(\mathbf{x}, t)$ is governed by the Liouville equation (Batchelor and Green, 1972a):

$$\frac{\partial f}{\partial t} + \nabla \cdot (\mathbf{V} f) = 0, \tag{3.14}$$

where $\mathbf{V}$ is the relative velocity of the colliding species. For specific cases such as steady-state probability distributions, it is useful to use a modified version of Reynolds Transport Theorem to re-write the pair collision rate as a surface integral. We define $\tilde{\mathbf{V}}(\mathbf{x}, t)$ as the velocity of the bounding surface of the collision volume. The lower portion of this surface is simply S_{col}, the original collision surface, as shown in Figure 3.3, on which $\tilde{\mathbf{V}} = 0$. Hence, the pair collision rate is given by

$$J_{12} = n_1 n_2 \int_{A_{col}} \hat{\mathbf{n}} \cdot \tilde{\mathbf{V}} \tilde{f}(\mathbf{x}) dA, \tag{3.15}$$

where $A_{col}(t)$ is the upper or expanding portion of the collision surface (see Figure 3.3), $\tilde{\mathbf{V}}$ is its velocity and $\hat{\mathbf{n}}$ is the outward unit normal to $A_{col}(t)$. The geometry of the problem for our specific context of collision of a particle with a spherical collision surface is illustrated in Figure 3.3. Although equation (3.15) is general (*i.e.*, it is valid for non-steady states), it is not very useful for unsteady states, given that the evaluation of $\tilde{\mathbf{V}}$ is not always straightforward. However, there are some properties of steady-state distributions that make this expression more useful. Namely, for a steady-state probability distribution, as the field $\mathbf{V}$ does not depend on time, the velocity $-\tilde{\mathbf{V}}$ coincides with the relative velocity $\mathbf{V}$ (note that $\mathbf{V}$ is inward, while $\tilde{\mathbf{V}}$ is outward) and $f(\mathbf{x}, t) = f(\mathbf{x}) = \tilde{f}(\mathbf{x})$. Moreover, we can extend the collision area A_{col} to infinity by using the continuity equation.

For a steady-state relative velocity field, the trajectories coincide with its integral curves. If we extend the collisional volume along a 'streamtube' of $\mathbf{V}(\mathbf{x})$ that contains all the points

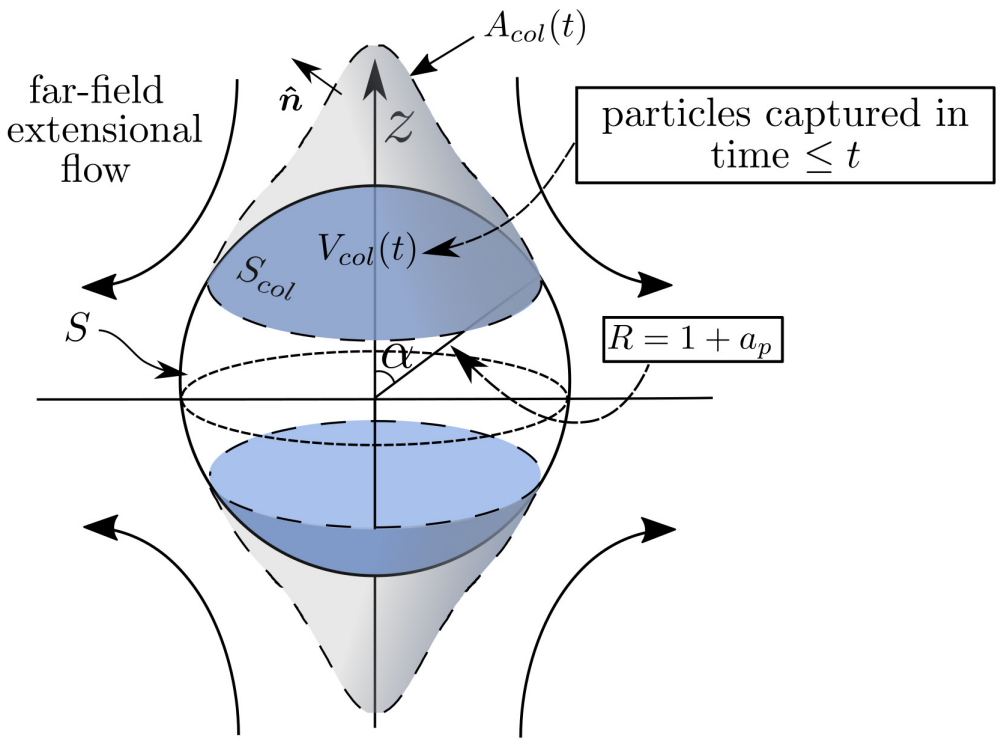

Figure 3.3: Illustration of the collision volume of a particle colliding with a collision surface S. The shaded S_{col} represents the portion of S where particles are effectively captured, whereas the non-shaded region is where particles are pulled away from the drop by the extensional flow faster than the drop expands. In our specific case of a particle colliding with an expanding drop under an external pure extensional field, S is a sphere of dimensionless radius $R = 1 + a_p$ (*i.e.*, the original drop radius plus particle radius) and S_{col} is located at the top and bottom of the sphere, starting at an elevation angle α to be determined. The collision volume $V_{col}(t)$ is the region composed of the starting positions that will lead to aggregation in a time less than or equal to t. $A_{col}(t)$ is the boundary of the collision volume with S_{col} excluded. Although the drop expands in time, S_{col} is kept fixed as V_{col} smoothly increases, because $V_{col}(t)$ is the suspension volume at time zero from which all particles will be collected by time t.

inside the collisional volume extending toward infinity, by the divergence theorem and equation (3.14), the probability flux, defined as the integral in equation (3.15), is equal in every section of the extended volume. This fact allowed most researchers to focus their analysis on a collision section far from the reference particle, where $f(\mathbf{x}) \sim 1$. This consideration allows writing equation (3.15) for a steady-state probability distribution as

$$J_{12} = -n_1 n_2 \int_{A_{col}^{\infty}} \hat{\mathbf{n}} \cdot \mathbf{V} dA, \tag{3.16}$$

where A_{col}^{∞} is a section (typically a horizontal cross-section) of the extended collisional volume far from the reference particle. Equation (3.16) is a practical way to evaluate the collision efficiency, as it does not rely on previous knowledge of the pair distribution function (Zeichner and Schowalter, 1977; Davis, 1984; Davis and Zinchenko, 2018). There are other works, such as Phan et al. (2003), that compute the collision efficiency by evaluating the integral over S_{col}. However, in order to avoid using the probability distribution explicitly, they assume that the relative velocity $\mathbf{V}$ is a solenoidal field, which is often not the case.

Regarding the case in the absence of a steady-state distribution, for an initially uniform probability distribution (*i.e.*, $f(\mathbf{x}, 0) = 1$), the rate of collision between two different species per unit volume is given by

$$n_1 n_2 \, dV_{col}/dt. \tag{3.17}$$

Equation (3.17) is essentially transient, as it assumes an initial distribution that is not at steady state, and, therefore, will only reach the steady-state collision efficiency if the chosen initial pair distribution also reaches a steady state. Throughout the subsequent sections, we show that this transient behavior is indeed the case for non-expanding droplets. Furthermore, we define the collision efficiency as the ratio between the pair collision rate and the ideal collision rate, which was calculated by Zeichner and Schowalter (1977) by using (3.16) considering the case of rigid non-expanding spherical particles in an extensional flow in the absence of hydrodynamical interactions. This ideal collision rate is given by

$$J_{12}^{id} = n_1 n_2 \frac{8\pi}{3\sqrt{3}} (a_1 + a_2)^3. \tag{3.18}$$

3.3.2 Important limiting cases

Physically, there are two distinct mechanisms that contribute to the capture of particles by expanding drops: convective capture due to the imposed flow and engulfment capture due to the drop's expansion. The interplay between these two mechanisms is characterized by the engulfment parameter Eg, which was defined in the first section of this chapter. Here, we analyze the limits where $Eg = 0$ and $Eg \to \infty$.

In the first case, where $Eg = 0$, the drop does not expand and the steady problem reduces to the one described in Davis and Zinchenko (2018). For this case, the collision efficiency at steady-state is solely due to flow and given by

$$E_{col}^{fl} = \frac{1}{\phi^3(R)}, \tag{3.19}$$

where the function $\phi(r)$ involves an integral over the relative particle distance and is defined as

$$\phi(r) = \exp\left(\int_r^\infty \frac{A(r') - B(r')}{1 - A(r')} \frac{dr'}{r'}\right). \tag{3.20}$$

In the second limiting case, where $Eg \to \infty$, the drop expands and flow effects are negligible. In this limit, particle capture due to pure expansion happens much faster than the particle motion, and, hence, relaxation of the probability distribution is negligible. Thus, we can use equations (3.6), (3.17) and (3.18) to derive the collision efficiency, resulting in

$$E_{col}^{exp}(t) = \frac{3\sqrt{3}}{2} \frac{(a_d(t) + a_p)^2}{(1 + a_p)^3} \frac{Eg}{(a_d(t))^3}. \tag{3.21}$$

At large times, for $a_d(t) \gg a_p$, this function slowly decays in proportion to $t^{-1/4}$, using (3.6). Of considerable practical importance is that the collision efficiency in this limit remains nonzero for $a_p \to 0$, whereas the collision efficiency for flow-induced capture becomes very small as $a_p \to 0$, due to hydrodynamic interactions.

3.3.3 Characteristic times and population dynamics at short times

At time zero, before any collection takes place, the only species present in the suspension are particles and drops. For simplicity, we consider that the particles are all of the same size and do not form agglomerates. In this case, the population dynamics for the particle phase is given by:

$$dn_p/dt = -Jn_p n_d. \tag{3.22}$$

When the particles are much smaller than the droplets, the capture of a single particle does not affect the capture efficiency of an additional particle by a given droplet. Hence, we can consider the resultant agglomerate as a single drop. In this case, n_d is a constant. By a scaling analysis of (3.22) and knowing that $J = dV_{col}/dt$, the characteristic time of bulk capture is given by:

$$\tau_{bulk} = T/(a_{d0}^3 n_d) = 4\pi T/(3\phi_0), \tag{3.23}$$

where $\phi_0 = 4\pi a_{d0}^3 n_d/3$ is the initial volume fraction of droplets and we choose the characteristic microscopic capture time T to be:

$$T = (1/\tau_{fl} + 1/\tau_{eng})^{-1}, \tag{3.24}$$

so that it scales with the smaller of the flow and engulfment times. Since $\phi_0 \ll 1$ for dilute systems governed by pairwise interactions, the time scale for bulk capture of particles is long compared to the pairwise capture dynamics. Equation (3.22) can be solved analytically for an initially uniform pair distribution function, yielding (in nondimensional quantities)

$$n_p = n_{p0} \exp\left(-V_{col}(t)/\tau\right), \tag{3.25}$$

where $\tau = \tau_{bulk}/T$ is the ratio between the characteristic bulk capture time and microscopic capture time. Thus, $V_{col}(t)$ is as a direct measure of particle capture over time. For the practical systems discussed in Section 3.1.1, the dimensional time scales are $\tau_{fl} = \dot{\gamma}^{-1} = 10^{-3}$ s and $\tau_{eng} = a_{d0}/(KRTc_0) = 10^{-4} - 10^{-2}$ s for the parameters cited by Davis and Zinchenko (2018), and $\tau_{fl} = 1$ s and $\tau_{eng} = 0.1 - 10$ s for the experiments of Matsumoto et al. (1980). For a dilute suspension with $\phi_0 \lessapprox 0.01$, τ_{bulk} is more than 100−fold larger.

3.3.4 Initial rate of collision with an expanding drop

In this subsection, we derive an analytical solution for the initial rate of collision of a rigid spherical particle with an expanding drop, in the case of an initially uniform pair distribution function. This solution is then used in subsequent sections to confirm the transient results obtained via numerical simulations.

In the present problem, the relative radial velocity at the collisional surface at time zero (*i.e.*, the surface of a sphere with radius $R = 1 + a_p$) is, from (3.7) and (3.4),

$$V_{rel} = V_r - \frac{da_d}{dt} = \frac{(1-A)}{(B-A)} E\, r - \frac{Eg}{a_d^3}. \tag{3.26}$$

At $t = 0$, when $r = R = 1 + a_p$, the relative radial velocity is

$$V_{rel} = R(1 - A_0)(1 - 3\cos^2(\theta)) - Eg, \tag{3.27}$$

where A_0 is the mobility function A evaluated at the collisional radius R. Although $1 - A_0$ is zero for two solid particles, it has a non-zero value if one (or both) of the spheres is permeable, as noted by Davis and Zinchenko (2018). To calculate the rate of collision, we need to restrict the domain of the collisional surface to the locations with negative relative velocity (so that the capture occurs). In this case,

$$\cos^2(\theta) > \frac{1}{3}\left(1 - \frac{Eg}{R(1-A_0)}\right). \tag{3.28}$$

Thus, the domain of integration is restricted to $\theta \in D = [0, \alpha] \cup [\pi - \alpha, \pi]$, with

$$\alpha = \begin{cases} \arccos\left\{ \left[\frac{1}{3}\left(1 - \frac{Eg}{R(1-A_0)}\right)\right]^{1/2} \right\} & \text{for } Eg < R(1-A_0) \\ \pi/2 & \text{for } Eg > R(1-A_0) \end{cases}. \tag{3.29}$$

This domain is shown as the shaded area in Figure 3.3. Therefore, for an initial uniform probability distribution, the integral in equation (3.15) at time zero is given by

$$\begin{aligned} \int_{S_{col}} \tilde{\mathbf{V}} \cdot \hat{\mathbf{n}} \, dS &= \int_{S_{col}} \left[Eg - R(1-A_0)(1 - 3\cos^2(\theta)) \right] \, dS \\ &= S_{col} \left[Eg - R(1-A_0) \right] + 12\pi R^3 (1-A_0) \int_0^{\alpha} \cos^2(\theta) \sin(\theta) d\theta \\ &= 4\pi R^2 (1 - \cos(\alpha)) \left[Eg - R(1-A_0) \right] + 4\pi R^3 (1-A_0)(1 - \cos^3(\alpha)). \end{aligned} \tag{3.30}$$

Dividing the collision rate at time zero by the ideal collision rate (3.18) yields the initial collision efficiency:

$$E_{col}(0) = \frac{3\sqrt{3}}{2} \left[\frac{Eg}{R}(1 - \cos(\alpha)) + (1-A_0)(\cos(\alpha) - \cos^3(\alpha)) \right], \tag{3.31}$$

where α is given by equation (3.29). For engulfment values larger than $R(1-A_0)$, all the cosines in (3.31) vanish, indicating that the collision efficiency for these cases is initially dominated entirely by expansion. In other words, the expansion is then fast enough to capture particles on all parts of the drop surface at time zero, even in regions where the extensional flow pulls particles away from the drop.

Figure 3.4 shows a plot of the initial collision efficiency versus the engulfment parameter for several values of the nondimensional permeability. The results for $Eg = 0$ are

$$E_{col}(0)\Big|_{Eg=0} = \frac{3\sqrt{3}}{2}(1-A_0)(\cos(\alpha) - \cos^3(\alpha)). \tag{3.32}$$

The collision efficiency for $K^* = 0$ is necessarily zero in this limit, for which $A_0 = 1$, due to lubrication preventing the contact of impermeable spheres (when, at least, one

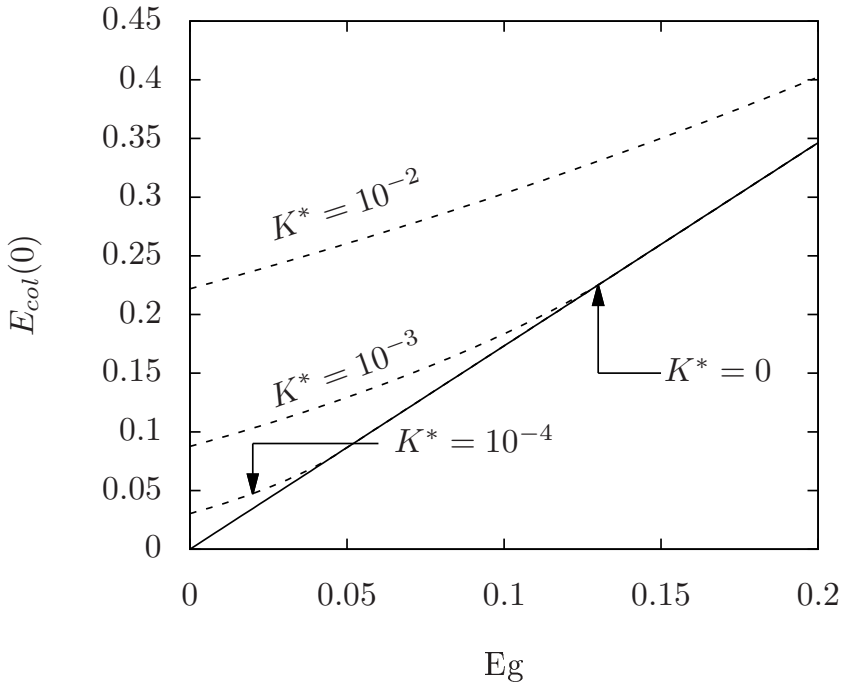

Figure 3.4: Initial collision efficiency versus the engulfment parameter for $a_p = 0.5$ and different values of nondimensional permeability. The solid line represents the limit where $K^* \to 0$, and, hence, $(1 - A_0) = 0$.

of them is solid) in a finite time under the action of finite forces (Barnocky and Davis, 1989). However, the collision efficiency quickly increases in the presence of even small permeabilities. The initial collision efficiency, then, increases as Eg increases, due to the increasing role of engulfment aiding the convective capture due to the extensional flow.

In the opposite limit of $Eg \gg 1$, $\alpha = \pi/2$ and the initial collision from (3.31) is simply

$$E_{col}(0) = 3\sqrt{3}\, Eg/(2R). \tag{3.33}$$

The initial collision efficiency then increases linearly with the engulfment parameter and is independent of permeability (other than the dependence of the engulfment parameter on permeability per (3.5)). Equation (3.33) corresponds to the solid line for $K^* = 0$ with $R = 1.5$ in Figure 3.4. Moreover, from (3.21) and using (3.6), the collision efficiency for pure engulfment ($Eg \gg 1$) is

$$E_{col}(t) = \frac{3\sqrt{3}\left[(1+4Egt)^{1/4} + a_p\right]^2 Eg}{2(1+a_p)^3(1+4Egt)^{3/4}}, \tag{3.34}$$

valid for all times. Equation (3.34) reduces to (3.33) for $t = 0$, using $R = 1 + a_p$. As noted before, the collision efficiency in this limit also remains finite for small particles ($a_p \ll 1$).

3.3.5 Transient microstructure and collision efficiency

In this section, we provide a numerical solution of the transient pair distribution function $f(\mathbf{x}, t)$. This solution can be used to better understand the transient behavior of the collision efficiency of a particle with a non-expanding drop.

The pair distribution function is governed by equation (3.14). Considering the motion of a particle relative to a non-expanding droplet, for which the vector field $\mathbf{V}$ given by equation (3.7) is in a steady state, equation (3.14) can be re-written as (Batchelor and Green, 1972a)

$$\frac{D}{Dt}\left(\frac{f(\mathbf{r}, t)}{q(r)}\right) = 0, \tag{3.35}$$

where $D/Dt = \partial/\partial t + \mathbf{V} \cdot \nabla$ and $q(r)$ is given by $(1 - A)^{-1}\phi^{-3}(r)$. Hence, for an initially uniform pair density function, equation (3.35) can be solved by the method of characteristics, yielding

$$f(\mathbf{r}, t) = \frac{q(r)}{q(R(\mathbf{x}, t))}, \tag{3.36}$$

where $R(\mathbf{x}, t)$ is the radial component of the starting position $\mathbf{R}$ that ends in $\mathbf{x}$ at time t. Due to the kinematic reversibility characteristic of Stokes flows, $\mathbf{R}(\mathbf{x}, t)$ can be evaluated using the inverse flux of the dynamical equations. It should be noted that the solution by the method of characteristics is only valid at points for which the position at time t can be traced back to an initial point in space. That means the collision volume of the inverse dynamics represents a particle depletion region adjacent to the collision surface. This

region is also referred as wake region by Wilson (2005). For points away from the wake region, where the particles come from infinity, we have $\lim_{t\to\infty} q(R(\mathbf{x}, t)) = 1$, and, thus, the pair distribution function approaches $q(r)$ at large times, which is the analytical result given by Batchelor and Green (1972a).

Coupling the analytical transient solution given by (3.36) with our trajectory simulations, we were able to find numerical values for the pair distribution function, which are displayed in Figure 3.5 for $K^* = 10^{-4}$ and $a_p = 0.5$, at $t = 0.25$, 0.75, 1.0, and 1.5. From these results, we see the formation of the wake region near the xy plane, which increases outward in time as the probability distribution approaches a steady state. Moreover, although the wake region continues to increase with time, comparison with the theoretical steady state shows that the pair distribution function away from this wake region becomes close to the theoretical steady state for $t = \mathcal{O}(1)$.

On the upper region of the collision sphere, we can see an increase of the pair distribution function with time. This increase physically means that there is a higher probability of encountering a particle at this region, which results in an increase of the probability flux, and, hence, the collision efficiency should increase with time until it reaches a steady state.

3.4 Numerical results and discussion

In this section, we present the results of numerical computation of the collision efficiency. We start with the shapes of the collision volumes, which were obtained by numerical interpolation of the collision time as a function of starting position. We then present results on the change of the collision volume and collision efficiency with time.

3.4.1 Collision boundaries

The collision boundaries are, by definition, the level surfaces of the function $t_{col}(\mathbf{x}_0)$ (*i.e.*, the collision time of a certain trajectory starting at a point $\mathbf{x}_0$). Using data from multiple

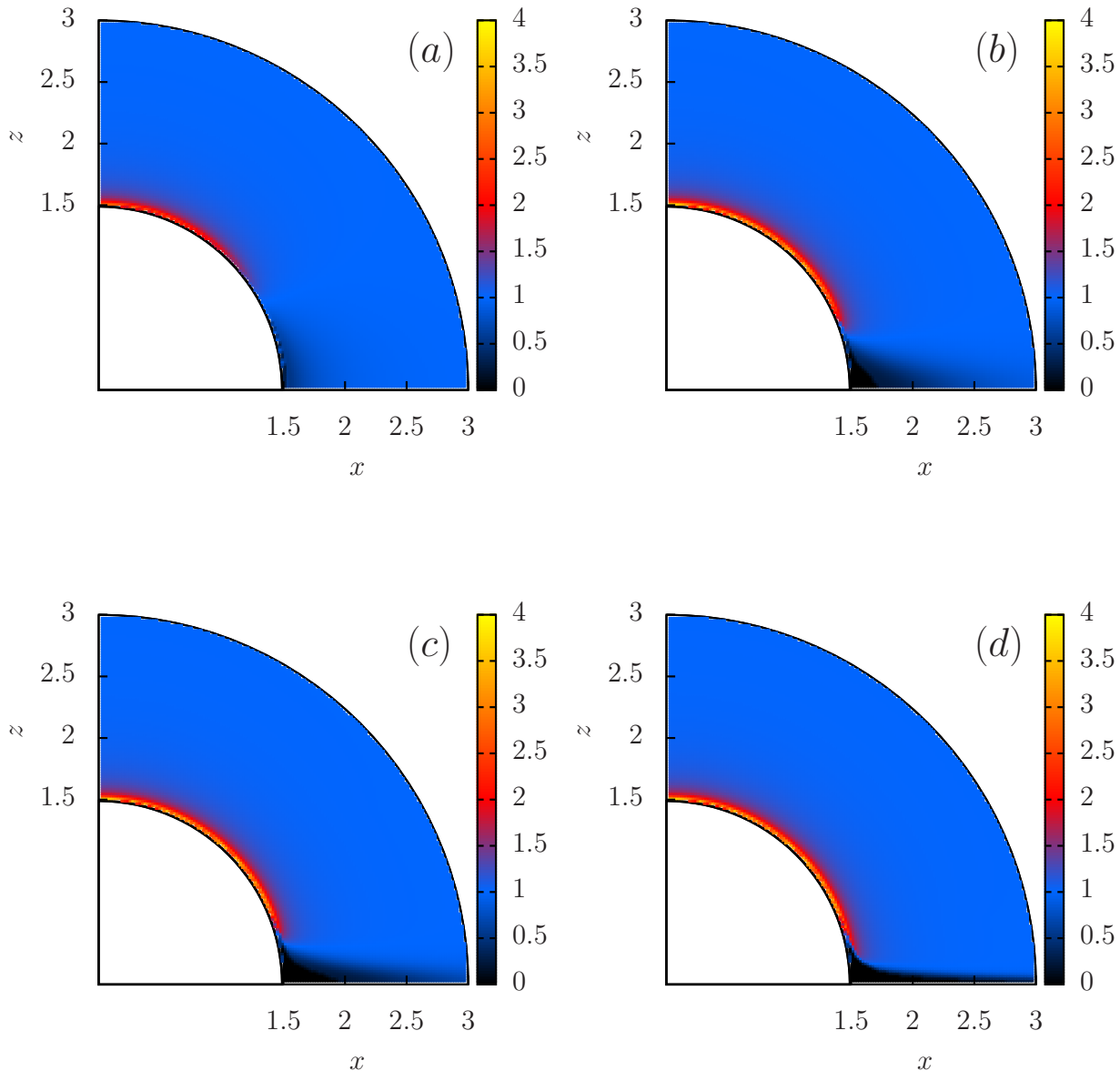

Figure 3.5: Numerical results for the transient pair distribution function for a rigid particle and a non-expanding permeable drop at distinct times. The values for the non-dimensional permeability and particle radius are $K^* = 10^{-4}$ and $a_p = 0.5$, at times (a) $t = 0.25$, (b) $t = 0.75$, (c) $t = 1.0$ and (d) $t = 1.5$. The white region surrounding the origin is the excluded volume bounded by the collision surface.

trajectory simulations, we obtained numerical values for these boundaries by numerical interpolation of the data for $t_{col}(\mathbf{x}_0)$, which are found by calculating multiple trajectories for different starting positions. As an example, Figure 3.6 shows the collision boundaries for different values of t and Eg = 1. Note that, as t increases, the collision surface converges to a limit surface, except near the axis of symmetry, where there will be a collision tube as $t \to \infty$. In the absence of engulfment, this limit curve should be the same as the one predicted by Davis and Zinchenko (2018).

For non-expanding drops, the regular interpolation method fails to obtain some of the points on the collision boundary next to the drop at larger times, due to computational time constraints, as particle capture takes longer in the absence of drop expansion. Thus, in these cases, we used an auxiliary method that makes use of the fact that, for a stationary field $\mathbf{V}(\mathbf{r})$, points on A_{col} change in time with velocity $-\mathbf{V}(\mathbf{r})$. Thus, the inverse flux of the original dynamical system gives us a homotopy between surfaces S_{col} and A_{col} (*i.e.*, we can continuously deform one surface into the other). Numerically, we permeate points throughout S_{col} and evolve them using the velocity $-\mathbf{V}(\mathbf{r})$, which helps construct A_{col}.

The shapes of the collision boundaries displayed in Figure 3.6 result from the interplay between the flow and expansion mechanisms. The different shapes of the collision volume for $t = 0.5$ are shown in Figure 3.7 for the cases of pure flow, pure expansion and combination of both effects. Due to the extensional flow, in which the flow is toward the drop near the axis of symmetry and away from the drop near the equator, non-expanding droplets display a lateral region in which particles are not captured. For engulfment parameters higher than $R(1 - A_0)$, this region ceases to exist (See Eq. (3.29)) and, instead, there is a finite capture layer that results from the balance between drop expansion effects (which decay with time) and pulling of particles away from the drop due to the extensional flow.

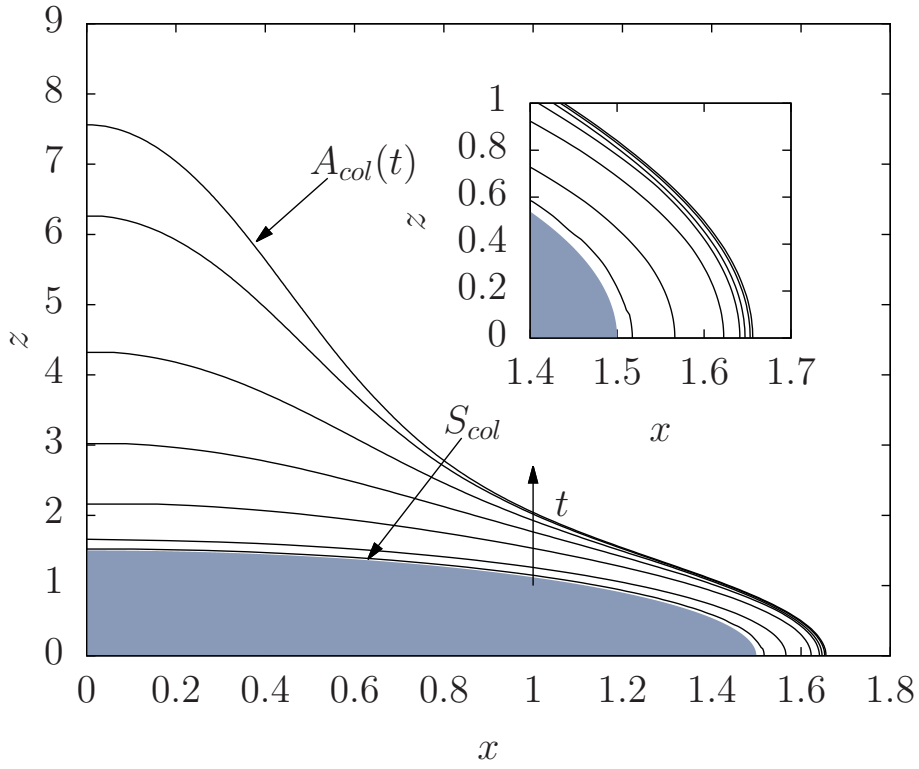

Figure 3.6: Collision boundaries for Eg = 1.0, $K^* = 10^{-4}$, $a_p = 0.5$, and (in to out) t = 0.02, 0.1, 0.3, 0.5, 0.7, 0.9, and 1.0. The inset shows a zoom of the details of the right region of the graph, where the curves start to coincide. The shaded region represents the inside of the collision surface $r = 1 + a_p$. The collision volume (V_{col}) is the unshaded region between the collision surface (S_{col}) and the collision boundary (A_{col}).

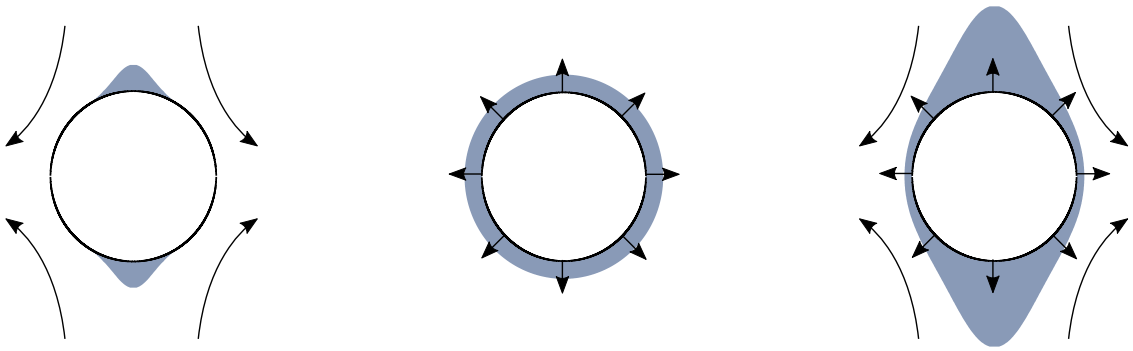

Figure 3.7: Different geometries of the collision volume for t = 0.5 and $K^* = 10^{-4}$. The combined case and pure expansion consider Eg = 1.0.

3.4.2 Collision efficiency

Using knowledge about the collision boundaries, together with their symmetry about the $z-$axis, we are able to calculate the collision volume numerically for distinct points in time using a simple trapezoidal method. Moreover, to validate our results, we use the analytical solution in equation (3.30) to predict the initial slope of the curve $V_{col}(t)$. Figure 3.8 shows the collision volume versus time for engulfment parameters $Eg = 0$, 0.125, 0.25, 0.5 and 1.0 for $a_p = 0.5$ and $K^* = 10^{-4}$. The values shown in Figure 3.8 (a) correspond to the actual values of the collision efficiency, whereas the values in 3.8 (b) are normalized by the initial slope, which was calculated using equation (3.31) combined with the definition of collision efficiency. The dashed line in Figure 3.8 (b) is a straight line starting at the origin with unit slope. The collision volume grows noticeably faster for larger values of Eg, which indicates a larger collision efficiency. The normalization in 3.8 (b) allows us to perceive a transition in behavior as the engulfment number increases. There is a transition of patterns at short times, which occurs at values of engulfment near 0.5. Namely, as the engulfment number increases, the collision volume curves transition from a flow-like behavior to an expansion-like one (represented by the shaded region in Figure 3.8). By examining the slopes of the curves in Figure 3.8, we see that, for small values of Eg, the collision efficiency initially increases with time. In contrast, for $Eg = 1$, although the initial value is much larger, the collision efficiency decreases at short times. This decrease can be explained by the dominance of the expansion mechanism in the collision efficiency for large engulfment parameters, which slows with time due to dilution of the salt water inside the drop, resulting in a reduction in the collision efficiency.

The numerical values for the collision efficiency were obtained by numerical differentiation of $V_{col}(t)$, according to equation (3.17). To reduce the numerical noise due to interpolation, we applied a smoothing spline to the collision volume function before taking the numerical derivative. The results for the collision efficiency obtained by this numerical differentiation are shown in Figure 3.9. Note that the results agree with the

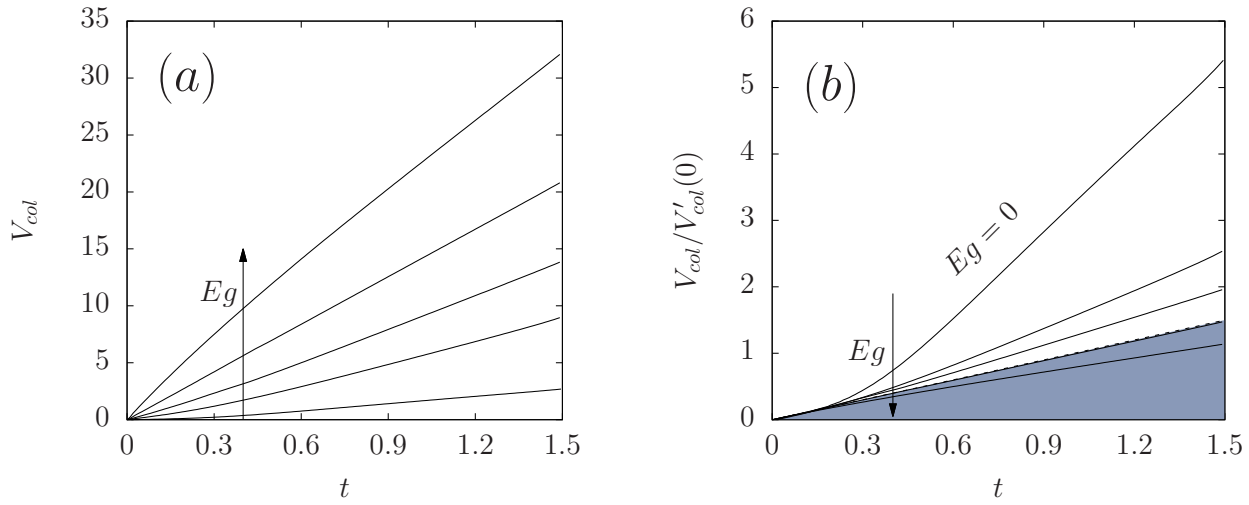

Figure 3.8: Collision volume increase with time for $K^* = 10^{-4}$, $a_p = 0.5$ and engulfment parameters of Eg = 0, 0.125, 0.25, 0.5 and 1.0. Here, (a) shows the values for the collision volume, whereas the values in (b) are normalized by their initial slopes predicted by the analytical solution for the initial collision rate. The solid curves represent the results obtained by numerical integration. The dashed line in (b) is a straight line with unit slope. The shaded area in (b) represents the region in which particle capture is dominated by expansion at short times.

prediction from the analytical solution for time zero. Moreover, in the case of a non-expanding droplet, the solution reaches a steady state with a numerical value close to the one predicted by Davis and Zinchenko (2018) (as indicated by the dashed line on the top right of Figure 3.9 (a)). As expected by the results and discussion in section 3.3.5, the collision efficiency increases monotonically as it approaches a steady state within a time near unity, due to the particles slowing down as they approach the drop, and, thus, building up in concentration. However, our results indicate that, even for small values of the engulfment parameter, the collision efficiency is much larger than for pure flow (Eg = 0). Another interesting feature is that, for small engulfment parameters such as Eg = 0.25, the shape of the collision efficiency curve is similar to the one without expansion. However, it should be noted that even small values of Eg can increase the collision efficiency by several times. Furthermore, from Figure 3.9 (d), increasing the engulfment parameter results in a shape transition from a monotonically increasing curve to a decaying behavior that is

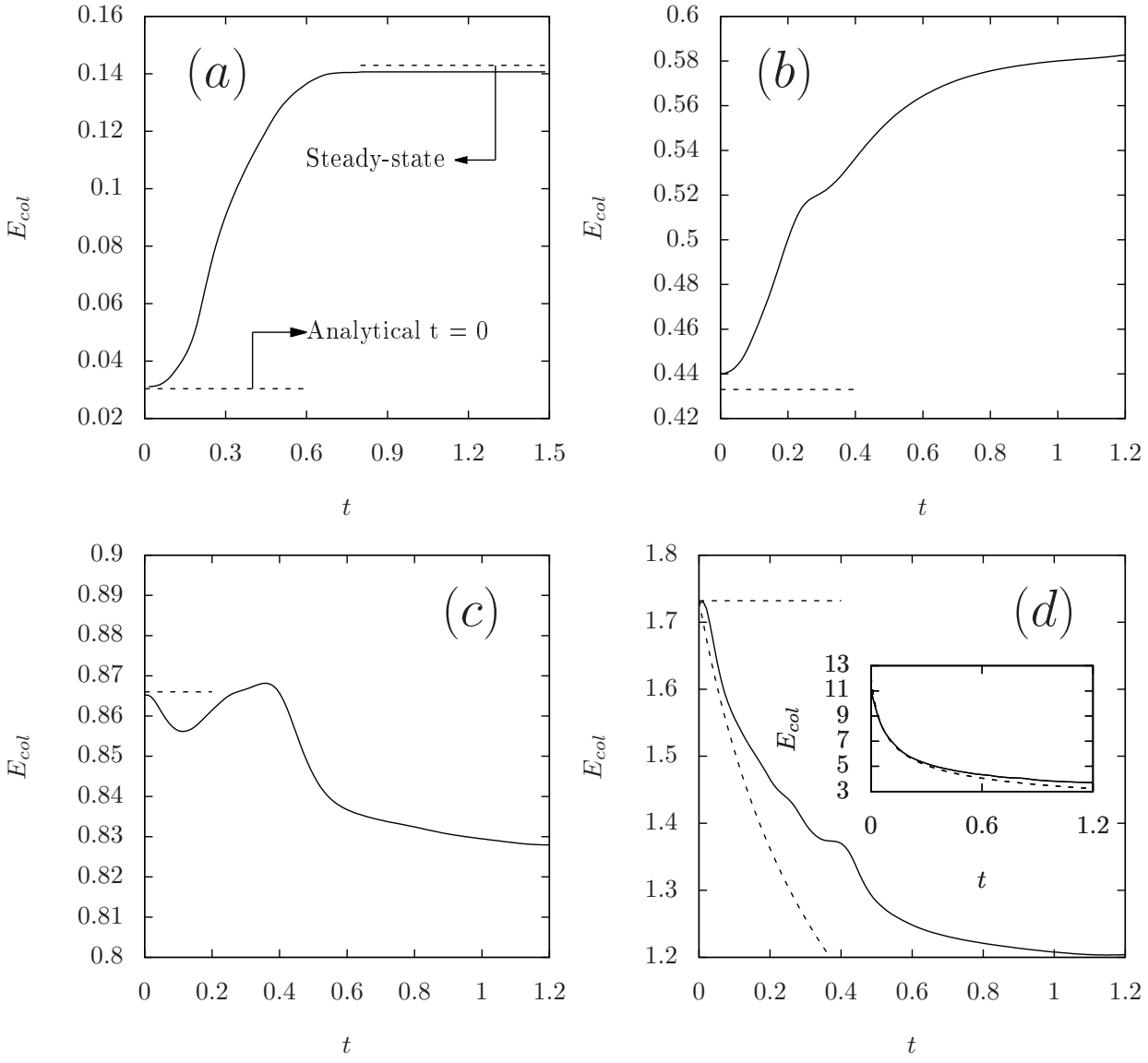

Figure 3.9: Numerical results for the transient collision efficiency versus time for $K^* = 10^{-4}$, $a_p = 0.5$, and engulfment parameters (a) Eg = 0, (b) Eg = 0.25, (c) Eg = 0.5, (d) Eg = 1.0, and 7.0 (in inset). The dashed lines represent the analytical solution at t = 0, and the value of the theoretical steady-state collision efficiency in (a). The dashed curve in (d) is the pure expansion collision efficiency, as described by equations (3.21) and (3.34).

closer to the one observed in the pure expansion efficiency given by (3.21). For $Eg = 1$, the hydrodynamic and engulfment and flow time-scales, τ_{eng} and τ_{fl}, are of the same order, and, thus, there is a substantial contribution of the far-field flow in particle capture, as the external flow drags particles closer to the drop, which is reflected, among other things, on the collision volume shape (see Fig. 3.7) and explains the difference between the curves. Moreover, engulfment dominates for short times when $Eg = 1$, but then the difference between the numerical results and the pure-engulfment approximation deviate at longer times as engulfment slows and convective capture becomes more important. For larger values of Eg, as $\tau_{eng} > \tau_{fl}$, the solution becomes closer to the pure expansion solution in (3.21) and (3.34), as can be seen in the inset of Figure 3.9 (d).

We further validate our numerical results by simulating the non-expanding case for different values of nondimensional permeability K^*. The results concerning the collision efficiency for different values of permeability are displayed in Figure 3.10. The numerical results for different permeabilities match within 0.01 with both theoretical solutions for steady-state and initial collision efficiencies.

We also plotted the results for different permeabilities in the case of expanding droplets (*i.e.*, $Eg \neq 0$). The results for these simulations are displayed in Figure 3.11 for values of the engulfment parameter (a) $Eg = 0.25$ and (b) $Eg = 1.0$. Figure 3.11 shows that the differences between the values of collision efficiency for different values of K^* shown in Figure 3.10 are mitigated with an increase of the engulfment parameter. The results displayed in Figure 3.11 (b) show that the increase of Eg results in the collapse of curves for different small permeabilities into a single limit curve. In this regime, engulfment is the primary capture mechanism, and, the collision efficiency is governed by particle expansion and the external flow far from the drop, which drags particles close to the drop so that they will be captured by engulfment.

Another parameter that is important in the determination of collision efficiency is the nondimensional particle radius. As mentioned before, previous works (*e.g.*, Barnocky

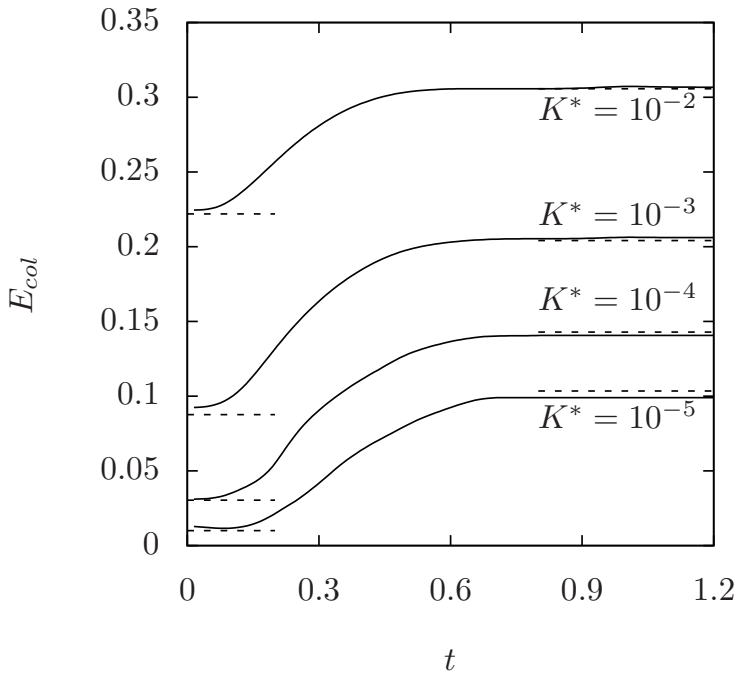

Figure 3.10: Numerical results for the transient collision efficiency with respect to time for Eg = 0, $a_p = 0.5$, and different values of nondimensional permeability: $K^* = 10^{-2}$, $K^* = 10^{-3}$, $K^* = 10^{-4}$ and $K^* = 10^{-5}$. The dashed lines represent the theoretical results for the initial and steady-state collision efficiencies.

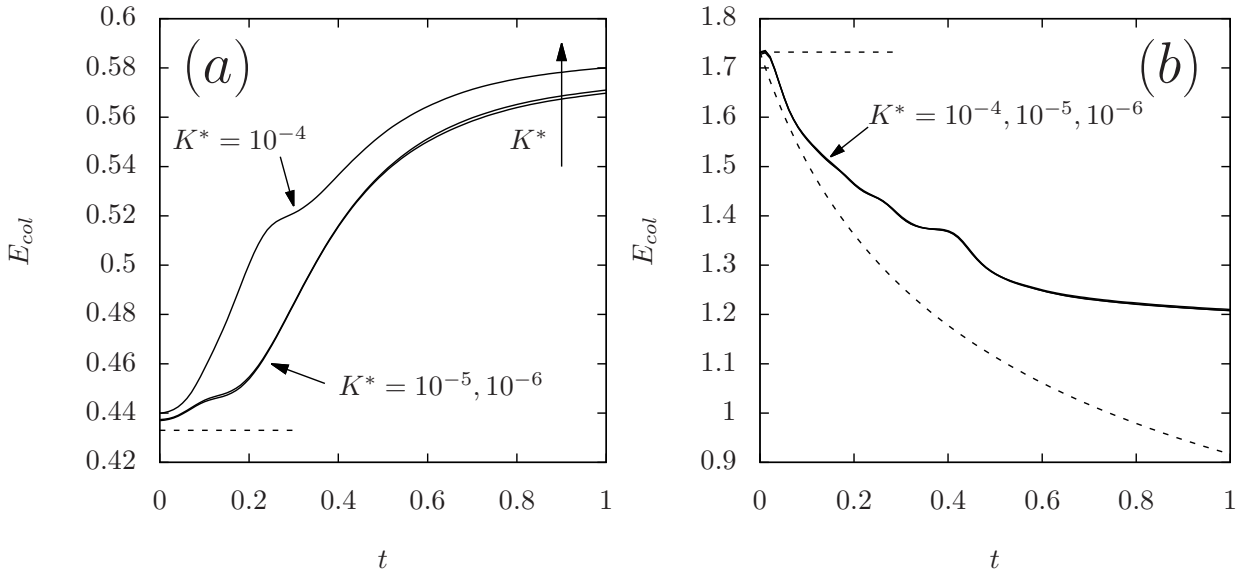

Figure 3.11: Numerical results for the transient collision efficiency with respect to time for (a) Eg = 0.25, (b) Eg = 1.0. The results are for $a_p = 0.5$ and different values of nondimensional permeability: $K^* = 10^{-4}$, $K^* = 10^{-5}$ and $K^* = 10^{-6}$. The dashed lines represent the theoretical results for the initial collision efficiency. The dashed curve in (b) is the pure expansion collision efficiency. For high values of Eg, the system becomes less sensitive to changes in permeability and the curves collapse onto a single curve.

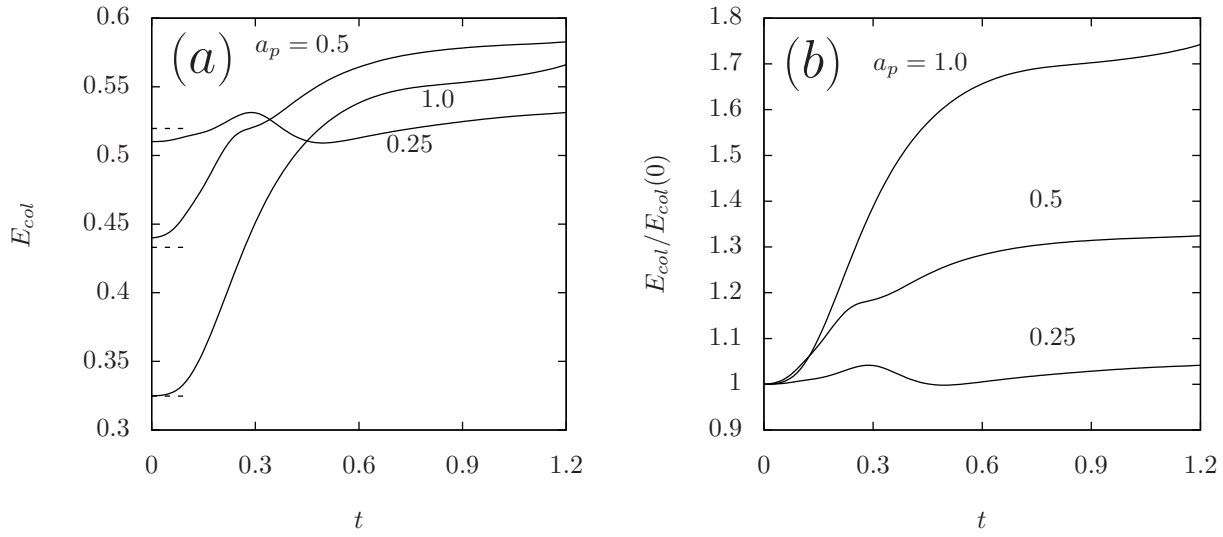

Figure 3.12: Numerical results for the transient collision efficiency for $Eg = 0.25$, $K^* = 10^{-4}$, and different values of particle radii: $a_p = 0.25$, $a_p = 0.5$, and $a_p = 1.0$. Here, (a) shows the values for the transient collision efficient, whereas, in (b), the results are normalized by the numerical value for the initial collision efficiency. The dashed lines represent the theoretical results for the initial and steady-state collision efficiencies.

and Davis (1989); Loewenberg and Davis (1994)) show that particle capture is hindered for small particle sizes. As shown in Davis and Zinchenko (2018), the presence of permeability increase capture efficiency at smaller radii. In fact, as we now show, the presence of particle engulfment further increases this efficiency. Figure 3.12 shows results for the transient collision efficiency for different values of particle radii, $K^* = 10^{-4}$, and $Eg = 0.25$. Due to the high influence of engulfment over particle capture and the $1/R$ dependence of the engulfment-dominated collision efficiency (*cf.*, (3.33) and (3.34)), the decrease in particle radius, in contrast to non-expanding cases, causes an increase in the collision efficiency at short times. However, by normalizing the results by the initial collision efficiency, as displayed in Figure 3.12 (b), we see that the increase of particle radius from 0.25 to 1.0 results in a larger percentage increase of the collision efficiency, given that such increase is caused by flow effects.

The strong effect of engulfment is demonstrated in a quantitative fashion in Table 3.1. Here, the collision efficiency at $t = 1$ is normalized with the steady-state collision efficiency

Table 3.1: Relative collision efficiency E^*_{col} at time $t = 1$ for $Eg = 0$, 0.25, 0.5, and 1.0. The first two result columns show the relative collision efficiency for $a_p = 0.5$ for distinct permeabilities, whereas the last three result columns show the relative collision efficiency for $K^* = 10^{-4}$ for different particle radii.

Eg	$K^* = 10^{-4}$	$K^* = 10^{-5}$	$a_p = 0.25$	$a_p = 0.5$	$a_p = 1.0$
0.00	1.00	1.00	1.00	1.00	1.00
0.25	4.13	5.77	7.36	4.13	3.06
0.50	5.90	8.70	11.57	5.90	4.56
1.00	8.59	12.21	18.31	8.59	6.00

for flow only, $E^*_{col} = E_{col}/E^{fl}_{col}$, for systems with the same dimensionless size ratio and permeability. For the conditions in this table, the increase in collision efficiency is roughly $3 - 18$ fold. The highest values occur at lower permeability, smaller particle radius, and higher engulfment parameter, as expected. It is also noteworthy that the largest increase occurs for small particles (which are the most difficult to capture).

3.5 Concluding remarks

We investigated the interaction between an expanding spherical droplet and a solid particle in an external extensional flow. Using the results of relative particle trajectories obtained via numerical simulation, we calculated the transient collision efficiencies for different parameter values. Further, we derived an analytical expression for the initial collision efficiency and numerical results for the pair distribution function.

In contrast with previous works (*e.g.*, Zeichner and Schowalter (1977); Davis (1984); Davis and Zinchenko (2018); Roure and Cunha (2018)), we have not restricted our analysis to a steady-state pair distribution function. Rather, by starting with a uniform pair distribution, we demonstrated the evolution of the collision efficiency at short times. We applied the numerical solutions of the relative dynamics of the rigid particle to find a numerical solution of the transient pair distribution function for the case of non-expanding droplets. This solution allowed us to investigate the transiency of the collision efficiency

and the time it takes to reach a steady state. For non-expanding droplets, the collision efficiency increases with time and approaches the steady state predicted by Davis and Zinchenko (2018). The time it takes for the system to reach a steady state is of order $\dot{\gamma}^{-1}$ and agrees with our microstructure simulations, which also explain the monotonically increasing behavior of the collision efficiency for these cases. The monotonicity, however, can be broken in the presence of engulfment.

The numerical results for the collision efficiency, obtained by numerical differentiation of the collision volume with respect to time, agree with theoretical results for both initial and steady-state collision efficiencies. Drop expansion effects decay slowly with time, as engulfment capture slows with time due to a decrease in the osmotic driving force, as the internal salt water is diluted. Overall, drop-expansion effects contribute to the increase of collision efficiency even for small values of the engulfment parameter Eg. Of particular importance is that engulfment capture is relative insensitive to particle size, and so is particularly effective relative to convective capture for small particles. Further increase of Eg results in a transition from a flow-dominated behavior of the collision efficiency, with a monotonically increasing curve to a engulfment-dominated behavior, where the collision efficiency decreases with time. At high values of Eg, the system becomes less sensitive to changes in the permeability, which indicates the predominance of the far-field flow and engulfment as the predominant capture mechanisms in these cases.

CHAPTER 4

DIFFUSION-LIMITED OSMOTIC SWELLING OF DROPLETS

This work was originally published in *Physics of Fluids* 33, no. 11 (2021)
with co-author Robert H. Davis

> 'That's quite enough—I hope I shan't grow any more—As it is, I can't get out at the door—I do wish I hadn't drunk quite so much!'
>
> Lewis Carroll, Alice in Wonderland

Synopsis

Swelling phenomena due to permeation appear in problems such as the swelling of hydrogels and water-in-oil-in-water (W/O/W) emulsions. In the osmotic swelling of W/O/W emulsions driven by an inner salt concentration, diffusive effects inside the drop can decrease its expansion rate considerably. Although these inner-diffusion effects can play a large role on hindering drop swelling, they have not usually been taken into account in most works concerning the swelling kinetics of W/O/W emulsions. We perform numerical simulations of the expansion-diffusion problem governing the diffusion inside an expanding spherical droplet containing salt and with a semi-permeable interface. We also present asymptotic solutions for the limiting cases of slow and fast diffusion, which we compare with our numerical results. The results indicate that diffusive resistance significantly reduces the swelling kinetics of droplets. Moreover, in the regime of large Péclet numbers, diffusive effects are localized near the drop's interface in a concentration boundary layer, as predicted by our theory.

The numerical results presented in this chapter are in agreement with the behavior observed in recent experiments on W/O/W emulsion swelling.

4.1 Introduction

Water-in-oil-in-water (W/O/W) emulsions are composed of oil films or droplets in a continuous phase of water, with water droplets entrapped inside the oil phase. These emulsions appear in a number of applications, such as in the food, pharmaceutical and mineral industries (Pawlik et al., 2010; Marti-Mestres and Nielloud, 2002; Florence and Whitehill, 1982; van Netten et al., 2014), and fundamentals of their formation have been studied as a prototype for less-stable antibubbles (Wang et al., 2019). The present work is motivated by a recently proposed application of water-in-oil-in-water emulsions in a particle-capture method designed to overcome the lack of efficiency of froth flotation for the capture of very small particles (van Netten et al., 2014, 2016, 2017; Davis and Zinchenko, 2018). The new method consists of the use of a binder composed of saltwater droplets covered with surfactant-stabilized oil layers. The presence of salt inside these droplets causes an osmotic gradient that induces permeation of water through the oil layers from outside to inside the drops, leading to swelling of the droplets and rapid capture of fine particles (van Netten et al., 2017; Matsumoto et al., 1980).

The phenomenon of drop swelling, as well as understanding its kinetics, has great importance in the study of W/O/W emulsions (Bahtz et al., 2016; Eisinaite et al., 2018). Of particular interest is the swelling rate, which is driven by the difference in concentration or activity of salt between the inner and outer edges of the oil film or membrane, which is permeable to water but not salt. However, the salt near the inner edge of the film becomes diluted due to the permeation of water across the film, so the rate of diffusion of salt from the interior of the drop to the interface is key to continued swelling. Moreover, the diffusion and swelling processes are coupled through the moving boundary of the expanding drop. These features and coupling represent an important problem in colloid

and interface science that needs to be addressed.

Because of the large range of applications of W/O/W emulsions, there have been several prior studies on this topic (Mezzenga et al., 2004; Leal-Calderon et al., 2012; Wan and Zhang, 2002; Yan and Pal, 2001; Mukhopadhyay et al., 2008; Khadem and Sheibat-Othman, 2020). In our recent analysis (Roure and Davis, 2021a), we investigated the effect of drop expansion on the capture efficiency of solid spherical particles. For simplicity purposes, in that work, we assumed the salt to be always uniformly distributed inside the droplet, as would occur for rapid salt diffusion. In real situations, however, diffusion limitation inside the drop leads to a lower salt concentration at the interface, which reduces the osmotic pressure gradient and, thus, lowers the drop expansion rate considerably, especially in cases of large Péclet numbers (*i.e.*, slow diffusion), as shown experimentally (DeIuliis et al., 2021). However, although there have been many quantitative models for the kinetics of the osmotic swelling of W/O/W emulsions that included effects such as leakage of the internal phase and occlusion due to the changing thickness of the oil layer, ranging from single-drop-membrane models (Mukhopadhyay et al., 2008) to more complex population-balance models for dilute double emulsions (Khadem and Sheibat-Othman, 2020), these models do not consider the effects of salt diffusion inside the drops. Thus, the main goal of the present work is to examine the moving-boundary problem of salt diffusion inside a single, expanding spherical droplet and to provide a correction for the expression calculated in Roure and Davis (2021a) due to finite-diffusivity limitations. Figure 4.1 shows a schematic of the problem.

The diffusion of salt inside an expanding drop is a moving-boundary problem (Crank, 1987). This class of problems was explored during recent decades in a number of other applications, such as phase transitions (solidification and evaporation) (Frank, 1950; Tredenick et al., 2021; McCue et al., 2008; Font, 2018; Sobac et al., 2015; Myers et al., 2020; Tonini and Cossali, 2021), hydrogel swelling (Bertrand et al., 2016), oxygen diffusion from blood to an oxygen-consuming tissue (Ahmed, 1999), surface diffusion (Amatore et al.,

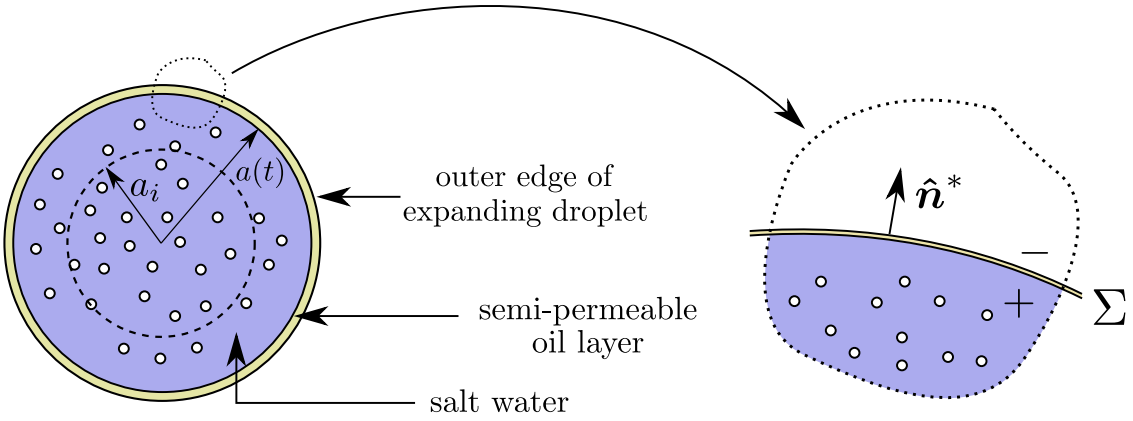

Figure 4.1: Schematic of a spherical drop undergoing osmotic swelling. The osmotic pressure gradient between the inside and outside of the droplet induces water permeation to the inside of the drop, which leads to expansion.

2009), and cancer progression (El-Hachem et al., 2020). Although some of these moving boundary problems present analytical similarity solutions (Frank, 1950; Birkhoff et al., 1958; Crank, 1987), most moving-boundary problems require numerical or asymptotic solutions, due to factors such as incompatibility of the similarity solution with the initial conditions or even possible non-linearities arising from the boundary conditions.

In this chapter, we perform asymptotic and numerical solutions of the diffusion-limited expansion problem inside a spherical drop in the presence of osmotic swelling. The numerical solution, obtained via a finite-differences scheme, enables us to investigate non-instant diffusion effects over the drop expansion in different regimes of arbitrary Péclet numbers. We also investigate the regimes of small and large Péclet numbers, where asymptotic solutions can be found. These asymptotic solutions are used to validate the numerical simulations and to better understand the underlying physical mechanisms in the limiting cases of slow and fast diffusion. A comparison with prior experimental work is then made. In the last part of the chapter, we also explore the limiting effects related to the presence of interfacial tension at the drop interface, which counteract drop expansion. In these cases, as shown in works such as Mezzenga et al. (2004), the presence of interfacial-tension effects may impose an upper limit for drop expansion. Our results indicate that, even in such situations, inner salt-diffusion effects can still play a large role

in the drop-swelling kinetics.

4.2 Governing equations

Considering the salt diffusion to be homogeneous and isotropic, the salt concentration inside the drop is governed by a standard advection-diffusion equation:

$$\partial c/\partial t + \nabla \cdot (\mathbf{u}c) = D\nabla^2 c, \tag{4.1}$$

where c is the salt concentration, $\mathbf{u}$ is the drift velocity due to the flow inside the droplet, and D is the diffusion coefficient. Here, we consider that internal diffusion effects happen much faster than internal convection, and, thus, we can neglect the convective term $\nabla\cdot(\mathbf{u}c)$ in (4.1). That is true for a number of cases, such as tangentially immobile interfaces and gel-like droplets. In our case, we consider a low salt concentration, so buoyancy effects are negligible. In addition, the values for water permeability at the interface are usually very small and drop expansion does not affect the velocity boundary conditions, as shown in Roure and Davis (2021a), and, thus, we can neglect internal convective effects. The internal phase is assumed to be homogeneous (*i.e.*, without a microstructure that changes upon swelling), so that the diffusion coefficient is constant.

The initial condition is that the drop starts with an initially uniform salt concentration $c_i = 3N/(4\pi a_i^3)$, where N is the number of moles of salt molecules and a_i is the initial drop radius. We assume spherical symmetry of the diffusion-expansion problem, which, for smooth functions, implies that the radial derivative must vanish at $r = 0$. The remaining boundary condition is given by the jump condition at the interface. Namely, a mass balance on the interface yields $\hat{\mathbf{n}}^* \cdot [\![\mathbf{V}_s c - \mathbf{j}]\!] = 0$, where $\hat{\mathbf{n}}^*$ is the normal vector at the interface (for a spherical drop, $\hat{\mathbf{n}}^* = \hat{\boldsymbol{e}}_r$), $\mathbf{V}_s$ is the velocity of the interface, $\mathbf{j} = -D\nabla c$ is the diffusive mass flux given by Fick's law and $[\![G]\!] = G^+ - G^-$ is the jump operator, which measures the discontinuity of properties at the interface. This condition yields

$$c\, da/dt|_{r=a(t)} = -D\, \partial c/\partial r|_{r=a(t)}, \tag{4.2}$$

where $a(t)$ is the drop radius as a function of time.

The rate of change of the drop radius is found by considering a mass balance inside a drop. The permeation flux from the outside to the inside of the drop is given by Darcy's law: $-\mathbf{q}\cdot\hat{\mathbf{n}}^*|_\Sigma = K\Pi$, where K is the interface's permeability and Π is the osmotic pressure, which can be approximated by Van't Hoff's law: $\Pi = RTc|_\Sigma$, where R is the gas constant, T is the absolute temperature, and $c|_\Sigma \equiv c_w$ is the inner salt concentration evaluated at the boundary Σ. Hence, by equating the amount of fluid going inside the drop to the rate of change in volume, and considering that the drop keeps its spherical shape, one finds

$$da/dt = KRTc|_{r=a(t)} \equiv Ac|_{r=a(t)}. \tag{4.3}$$

Following related experiments (van Netten et al., 2017; DeIuliis et al., 2021), we assume that the film surrounding the drop is thin; its dynamics are neglected, except the effects of its interfacial tension, which are considered at the end of the chapter. For simplicity, the permeability K is treated as a constant even though the film thins with drop expansion.

For the nondimensionalization of the problem, we use the initial drop radius a_i and the characteristic expansion time $a_i/(Ac_i)$ as length and time scales, respectively, where $A = KRT$. Hence, we can define nondimensional quantities by substituting $c \to c_i c$, $a \to a_i a$, $r \to a_i r$, and $t \to a_i t/(Ac_i)$. The governing set of equations, together with initial and boundary conditions, in terms of nondimensional quantities, becomes:

$$
\begin{cases}
\dfrac{\partial c}{\partial t} = \dfrac{1}{Pe}\dfrac{1}{r^2}\dfrac{\partial}{\partial r}\left(r^2\dfrac{\partial c}{\partial r}\right), \\
\dfrac{da}{dt} = c|_{r=a(t)}, \\
a(0) = 1,\ c(r,0) = 1, \\
\partial c/\partial r|_{r=0} = 0, \\
\partial c/\partial r|_{r=a(t)} = -Pe\ c^2|_{r=a(t)},
\end{cases}
\tag{4.4}
$$

where $Pe = Ac_i a_i/D$ is the Péclet number, which measures the initial ratio between the diffusion and expansion time scales. It is instructive to note that the Péclet number defined here differs from the traditional definition of a Péclet number in the sense that it does not refer to internal convective effects. However, the present nomenclature is justified given that, when one considers a reference frame normalized by the changing drop radius, the drop expansion appears as a convective term in the diffusion equation. Moreover, as drop expansion is driven by osmosis, if we consider the osmotic pressure to be given by Van't Hoff's law and the diffusivity of salt crystals given by the Stokes-Einstein equation, we find that Pe does not depend on temperature.

The initial and boundary value problem in (4.4), although governed by a linear differential equation, is generally not straightforward to solve analytically due to the moving boundary. Similarity solutions to these spherical moving-boundary problems exist for specific cases in terms of a similar variable $\eta \propto x/t^{1/2}$. These solutions, however, are usually for the so-called Stefan boundary conditions (Crank, 1987) and do not, in general, satisfy the initial condition for the concentration. In the present case, the non-linear boundary conditions are equivalent to the boundary conditions in Stefan problems with kinetic undercooling (Evans and King, 2000). Such problems have appeared in a large range of applications, such as kinetic undercooling problems (Back et al., 2014), sorption of solvents in polymers (Astaluta and Sarti, 1978; Astarita and Joshi, 1978), drug delivery (Cohen and Erneux, 1988; McCue et al., 2011), and others. Like such papers, our analysis employs asymptotic and numerical solutions. However, the asymptotic analyses

presented in this chapter follow a slightly different approach compared to these and other works(Evans and King, 2000).

4.3 Methods, results and discussion

As a preamble and framework for the analysis and rest of the results, Figure 4.2 shows numerical results for the salt concentration profiles inside the drop for Péclet numbers $Pe = 0.1$, 1, 10 and 100. For $Pe = 0.1$, the concentration is nearly uniform due to fast diffusion but declines with time due to dilution as the drop expands while the total salt content remains the same. In contrast, for $Pe = 100$, the concentration remains at its original value in the core but then drops to the edge value (which also decreases with increasing time) over a relatively thin growing boundary layer near the outer edge of the expanding drop. Thus, our approach proceeds from an asymptotic expansion at small Pe (section 4.3.1) to a boundary-layer analysis (section 4.3.2) at large Pe and short/moderate times and then a finite-difference numerical solution for arbitrary Péclet numbers (section 7.3), with which we compare our asymptotic results. Comparison with prior experimental results is provided in section 4.3.4. Finally, interfacial effects, which can arrest drop expansion altogether, are considered in section 4.3.5.

4.3.1 Drop expansion for fast diffusion

In this section, we provide an asymptotic correction of the fast-diffusion expansion described by our prior work (Roure and Davis, 2021a) for small values of Pe. When $Pe \ll 1$, the internal diffusion is fast relative to expansion from osmotic flow. To investigate equation (4.4) in this regime of fast diffusion, we perform regular asymptotic expansions for the concentration and drop radius in terms of the Péclet number:

$$\begin{aligned} c(r,t) &\sim c_0(r,t) + c_1(r,t)Pe + o(Pe), \\ a(t) &\sim a_0(t) + a_1(t)Pe + o(Pe). \end{aligned} \tag{4.5}$$

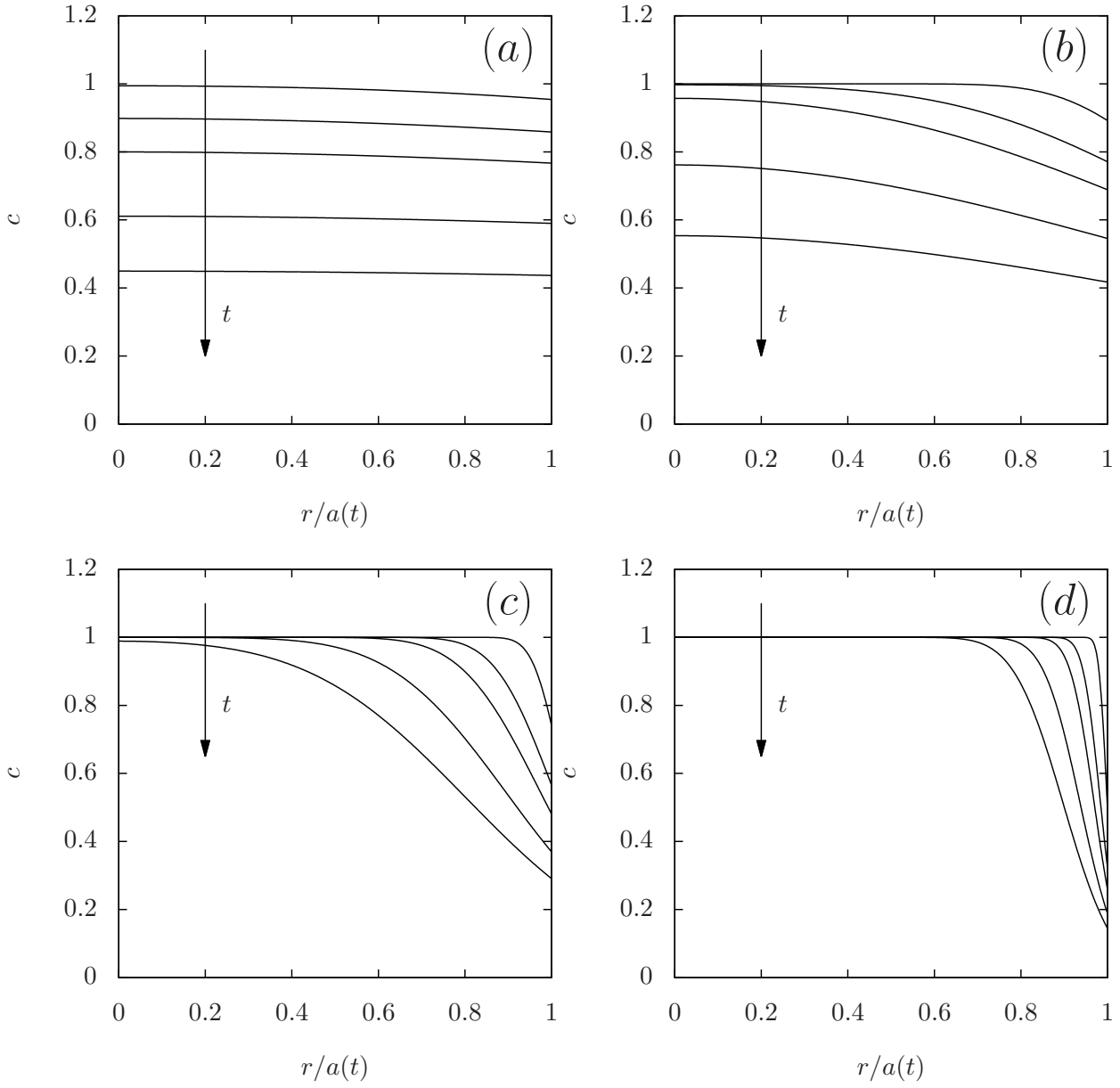

Figure 4.2: Concentration profile evolution for distinct Péclet numbers (a) $Pe = 0.1$, (b) 1.0, (c) 10, and (d) 100 at times $t = 0.01$, 0.05, 0.10, 0.25, and 0.50 (from top to bottom). The results are plotted as a function of the normalized radial coordinate $r/a(t)$.

The first order of these asymptotic expansions can be calculated by taking the limit $Pe \to 0$, in which the governing diffusion equation for the concentration in (4.4) reduces to

$$\frac{1}{r^2}\frac{\partial}{\partial r}\left(r^2\frac{\partial c_0}{\partial r}\right) = 0. \tag{4.6}$$

It is important to note that equation (4.6) has no time derivative, due to the instant relaxation of the initial condition, and, thus, this solution will not depend on the initial condition. Therefore, an auxiliary condition is needed for closure. To this end, we use the integral constraint of salt conservation inside the droplet, given by

$$\int_0^{a(t)} c(r,t)r^2 dr = \frac{1}{3}. \tag{4.7}$$

Solving equation (4.6) and applying the boundary conditions, we find that the concentration $c_0(t)$ is a function of time only. Moreover, the conservation of salt inside the droplet at leading order gives $c_0(t) = a_0^{-3}(t)$. It is instructive to note that time dependence of c_0 only occurs because of the moving boundary. In the case of a steady boundary, the first-order concentration would be a constant and all the subsequent terms of the asymptotic expansion would vanish. By using the result for c_0 in the drop expansion equation and collecting $\mathcal{O}(1)$ terms, we find the leading order for the drop radius evolution with time is given by

$$a_0(t) = (1+4t)^{1/4}, \tag{4.8}$$

which, as expected, is the same result as found in Roure and Davis (2021a).

To obtain the first-order correction for the concentration, we substitute the asymptotic expansions into the governing equations (4.4). Moreover, the boundary condition at the drop surface is expanded in a Taylor series. Hence, collecting the $\mathcal{O}(Pe)$ terms, one finds

$$\frac{1}{r^2}\frac{\partial}{\partial r}\left(r^2\frac{\partial c_1}{\partial r}\right) = \frac{\partial c_0}{\partial t}, \tag{4.9}$$

with boundary conditions

$$\left.\frac{\partial c_1}{\partial r}\right|_{r=0} = 0 \qquad \text{and} \qquad \left.\frac{\partial c_1}{\partial r}\right|_{r=a_0} = c_0^2|_{r=a_0}. \tag{4.10}$$

These two boundary conditions are redundant for determining the coefficients of the general solution of (4.9), and, hence, we need an extra condition, which is given again by the conservation of salt inside the droplet in equation (4.7), which we expand in an asymptotic series in terms of Pe, yielding

$$\frac{1}{3} = \int_0^{a(t)} c(r,t)r^2 dr \sim \frac{1}{3} + \left(\frac{a_1}{a_0} + \int_0^{a_0(t)} c_1(r,t)r^2 dr\right) Pe + o(Pe). \tag{4.11}$$

Substituting the expressions for c_0 and c_1 in (4.11) and collecting $\mathcal{O}(Pe)$ terms yields a parabolic concentration profile in the form of

$$c_1(r,t) = \frac{1}{2a_0^5(t)}\left[\frac{3}{5} - \left(\frac{r}{a_0(t)}\right)^2\right] - \frac{3a_1(t)}{a_0^4(t)}. \tag{4.12}$$

From equation (4.12), the parabolic correction diminishes with time, meaning that the concentration profile becomes flatter for large times. This result is expected, given that, as the drop expands, the expansion rate decays due to the dilution of salt, and, hence, diffusive effects become even more dominant over expansion ones. Collecting the first-order terms in the drop expansion equation, we find that the evolution of $a_1(t)$ is governed by

$$\frac{da_1}{dt} + 3\frac{a_1}{a_0^4} = -\frac{1}{5a_0^5}. \tag{4.13}$$

Equation (4.13) can be solved analytically by elementary methods. Hence, considering the initial condition $a_1(0) = 0$, the solution $a_1(t)$ is given by

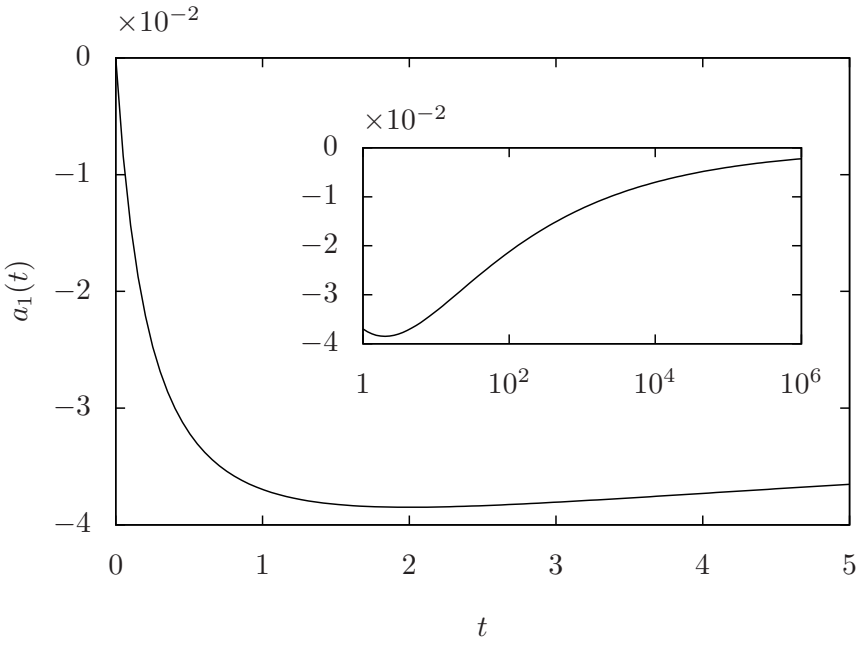

Figure 4.3: First-order correction for the drop radius, given by equation (4.14). The inset on the graph shows the behavior of the function $a_1(t)$ at large times, where the contribution of the first-order correction slowly decays, as the expansion rate slows with time.

$$a_1(t) = \left[(1+4t)^{-3/4} - (1+4t)^{-1/4}\right]/10. \tag{4.14}$$

The behavior of equation (4.14) is displayed in Figure 4.3. From analyzing the orders-of-magnitude of a_1, one can see that, although there is a significant contribution of this first-order correction on the salt distribution profile, the contribution of this first-order correction on drop expansion is quite small for $Pe \ll 1$. In the following sections, we will show that this asymptotic solution agrees with the numerical simulations for small values of Pe.

4.3.2 Drop expansion for slow diffusion: short-time boundary layer asymptotics

In the limit of large Péclet numbers, one could naively try a regular expansion approach similar to the one done in the prior section. This approach, however, inevitably leads to some issues near the boundary. Namely, the differential equation for c at leading order

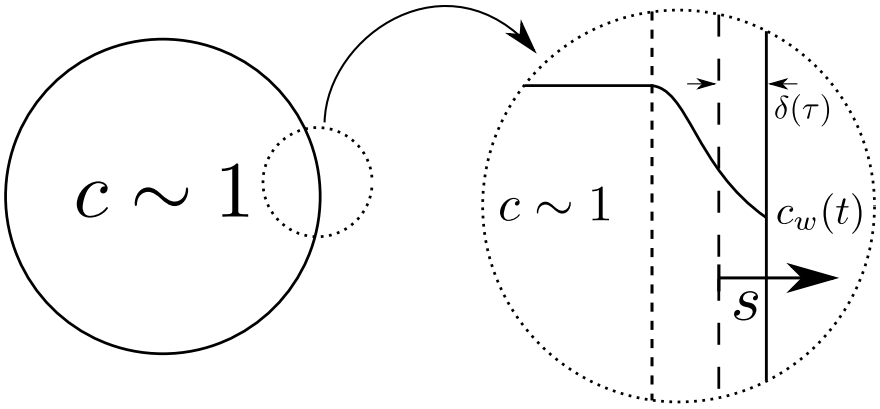

Figure 4.4: Boundary layer near the drop's interface where diffusion effects are not negligible even for large values of Pe. In the closeup, the solid vertical line represents the edge of the drop, at $r = a(t)$, the long-dashed vertical line is the initial edge of the drop, at $r = 1$, and the short-dashed vertical line is the inside edge of the concentration boundary layer.

reduces to $\partial c/\partial t = 0$, which means that $c(r)$ is a function of space only. From the initial condition, we know that $c(r) = 1$. This solution, however, is incompatible with the boundary condition at the interface, which states that the leading-order concentration should be zero at the boundary. For infinite Péclet numbers, this issue arises because, as there is no diffusion occurring inside the drop, we would end up only with an infinitesimal expansion of the drop, which would create a salt-free layer near the drop interface, eliminating the osmotic driving force and, thus, ceasing drop expansion. In contrast, for finite Péclet numbers, there is always a region near the drop's interface where diffusive effects are not negligible, and, thus, there will be a slow expansion of the drop. This thin region is illustrated in Figure 4.4.

To investigate the behavior of the concentration profile near the drop interface for short times, we perform a change of variables in the radial and time coordinates, introducing new variables s and τ such that $r = 1 + sPe^{-1}$ and $\tau = t\,Pe$, so that expansion and diffusion effects balance each other in a thin region near the drop interface. As $Pe^{-1} \ll 1$, collecting the leading-order terms in the diffusion equation results in a differential equation for the leading-order boundary approximation for the concentration:

$$\frac{\partial c}{\partial \tau} = \frac{\partial^2 c}{\partial s^2}, \tag{4.15}$$

with the following initial, matching, and boundary conditions:

$$\begin{aligned} & c(s,0) = 1 - H(s), \\ & c(s \to -\infty, t) = 1, \\ \text{and} \qquad & \partial c/\partial s|_{s=\delta(t)} = -c^2|_{s=\delta(\tau)}, \end{aligned} \tag{4.16}$$

where $H(s)$ is the unit step function and $\delta(\tau) = Pe\,(a(t) - 1)$ is the re-scaled thickness of the expansion layer, which varies according to $d\delta/d\tau = c(\delta, \tau)$. The balancing of diffusion and expansion terms in this region suggests the introduction of a similarity variable, $\eta = s/\tau^{1/2}$. Assuming that the concentration profile is a function of the similarity variable η only, the change of variables in the diffusion equation gives

$$-\frac{1}{2}\eta\frac{dc}{d\eta} = \frac{d^2 c}{d\eta^2}, \tag{4.17}$$

with boundary conditions $c(\eta \to \infty) = 0$ and $c(\eta \to -\infty) = 1$. Solving the equation and applying the boundary and initial conditions, we find that the concentration profile c is given by the self-similar solution $c(\eta) = \mathrm{erfc}(\eta/2)/2$.

In subsequent sections, we will see that this similarity solution is indeed a good approximation for the concentration profile for large Péclet numbers and moderately short times. However, it fails to consider the transient effects near the drop's boundary at very short times (*i.e.*, $\tau \ll 1$), as the concentration at the interface instantly decays to $c_w \sim 1/2$ for nonzero times $\tau \ll 1$, which is not physical and suggests the need for further investigation for the regime of $\tau \ll 1$. Moreover, in contrast to the solution for small Péclet numbers, it is not possible to use the non-linear boundary condition for boundary tracking without going to higher orders or performing some sort of re-scaling.

Boundary tracking for very small times

As the general similarity solution for the boundary-layer problem does not allow for boundary tracking and is not able to fully describe the behavior of the concentration profile for small values of τ, a different analysis is required for this regime. The naive approach to investigate the short-time behavior of the boundary layer would be to expand $c(s,\tau)$ in a series in terms of powers of τ, such that $c \sim c_0(s) + c_1(s)\tau + \ldots$. However, the terms in the main equation and in the boundary conditions would not balance appropriately. A more appropriate method is to represent c as a function of the re-scaled variable $\eta = x/\tau^{1/2}$ and time, giving $c(\eta,\tau)$. In terms of these variables, the governing equation becomes

$$\tau\frac{\partial c}{\partial \tau} - \frac{\eta}{2}\frac{\partial c}{\partial \eta} = \frac{\partial^2 c}{\partial \eta^2}, \tag{4.18}$$

with boundary conditions

$$\begin{aligned} & c(\eta < 0, 0) = 1, \\ & c(\eta \to -\infty, \tau) = 1, \\ \text{and} \qquad & \partial c/\partial \eta|_{\eta=\Delta_b} = -\tau^{1/2} c^2|_{\eta=\Delta_b}, \end{aligned} \tag{4.19}$$

where $\Delta_b = \delta/\tau^{1/2}$ is the re-scaled expansion-layer thickness. We can now proceed to expand $c(\eta,\tau)$ in powers of $\tau^{1/2}$, such that

$$c(\eta,\tau) \sim c_0(\eta) + c_1(\eta)\tau^{1/2} + c_2(\eta)\tau + \mathcal{O}(\tau^{3/2}). \tag{4.20}$$

From the governing equation and the initial and boundary conditions at leading order, $c_0(\eta) = 1$. From this result, combined with the boundary evolution equation, we see that $\Delta_b \sim \mathcal{O}(\tau^{1/2})$. Hence, substituting the expansion (4.20) in the governing equation and collecting order $\mathcal{O}(\tau^{1/2})$ terms we write the equation for the first-order correction $c_1(\eta)$ as

$$\frac{1}{2}c_1 - \frac{\eta}{2}\frac{dc_1}{d\eta} = \frac{d^2 c_1}{d\eta^2}. \tag{4.21}$$

The matching boundary condition at $-\infty$ is given by $c_1(-\infty) = 0$ and the boundary condition related to the flux at the interface can be found by substituting the expansion (4.20) in the moving boundary condition of (4.19) and expanding the boundary terms in a Taylor series around $\eta = 0$ (as $\Delta_b \sim \mathcal{O}(\tau^{1/2})$). Collecting the terms of order $\mathcal{O}(\tau^{1/2})$ and using c_0 constant, we find $dc_1/d\eta|_{\eta=0} = -1$. The solution of equation (4.21) is then given by

$$c_1(\eta) = -\eta\,(\mathrm{erf}\,(\eta/2) + 1) - 2e^{-\eta^2/4}/\sqrt{\pi}. \tag{4.22}$$

This expression describes a small correction accounting for the decay in salt concentration near the drop interface at very short times, which is valid for $\eta \ll \mathcal{O}(\tau^{-1/2})$, or, equivalently, $s \ll \mathcal{O}(1)$. To obtain an approximation for the expansion thickness δ, we expand the terms in the boundary evolution equation around $\eta = 0$ and collect terms up to order $\tau^{1/2}$, yielding

$$d\delta/d\tau \sim 1 - 2\tau^{1/2}/\sqrt{\pi} + \mathcal{O}(\tau), \tag{4.23}$$

which gives us an asymptotic expression for the expansion-layer thickness for small values of τ:

$$\delta(\tau) \sim \tau - 4\tau^{3/2}/(3\sqrt{\pi}) + \mathcal{O}(\tau^2). \tag{4.24}$$

By repeating the same procedure, we can improve this approximation by going to the next order. In this case, the governing equation for c_2 is given by

$$c_2 - \frac{\eta}{2}\frac{dc_2}{d\eta} = \frac{d^2c_2}{d\eta^2}, \tag{4.25}$$

and the flux boundary condition is given by $dc_2/d\eta|_{\eta=0} = 5/\sqrt{\pi}$. Thus, the solution for c_2 is given by

$$c_2(\eta) = \frac{5}{4}\left[(\eta^2+2)\,(\mathrm{erf}(\eta/2)+1) + 2\eta e^{-\eta^2/4}/\sqrt{\pi}\right] \tag{4.26}$$

and the expansion-layer thickness $\delta(\tau)$, up to order $\mathcal{O}(\tau^2)$, is given by

$$\delta(\tau) \sim \tau - 4\tau^{3/2}/(3\sqrt{\pi}) + 3\tau^2/4 + \mathcal{O}(\tau^{5/2}). \tag{4.27}$$

In subsequent sections, we compare these asymptotic expressions for $\delta(\tau)$ with the results from the numerical simulations.

4.3.3 Numerical solution for arbitrary Péclet numbers

There are many different approaches for numerically solving moving-boundary problems (Crank, 1987). In this chapter, for the numerical solution of the moving-boundary problem, we use a finite-difference scheme with a fixed grid. To this end, we re-scale the spatial variable r using the instantaneous radius of the drop $a(t)$. Thus, introducing the new scaled variable $u = r/a(t)$, the governing equation takes the form of

$$\frac{\partial c}{\partial t} = u\frac{\dot{a}}{a}\frac{\partial c}{\partial u} + \frac{1}{Pe}\frac{1}{a^2u^2}\frac{\partial}{\partial u}\left(u^2\frac{\partial c}{\partial u}\right), \tag{4.28}$$

which must be solved simultaneously with the expansion equation $\dot{a}(t) = c(1,t)$ together with the initial condition for the drop radius $a(0) = 1$. The initial and boundary conditions for the problem in terms of the new variable u are given by

$$\begin{cases} c(u,0) = 1, \\ \partial c/\partial u|_{u=1} = -a\ Pe\ c^2|_{u=1}, \\ \partial c/\partial u|_{u=0} = 0. \end{cases} \tag{4.29}$$

Thus, the moving-boundary problem has been converted into a fixed-boundary one. It should be noted that, as pointed out in previous sections, this transformation changes the diffusion equation into an advection-diffusion equation, where drop-expansion effects now appear explicitly in equation (4.28) as a convective contribution, hence justifying

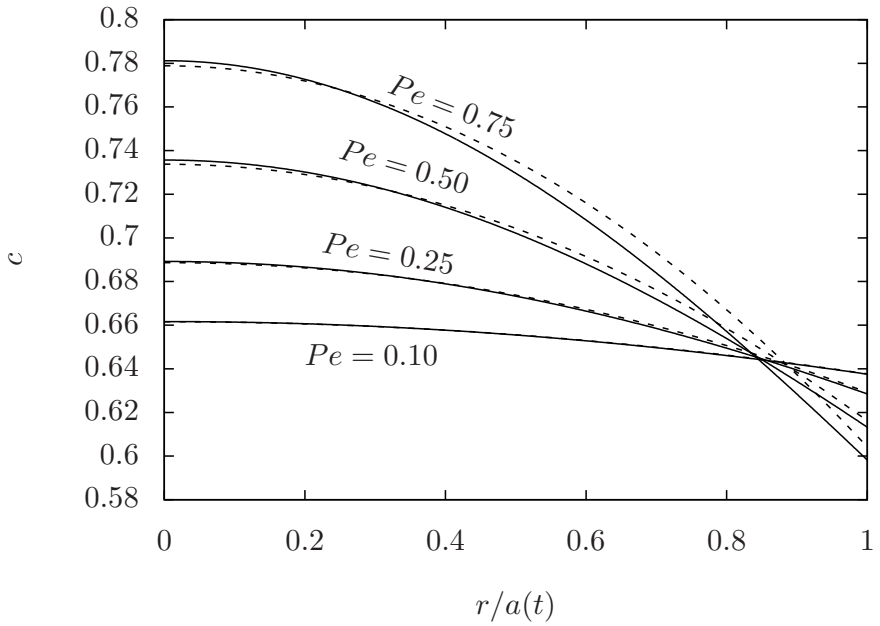

Figure 4.5: Numerical and asymptotic results for the concentration profile versus the scaled radial coordinate $u = r/a(t)$ for time $t = 0.2$ and different values of Péclet number: $Pe = 0.1$, $Pe = 0.25$, $Pe = 0.5$, $Pe = 0.75$. The solid lines are the curves obtained by numerical simulation. The dashed lines represent the first-order asymptotic results for small values of Pe.

the present definition for the Péclet number. The system of coupled equations can be solved numerically using an explicit, finite-difference scheme with a forward-time, central-space (FTCS) discretization. The boundary conditions are implemented by considering virtual elements adjacent to the boundaries, where the function $c(u, t)$ has its first spatial derivatives prescribed. We used 600 nodes for space discretization and a time step Δt small enough to guarantee numerical diffusion stability. For small values of Pe, ranging from 0.1 to 1, we used $\Delta t = 10^{-8}$, whereas for large values of Pe (*i.e.*, $Pe \geqslant 10$) we used $\Delta t = 10^{-6}$.

To validate the numerical results, we compare the results obtaining via the finite-difference scheme for small values of Pe with the asymptotic solution from section 4.3.1. Figure 4.5 shows the comparison between numerical and asymptotic results for values of Péclet $Pe = 0.1$, $Pe = 0.25$, $Pe = 0.5$, and $Pe = 0.75$ for a given time $t = 0.2$. There is excellent agreement between the numerical and asymptotic solutions for $Pe = 0.1$ and

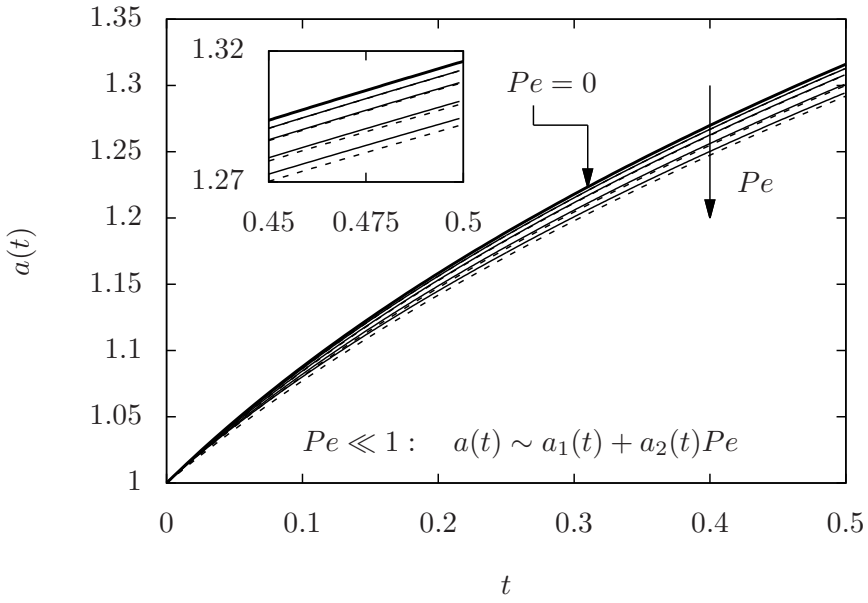

Figure 4.6: Numerical and asymptotic results for the radius evolution versus time for different values of the Péclet number: $Pe = 0.1$, 0.25, 0.5, and 0.75. The thicker solid line at the top represents the limit $Pe = 0$, governed by equation (4.8). The other solid lines represent the values obtained by numerical simulation, whereas the dashed lines represent the first-order asymptotic correction for small Pe.

$Pe = 0.25$. Moreover, the asymptotic solution also provides a good approximation for $Pe = 0.5$ and $Pe = 0.75$, with errors of less than 2%.

We also compare the numerical results for the evolution of drop radius over time with the asymptotic expression found in section 4.3.1. The comparison between numerical and asymptotic results for drop radius versus time are shown in Figure 4.6 for the same values of Pe used in Figure 4.5. From the zoomed-in view displayed in the inset of Figure 4.6, one can see clearly that the first-order correction for fast diffusion describes the drop expansion to a good approximation for $Pe < 1$.

The results for the concentration profile evolution for a wide range of Péclet numbers are displayed in Figure 4.2, presented at the beginning of section 4.3. We note that the concentration profile transitions from a flatter, slightly parabolic shape (as predicted by the small Pe asymptotics) to a behavior that resembles the one predicted by the boundary-layer asymptotics for large Pe and short times, for which the profile displays a flat shape away from the drop's surface and all diffusive effects are constrained to a boundary-layer region

near the drop's interface. We check the validity of this last assertion by comparing the results for the concentration profiles for large Péclet numbers to the ones predicted by the boundary-layer similarity solution. This comparison is shown in Figure 4.7 for $Pe = 100$ and $Pe = 200$. For the most part, there is an excellent agreement between the numerical results for the concentration profile and the similarity solution for the boundary-layer problem.

As seen in the insets in Figure 4.7, discrepancies between the numerical results and the self-similar concentration profile occur near the drop interface, especially for shorter times, as expected from the transient analysis for short times discussed in section 4.3.2. Moreover, the radius evolution for large Péclet numbers is displayed in Figure 4.8(a) for $Pe = 100$, 150, and 200. By performing a change of coordinates on the numerical results presented in Figure 4.8(a) to the variables s and τ introduced in section 4.3.2, we observe that all results for radius evolution at large Péclet numbers collapse into a 'universal' profile for the boundary thickness $\delta(\tau) = Pe\,(a(t) - 1)$, as expected by the boundary-layer analysis in section 4.3.2. This result is shown in Figure 4.8(b). The inset in Figure 4.8(b) shows the comparison between the numerical curve for $\delta(\tau)$ and the asymptotic expressions for short times presented in equations (4.24) and (4.27). As expected, the higher-order asymptotic solution yields a better approximation for the expansion-layer thickness for short times.

It is noted that $\delta(\tau)$ should not follow a single power law, due to the presence of different behaviors at distinct times. Nonetheless, it is possible to obtain a numerical fit of this curve with a heuristic power law for the values of τ shown in Figure 4.8, which may be useful for numerical simulations involving drop expansion, such as the ones performed in Roure and Davis (2021a). Such numerical fit gives $\delta(\tau) \approx 0.787\ \tau^{0.675}$, with an average absolute error of 0.05 for $\tau \leqslant 100$, with the larger discrepancies being at small values of τ, where the expansion behavior is more complex, as shown in the asymptotic analysis presented in section 4.3.2. For larger values of τ, however, the expansion appears to be

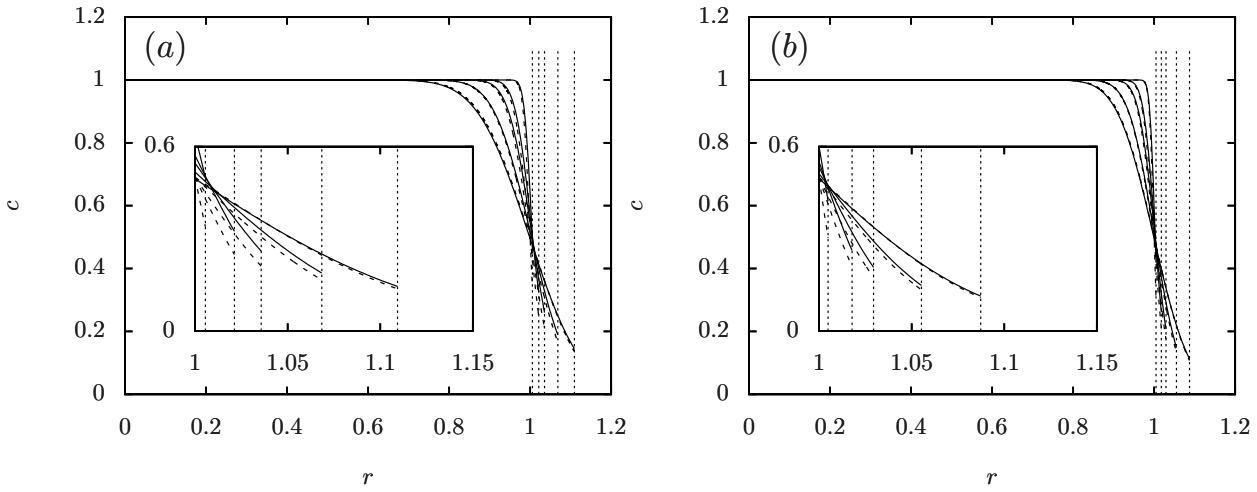

Figure 4.7: Comparison between numerical results and the boundary-layer theory for large Péclet numbers (a) $Pe = 100$ and (b) $Pe = 200$ for times $t = 0.01$, 0.05, 0.1, 0.25, and 0.5. The solid lines in the main portion of the graph represent the numerical solution of the concentration profile, the long-dashed lines represent the concentration profile predicted by the boundary-layer theory, the short-dashed vertical lines represent the interface position for the different times. The insets in (a) and (b) show in detail the discrepancies between numerical and similarity concentration profiles near the drop interface.

linear with $\tau^{1/2}$, which is characteristic of similarity solutions and recent scaling and experimental observations (DeIuliis et al., 2021). This scaling can be verified by fitting the numerical data for large values of τ with a curve that is linear with $\tau^{1/2}$, resulting in $\delta(\tau) \approx 2.674\,\tau^{1/2} - 12.24$ for large values of τ (*i.e.*, $\tau \gtrsim 100$). The comparison between this fitting and the universal curve $\delta(\tau)$ is shown in Figure 4.9.

Another result we can analyze is the salt concentration at the interface, which controls the rate of drop expansion. Namely, by (4.4), the salt concentration at the interface gives the rate of change of the drop radius. The numerical results for the concentration c_w as a function of time for different Péclet numbers are shown in Figure 4.10. As predicted by the theoretical analysis, at large values of Pe, there is a fast decay in the concentration at the drop interface, as diffusion happens much slower than expansion. This fast transient decay happens in a dimensionless time $t \ll 1/Pe$. At large times, as drop expansion slows down as the drop grows, diffusion will start to dominate over expansion effects and the

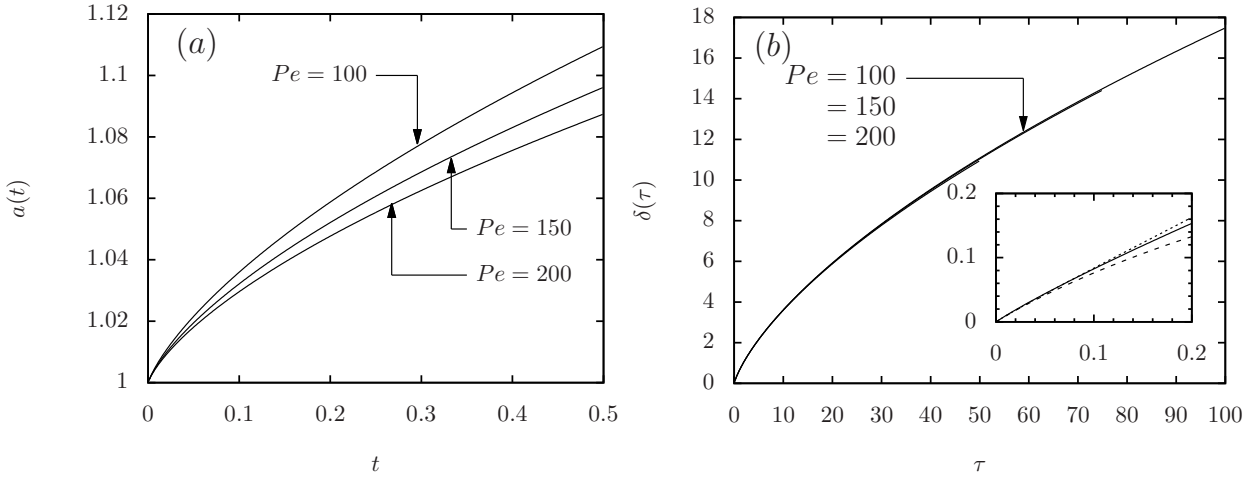

Figure 4.8: Radial evolution for high Péclet numbers in terms of (a) (r, t) coordinates and (b) (s, τ) coordinates. The results for high Péclet numbers in terms of (s, τ) coordinates seem to all obey the same relationship between δ and τ. The inset in (b) compares this curve, represented by the solid curve, to the asymptotic expressions for δ at short times for order $\mathcal{O}(\tau^{3/2})$ and $\mathcal{O}(\tau^2)$, represented by the long-dashed and short-dashed curves, respectively.

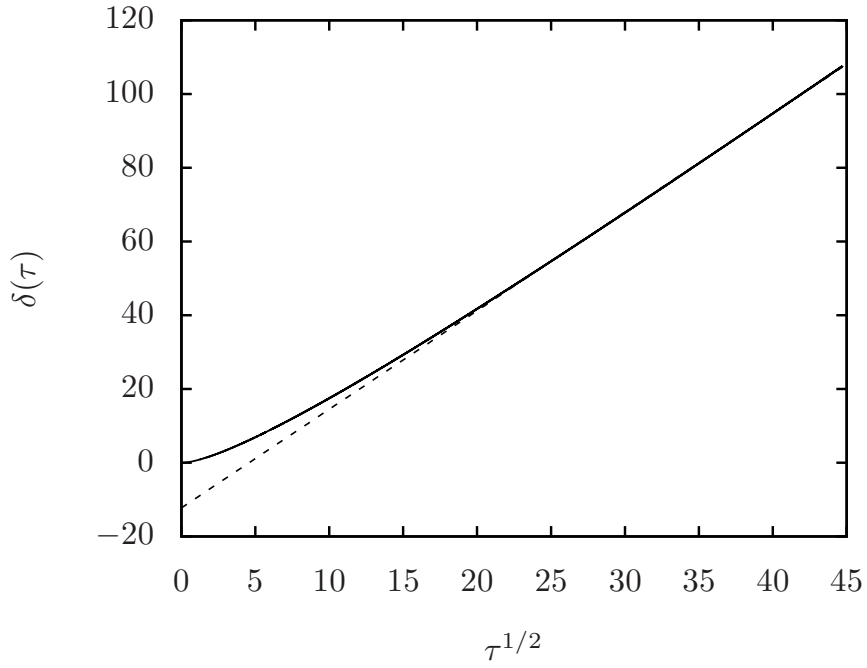

Figure 4.9: Large-τ behavior of the 'universal' curve $\delta(\tau)$. The solid curve is the data obtained via numerical simulations for $Pe \gg 1$. At large values of τ, the curve displays a linear behavior with respect to $\tau^{1/2}$, which can be approximated by the numerical fit $\delta(\tau) \approx 2.674\,\tau^{1/2} - 12.24$ (dashed curve).

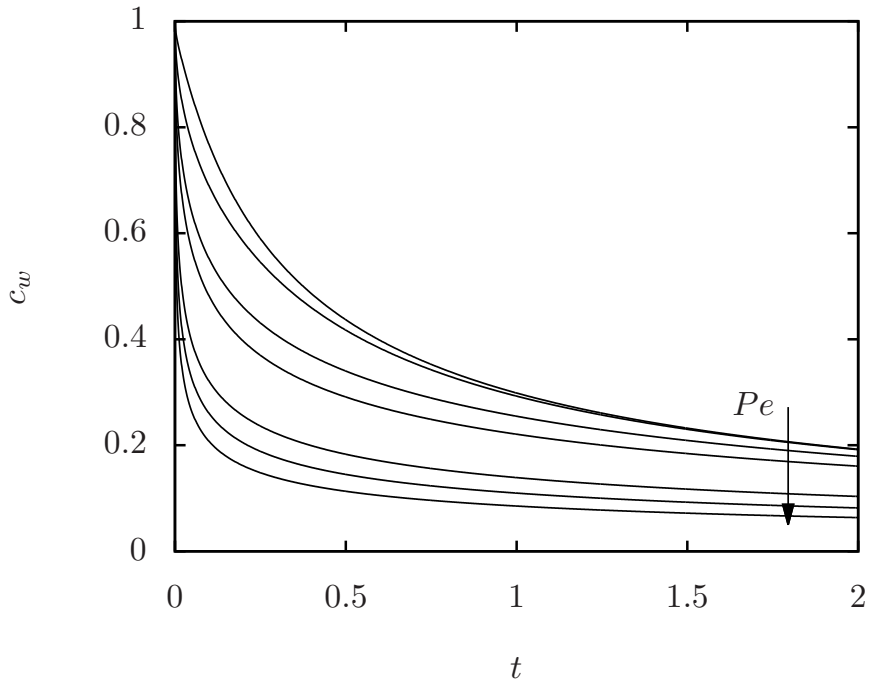

Figure 4.10: Salt concentration at the drop interface as a function of time for different Péclet numbers (from top to bottom) $Pe = 0.1$, 1.0, 5.0, 10.0, 50.0, 100, and 200.

salt inside the droplet will be uniformly distributed. Hence, the drop will grow in a rate similar to the one for small Péclet numbers at large times.

4.3.4 Comparison with experimental data

To illustrate the applicability of our theory, we compare the numerical and asymptotic analyses performed in the previous sections to the experimental data from the literature (DeIuliis et al., 2021). Rather than single spherical drops, the experiments used cylindrical "rivulets" composed of highly concentrated, microscale saltwater droplets held together by nanoscale oil/surfactant layers. The initial rivulets were 90 wt% aqueous phase containing 3 wt% NaCl, with 2.5 wt% dodecane and 2.5 wt% sorbitan monooleate forming the oil film (DeIuliis et al., 2021). The rivulets were placed in fresh water, and the change of their diameter was observed over time. As discussed previously (DeIuliis et al., 2021), the diffusion process in these rivulets is controlled by water permeation from outside to inside through successive oil films and swelling saltwater droplets, resulting in a slow counter-

diffusion of salt. Assuming the existence of a hydrodynamic limit from this lattice-like diffusion to a continuous diffusion problem, it should be possible to calculate an effective diffusivity for such systems by fitting the numerical data of expansion versus time with our model.

It is noted that, although the experimental data (DeIuliis et al., 2021) concerns cylindrical agglomerates, the regime of high Péclet numbers is still governed by a thin boundary-layer region at the interface, and, hence, much of the analysis presented in section 4.3.2 is valid for the cylindrical geometries, as the governing equations are applied near the interface and there is no geometrical terms in the boundary conditions. Thus, the main interest is the radius evolution equation. Following the prior discussion (DeIuliis et al., 2021), the governing equation for the cylinder radius for an isotropic expansion coincides with the one for a sphere. In contrast, for the case of a fixed-length constriction, the governing equation for the cylinder radius would have to be changed to $da/dt = 2c_w/3$, where a is the cylinder radius. For simplicity, we will assume an isotropic expansion of the cylindrical shape, so that we can use the spherical analysis from this chapter without further changes in the model.

From the large τ numerical fitting shown in Figure 4.9, we have $\delta(\tau) \approx 2.674\,\tau^{1/2} - 12.24$ at large values of τ. In terms of dimensional quantities, this relationship is $a - a_i \approx 2.674\ (Dt)^{1/2} - 12.24\ D/(KRTc_i)$. One should note that the slope in this expression is independent of the permeability K or other parameters besides the diffusivity, and, hence, can be used to calculate an effective diffusivity from the experimental data. Moreover, it is also noted that the vertical intercept does not depend on the initial radius, and, hence, this fitting for $a - a_i$ should be valid for different drop sizes, as long as other parameters such as initial salt concentration and permeability are kept constant.

The comparison between the current model and prior experimental results (DeIuliis et al., 2021) is shown in Figure 4.11. Five different initial rivulet diameters were used in these experiments, ranging from $2a_i = 220$ μm to 995 μm. Unfortunately, neither the

effective diffusivity nor the water permeability were known *a priori* for the experimental system, but they are model parameters that may be estimated by fitting to the theory. In Figure 4.11, the symbols are the average of the five experiments for each time point, and the error bars represent plus and minus one standard deviation. Although there is moderate scatter in the data within each experiment, and between experiments (DeIuliis et al., 2021), the change in radius with time appears to fall on a universal curve, independent of the initial radius, but with two distinct regions that display linear behavior for $a - a_i$ versus $t^{1/2}$.

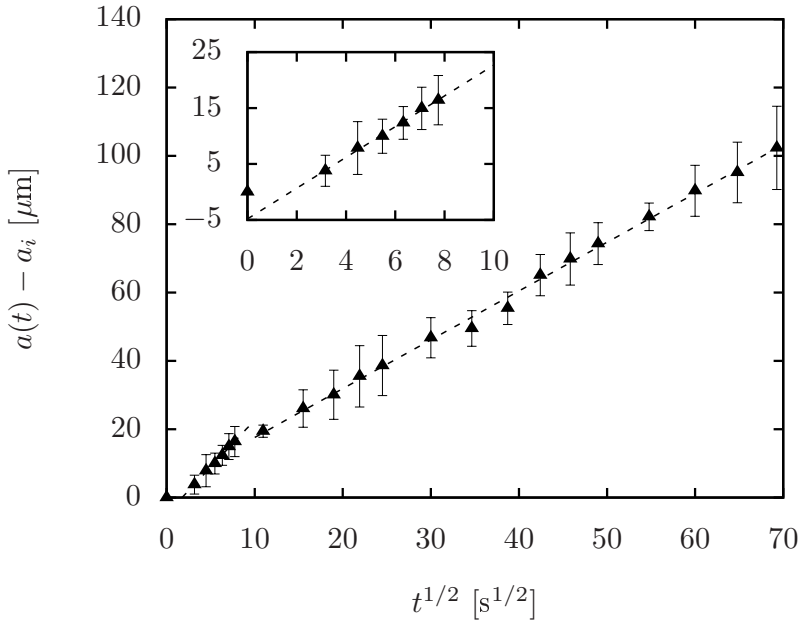

Figure 4.11: Comparison between our theoretical model and the experimental data from (DeIuliis et al., 2021) for the expansion of cylindrical agglomerates with an initial 3 wt% internal NaCl concentration. The data for the cylinder radial increment $a - a_i$ was taken from the experimental results shown in Figure 4(b) from that paper. The data was averaged over the different experiments for distinct initial sizes. The inset shows a zoom-in of the short-time regime, where we can observe an apparent linear behavior with $t^{1/2}$ as predicted by our boundary layer analysis.

First, there is a short-time region ($t \leqslant 60$ s), shown in the inset of Figure 4.11, where there is a higher slope and a negative intercept, similar to the theory fit (dashed line) shown in Figure 4.9. Using a least-squares fit on the experimental data to the model yields $D = 1.1 \pm 0.5$ $\mu m^2/s$ using the line slope and its 90 % confidence interval. The data point

at $t = 0$ s was not included in the fit, as the first several seconds of swelling correspond to the initial transient transient of the solid curve in Figure 4.9, whose behavior gradually transitions from the short-τ theoretical prediction $\delta(\tau) \sim \tau$ from equation (4.27) to the $\tau^{1/2}$-linear behavior shown by the dashed curve in the same figure. We should be able to use the same fit to determine the permeation flux J_i. This fit yields $J_i = 2.7 \pm 2.5$ μm/s for the initial water flux into the rivulet, using the best-fit intercept and its 90 % confidence interval, indicating that the experimental data have too much relative uncertainty at short-time regions and, thus, fail to provide an accurate estimate for the permeation flux. However, using the best-fit value for J_i and the range of initial rivulet radii, the Péclet number, $Pe = J_i a_i/D$ is in the range $250 - 1300$ for these experiments, as required for $Pe \gg 1$ analysis shown in Figures 4.8 and 4.9. The re-scaled time $\tau = J_i^2 t/D$ is of order $\tau \approx 400$ for $t = 60$ s at the end of the short-time region, which is within the range of accuracy of the linear fit (dashed line) in Figure 4.9. Finally, in principle, the permeability $K = J_i/(RTc_i)$ may be estimated as $K \approx 0.2$ μm/s-atm, but the uncertainty has similar magnitude to this best-fit value.

Second, there is a long-time region ($t \geqslant 120$ s), which has a lower slope, but still shows a linear relationship between $a - a_i$ and $t^{1/2}$, as shown in the main plot of Figure 4.11. Fitting a straight line to this portion of the data yields a lower apparent diffusivity of $D = 0.29 \pm 0.05$ $\mu m^2/s$ from the best-fit slope and its 90 % confidence intervals. However, the initial flux and permeability can no longer be determined from the intercept. Our hypothesis for the different slopes between the short-time and long-time portions of the data in Figure 4.11 is based on the discrete microstructure of the rivulets used in the experiments. Namely, it is possible that effects arising from the discrete nature of the diffusion process come into play at short times, when the boundary-layer thickness is not much greater than diameter of the individual droplets comprising the rivulet. Also, the outer edge of the rivulet may have a different microstructure than the interior, due to shearing as the rivulet was formed. Moreover, changes in the permeation resistance

can come into play at larger times as the oil films are stretched. Our current continuous homogeneous model, however, is not suitable to investigate such effects. We also note that the long-time data show variations between experiments that are larger than the uncertainties within each experiment (DeIuliis et al., 2021), so were not lumped together - instead, the best-fit slope was found for each experiment and then averaged to determine the effective diffusivity for long times. The differences in the slopes are presumably due to small differences in the microstructure of the rivulets, as there is not a systematic variation with rivulet diameter (DeIuliis et al., 2021). In contrast, the short-time data had larger uncertainties within each experiment, due to fewer data points and larger relative errors, so these data were combined for the linear regression. As an aside, salt was added not only to promote drop swelling but also to inhibit Ostwald ripening (van Netten et al., 2017; DeIuliis et al., 2021). A plot of a^3 versus t does not exhibit the linear behavior characteristic of Ostwald ripening.

4.3.5 Interfacial tension effects

So far, all solutions discussed here display an indefinite (but slowing) drop growth. In practical systems, however, additional effects may eventually limit drop growth and impose an equilibrium radius. One such limiting effect is the presence of interfacial tension at the drop interface, balancing the osmotic pressure. Another might be material tension, as observed in the swelling of hydrogels (Holback et al., 2011; Doi, 2013).

We incorporate interfacial-tension effects in our model by introducing a capillary pressure jump in the expression for the mass flux of water at the interface. Namely,

$$-\mathbf{q} \cdot \hat{\mathbf{n}}^*|_\Sigma = K\left(\Pi - 2\kappa_m \sigma\right), \tag{4.30}$$

where $\kappa_m = 1/a(t)$ (in dimensional quantities) is the mean curvature of the the spherical droplet and σ is the interfacial tension, which, for a uniform distribution of surfactants on

the interface, can be written, in terms of dimensional quantities, as (Safran, 2018)

$$\sigma = \sigma_0 - \frac{RTN_{surf}}{4\pi a(t)^2}, \tag{4.31}$$

where N_{surf} is the total number of moles of surfactant. Going back to dimensionless quantities, we can rewrite the radial evolution equation as

$$da/dt = \left(c_w - \mathscr{A}/a + \mathscr{B}/a^3\right), \tag{4.32}$$

where $c_w(t)$ is the normalized salt concentration at the interface and the non-dimensional parameters

$$\mathscr{A} = \frac{4\pi a_i^2 \sigma_0}{3NRT} \qquad \text{and} \qquad \mathscr{B} = \frac{2N_{surf}}{3N} \tag{4.33}$$

control the effect of interfacial tension. With this new expression for the surface motion, the moving boundary condition of equation (4.4) becomes

$$\left.\frac{\partial c}{\partial r}\right|_{r=a(t)} = -Pe\, c_w \left(c_w - \frac{\mathscr{A}}{a} + \frac{\mathscr{B}}{a^3}\right). \tag{4.34}$$

From equation (4.32), we can calculate the equilibrium radius a_{eq}, which is given by

$$a_{eq} = \left(\frac{1+\mathscr{B}}{\mathscr{A}}\right)^{1/2}. \tag{4.35}$$

The equilibrium radius in (4.35) is similar to the equilibrium result presented in Mezzenga et al. (2004), and, much like that model, our model accounts for both drop swelling ($a_{eq} > 1$) and shrinking ($a_{eq} < 1$). From (4.35), we see that low values of interfacial tension and the presence of surfactants at the interface result in a larger limiting radius of the droplet, whereas higher values of interfacial tension can impose a more narrow limit for drop swelling. Furthermore, in the case of instant diffusion, the drop radius is given by the following implicit expression:

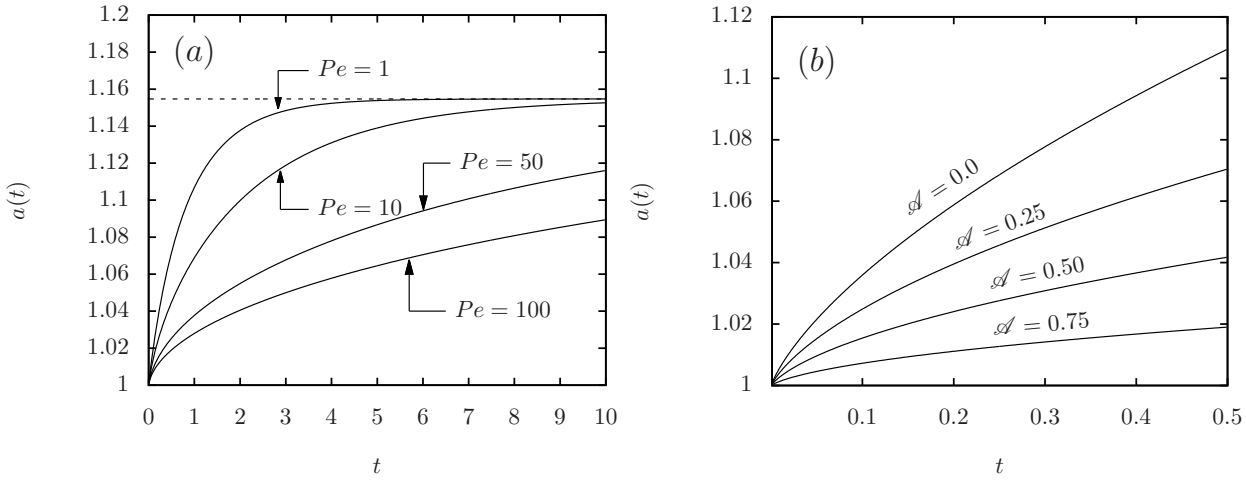

Figure 4.12: Effects of interfacial tension on diffusion-limited expansion. Figure (a) shows the numerical results for drop radius evolution for different values of Pe, $\mathscr{A} = 0.75$, and $\mathscr{B} = 0$. The dashed horizontal line represents the limiting radius a_{eq} predicted by the theory. Figure (b) shows the numerical results for drop radius for $Pe = 100$, $\mathscr{B} = 0$, and (from top to bottom) $\mathscr{A} = 0.0$, 0.25, 0.5, and 0.75.

$$-\frac{a^2-1}{2\mathscr{A}} - \frac{1+\mathscr{B}}{2\mathscr{A}^2}\log\left(\frac{1-(a/a_{eq})^2}{1-(1/a_{eq})^2}\right) = t. \tag{4.36}$$

For the numerical simulation of the full diffusion-expansion problem for arbitrary Péclet numbers and nonzero interfacial-tension effects, we use the same finite-difference scheme presented in section 7.3 with the appropriate changes in the boundary condition and the radial evolution given by equations (4.34) and (4.32), respectively. The results obtained from these simulations are shown in Figure 4.12. As expected, the presence of interfacial tension imposes a maximal bound for drop expansion, to which the drop radius converge at large times. We also note that drop expansion slows down significantly for nonzero values of $\mathscr{A}$. Namely, for $t = 0.5$, $\mathscr{B} = 1$, and $Pe = 100$, there is a decrease of more than 80% in the radial variation of the drop for values of $\mathscr{A}$ ranging between 0 and 0.75. The presence of inner diffusion continues to play an important role on drop expansion, as it significantly increases the time taken for the drop to reach a steady state, as shown by the results in Figure 4.12.

4.4 Concluding remarks

Osmotic swelling of emulsions, gels, and other soft materials is of fundamental importance in many applications. Although prior studies have considered this important problem (Mezzenga et al., 2004; Leal-Calderon et al., 2012; Wan and Zhang, 2002; Yan and Pal, 2001; Roure and Davis, 2021a; DeIuliis et al., 2021), the current work presents the first quantitative model that describes both osmotic permeation into the swelling droplet and the salt counterdiffusion from the droplet interior to the diluted region where the fresh permeate has entered. In contrast to other similar diffusion-expansion models, such as the ones found in works concerning evaporation (Frank, 1950; Tredenick et al., 2021; Font, 2018; Sobac et al., 2015), our model involves a non-linear boundary condition to describe the balance of permeation and diffusion at the moving interface which is similar to the moving-boundary conditions in the so-called Stefan problems with kinetic undercooling (Cohen and Erneux, 1988; Evans and King, 2000; Back et al., 2014; McCue et al., 2011). This non-linearity leads to multiple time scales and a challenging solution. In this work, we have presented asymptotic and numerical solutions for the moving-boundary problem that governs the system, as well as the inclusion of interfacial-tension effects, which impose a finite limit to drop expansion. We also compared our theoretical results to the experiments performed previously(DeIuliis et al., 2021). Our primary hypothesis is that diffusion limitations are present in typical systems and slow down the swelling process.

The numerical analysis of the problem was undertaken by first performing a coordinate transformation that transforms the moving-boundary problem into a fixed-boundary one and then solving it numerically using a forward-time, central-space, finite-differences scheme. The asymptotic analysis of the problem for fast diffusion resulted in a small correction for the drop-radius expression for the case of instant diffusion, presented in Roure and Davis (2021a), for small Péclet numbers. These results are in excellent agreement when compared to the full numerical solutions by finite differences.

As hypothesized, the presence of salt-diffusion resistance inside the droplet slows

down drop expansion considerably. Moreover, in the regime of slow diffusion (*i.e.*, large Péclet numbers), as are typical of the experiments considered (DeIuliis et al., 2021), the diffusion effects are constrained to a boundary-layer region located adjacent to the drop interface. In this regime, we obtained a similarity solution, valid for short times, for the concentration profile in the boundary layer. We also developed an asymptotic expression for the boundary-expansion thickness in the regime of small values of the re-scaled time $\tau = t\ Pe$. This novel theoretical prediction is also observed in the numerical results for very large Péclet numbers. These numerical results match those predicted by the similarity solution, except near the drop interface at very short times, which is, instead, described by our asymptotic analysis for small values of τ. In this boundary-layer regime, the re-scaled expansion thickness $\delta(\tau) = Pe(a(t) - 1)$ displays a 'universal' behavior (*i.e.*, independent of Pe) when plotted as a function of the re-scaled time variable τ, a feature that is also verified by the numerical simulations. We can approximate this curve with a good precision for $t \lesssim 100$ with a heuristic power-law curve $\delta(\tau) \approx 0.787\ \tau^{0.675}$, which can potentially be used for future studies involving short-time kinetics of gels or droplets with very slow inner salt diffusion. The exponent predicted by this numerical fit is, as expected, in between the two characteristic scales of $\tau^{1/2}$ and τ, which are related to the behavior of the curve $\delta(\tau)$ for medium and short times, respectively.

The comparison with the experimental data for emulsion binders (DeIuliis et al., 2021) shows a remarkable similarity between our boundary-layer theory and the experimental results. In particular, after a very short initial transient, both theory and experiment exhibit a linear relationship between the increase of drop radius and the square root of time, with a slope directly proportional to the square root of the effective diffusivity within the water-in-oil-in-water emulsion. Moreover, the $\tau = 0$ intercept of this linear relationship may, in principle, be used in the theory to determine the water permeability of the interface surrounding the drop or emulsion, but the experimental data unfortunately had too much uncertainty to provide an accurate value.

Furthermore, we also considered the effects of interfacial tension on drop expansion by balancing osmotic and interfacial-tension effects. Such effects have been considered by prior works on swelling kinetics, such as Mezzenga et al. (2004), but in the absence of internal diffusion. In this case, the presence of interfacial tension imposes an upper limit to the drop radius. As shown by our simulations, internal diffusion may still play a fundamental role in such cases by slowing down drop expansion, especially for large Péclet numbers. This key finding represents an improvement in the present work compared to prior studies of emulsion swelling (Mezzenga et al., 2004; Leal-Calderon et al., 2012; Wan and Zhang, 2002; Yan and Pal, 2001; Roure and Davis, 2021a; DeIuliis et al., 2021).

Diffusion-limited expansion problems appear in many other contexts, such as the swelling of clays, drilling mud, and hydrogels (Bertrand et al., 2016; Holback et al., 2011). Thus, we expect that the analysis presented here may also apply, to some extent, to these related problems. In addition to these and other applications, our vision for future work includes carefully-controlled, short-time experiments that allow for observation of the predicted nonlinear asymptotic behavior and accurate determination of the interfacial permeability.

CHAPTER 5

EFFECTS OF DIFFUSION-LIMITED SWELLING ON PARTICLE CAPTURE

This work was originally published in the *Journal of Fluid Mechanics* 948 (2022) A36 with co-authors Jenna Trost and Robert H. Davis

Synopsis

This chapter examines the dynamics of a rigid spherical particle and a semi-permeable spherical drop that expands due to osmosis in an external, pure-extensional flow field. The droplet is governed by an expansion-diffusion problem, which is coupled to the set of dynamical equations governing the relative particle trajectory. By performing multiple trajectory simulations, we calculate transient collision efficiencies, which can be used to determine the collision kernel for population dynamics. We also use these simulations to better understand the evolution of the microstructure by determining the transient behavior of the pair distribution function. Our results indicate that the presence of drop expansion increases the collision efficiency of the system, especially for very small particles, which are the most difficult to capture by froth flotation. Moreover, although the presence of slow salt diffusion inside the drops can mitigate this improvement, the contribution of expansion to the collision efficiency may still be considerable, even in the absence of hydrophobic or other attractive forces.

5.1 Introduction

Froth flotation by small air bubbles has traditionally been used in industry to capture fine minerals and other hydrophobic particles (Kitchener, 1984; Wills and Napier-Munn, 2006). However, this method is not efficient for capturing very small particles of

about 10-20 μm in diameter or less (Miettinen et al., 2010; Leja, 2012). In such cases, the lubrication resistance between the floating bubbles and particles hinders collision, making the particles move around the bubble instead of being captured (Barnocky and Davis, 1989; Loewenberg and Davis, 1994; Mehrotra et al., 1983; Miettinen et al., 2010). An alternative to froth flotation is provided by the more efficient hydrophobic oil-binder techniques (Mehrotra et al., 1983; Sirianni et al., 1969; van Netten et al., 2014, 2016). These techniques, however, can be expensive due to large amount of oil required. More recently, an alternative binder method was proposed using a water-in-oil-in-water (W/O/W) emulsion containing salt-water droplets covered by semi-permeable, surfactant-stabilized oil layers (van Netten et al., 2017; Galvin and van Netten, 2017; Sahasrabudhe et al., 2021). Besides using much less oil than other oil-binder techniques, this new method has been shown to be very efficient, as the permeability of the oil layer mitigates the lubrication forces between particle and droplet, allowing for an increased capture rate (Davis and Zinchenko, 2018; Baysinger and Davis, 2021). Moreover, the expansion of the droplets, caused by an osmotic flux of water entering the droplet due to the presence of salt inside the droplets, also contributes to a higher collision efficiency (Roure and Davis, 2021a). However, the influx of fresh water dilutes the salt water just inside the droplets, which slows down the drop expansion and reduces the particle engulfment rate, so that the quantitative benefits of osmotic drop expansion on particle capture are unclear.

To better understand the physics underlying this novel particle-capture method, we focus on the investigation of binary interactions between droplets and particles. This type of two-particle analysis has been extensively used in the literature to investigate particle collision and agglomeration (*e.g.*, Zeichner and Schowalter (1977); Davis (1984); Rother and Davis (2001); Phan et al. (2003); Roure and Cunha (2018); Reboucas and Loewenberg (2021); Rother et al. (2022)). More specifically, to model the different aspects involved in the novel agglomeration method by emulsion binders, the works by Davis and Zinchenko (2018) and Roure and Davis (2021a) investigated, respectively, the effects of permeability

and osmotic swelling on particle capture. The work by Davis and Zinchenko (2018) presents analytical and asymptotic solutions for the hydrodynamic problem of a rigid particle interacting with a droplet covered with a semi-permeable film and then uses the solution to investigate the collision efficiency of particles and non-expanding droplets. In Roure and Davis (2021a), this investigation of collision efficiencies is extended to the case of expanding droplets. In this context, the use of standard collision theory to calculate the collision efficiency ceases to be valid, and the collision efficiencies (as well as the collision kernels for the population dynamics) are time dependent. One of the main assumptions in the prior work is that the diffusion of salt inside the drop occurs instantly, corresponding to small Péclet number. However, in most cases, the influx of fresh water and the non-instantaneous diffusion of salt from the drop center to its interface diminish the concentration of salt at the inner drop interface, slowing down subsequent osmosis and drop expansion considerably. In recent works, this interplay between diffusion and expansion was investigated theoretically and experimentally (DeIuliis et al., 2021; Roure and Davis, 2021b; DeIuliis et al., 2022). In Roure and Davis (2021b), the drop expansion was modeled as a diffusion problem with non-linear, moving boundary conditions similar to the ones found in Stefan problems with kinetic undercooling (Evans and King, 2000; McCue et al., 2011; Back et al., 2014). For high Péclet numbers, the theoretical calculations predict a low-concentration boundary layer near the drop interface, which substantially slows drop expansion. The results from the expansion-diffusion model have shown good agreement with experimental results for osmotic swelling of W/O/W emulsion binders (DeIuliis et al., 2021, 2022).

The main goal of this work is to quantify the effects of slow diffusion on the capture of particles by swelling droplets, extending the results of Roure and Davis (2021a) to the case where diffusion limitations slow down drop expansion. To this end, we investigate the dynamics of a rigid spherical particle near a spherical drop with a semi-permeable interface that expands due to osmosis in an external, pure-extensional flow field. To model the

diffusion-limited osmotic swelling of the droplet, we use the diffusion-expansion model presented in Roure and Davis (2021b), which is then coupled to the set of dynamical equations governing the relative particle trajectory. By performing multiple trajectory simulations, we calculate the transient collision efficiencies, which can be used to determine the collision kernel for population dynamics. We are especially interested in determining if, and by how much, the collision efficiency for very small particles is increased by osmotic expansion of droplets, potentially overcoming the limitations of froth flotation.

5.2 Methods

To investigate the capture dynamics of particles, we focus on the binary interactions between particles and droplets, as done in Davis and Zinchenko (2018) and Roure and Davis (2021a). The particle and droplet are both spherical and interact in a surrounding linear flow with conditions of creeping flow (small Reynolds number). A sketch of the problem is shown in Figure 5.1. For the non-dimensionalization of the problem, we follow the same procedure used in Roure and Davis (2021a). Namely, we use the inverse shear rate $\dot{\gamma}^{-1}$ as the characteristic time scale and the initial drop radius, a_i, as the characteristic length scale.

For modeling the binary interactions between particles and drops, we consider the particle and drop to be free of net forces and torques (i.e., a mobility problem). Attractive forces, such as van der Waals or hydrophobic interactions, are neglected, as it is anticipated that permeation of fluid into the drop will reduce the lubrication resistance to allow for contact without attractive forces (Davis and Zinchenko, 2018). Also, like in Roure and Davis (2021a), we focus our analysis on the case where the external flow is given by a uniaxial extensional flow having inflow along the z axis, with $\mathbf{u}^\infty = \mathbf{E}^\infty \cdot \mathbf{x}$ and $\mathbf{E}^\infty = \dot{\gamma}(\hat{\boldsymbol{e}}_x\hat{\boldsymbol{e}}_x + \hat{\boldsymbol{e}}_y\hat{\boldsymbol{e}}_y - 2\hat{\boldsymbol{e}}_z\hat{\boldsymbol{e}}_z)$, where $\mathbf{x} = (x, y, z) \equiv r\,\hat{\boldsymbol{e}}_r$ is the position vector with origin at the center of the drop. In this context, the non-dimensional governing equations for the

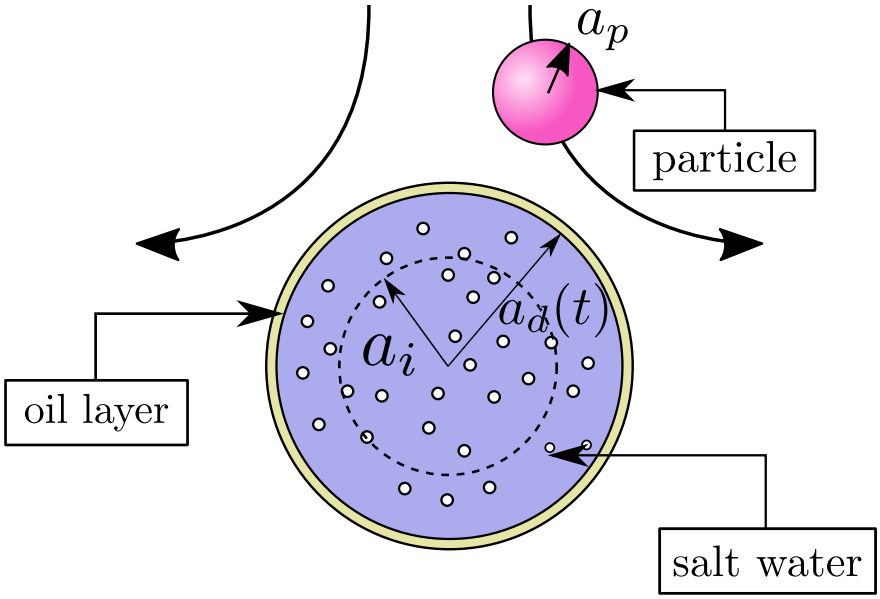

Figure 5.1: Sketch of the binary interaction model between a spherical particle and a semi-permeable drop in the presence of an external linear flow. The presence of salt inside the droplet leads to its swelling, which can be mitigated by a slow diffusion of salt inside the drop. The dashed circle represents the starting configuration of the droplet, with starting radius a_i. The drop radius a_d changes with time as the drop expands due to the water permeation caused by osmosis.

relative motion of the solid particle, in Cartesian coordinates, are (Batchelor and Green, 1972b)

$$\begin{aligned} dx/dt &= (1-B)x + E\,x, \\ dy/dt &= (1-B)y + E\,y, \\ \text{and} \qquad dz/dt &= -2(1-B)z + E\,z, \end{aligned} \tag{5.1}$$

where

$$E = (B-A)(x^2+y^2-2z^2)/r^2 \tag{5.2}$$

and $A(r,t)$ and $B(r,t)$ are the mobility functions, which account for the hydrodynamic interactions between the particle and drop. These functions depend on the center-to-center separation r and on physical and geometric parameters such as oil-layer permeability K (more specifically, its non-dimensional counterpart $K^* \equiv K\mu/a_i$, where K is the ratio

between permeate flux and pressure difference across the oil layer and μ is the dynamic viscosity of the surrounding fluid, which we consider to be the same as the inner solution) and the ratio between radii a_d/a_p, which changes over time as the drop swelling occurs. As shown in Roure and Davis (2021a), although the system of differential equations in (5.1) is non-autonomous, the only dependence of the mobilities on time comes from a quasi-steady contribution of the radius change, as the drop expands quiescently, without changing the boundary conditions, allowing us to use the mobility calculations from Davis and Zinchenko (2018) for a non-expanding permeable drop. Hence, the system of equations in (5.1) must be supplemented with an equation for the drop radius evolution.

In Roure and Davis (2021a), the assumption that the salt inside the drop diffused instantly (so that the salt concentration remained uniform throughout the drop volume but slowly declined with time due to dilution by the influx of fresh water) allowed us to simplify the problem and to find an explicit equation for the drop radius as a function of time. However, in practical situations, inner salt-diffusion effects play an important role in the drop swelling process, as observed experimentally by DeIuliis et al. (2021). To model the swelling problem, we consider that the diffusion of salt inside the drop occurs faster than the inner flow. Note that, in the fast-agglomeration process, the "drop" is actually a binder fragment composed of many tiny emulsion drops that damp out inner flow and exhibit an effective diffusivity that is lower than the molecular diffusivity van Netten et al. (2017); DeIuliis et al. (2021). Hence, the diffusion of salt is governed by a standard diffusion equation, with a boundary condition at the moving boundary $r = a_d(t)$ related to the influx of water due to the jump in osmotic pressure driven by the salt concentration at the interface. Moreover, we also consider that the diffusion problem retains a spherical symmetry and that there are not convective currents (i.e., the salt is sufficiently dilute that a buoyancy-driven flow does not come into play). Hence, we couple the system of equations (5.1) with the following diffusion-expansion problem:

$$\frac{\partial c}{\partial t} = \frac{Eg}{Pe}\,\frac{1}{r^2}\frac{\partial}{\partial r}\left(r^2\frac{\partial c}{\partial r}\right), \tag{5.3}$$

$$\frac{da}{dt} = Eg\; c|_{r=a_d(t)}, \tag{5.4}$$

with initial and boundary conditions given by

$$\begin{cases} a(0) = 1\ ,\ c(r,0) = 1, \\ \partial c/\partial r|_{r=0} = 0, \\ \partial c/\partial r|_{r=a_d(t)} = -Pe\; c^2|_{r=a_d(t)}. \end{cases} \tag{5.5}$$

The initial and boundary conditions presented in (5.5) correspond, respectively, to the initial drop radius, initially uniform salt concentration inside the droplet, axisymmetry of the problem, and the osmotic water permeation through the interface (Roure and Davis, 2021b). Note that the salt concentration c is made dimensionless by the initial uniform concentration c_i. The non-dimensional parameters $Eg = KRTc_i/(\dot{\gamma}a_i)$ and $Pe = KRTc_i a_i/D$, are, respectively, the engulfment parameter and the Péclet number. Note that an ideal solution is assumed and that the water outside the drop is salt-free, so that RTc_e is the osmotic pressure difference across the film, where $c_e = c|_{r=a_d(t)}$ is the salt concentration inside the drop adjacent to the inner edge of the film. Here, c_i is the initial salt concentration inside the drop (assumed uniform), D is the inner salt effective diffusivity, T is the absolute temperature, and R is the ideal gas constant. The engulfment parameter Eg, introduced in Roure and Davis (2021a), is a ratio between the characteristic flow time and the initial drop expansion time. The name was chosen due to an analogy to phase-transition problems, where particles are engulfed by a solidifying or freezing interface as it advances. The Péclet number defined here is not the traditional ratio of convection and diffusion, but rather it measures the ratio between the diffusion and initial drop-expansion characteristic times. Equations (5.3) and (5.4) together with the boundary conditions (5.5) constitute a moving-boundary problem. The absence of convective terms in equation (5.3) indicates that the drop expansion is independent of the particle dynamics.

If that was not the case, the set of differential equations (5.1) and equations (5.3) and (5.4) would have to be solved simultaneously, even under the consideration of a quasi-stationary, passive drop expansion. Note that the effect of osmosis alone is for the interface of the drop to expand passively through the surrounding fluid, without causing internal flow (Roure and Davis, 2021a). Thus, the potential sources of inner flow are from the motion of a nearby particle, which would be very small for $K^* \ll 1$, or from density differences due to the salt concentration gradient inside the drop.

5.2.1 Trajectory simulations

For calculation of relative particle trajectories, we solve the system of equations (5.1) numerically using a fourth-order Runge-Kutta scheme with an adaptive time step. The drop expansion, governed by equations (5.3) and (5.4), is calculated in advance using the finite-difference scheme described in Roure and Davis (2021b) and then tabulated and used as an input in the kinematical calculations. To find the precise time of collision, we perform a linear extrapolation of the trajectory right before the numerical overlap step or for separations smaller than a given threshold. This last time increment is given by $\max\{0, \delta t_{col}\}$, with

$$\delta t_{col} = \begin{cases} (r^2 - R^2)/(2(\dot{a}_d R - \mathbf{r}\cdot\mathbf{V})) & \text{if } V = \dot{a}_d, \\ \dfrac{\dot{a}_d R - \mathbf{r}\cdot\mathbf{V} - \sqrt{(\dot{a}_d R - \mathbf{r}\cdot\mathbf{V})^2 - (r^2 - R^2)(V^2 - \dot{a}_d^2)}}{V^2 - \dot{a}_d^2} & \text{if } V \neq \dot{a}_d, \end{cases} \tag{5.6}$$

where $R(t) = a_d(t) + a_p$, $\mathbf{V}$ is the relative particle velocity, and $V = \|\mathbf{V}\|$. If the imaginary part of δt_{col} is nonzero, the particle does not collide with the drop.

One of the greatest challenges faced in the simulations performed in Roure and Davis (2021a) was to obtain precise values for the collision volume, which required a high resolution of the function $t_{col}(\mathbf{x})$ to be interpolated. However, using the analytical expressions for the mobilities, which are given in terms of infinite series, leads to high computational times, which made it hard to achieve such high resolution, considering that the numerical

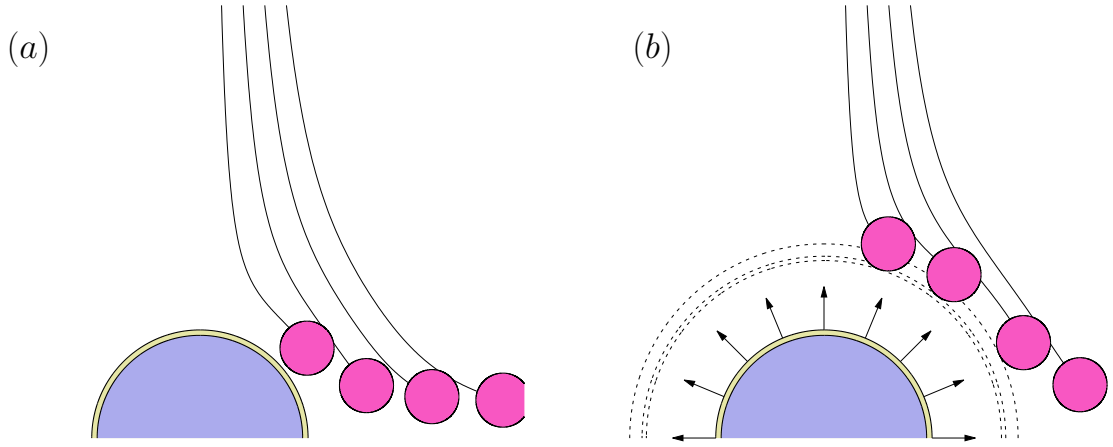

Figure 5.2: Numerical results for the relative particle trajectories for $K^* = 10^{-4}$, $a_p = 0.25$, $y_0 = 0$, $z_0 = 4.0$ and $x_0 = 0.2$, 0.4, 0.6, and 0.8 (left to right). (a) is the result for a non-expanding droplet, whereas (b) is the result for an expanding drop with $Eg = 2.0$ and $Pe = 0$. Although the trajectories all have the same starting position, more particles are captured in the presence of swelling. The dashed semi-circles in (b) are the drop interfaces at the time of capture.

calculation of t_{col} is of order $\mathcal{O}(h^{-2})$, where h is the space step. Hence, in that paper, we had to filter the noise of the function $V_{col}(t)$ before taking its time derivative to calculate the collision efficiency, which led to small discrepancies with theoretical results.

To overcome this issue, we incorporated the near- and far-field asymptotic expressions from Davis and Zinchenko (2018) for small and large separations, respectively. The constants present in the expressions for the near-field mobilities had to be tabulated for different size ratios, as the ratio between the drop and particle radii changes with time during the simulation. Moreover, we also tabulated the analytical values of the mobilities for intermediate separations. These tabulations made the code about 200× faster, which allowed us to improve the resolution of the function $t_{col}(\mathbf{x})$ and to get rid of the smoothing step, obtaining more precise results.

Figure 5.2 shows numerical results for the relative particle trajectories for $K^* = 10^{-4}$, $a_p = 0.5$, and different initial conditions. Figure 5.2(a) shows the results for a non-expanding droplet. In this case, none of the simulated trajectories leads to a collision

with the droplet. In contrast, as can be seen in Figure 5.2 (b), which shows results for an expanding drop with $Eg = 2.0$ and $Pe = 0$, the particles starting at $x = 0.2$, 0.4 and 0.6 are captured by the droplet.

The results shown in Figure 5.2 indicate that the main advantage of drop swelling capture is that it enables the capture of particles that would not be captured otherwise. For non-expanding droplets in a purely extensional flow, there is a region at the adjacency of the droplet where particles do not get captured, even when close to the droplet. The presence of drop swelling, however, can improve the capture of such particles. One way to quantify this improvement is to investigate the motion of particles in the xy plane. Figure 5.3 shows numerical results of the separation gap $s(t) = r(t) - R(t)$, where r is the center-to-center distance and $R(t) = a_d(t) + a_p$ is the sum of the drop and particle radii, versus time for particles in the xy plane (i.e., at $z = 0$) for $a_p = 0.5$, $K^* = 10^{-4}$, $Pe = 0$, (a) $Eg = 0$, (b) $Eg = 0.25$, (c) $Eg = 0.5$, and (d) $Eg = 1.0$ for different starting positions. For small values of the engulfment parameter Eg, particles starting on this plane do not get captured. However, for values of Eg above a certain threshold, we see the formation of an annular region with thickness δ where the particles get captured. This capture layer appears in theoretical studies of the collision efficiency of froth flotation (Yoon and Luttrell, 1989; Loewenberg and Davis, 1994), and it is directly related to the collision efficiency. For the froth flotation process, this layer appears because of the presence of attractive forces, as lubrication forces would impede particle collision from these regions otherwise. For our system, however, the existence of this adjacency layer happens because of drop expansion, even in the absence of attractive forces. The thickness of the capture layer, which corresponds to the bifurcation point in the diagrams in Figure 5.3, depends on the physical parameters of the problem.

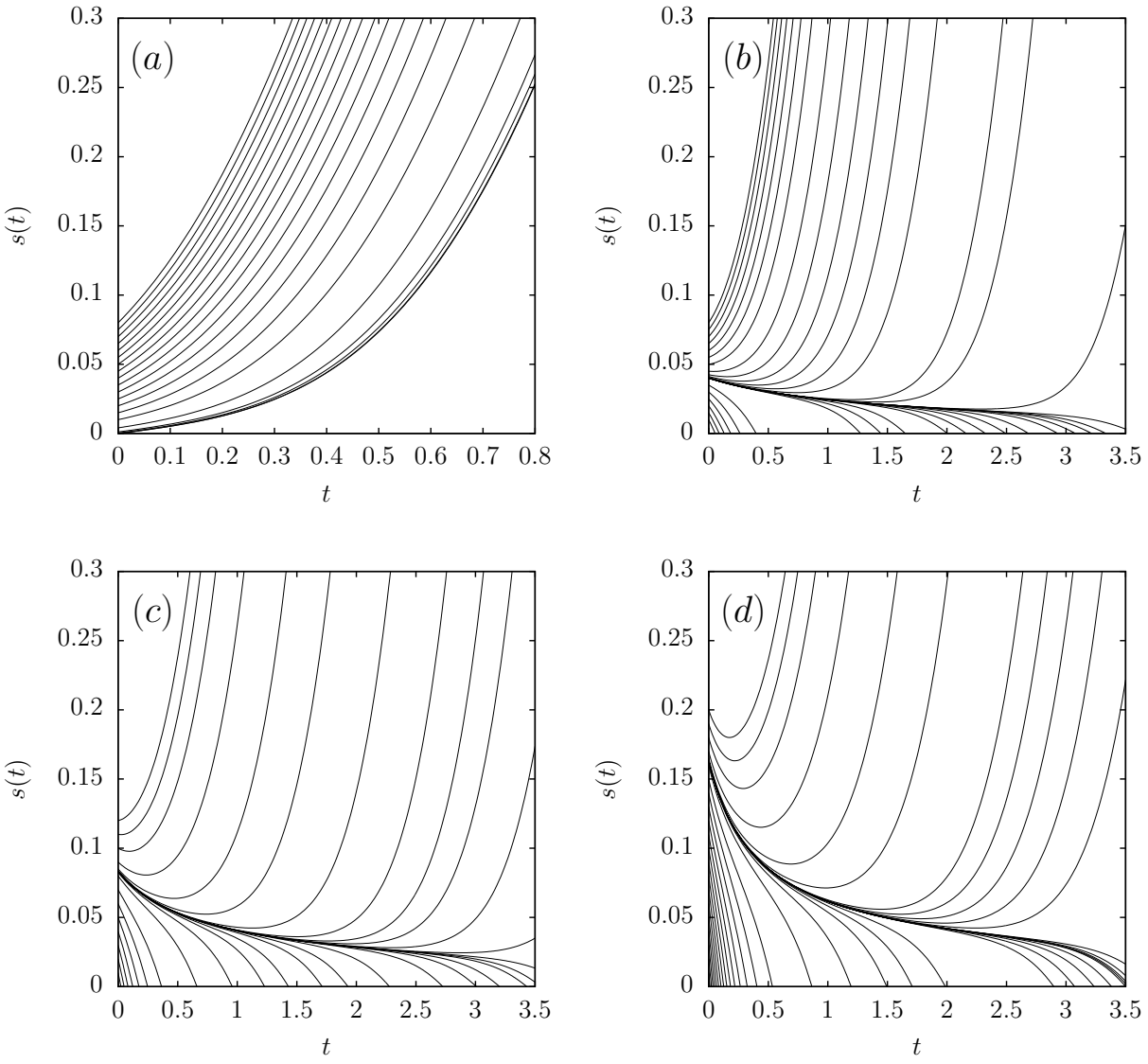

Figure 5.3: Separation gap versus time for particles starting in the xy plane (i.e., at $z = 0$) for $a_p = 0.5$, $K^* = 10^{-4}$, $Pe = 0$, (a) $Eg = 0$, (b) $Eg = 0.25$, (c) $Eg = 0.5$, and (d) $Eg = 1.0$ for different starting positions. For values of Eg above a threshold given by $R(0)(1 - A_0)$, there is a bifurcation in the behavior of the system, indicated by the formation of the lateral capture layer with thickness $\delta =$ (b) 0.04, (c) 0.083, and (d) $= 0.163$.

5.2.2 Calculation of collision efficiency

The main goal of our simulations is to calculate the collision efficiency between the particle and drop. The collision efficiency is defined as the ratio between the pair collision rate over the ideal pair collision rate (i.e., the collision rate in the absence of any interparticle interaction, where the particles are brought together by the external flow field). As discussed in Roure and Davis (2021a), for an initially uniform pair distribution function, the collision efficiency in an extensional flow can be calculated by

$$E_{col}(t) = \frac{3\sqrt{3}}{8\pi R_0^3}\frac{d|V_{col}|}{dt}, \tag{5.7}$$

where $R_0 = R(0) = a_i + a_p$ and $|V_{col}(t)|$ is the volume of the region V_{col}, which consists of starting points of trajectories that lead to a collision with the drop in a time less than or equal to t. Note that the collision efficiency is defined as the ratio of the actual collision rate to the collision rate due to external flow for no drop expansion and with hydrodynamic and molecular interactions neglected. We also define the collision area $A_{col}(t)$ as being the surface formed by the starting points of trajectories that will lead to a collision in a time t. The relationship between A_{col} and V_{col} is

$$V_{col}(t) = \bigcup_{\tau \leqslant t} A_{col}(\tau). \tag{5.8}$$

In many situations, the collision area $A_{col}(t)$ coincides with the external boundary of V_{col}, which we call A^*_{col}. We note that, in Roure and Davis (2021a), the surface defined as A_{col} is the A^*_{col} defined in this work. However, the two coincide for all cases considered in that paper. Another definition of interest is the one of the collision surfaces $S_{col}(t)$, which we define as the region of the collision sphere (i.e., the sphere with radius $R(t) = a_d(t) + a_p$) that is capable of capturing particles (i.e., $\boldsymbol{V} \cdot \hat{\boldsymbol{n}}|_{S_{col}(t)} < \dot{a}(t)$). This definition is a generalization of S_{col} defined in Roure and Davis (2021a). Namely, $S_{col} = S_{col}(0)$. There is a clear relationship between $S_{col}(t)$ and $A_{col}(t)$; if we consider the

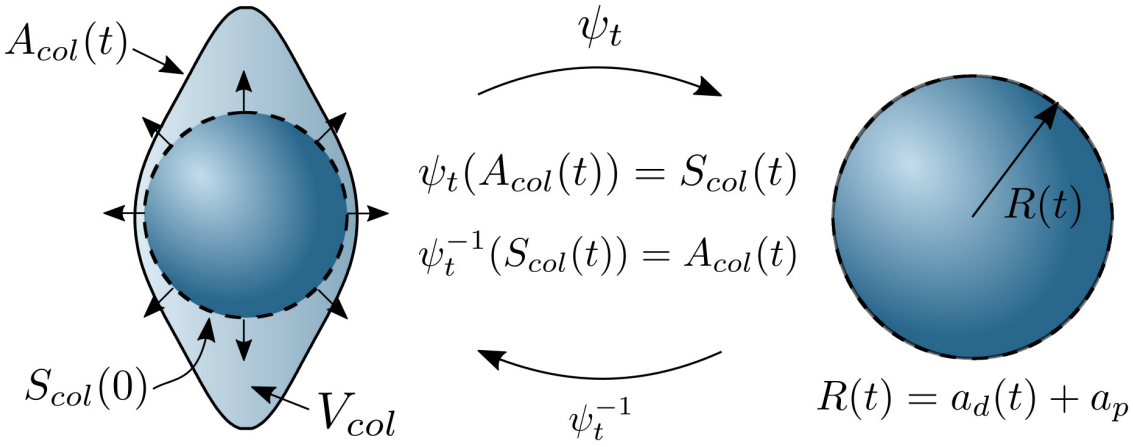

Figure 5.4: Sketch of the different geometries involved in the collision volume analysis and the relationship between them. V_{col} is the volume composed of starting points of trajectories that lead to a collision in a time $\tau \leqslant t$. A_{col} is the surface composed by starting points of trajectories that lead to a collision in a time t, S_{col} is the region of the collision sphere that is able to capture particles at a time t, and ψ_t is the time-evolution operator of the dynamical system.

time-evolution function ψ_t related to the dynamical system (5.1), such that $\psi_t(\mathbf{x}(0)) = \mathbf{x}(t)$, we have $\psi_t(A_{col}) = S_{col}(t)$, or, alternatively, $\psi_t^{-1}(S_{col}(t)) = A_{col}(t)$. These geometries, as well as the goemetrical relationship between $A_{col}(t)$ and $S_{col}(t)$, are illustrated in Figure 5.4. This geometrical relationship helps us understand why, in some cases, the surfaces A_{col} and A^*_{col} differ from each other, as previously stated. Namely, for an expanding droplet with sufficiently high Eg, for which A^*_{col} is path-connected, as the drop expansion diminishes with time, a no-capture region begins to form at the adjacency of the collision surface at large times, breaking the path-connectedness of $S_{col}(t)$, and, by consequence, $A_{col}(t)$.

This relationship between A_{col} and S_{col} can be used to calculate the collision volume by reversing the dynamical system (i.e., by solving $d\mathbf{r}/dt = -\mathbf{V}(\mathbf{r}, T - t)$ using the points in $S_{col}(t)$ as starting positions) and then using $A_{col}(t)$ to calculate $A^*_{col}(t)$ and $V_{col}(t)$. Such a procedure was used in Roure and Davis (2021a) to calculate the transient collision efficiency for non-expanding droplets, where $A_{col}(t) = A^*_{col}(t)$ and the time evolution operators form a one-parameter subgroup. Another method of calculation of $A^*_{col}(t)$, also

used in Roure and Davis (2021a), was to calculate, via numerical interpolation, the level sets $t_{col}(\mathbf{x}) = t$, where $t_{col}(\mathbf{x})$ is the collision time of a trajectory starting at $\mathbf{x}$.

An alternative expression for the collision efficiency can be given in terms of a surface integration over S_{col}, such that:

$$E_{col}(t) = -\frac{3\sqrt{3}}{8\pi R(0)^3} \int_{S_{col}(t)} f(\mathbf{x}, t)\hat{\mathbf{n}} \cdot \left(\mathbf{V} - \mathbf{V}^S\right) dS, \tag{5.9}$$

where $f(\mathbf{x}, t)$ is the pair distribution function, $\hat{\mathbf{n}}$ is the outward normal unit vector and $\mathbf{V}^S$ is the interface velocity. For a non-expanding drop, where $S_{col}(t) = S_{col}(0) = S_{col}$ and $\mathbf{V}^S \cdot \hat{\mathbf{n}} = 0$, this expression can also be used to calculate the steady-state collision efficiency, which coincides with the expression obtained in Davis and Zinchenko (2018). However, for transient systems, this expression requires the knowledge of the pair distribution function, which is governed by the Liouville equation

$$\frac{\partial f}{\partial t} + \nabla \cdot (\mathbf{V} f) = 0, \tag{5.10}$$

with initial condition $f(\mathbf{x}, 0) = f_0(\mathbf{x})$. In Roure and Davis (2021a), we provided a semi-analytical, transient, solution of equation (5.10) for the case of non-expanding drops. For expanding droplets, such transient solution ceases to be valid, as it is not possible to re-write the equation in the integrable form presented in Batchelor and Green (1972a). However, it is still possible to obtain a semi-analytical solution of equation (5.10). Namely, the pair distribution function is given by

$$f(\mathbf{x}, t) = f_0(\mathbf{x})|d\psi_t^{-1}|, \tag{5.11}$$

where $|d\psi_t^{-1}|$ is the Jacobian of the inverse of the time evolution function ψ_t. This relationship comes directly from the conservation form of (5.10). Similar relationships between the pair distribution function and the Jacobian of the time evolution operator have appeared before in works concerning the statistical mechanics of non-Hamiltonian

systems (Tuckerman et al., 1999; Ezra, 2004). For an initially uniform pair-distribution function, the relationship reduces to

$$f(\mathbf{x}, t) = |d\psi_t^{-1}(\mathbf{x})|. \tag{5.12}$$

As previously discussed, we can approximate the inverse time-evolution function by numerically solving the reverse dynamical system. Hence, we can obtain a numerical approximation for the Jacobian $|d\psi_t^{-1}(\mathbf{x})|$, and, thus, the pair distribution function $f(\mathbf{x}, t)$, by considering the deformation of a small square element by the reverse dynamical system. This method used for the numerical calculation of the Jacobian is somewhat similar to techniques used in dynamical systems to calculate Lyapunov exponents (Sandri, 1996; Cvitanovic et al., 2005).

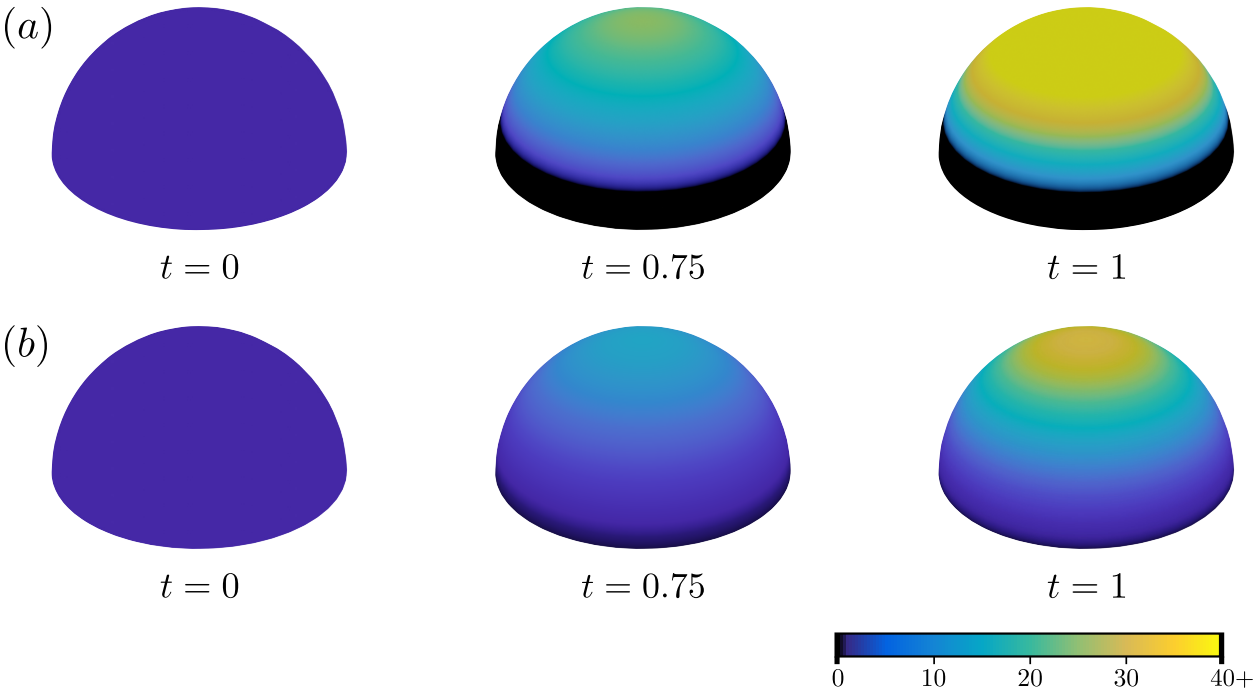

Figure 5.5: Numerical results for the pair distribution function $f(\mathbf{x}, t)$ for $K = 10^{-4}$, $Pe = 0$, $a_p = 0.5$, and (a) $Eg = 0$ and (b) $Eg = 1$. The results shown in the figure are evaluated at the surface of a sphere of radius $R(t) + 0.01$. For $Eg = 0$, there is a zero-probability region corresponding to the wake region. For non-zero values of Eg, the formation of such a region only occurs at larger times.

Figure 5.5 shows numerical results for the pair distribution function calculated by the

aforementioned method. For the simulations, we used $K^* = 10^{-4}$, $Pe = 0$, $a_p = 0.5$, and (a) $Eg = 0$ and (b) $Eg = 1$. We also evaluated the results at the surface of a sphere of radius $R(t) + 0.01$ (i.e., close to the collision sphere of radius $R(t)$). This small shift in radius is motivated by the fact that the probability distribution at the surface of the collision sphere can reach very high values, as expected from theoretical calculations, resulting in a less-detailed visualization. Like the results presented previously for non-expanding droplets, we observe the formation of a high-probability region at the top of the sphere (i.e., at the collision region), represented by the bright yellow region in Figure 5.5(a). In the same Figure 5.5(a), we also notice a dark region, where $f(\boldsymbol{x}, t) = 0$ for nonzero times. This region is associated with the wake region predicted by Wilson (2005) and observed in the previous transient simulations in Roure and Davis (2021a). The increase of the pair-distribution function at the top of the collision region for non-expanding spheres explains the transient increasing behavior of the collision efficiency observed in the previous numerical simulations.

In contrast, the results shown in Figure 5.5(b) for expanding spheres with $Eg = 1$ show lower values of the pair distribution function when compared to the non-expanding droplets. However, the increase in capture area (as well as surface area) together with a non-zero surface velocity, adds a positive contribution $E_{col}(t)|_{Eg}$ to the collision efficiency, where

$$E_{col}(t)|_{Eg} = \frac{3\sqrt{3}}{8\pi R(0)^3} \int_{S_{col}(t)} f(\boldsymbol{x}, t) \boldsymbol{V}^S \cdot \hat{\boldsymbol{n}} dS, \tag{5.13}$$

resulting in a higher overall collision efficiency when compared to the one of non-expanding droplets. This contribution, however, decays with time, as the surface velocity slows down with time due to dilution of the salt water inside the drop. For $Pe = 0$, the decrease occurs slowly, whereas for high Péclet numbers, the decrease in expansion rate can occur fast, resulting in a short-time transition between engulfment-dominated and flow-dominated capture, as we will show in section 5.3.2.

The physics behind this sharp decay can be better understood by analyzing the short-time behavior of the collision efficiency, given by equation (5.9). Namely, for sufficiently high values of Eg, such that $S_{col}(0)$ and $S_{col}(\delta t)$ are the whole surfaces of spheres with radii $R(0)$ and $R(\delta t)$, respectively, and considering an initially uniform pair distribution function, we can obtain an asymptotic expression for (5.9) such that

$$E_{col}(\delta t) \sim \frac{3\sqrt{3}}{2R(0)} \left[\dot{a}_d(0) + \delta t \left(\ddot{a}_d(0) - \frac{4R(0)^2}{5}\beta + \frac{2\dot{a}_d(0)^2}{R(0)} \right) \right], \tag{5.14}$$

where

$$\beta = (1 - A_0) \left(\frac{3}{R(0)}(A_0 - B_0) + \left. \frac{\partial A}{\partial r} \right|_{r=R(0),t=0} \right), \tag{5.15}$$

and A_0 and B_0 are the values of the mobility functions A and B, respectively, evaluated at the surface of the sphere of radius $R(0)$ at $t = 0$. In equation (5.14), the leading order is equal to the initial value of the collision efficiency predicted by Roure and Davis (2021a), as expected. Moreover, if the order $\mathcal{O}(\delta t)$ term related to the flow (i.e., the first-order term containing β) is zero, this expansion is compatible with the pure-engulfment collision efficiency obtained in the same paper, indicating that the contributions from the terms $\ddot{a}_d(0)$ and $2\dot{a}_d(0)^2/R(0)$ are purely due to drop expansion. Note that the flow term at order $\mathcal{O}(\delta t)$ does not depend on the swelling dynamics of the drop, which indicates that both effects (flow and expansion) are uncoupled at $t = 0$. However, as the swelling dynamics influences the time evolution of the pair-distribution function, the effects of flow and swelling start to blend as time goes by. The derivation of equation (5.14) can be made by performing a change of variables from $R(\delta t)$ to $R(0)$, followed by a regular expansion of both the integrand and the Jacobian in powers of δt. Then, we use the fact that the integrals

$$\int_{S_{col}(0)} V_r|_{t=0}\, dS, \tag{5.16}$$

$$\int_{S_{col}(0)} \partial V_r/\partial r|_{t=0}\, dS, \tag{5.17}$$

and

$$\int_{S_{col}(0)} \partial V_r/\partial t|_{t=0}\, dS, \tag{5.18}$$

all vanish when integrated over the whole sphere (here, $V_r \equiv \boldsymbol{V}\cdot\hat{\boldsymbol{e}}_r$). In equation (5.14), the term $\ddot{a}_d(0)$, which is the initial radial acceleration of the drop radius, gives a negative contribution to the first order of $E_{col}(\delta t)$. For $Pe = 0$, this term is equal to $-3\dot{a}_d(0)^2 = -3Eg^2$, which is larger in magnitude than the last term, resulting in an overall decreasing behavior for the collision efficiency from engulfment. For high Péclet numbers, the absolute value of $\ddot{a}_d(0)$ can be very large. In fact, the second derivative of the short-time expansion in Roure and Davis (2021b) is singular at $t = 0$, indicating that, although the initial value of the collision efficiency is not affected by the Péclet number, there is a sharp decay of E_{col} for $Pe \gg 1$ at very short times (physically, this decay occurs because of the sharp reduction in salt concentration, and, hence, osmotic expansion rate, when diffusion of salt from the drop interior to its inner edge is slow). For $Pe = 0$ we can use this short-time expansion to determine the critical value of engulfment, Eg^*, for which the particle capture at short times will transition from flow dominated to engulfment dominated. Namely, this transition happens when the term of order $\mathcal{O}(\delta t)$ (i.e., the derivative of the collision efficiency at $t = 0$) changes sign. Hence, if Eg^* exists, it is given by:

$$Eg^* = \left(\frac{4R(0)^3\beta}{5\,(2-3R(0))}\right)^{1/2}. \tag{5.19}$$

When drop expansion happens slowly compared to the imposed flow velocity, it is also expected that, for long times, the pair distribution function $f(\boldsymbol{x}, t)$ will converge to a quasi-steady-state limit similar to the analytical expression by Batchelor and Green (1972a), $f(\boldsymbol{x}, t) \sim (1 - A_t(R(t)))^{-1}\phi_t(R(t))$, where $A_t(R(t))$ is a shorthand notation for the

mobility at time t evaluated at $r = R(t)$, we define $B_t(R(t))$ in the same way. Similarly, ϕ_t is the function ϕ, defined by

$$\phi(r) = \exp\left(\int_r^\infty \frac{A(r') - B(r')}{1 - A(r')} \frac{dr'}{r'}\right), \tag{5.20}$$

evaluated at time t (i.e., using the mobilities A_t and B_t instead of A and B). Hence, by plugging the quasi-steady pair distribution in equation (5.9), we can derive an expression for the quasi-steady collision efficiency, given by

$$E_{col}(t) \sim \frac{3\sqrt{3}}{2\left[\phi_t(R(t))\right]^3} \left(\frac{R(t)}{R(0)}\right)^3 \left[(\cos(\alpha) - \cos(\alpha)^3) + \frac{\dot{a}}{R(t)} \frac{(1 - \cos(\alpha))}{1 - A_t(R(t))}\right], \tag{5.21}$$

where $\alpha(t)$ is the angle determining the collision region at time t. Similarly to Roure and Davis (2021a), we have:

$$\cos(\alpha) = \begin{cases} \dfrac{1}{\sqrt{3}} \left(1 - \dfrac{\dot{a}(t)}{R(t)(1 - A_t(R(t)))}\right)^{1/2} & \text{for } \dot{a}(t) \leqslant R(t)(1 - A_t(R(t))), \\ 0 & \text{for } \dot{a}(t) \geqslant R(t)(1 - A_t(R(t))). \end{cases} \tag{5.22}$$

For non-expanding droplets, where $R(t) = R(0)$ and $\cos(\alpha) = 1/\sqrt{3}$, the analysis yields $E_{col} = \phi(R(0))^{-3}$, as expected.

5.3 Results and discussion

5.3.1 Drop expansion

Before presenting the results for the collision efficiency, we discuss some of the numerical results related to the diffusion-limited swelling of droplets. These results for the expansion kinetics of a drop are tabulated and used as inputs for the mobility simulations.

Figure 5.6 shows numerical results for the evolution of salt concentration profile inside a drop for (a) $Pe = 2$ and (b) $Pe = 200$. These results were obtained by the finite-difference scheme proposed in Roure and Davis (2021b). For large Péclet numbers (i.e., slow salt

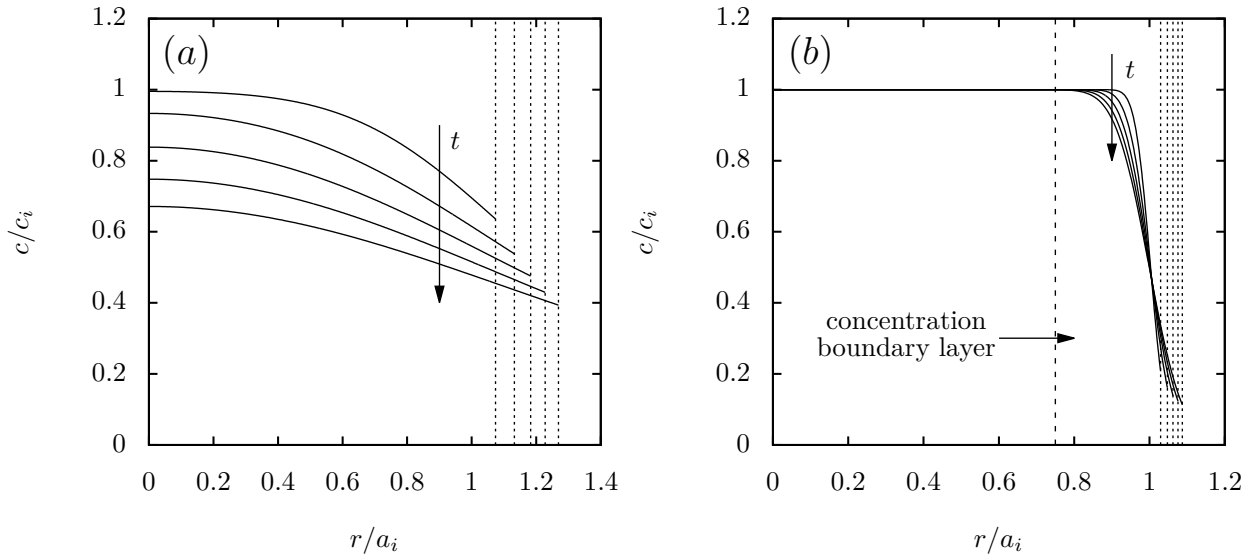

Figure 5.6: Evolution of the salt concentration profile for (a) $Pe = 2$ and (b) $Pe = 200$ and times $t = 0.1$, 0.2, 0.3, 0.4, and 0.5. For high Péclet numbers, the diffusion effects are constrained to a concentration boundary layer, as predicted in Roure and Davis (2021b). The vertical dashed lines are the drop radius at the specific time.

diffusion), the concentration profile remains unaltered at the central portion of the droplet and all diffusive effects are confined to a boundary-layer region, as described in Roure and Davis (2021b). The increase in Péclet number leads to a lower concentration of salt at the drop surface, resulting in a slower drop expansion, as seen in the results shown in Figure 5.7. Namely, as diffusion occurs slowly, the flux of salt from the center to the inner drop surface (where the salt water is diluted by the influx of fresh water) requires a large concentration gradient and balances a reduced osmotic expansion rate (due to the lower salt concentration).

5.3.2 Collision efficiency

Besides the Péclet number and the engulfment parameter, there are other physical parameters that influence particle capture, such as the nondimensional permeability K^* and particle size a_p. In practice, a large range of parameter values is possible. Davis and Zinchenko (2018) estimated K^* values in the ranges of 10^{-6} to 10^{-4} for small drops and particles with reduced radii of $1 - 100$ μm in water, whereas even smaller values may be

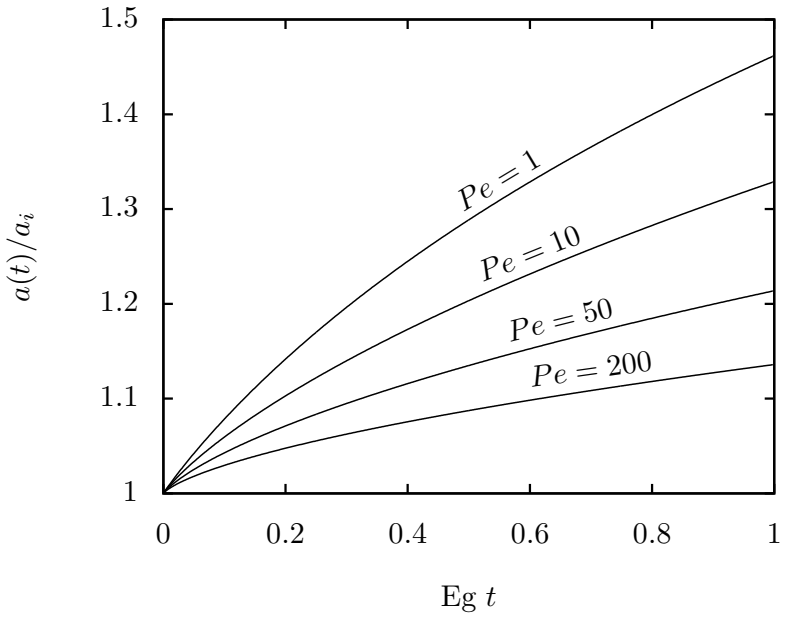

Figure 5.7: Radial evolution of a spherical droplet size for different Péclet numbers. As the diffusion becomes slower, the salt concentration at the drop surface diminishes, reducing the osmotic influx and leading to a slower expansion.

estimated from experiments with larger (millimeter-sized) agglomerates (DeIuliis et al., 2021; Roure and Davis, 2021b). These same experiments yielded $Pe = \mathcal{O}(10^2 - 10^3)$, but smaller values are expected for smaller drops (Roure and Davis, 2021b). The engulfment parameter can be recast as $Eg = K^* R T c_i/(\mu\dot{\gamma})$ and so can take on a wide range of values of $\mathcal{O}(1)$ or less. Similarly, since drops (or bubbles) tipically capture smaller particles, $a_0 < 1$ is expected.

Roure and Davis (2021a) determined collision efficiencies for the case of fast inner diffusion (i.e., $Pe = 0$) and relatively large particles ($0.25 \leqslant a_p \leqslant 1$). In this section, we consider more realistic scenarios of $0 \leqslant Pe \leqslant 200$, $K^* = 10^{-6}$ and 10^{-4}, $0 \leqslant Eg \leqslant 3$ and $0.05 \leqslant a_p \leqslant 1$. The larger values of Pe allow us to examine the degree to which diffusion limitations slow the drop expansion and collision efficiency, while the smaller size ratios allow us to examine the effectiveness of engulfment due to drop expansion in capturing very fine particles.

Figure 5.8 shows numerical results for the collision efficiency for $a_p = 0.5$, $Eg = 1$ and

$Pe = 0.1, 5, 25$, and 200. The solid curves in Figure 5.8 represent the results for $K^* = 10^{-4}$, whereas the dashed curves are the results for $K^* = 10^{-6}$. Though difficult to see, the initial value of collision efficiency for all cases is the same, $E_{col} = \sqrt{3}$, as given by the theoretical expression in equation (5.14). As in our previous work, where we observed a decreasing collision efficiency versus time in expansion-dominated capture, a similar trend is observed here. As expected from the discussion presented in section 5.3.2, it is noted that an increase in Péclet number also results in a sharper decay of the collision efficiency at short times due to the rapid reduction in drop expansion with slow salt diffusion. This initial decay is is noticeably sharp in the cases where the Péclet number is large, as there is a fast depletion of salt at the drop surface. The short-time region of the curves in Figure 5.8 display a similar behavior to the results for the evolution of salt concentration at the drop interface presented in Roure and Davis (2021b). This result is expected, as the salt concentration at the interface is the main driver behind the osmotic swelling. However, in contrast to the salt depletion at the interface, the collision efficiency curves are not necessarily monotonically decreasing. Namely, for high Péclet numbers, as time increases, it is possible to observe an increasing behavior of the collision efficiency, which is characteristic of flow-dominated capture. This behavior occurs when the characteristic time of the initial sharp decay of salt concentration at the interface is much smaller than the characteristic flow time. In the limit of $Pe \to \infty$, we expect $dE_{col}/dt|_{t=0}$ in our model to be singular, with the collision efficiency presenting an instant decay from the theoretical initial collision efficiency at the given engulfment parameter to the initial collision efficiency for $Eg = 0$, as the salt would not be able to diffuse to the diluted water at the inner edge of the drop and expansion would cease. Moreover, it is noted that the numerical results for $K^* = 10^{-6}$, indicated by the dashed lines in Figure 5.8, are practically identical to the ones for $K^* = 10^{-6}$. A similar behavior of the collision efficiency curves coinciding for small values of K^* was observed in Roure and Davis (2021a) in the absence of inner diffusion for $Eg = 1$; under these conditions, the collision efficiency is dominated

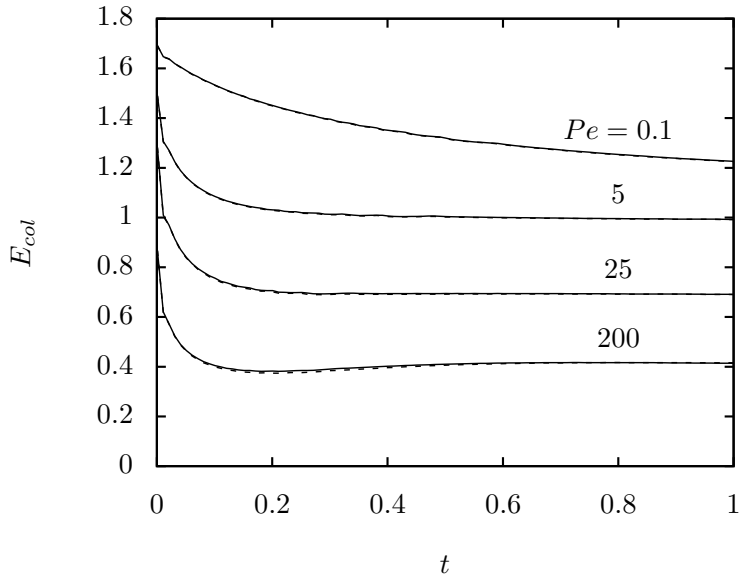

Figure 5.8: Collision efficiency versus time for $a_p = 0.5$, Eg $= 1$, and $K^* = 10^{-4}$ (solid lines) and $K^* = 10^{-6}$ (dashed lines) for different Péclet numbers. Although all of the curves start at the same value, the increase in the Péclet number results in a faster decay in salt concentration at the boundary at short times, which leads to a slower drop swelling, and, thus, lower collision efficiency.

by engulfment. Hence, the results in Figure 5.8 indicate that the engulfment dominance of the collision efficiency can persist for considerably large times, even for large Péclet numbers. Of course, since $Eg = KRTc_i/(\dot{\gamma}a_i)$, a reduction in the permeability K with all else unchanged would lead to reduced engulfment and a lower collision efficiency.

Figure 5.9 shows the collision efficiency versus time for $a_p = 0.5$, $K^* = 10^{-4}$, $Pe = 200$ and Eg $= 0$, 0.25, 1.0, 2.0, and 3.0. As expected, the collision efficiency is greater for larger values of Eg. The short-time decay of E_{col} for high Eg is slower when compared to lower values of Eg. Moreover, as seen before in Figure 5.8 and in the results presented in Roure and Davis (2021a), the slowing of drop swelling also produces a change in the curve's shape. Namely, for high values of Eg, the collision efficiency presents a decreasing behavior with time, as expected in expansion-dominated capture, whereas, for smaller values of the engulfment parameter, we observe a short-time decay followed by an increasing collision efficiency and a slow decrease for even larger times. Also, in contrast to the results shown in Figure 5.8, decreasing the value of Eg also decreases the

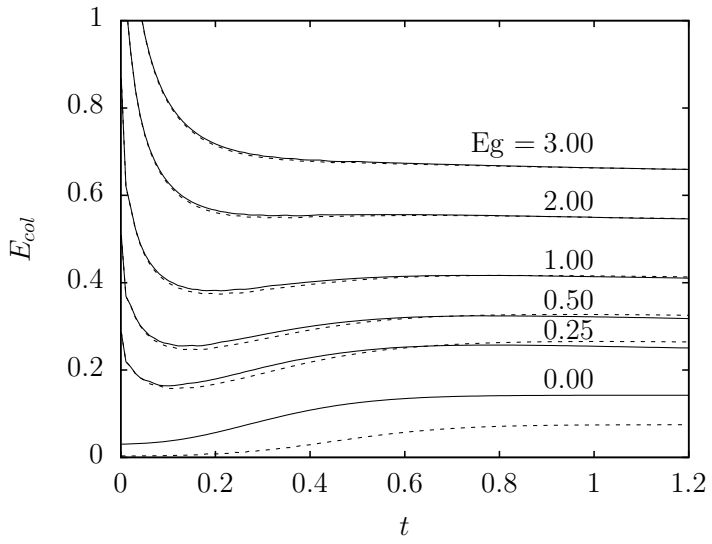

Figure 5.9: Collision efficiency versus time for $a_p = 0.5$, $Pe = 200$ and different values of the engulfment parameter Eg. The solid lines represent the results for $K^* = 10^{-4}$, whereas the dashed lines are the results for $K^* = 10^{-6}$. For large values of Eg, the collision efficiency is dominated by engulfment and the results coincide. For non-expanding droplets, however, the collision efficiency for permeability $K^* = 10^{-4}$ at larger times is about twice as large as the one for $K^* = 10^{-6}$.

initial collision efficiency. Hence, the sharp decay observed at short times in Figure 5.8 for drops with slower swelling rate is no longer present.

Figure 5.10 show numerical results for the collision efficiency versus time for $K^* = 10^{-4}$ and $a_p = 0.1$, 0.25, 0.5, and 1.0 for (a) Eg $= 0$ and (b) Eg $= 1$ and $Pe = 200$. In (a), the collision efficiency without engulfment presents an increasing behavior until it reaches the steady state predicted by collision theory, represented by the dashed lines. The agreement between the transient simulations and collision theory is much better than in Roure and Davis (2021a), because of the increase in resolution allowed by the tabulation of the mobility functions described in section 5.2.1. From Figure 5.10(a), we see that, for smaller particles, the collision efficiency, and, thus, the pair-distribution function, takes a longer time to reach a steady state. Moreover, the collision efficiency becomes small for small particles, which tend to flow around non-expanding droplets. In (b), the behavior is initially dominated by engulfment. In this regime, smaller particles have

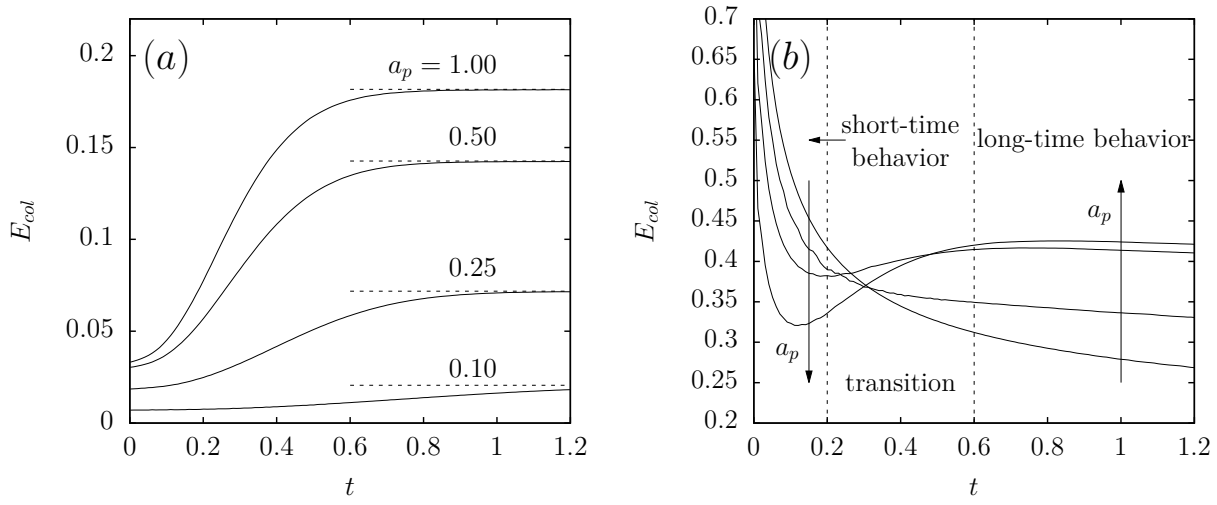

Figure 5.10: Collision efficiency versus time for $K^* = 10^{-4}$ and $a_p = 0.1$, 0.25, 0.5, and 1.0 for (a) Eg = 0 and (b) Eg = 1 and Pe = 200. In (a), the collision efficiency presents an increasing behavior until it reaches the steady state predicted by collision theory, represented by the dashed lines. In (b), the behavior is initially dominated by engulfment, but transitions to a long-time, quasi-steady behavior.

higher collision efficiencies compared to larger particles, as predicted by the expression for pure expansion. However, at larger times, when the drop expansion rate decreases, the capture transitions to a more flow-like behavior. In this regime, the collision efficiency presents a more quasi-steady behavior and, as expected from flow-induced capture, the collision efficiency for finer particles is smaller. Because the expansion rate decays slowly, the influence of drop expansion is still present in the sense that the collision rate is still much higher than for flow capture without expansion shown in Figure 5.10(a).

Although the results in Figure 5.10(b) show an increasing behavior of collision efficiency with radius for larger times, this behavior is non-monotonic, as in the results for non-expanding permeable droplets in Davis and Zinchenko (2018). To better understand this behavior, we investigated how different physical parameters, such as the particle size a_p, Péclet number Pe, and engulfment parameter Eg, affect the collision efficiency at moderate times. Figure 5.11 shows numerical results for the collision efficiency at time t = 1 versus the non-dimensional particle radius for $K^* = 10^{-4}$ and different values of

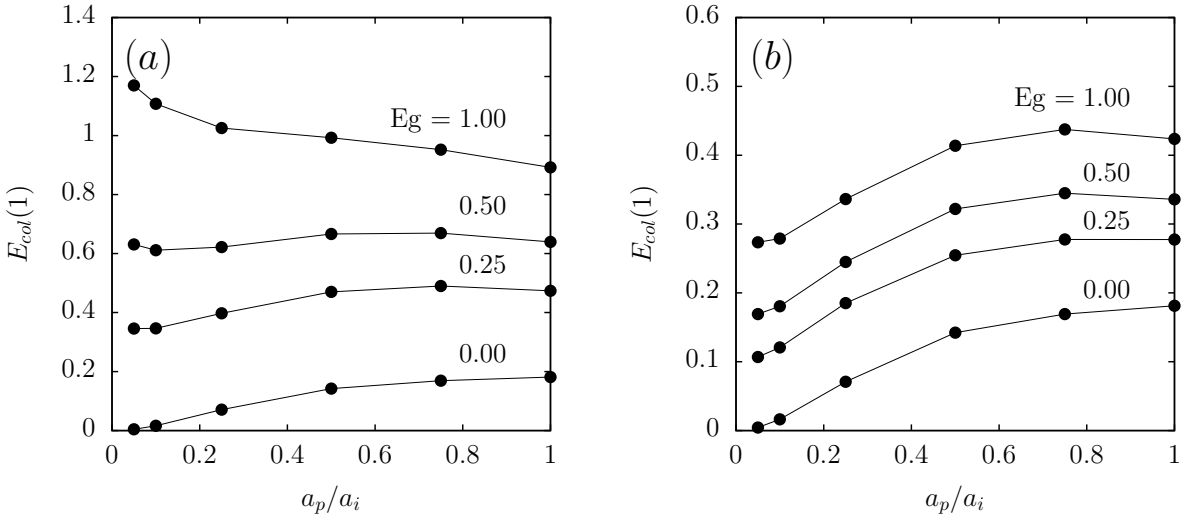

Figure 5.11: Collision efficiency at time $t = 1$ versus non-dimensional particle radius for $K^* = 10^{-4}$ and different values of the engulfment parameter Eg. (a) shows the results for $Pe = 5$, whereas (b) shows the results for $Pe = 200$.

Eg. Figure 5.11(a) shows the results for $Pe = 5$. For this small Péclet number, we see that, even for moderate values of Eg, the collision efficiency at time $t = 1$ is still dominated by engulfment. Namely, for Eg $= 1$, the collision efficiency decreases with increasing particle radius a_p, which is characteristic of engulfment-dominated capture. For smaller values of Eg, we see a non-monotonic behavior characteristic of flow-dominated capture. In contrast, the results in Figure 5.11(b), which shows numerical results for $Pe = 200$, present a flow-dominated behavior even for Eg $= 1$. However, it is also noted that the collision efficiencies for larger values of Eg are considerably higher than for non-expanding droplets, especially for smaller particles. Thus, engulfment due to drop expansion provides a significant enhancement to the capture of very fine particles.

The preceding figure and discussion suggest a transition from flow-dominated particle capture to engulfment-dominated particle capture. This concept is further examined in Figure 5.12, which shows a "phase diagram" for the dominant capture mechanism for $a_p = 0.5$ and $K^* = 10^{-4}$. In contrast to the critical engulfment parameter Eg^* defined by equation (5.19), which is related to the behavior of the collision efficiency at $t = 0$, the

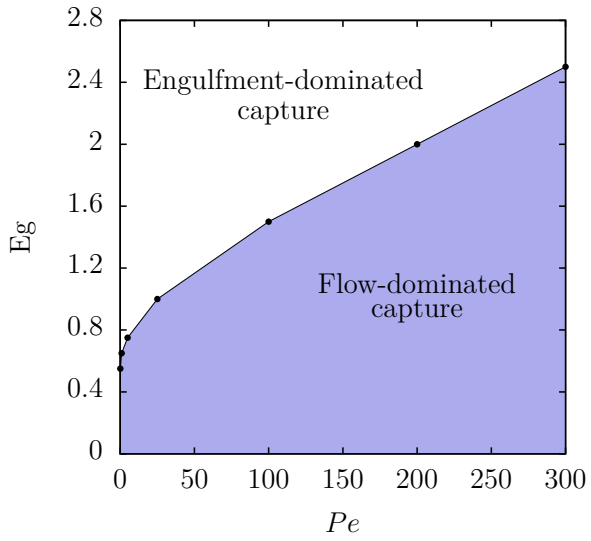

Figure 5.12: Phase diagram representing the transition between flow- and engulfment-dominated particle capture for $a_p = 0.5$ and $K^* = 10^{-4}$ and $Pe = 0.1, 1, 5, 25, 100, 200$, and 300. For each Péclet number, we identify a critical engulfment parameter, Eg_c, represented by the solid curve, at which there is a transition between particle-capture mechanisms. The region above the transition curve represents engulfment-dominated particle capture, whereas the shaded area below is the region of flow-dominated particle capture.

previous results in this section indicate an alternative way to characterize the transition between flow- and engulfment-dominated behavior by noting the presence of a local minimum at short times for flow-dominated capture, which is followed by a subsequent increase in collision efficiency. To this end, we performed a series of numerical simulations at various values of Pe and Eg. By analyzing the results for each Péclet number, we can estimate a critical value of Eg, Eg_c, for which the collision efficiency ceases to be monotonically decreasing, indicating a transition in the dominant capture mechanism. The numerically calculated values of these transition points are shown by the curve in Figure 5.12. Above the curve is the region of engulfment-dominated particle capture, whereas the shaded area below the curve is the region of flow-dominated capture. As expected, the value of Eg_c increases monotonically with Pe due to the fast depletion of salt at the inner drop interface. From Figure 5.12, it is also noted that there is a sharp increase in the critical engulfment parameter from small to moderate Péclet numbers,

which transitions to a slower increasing behavior that is nearly linear with Pe.

5.4 Comparison between flotation and agglomeration

One important comparison to make is between our theoretical results for the capture efficiency of the agglomeration process and previous theoretical results regarding froth flotation. To this end, in this section, we compare the results from our model with the theoretical results obtained for froth flotation by Loewenberg and Davis (1994). Following the discussion at the beginning of section 5.3.2, we focus our attention to the limits of the permeability range estimated in Davis and Zinchenko (2018), with $K^* = 10^{-6}$ and 10^{-4}, $Pe = 200$ and small values of Eg.

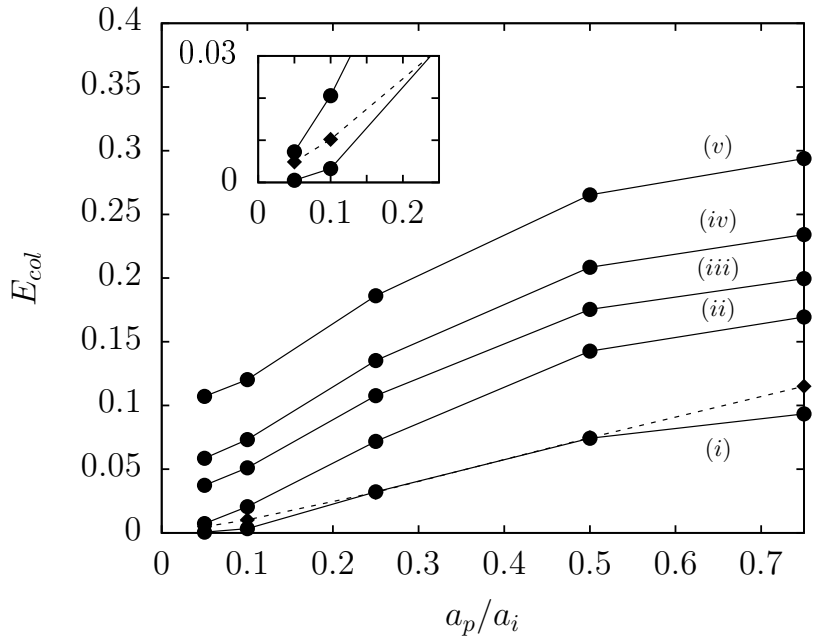

Figure 5.13: Numerical results for the collision efficiency versus particle radius. The dashed curve is the reference result for the steady-state collision efficiencies of froth flotation obtained by Loewenberg and Davis (1994) for different particle radii and $H \equiv A/(RT) = 1$. The solid curves are the results for the fast agglomeration method for and (i) $Eg = 0$, $K^* = 10^{-6}$, (ii) $Eg = 0$, $K^* = 10^{-4}$, (iii) $Eg = 0.05$, $K^* = 10^{-6}$, (iv) $Eg = 0.1$, $K^* = 10^{-6}$, $Pe = 200$, and (v) $Eg = 0.25$, $K^* = 10^{-6}$, $Pe = 200$. The inset shows a closeup of the region for smaller particle sizes. The results for non-expanding droplets are at steady state, whereas the results for expanding droplets are evaluated at $t = 1$.

Figure 5.13 shows numerical results for the collision efficiency evaluated at the non-dimensional time $t = 1$ (expanding drops) or steady state (non-expanding drops) for different particle sizes. The dashed curve is the reference result for the steady-state collision efficiencies of froth flotation obtained by Loewenberg and Davis (1994) for different particle radii and $H \equiv A/(RT) = 1$, where A is a measure of the van der Waals atraction, as described by Hamaker (1937). The solid curves are the results for the agglomeration method investigated in this work with and without engulfment. The inset shows a closeup of the region for smaller particle sizes. For non-expanding ($Eg = 0$) drops, the permeable interfaces for flow-induced capture lead to collision efficiencies without attractive forces that are comparable to ($K^* = 10^{-6}$) or larger than ($K^* = 10^{-4}$) the flotation capture efficiencies with van der Waals attraction but no permeation. However, both mechanisms yield very low efficiencies for $a_p < 0.05$ (i.e., small particles of radii less than 5% of the drop or bubble radius).

Fortunately, even the smallest engulfment examined ($Eg = 0.05$, $K^* = 10^{-6}$) provides considerable enhancement in the collision efficiency for the new process of fast agglomeration with emulsion binders, with the enhancement the greatest on a relative basis for smallest particles. This prediction supports the experimental observations of van Netten et al. (2017) that the process rapidly captures particles of all sizes. Moreover, the current analysis of the agglomeration process neglects molecular attractive forces, which would further increase the collision efficiency for very small permeabilities and engulfment parameters.

5.5 Concluding remarks

Particle capture by small, salt-water drops covered with a thin permeable film was analyzed by solving the transient diffusion problem inside the expanding drops and the two-sphere mobility equations for the drop-particle interaction in an extensional flow field. Osmotic flow into the drops is characterized by an engulfment parameter (ratio of

permeate flow to imposed external flow), while salt diffusion inside the drop is characterized by a Péclet number (ratio of osmotic flow to diffusive flux). As expected, increasing the engulfment parameter increases the particle-drop collision efficiency, especially for very small particles, which tend to flow on streamlines around non-expanding drops rather than collide with them. Increasing the Péclet number decreases the collision efficiency, however, as the slower diffusion of salt from the drop center to its edge leads to a diffusion boundary-layer of declining salt concentration near the inner edge of the drop interface and a reduced driving force for osmotic flow and drop expansion. Nevertheless, this effect is relatively weak; Figure 5.8 shows a decline in collision efficiency of less than one-half at $t = 1$ as Pe is increased from 0.1 to 25 and less than two-thirds as Pe is increased from 0.1 to 200, for $Eg = 1$, $K^* = 10^{-4}$ and $a_p = 0.5$. Further, for very small particles, even a small amount of engulfment can provide a substantial relative increase in the collision efficiency over that without engulfment. For example, Figure 5.13 shows, for $a_p = 0.05$, a 12-fold increase in the collision efficiency from 0.005 for froth flotation to 0.06 for fast agglomeration with $Eg = 0.1$, $K^* = 10^{-6}$ and $Pe = 200$.

The engulfment parameter is defined as $Eg = KRTc_i/(\dot{\gamma} a_i)$. Besides decreasing the imposed shear rate $\dot{\gamma}$ (which would reduce the base collision rate proportionately) or increasing the initial salt concentration, c_i, Eg can be increased by using drops with smaller radius a_i. Smaller drops have smaller Péclet number, $Pe = KRTc_i a_i/D$, with less diffusional resistance and, hence, higher collision efficiencies. Moreover, the particle-to-drop size ratio is increased for smaller drops, which further increases the collision rate. Thus, smaller drops are recommended where feasible. Regardless, the simulations show that fast agglomeration is a suitable alternative for froth flotation of even very small particles, as long as modest engulfment due to osmotic flow into expanding drops is present.

CHAPTER 6

PERMEATION NETWORK MODEL FOR THE SWELLING OF W/O/W EMULSIONS

Synopsis

Previously, we have developed a model for the fast agglomeration technique for particle capture by considering binary interactions between single droplets and particles. In practical situations, however, particles collide with agglomerates that are comprised of multiple droplets. In such situations, the osmotic flux is limited by the permeation of water between the saltwater droplets composing the agglomerate. Under certain conditions, this water permeation gives rise to an effective salt diffusivity in the scale of the agglomerate. However, there are situations where the microstructure of the agglomerate can play a key role in the swelling kinetics. To account for possible effects of agglomerate microstructure, we propose a simple permeation network model for the swelling kinetics dominated by interdroplet water permeation. The model consists of spherical saltwater droplets packed inside a spherical oil droplet. We consider shape relaxation and salt diffusivity inside each constituent droplet to be faster than water permeation. At each time step, the microstructure is determined by a sphere-packing Monte-Carlo algorithm, which determines a dynamic permeation network where water permeation between neighboring droplets occurs. We compare the results from our permeation network model to the ones from effective diffusion by averaging over different microstructures. For smaller droplets, we can observe an average concentration profile similar to the concentration-boundary-layer structure that appears in the effective-diffusion model. Also, similarly to the continuous model and experimental results, the swelling of the agglomerate displays a fast expansion behavior followed by a $\propto t^{1/2}$ behavior for longer times. Lower volume fractions and larger droplets decrease effective diffusivity, resulting in a slower swelling, while being more sensitive to changes in the microstructure.

6.1 Introduction

In recent years, double emulsions, which are characterized by the presence of smaller droplets of typically the continuous phase within larger droplets of the dispersed phase, have gained significant popularity across various industries, including food, cosmetics, pharmacology, mineral, and biomedical (Pawlik et al., 2010; Marti-Mestres and Nielloud, 2002; Florence and Whitehill, 1982; van Netten et al., 2017; Rajian et al., 2011). Among the most prevalent types of double emulsions, water-in-oil-in-water (W/O/W) emulsions are of particular importance. Similar to the case of some soft particles, such as hydrogels, double emulsions may present osmotic swelling under the presence of an osmotic pressure gradient between the internal and external phases (Yan and Pal, 2001; Mezzenga et al., 2004). This pressure gradient can be produced by different effects such as the presence of surfactants (Yan and Pal, 2001) or salt inside the internal water phase (DeIuliis et al., 2021). There have been several prior studies to model the swelling of droplets and double emulsions, ranging from simple mass-balance models to more complex population-balance models for dilute double emulsions (Mezzenga et al., 2004; Leal-Calderon et al., 2012; Wan and Zhang, 2002; Yan and Pal, 2001; Mukhopadhyay et al., 2008; Khadem and Sheibat-Othman, 2020).

One of the most recent applications of W/O/W emulsions is the process of fast agglomeration by emulsion binders to capture fine, hydrophobic particles, which was developed as an alternative to froth flotation van Netten et al. (2017). This method of particle agglomeration involves mixing an aqueous particle suspension with a water-in-oil emulsion consisting of saltwater-filled droplets covered with semi-permeable oil layers, resulting in a W/O/W emulsion with particles initially in the external continuous phase. Recently, we developed a physical model to investigate the capture of fine particles in this new method method (Roure and Davis, 2021a; Roure et al., 2022). By considering binary interactions between single droplets and particles, we found that both permeability and emulsion swelling highly influence the capture of small particles, with the latter being the main

effect. To model the swelling of small droplets, we considered a simple diffusion-limited swelling model (Roure and Davis, 2021b). For small Péclet numbers (i.e., fast diffusion or small droplets), a regular asymptotic solution shows that the droplet radius swells like $t^{1/4}$ for large times. In contrast, for slow diffusion or large droplets at sufficiently short times, drop swelling is governed by a concentration boundary layer near the drop interface, displaying a fast expansion for very short times followed by a $t^{1/2}$ expansion, for which the concentration profile displays a self-similar behavior. We have also shown that such behavior is universal for large Péclet numbers. This expansion behavior matched the experimental observations by DeIuliis et al. (2021, 2022). However, the effective diffusivity obtained by fitting the experimental data to the theory is much lower than the molecular diffusivity of salt in water.

The reason behind the difference between effective and molecular diffusivities is due to the fact that, in both experiments and practical applications, particles collide with agglomerates comprised of multiple droplets. In such situations, as noted in DeIuliis et al. (2021), the mass transfer inside the agglomerate is limited by the permeation of water between adjacent saltwater droplets that comprise the agglomerate. Because water permeation between droplets occurs much slower than the molecular diffusion of salt inside each droplet, the effective diffusivity on the scale of the agglomerate is relatively small. Moreover, the microstructural properties of the agglomerate, such as droplets' size, polydispersity, and the spatial distribution the agglomerate, can play a role in the swelling kinetics. To assess such effects, in this work, we propose a simple permeation network model for the swelling kinetics dominated by interdroplet water permeation. The model consists of spherical saltwater droplets packed inside a spherical oil droplet. We consider shape relaxation and salt diffusivity inside each constituent droplet to be faster than water permeation between droplets. At each time step, the microstructure is determined by a sphere-packing Monte-Carlo algorithm, which determines a dynamic permeation network where permeation occurs. We compare the results from our new

permeation network model to results using a continuum model with an effective salt diffusion by averaging the agglomerate properties over a randomly-generated ensemble of microstructures.

6.2 Dynamic network model for drop swelling

The swelling physics of a double emulsion is a complex, computationally prohibitive problem that involves hydrodynamic interactions between the constituent droplets, drop deformation, and a precise modeling of the mass-transfer processes. However, if our goal is to assess the effects of agglomerate microstructure on the effective mass transfer inside the agglomerate, it is possible to use a much simpler model to do so. To this end, we propose a permeation model for which water permeation occurs only between neighboring droplets. This "connection" between neighboring droplets characterizes a dynamical network that can change with time as the spatial configuration of the agglomerate evolves. As the double emulsions investigated in our problem are stabilized due to the presence of surfactant and salt, which hinder coalescence and Ostwald ripening, we consider that the number of droplets in the agglomerate is kept constant. As water permeation across the oil layers occurs much slower than the salt molecular diffusion inside each drop, we consider the salt concentration inside each saltwater droplet to be homogeneous. This assumption is justified by the scaling analysis performed in DeIuliis et al. (2021). Moreover, considering that the fluid velocity inside the droplets is small, due to the small permeation K, we do not consider convective effects inside the droplets. Under these circumstances, the rate of change in volume for each droplet is governed by

$$\frac{dV_i}{dt} = \sum_{j \in \mathcal{N}_i(t)} \zeta_{ij}(t) \left(c_i(t) - c_j(t) \right), \tag{6.1}$$

where V_i is the volume of a droplet i, $\mathcal{N}_i(t)$ is the set of neighbors of the droplet i, which for droplets near the interface, also includes the outside region (see, for example, Figure 6.1(c)), $c_i(t)$ is the uniform salt concentration inside the droplet i, and ζ_{ij} is the

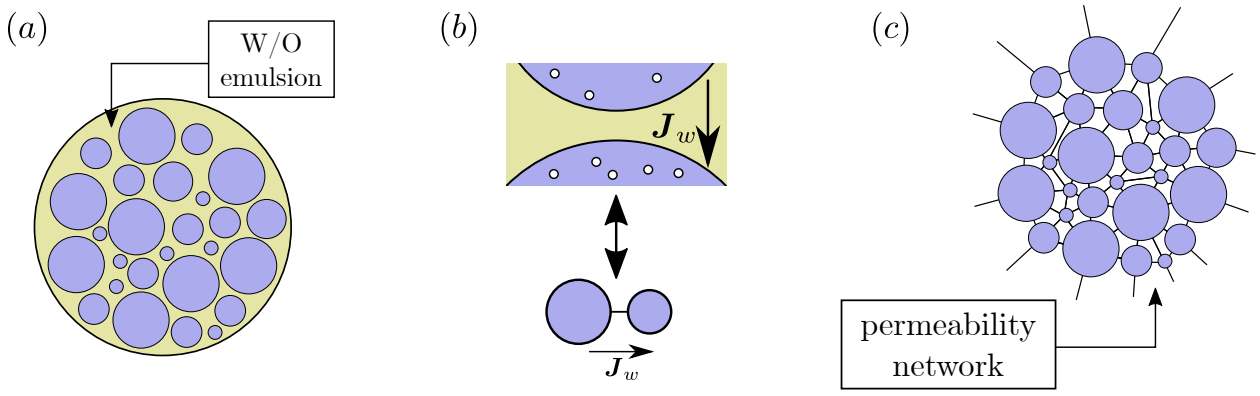

Figure 6.1: Sketch of our simple permeation network model. (a) Spherical saltwater droplets are initially randomly distributed inside a spherical oil droplet. (b) At each time step, the salt concentration difference between two neighboring droplets produces an osmotic water flux between the pair of droplets. (c) The permeation of water between neighboring droplets corresponds to an edge of a dynamical graph network, which can change with time during structure relaxation, numerically performed using a swelling Monte-Carlo algorithm.

permeability kernel, which is related to the permeation flux between two droplets i and j. Note that both the set of neighbors $\mathcal{N}_i$ and the permeability kernel ζ_{ij} can change with time, as they depend on the physical configuration of the internal droplets. Equation (6.1) alone is not a complete physical model, as both the network configuration and the permeability kernel ζ_{ij} depend on further physical assumptions (see below and Section 6.3). Moreover, a rule for determining the set of neighbors $\mathcal{N}_i$ is also needed.

In general, except for very simple cases, the solution of equation (6.1) has to be performed numerically. This task is done by evolving the microstructure according to the new target volumes:

$$V_i^T(t+\Delta t) \approx V_i(t) + \left[\sum_{j\in\mathcal{N}_i(t)} \zeta_{ij}(t)\,(c_i(t)-c_j(t))\right]\Delta t. \tag{6.2}$$

To explore the effect of random agglomerate microstructure, we must generate a random initial configuration of droplets and evolve it with time. Technically, the model represented by equation (6.1) is quite general in the sense that it can be applied even for more complex models for agglomerate microstructure (e.g., deformable packed droplets such as

in Zinchenko and Davis (2021)). However, since we want to calculate averaged properties over an ensemble of microstructures, these complex models would result in prohibitively large computational times. Hence, we need to perform further simplifications in our model beyond the consideration of fast salt diffusion inside droplets. One possible simplification is to assume that the agglomerate is composed by spherical, randomly-distributed saltwater droplets inside a larger, spherical oil droplet. A sketch of the model is shown in Figure 6.1. For the generation of the microstructure, we use an expanding-hard-spheres Monte-Carlo simulation similar to the one proposed in Roure et al. (2023) for the case of two-dimensional disks. Namely, for the generation of the initial configuration, we draw points from a uniform probability distribution and assign to each one of these points a target radius a_i^0. We then perform multiple Monte-Carlo steps consisting of translation (conditioned to a hard-sphere potential) followed by swelling towards the target radius. The numerical implementation of this method follows the same procedure outlined in Roure et al. (2023) but is slightly simpler, as our container is always spherical. We also use the same method to account for the time evolution of the agglomerate microstructure at each time step, by using the previous configuration as the starting configuration and assigning new target radii based on equation (6.2) and running extra Monte Carlo steps.

6.3 Determination of the permeation kernel

Besides the determination of the microstructure, another crucial physical aspect of the model is the choice of an appropriate permeation kernel. To this end, as a simple initial approximation, we consider ζ_{ij} to be proportional to the reduced radius a_{ij} of a pair of saltwater droplets. Intuitively, one way to interpret this relationship is in terms of a scaling analysis. Namely, the mass-transfer rate is given by a flux times the permeation area. As the water permeation is diffusive, a characteristic flux is given by $D_{wo}\Delta c_w/h_0$, where D is the diffusivity of water in oil, Δc_w is the difference in dissolved water concentration across the oil layer separating the two droplets, and h_0 is the minimum separation between two

droplets. Like in previous works for the effective thermal conductivity of concentrated suspensions (Zinchenko, 1998), we consider that the main contribution to the diffusive flux between two spheres comes from the "lubrication" region where the interfaces are close to each other (see Figure 6.1(b)). Under these circumstances, the characteristic permeation area is $h_0 a_{ij}$, where a_{ij} is the reduced droplet radius of a pair of droplets i and j, meaning that a characteristic mass-transfer rate is given by $D_{wo}\Delta c_w a_{ij}$.

Below, we give a more precise formulation of the aforementioned argument. We start by considering a pair of droplets in close proximity, such as shown in Figure 6.1(b). We label the upper droplet i and the bottom one j. We introduce a cylindrical coordinate centered along the symmetry axis of the pair of droplets and at the interface of drop j. Similarly to the procedure for lubrication theory, near the region of proximity, the droplet interfaces can be approximated by paraboloids

$$z_i \sim h_0 + \frac{1}{2a_i} r^2 \tag{6.3}$$

$$\text{and} \qquad z_j \sim \quad -\frac{1}{2a_j} r^2. \tag{6.4}$$

The calculation of the total mass-transfer rate of water through the oil layer between the two spheres is then given by the integral of the flux over a disk of radius R_p, where R_p would be determined by asymptotic matching with an outer solution of the problem, such as in the case for lubrication forces between two spheres (Kim and Karrila, 2013). Assuming that, in this regime, the flux can be expressed as a general function of the separation $h(r) = z_i - z_j$, we have

$$J_{ij}^{w} \sim 2\pi \int_0^{R_p} F(h(r)) r \, dr = 2\pi a_{ij} \int_{h_0}^{h(R_p)} F(h) dh = a_{ij} \Delta c \, \mathcal{F}(h_0; R_p), \tag{6.5}$$

where $a_{ij} = a_i a_j/(a_i + a_j)$ is the reduced radius between the pair of droplets and Δc is the difference in salt concentration between the two droplets, which drives the osmotic flux of water. Considering that the nature of the water permeation through the oil layer is

diffusive, that the concentration of water in oil at the water/oil interface is linearly related to the pressure via a solubility constant, and that the osmotic pressure is given by van't Hoff's law, we have:

$$\mathcal{F}(h_0; R) = \int_{h_0}^{h(\mathscr{R})} \frac{RTD_{wo}H_s}{h} dh = RTD_{wo}H_s \log\left(1 + \frac{\mathscr{R}^2}{2}\right). \tag{6.6}$$

Here, H_s and D_{wo} are, respectively, the solubility and diffusivity of water in oil, R is the gas constant, T is the absolute temperature, and $\mathscr{R} = R_p/\sqrt{a_{ij}h_0}$ is the dimensionless permeation radius, which, for near-field theories, is of $\mathcal{O}(1)$. This result yields a permeation kernel $\zeta_{ij} = RTD_{wo}H_s \log(1 + \mathscr{R}^2/2)a_{ij} \equiv \zeta_0 a_{ij}$. As mentioned before, in general, the determination of R would have to be done by matching with an outer solution. For simplicity, we consider that R does not substantially change throughout the agglomerate. Moreover, as we consider that droplets need to be close to each other for water permeation to happen, we adopt a simple criterion that $h_0 < a_{ij}$ for determining the neighboring droplets (i.e., the edges of the permeation network).

One interesting feature of this form of the permeation kernel is that, under certain circumstances, it recovers a diffusion equation for salt concentration. To see that, let us consider the dimensionless form of equation (6.1), given by:

$$\frac{dV_i}{dt} = C \sum_{j \in \mathcal{N}_i(t)} a_{ij}(c_i(t) - c_j(t)), \tag{6.7}$$

where lengths are made dimensionless by using the initial agglomerate radius a_0, concentrations are made dimensionless by using the initial salt concentration inside the saltwater droplets c_0 (considered to be uniform at $t = 0$), and the time scale for nondimensionalizing time is $Ca_0^2/(\zeta_0 c_0)$, where C is an arbitrary dimensionless constant. From this point on, our discussion will focus only on dimensionless quantities. We now consider the situation where small saltwater droplets of the same radius a_s are arranged in a cubic lattice and that droplets do not present noticeable swelling. In this case, we have

$$\frac{dc_i}{dt} \approx \frac{6C}{4\pi} \sum_{j \in \mathcal{N}_i(t)} \frac{(c_i(t) - c_j(t))}{(2a_s)^2}. \tag{6.8}$$

If the center-to-center distance between the droplets is approximately equal to $2a$, equation (6.8) is the finite-difference approximation for a diffusion equation with a dimensionless diffusivity $6C/(4\pi)$. We note that the time scale used to nondimensionalize time here is slightly different from the one in Roure and Davis (2021b), as the latter uses the permeation time for water to permeate into a single spherical droplet in fresh water, whereas here we use a typical permeation time of water between two droplets.

6.4 Numerical results

With our approximation for the permeation kernel and the swelling Monte-Carlo algorithm, we can perform numerical simulations of our model. We use the dimensionless form of our network model in equation (6.7), combined with the method outlined in section 6.2. For numerical reasons, to keep our simulations running for times of $\mathcal{O}(1)$ in our parameter range of interest, we set $C = 0.3$. Note that this choice of C just re-scales time and does not affect the interpretation of our results. We also use a numerical time step $\Delta t = 0.01$. Figures 6.2(a) and 6.2(b) show examples of monodisperse and polydisperse initial configurations. The beginning of this section focuses on on results for initially monodisperse agglomerates. Details regarding the generation of polydisperse microstructures and the effects of polydispersity are discussed in the end of this section. Figure 6.2(c) shows an example of a typical simulation of an initially monordisperse agglomerate using our model.

For an initially monodisperse distribution of saltwater droplets, the main parameters that govern the agglomerate microstructure are the initial volume fraction of saltwater droplets ϕ_0 and the number of saltwater droplets inside the agglomerate, N_d. Typically, the main result explored in diffusion-like models is the evolution of the concentration profile. As, in our model, the salt concentration is discrete for a given configuration,

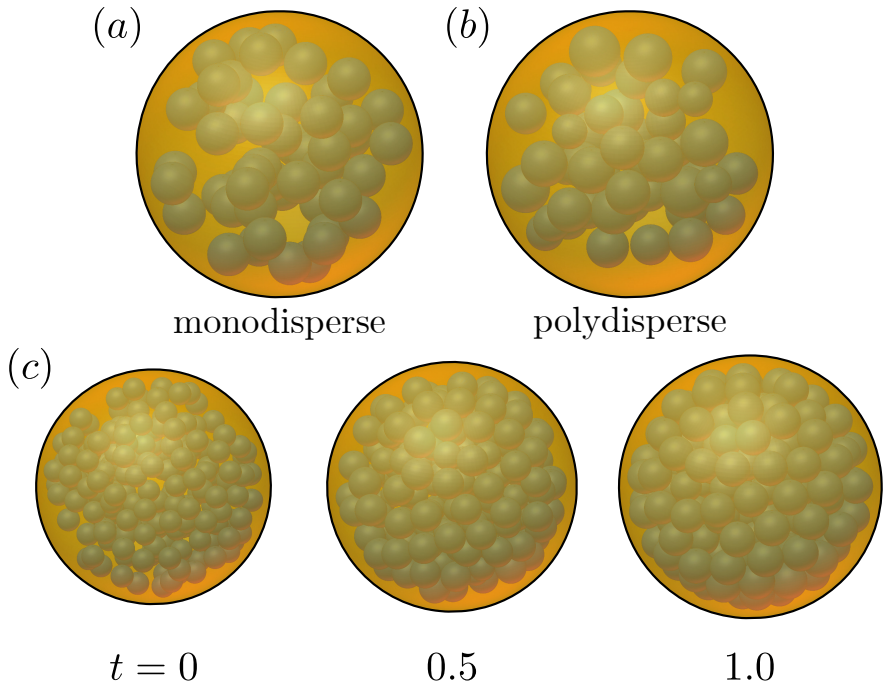

Figure 6.2: Initial configuration and time evolution of a droplet agglomerate. Figures (a) and (b) show initial randomly-generated configurations for initially (a) monodisperse and (b) polydisperse agglomerates with $\phi_0 = 0.2$, $N_d = 50$, and polydisperity index $PDI = 0.1$ for the polydisperse case, for which the initial droplet radii are drawn from a log-normal distribution. Figure (c) shows a typical time evolution of the swelling of an initially monodisperse agglomerate for $\phi_0 = 0.2$, $N_d = 200$.

there are a few different approaches for obtaining an effective concentration profile. One approach is to calculate an effective radial concentration profile $c_s(r)$ by taking the mean of the saltwater concentration of all saltwater droplets that intersect a spherical shell S_r of radius r. That is,

$$c_s(r) = \frac{1}{N_r} \sum_{V_i \cap S_r \neq \emptyset} c_i, \tag{6.9}$$

where V_i is the volume region of the droplet i and N_r is the number of saltwater droplets intersecting with S_r. This quantity can also be averaged over multiple microstructures, resulting in an averaged concentration profile $\langle c_s \rangle(r)$. We can also define a similar parameter to quantify the size distribution of saltwater droplets inside the agglomerate. Namely, we define α_{sp} as

$$a_{sp}(r) = \frac{1}{N_r} \sum_{V_i \cap S_r \neq \emptyset} a_i. \tag{6.10}$$

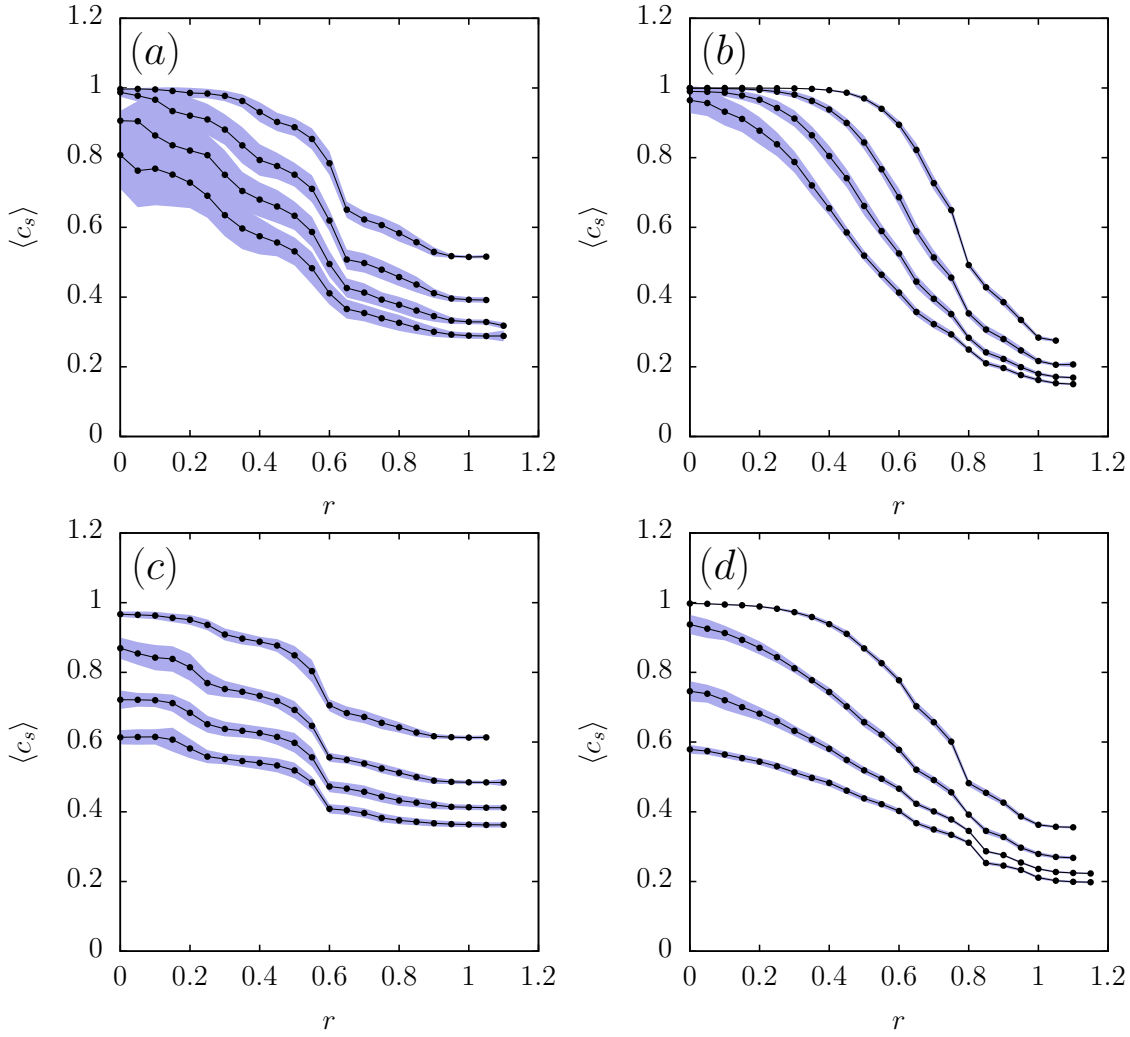

Figure 6.3: Time evolution of the concentration profile for $N_d = 50$ ((a) and (c)) and 500 ((b) and (d)) and $\phi_0 = 0.1$ ((a) and (b)) and 0.2 ((c) and (d)) for different times $t = 0.25$, 0.5, 0.75, 1.0 (top to bottom). The respective initial radii of the saltwater droplets are (a)$a_{i0} = 0.126$, (b) 0.058, (c) 0.159, and (d) 0.074. The results were averaged over 30 different initial, randomly-generated configurations. The point-line curves represent the average results whereas the blue shades are the sample standard deviation.

Figure 6.3 shows typical numerical results for the average salt concentration profile inside the droplet obtained from equation (6.9) averaged over different microstructures. The shaded region in the figures represent the sample standard deviation. For all simulations, the overall behavior of the concentration profile is the one expected from the

effective-diffusion problem. Namely, the salt concentration is higher near the center of the agglomerate, and the salt concentration seems to become more homogeneous over time. For a small number N_d (e.g., Figures 6.3(a) and 6.3(c)) of saltwater droplets, the concentration profile presents an irregular shape that bears little resemblance to the boundary-layer profiles described in Roure and Davis (2021b). When increasing the number of saltwater droplets, however, the concentration profile shape becomes smoother and, for lower volume fractions, like in Figure 6.3(b), we can see a boundary-layer-like behavior for short times (e.g,. $t = 0.25$), characterized by a flat concentration profile near the center of the droplet and then a rapid decrease in concentration near the edge of the droplet due to the influx of fresh water. This behavior is less pronounced for higher volume fractions (e.g., Figure 6.3(d)). Moreover, as expected, agglomerates with a larger number of droplets N_d present a smaller standard deviation for the same initial volume fraction ϕ_0. For low values of N_d and ϕ_0, as shown in Figure 6.3(a), the standard deviation is larger due to the presence of a larger volume of the oil phase, where the droplets can freely move.

One of the reasons behind the different behavior of the concentration profiles for different volume fractions ϕ_0 is due to the size distribution of saltwater droplets. As the amount of salt molecules inside each droplet is always constant, the drop size present an opposite trend compared the concentration profiles, meaning that droplets near the agglomerate interface are larger than the ones in the center, as water permeation to the center of the agglomerate needs to go through multiple layers to reach the droplets near the center of the agglomerate. As the size of the droplets near the interface is limited by the agglomerate geometry, smaller droplets (e.g., for lower volume fractions) have more room to expand (and, therefore, lower salt concentration) than larger droplets. We also note that even the depletion near the interface seen in Figure 6.3(b) is different from the continuous theory. More specifically, the results for high Péclet numbers in Roure and Davis (2021b) display a fast sort-time salt depletion at small times near the interface, described by short-time asymptotic regime, followed by an increase in salt concentration

near the interface for longer times in the similarity regime, resulting in a intersection between concentration profiles for different times near the interface which is not observed in our permeation model.

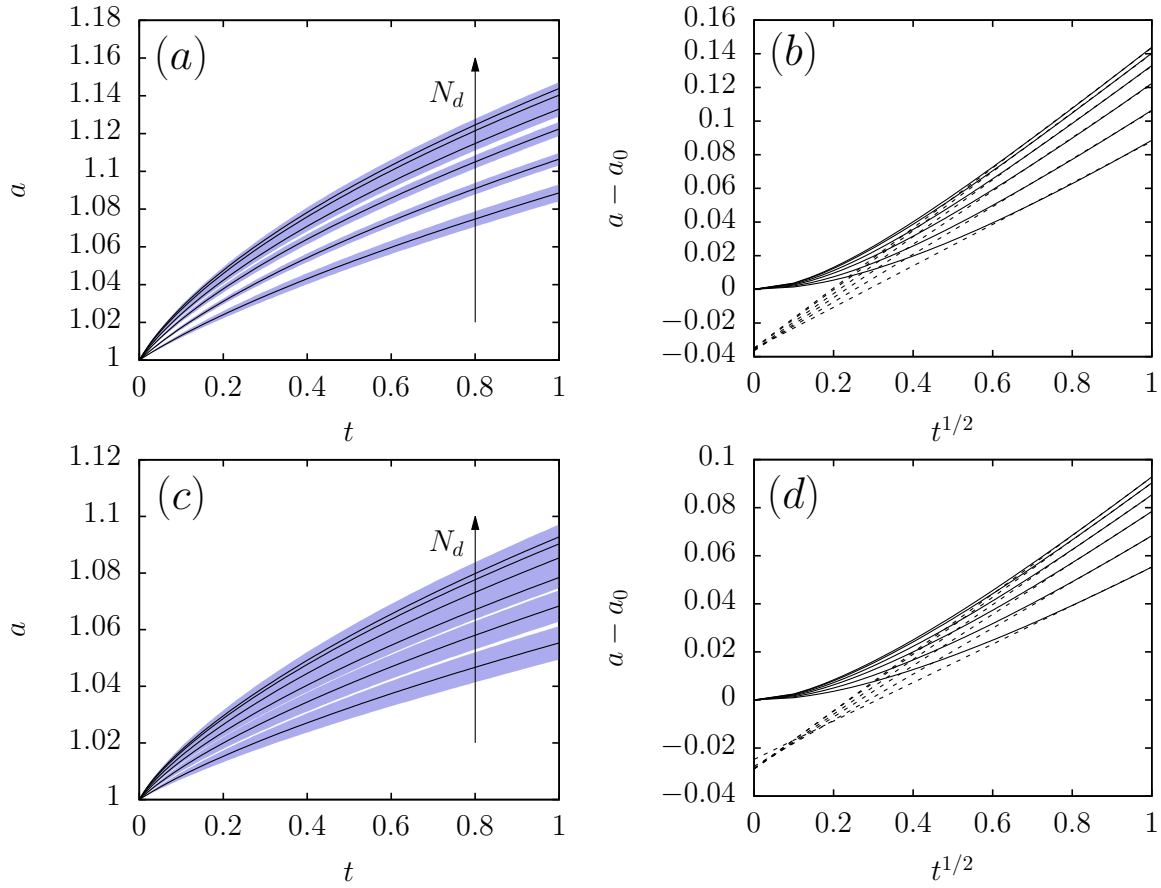

Figure 6.4: Numerical results for agglomerate radius versus time. The panels on the left show results for the same initial salt concentration, different numbers of saltwater droplets $N_d = 50$, 100, 200, 300, 400, and 500 (from bottom to top), and initial volume fractions (a) $\phi_0 = 0.2$ and (c) 0.1. In terms of drop size, we have (from top to bottom) $a_{i0} = 0.058$, 0.063, 0.069, 0.079, 0.1, and 0.126 for (a) and (b) and $a_{i0} = 0.074$, 0.079, 0.087, 0.1, 0.126, and 0.159 for (c) and (d). The solid curves represent the average results over 30 distinct, randomly-generated initial configurations whereas the blue shades are the sample standard deviation. The panels on the right show the same data from their left counterparts, but in terms of radial variation versus $t^{1/2}$ (solid curves). The dashed straight lines in (b) and (d) highlight the radial expansion proportional to $t^{1/2}$ for longer times, similarly to the regime of high Péclet numbers in Roure and Davis (2021b).

Next, we analyze the radial evolution of the agglomerate. Figure 6.4 shows numerical results for the droplet expansion for fixed initial volume fractions $\phi_0 = 0.2$ (top panels)

and 0.1 (bottom panels) and different number of droplets N_d inside the agglomerate. For an initially monodisperse configuration and constant initial volume fraction ϕ_0, N_d is also an inverse measure of initial saltwater drop size (relative to the initial agglomerate size). Namely, $a_{i0} = (\phi_0/N_d)^{1/3}$. For a constant initial volume fraction ϕ_0, as the number of droplets inside the agglomerate increases, so does its swelling rate. This result means that, although smaller droplets lead to a smaller permeation kernel, they can lead to more effective mass transfer inside the agglomerate. We also note that, the difference between the swelling curves decreases as N_d increases, indicating the existence of a limit curve, which would correspond to a foam limit. Moreover, the results for lower volume fractions $\phi_0 = 0.1$ display a slower swelling and higher fluctuations when compared to the results for $\phi_0 = 0.2$, meaning that, like the results for concentration profiles, agglomerates with a lower volume fraction are more sensitive to changes in microstrucutre, even for smaller droplets. Motivated by the results by Roure and Davis (2021b), we also analyze the behavior of the radial expansion of the agglomerate versus $t^{1/2}$ instead of t; this result is shown in Figures 6.4(b) and 6.4(d). We observe that, even though the concentration profile for lower values of N_d, where the concentration profile is substantially different from the ones predicted by the boundary-layer theory in Roure and Davis (2021b), the drop expansion presents a similar behavior to the one predicted by the theory and observed in the experiments by DeIuliis et al. (2021). Namely, we see a fast expansion for short times followed by a radial expansion proportional to $t^{1/2}$, which can be seen by fitting a straight line to the long-time data in the a versus $t^{1/2}$ plot.

From the straight-line fittings shown in Figure 6.4, we note that, the slope of the fitting curve increases with the value of N_d. In contrast, the $y-$intercept remains practically unaltered for all cases. From Roure and Davis (2021b), the drop expansion at larger times (i.e., in the $\propto t^{1/2}$ region) was governed by a curve of the type

$$a - a_0 \approx 2.674\,(\tilde{t}/Pe)^{1/2} - 12.24/Pe, \tag{6.11}$$

where the Péclet number $Pe = KRTc_0a_0/D$ is a ratio between the characteristic effective-diffusion time over the characteristic time for external water permeation and $\tilde{t}$ is time made nondimensional by $t_p = a_0/(KRTc_0)$. Here, K is the effective permeability of the external oil layer and D is the effective diffusivity used in the model by Roure and Davis (2021b). The two nondimensionalizations are related by $\tilde{t} = S\,t$, where S is the ratio between the characteristic times for internal and external permeation, i.e., $S = t_{pi}/t_p = CKRTa_0/\zeta_0$. The almost-constant $y-$intercept for all the curves in Figure 6.4 is compatible with the theory, and can be used to calculate an apparent Péclet number. The numerical results for apparent Péclet numbers obtained by this approach are shown in Figure 6.5 (a) for different initial volume fractions. The results show a decreasing behavior of Pe with respect to ϕ_0, ranging from $Pe \sim 320$ for $\phi_0 = 0.2$ and ~ 410 for $\phi_0 = 0.1$. The results in $6.5(a)$ were calculated by fitting the average radial expansion curve with the expression in (6.11) for larger times and averaged between $N_d = 100$, 200, 300, 400, and 500. The range of values found by these calculations is consistent with both the high Péclet number assumption underlying the boundary-layer theory and experimentally observed values. Note that, in contrast to the effective diffusion model, the Péclet number here is an outcome of the model, instead of an input. It is because, as the effective diffusivity is determined by water permeation between adjacent droplets, there is an intrinsic coupling between osmotic permeability and effective-diffusion effects.

Moreover, the increasing values of slope with respect to N_d seem to be incompatible with the universality of the curve. One way to interpret this incompatibility is to note that in this model, the time is made dimensionless by scaling it with the water permeability inside the microstructure, whereas in Roure and Davis (2021b), we scaled time with the permeation time for a single, larger droplet with effective inner diffusivity. Similarly to what was done when fitting our model to experimental results, we can interpret the ratio $S/Pe = D/(\zeta_0 c_0/C)$ as a dimensionless apparent salt diffusivity D_e, coming from the bulk behavior of water permeation between droplets. Therefore, in terms of our

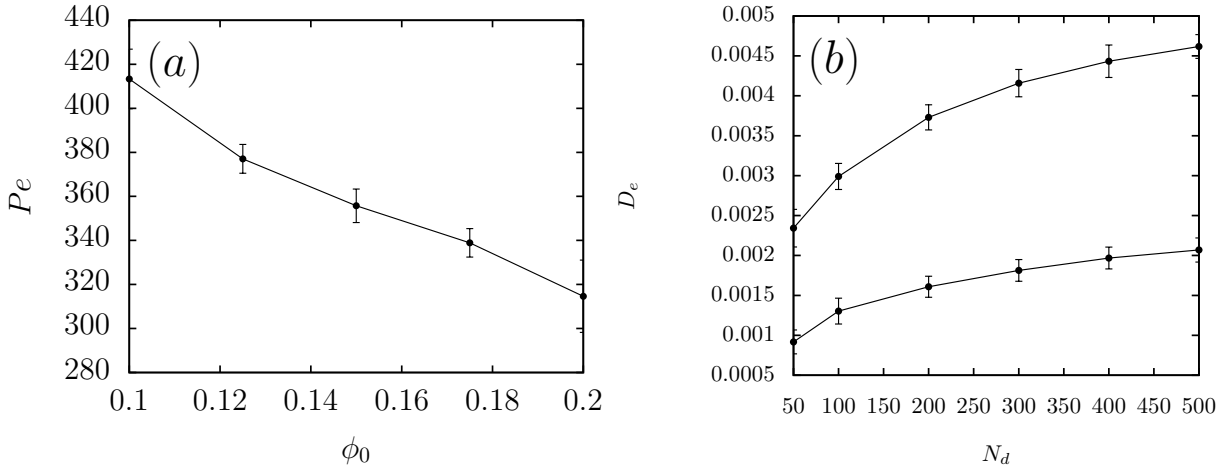

Figure 6.5: Numerical results for the (a) apparent Péclet number versus initial volume fraction ϕ_0 and (b) apparent diffusivity versus number of droplets N_d for $\phi_0 = 0.1$ and 0.2 (bottom to top). The points connected by solid lines are the average results whereas the error bars are the sample standard deviation. Both parameters were calculated calculated by fitting the large-time agglomerate-expansion data (e.g., Figure 6.4) with equation (6.12).

nondimensionalization, we have:

$$a - a_0 \approx 2.674 \left(D_e t\right)^{1/2} - 12.24/Pe. \tag{6.12}$$

Hence, we can interpret the increase in slope shown in Figures 6.4(b) and 6.4(c) as an increase in effective diffusivity, which results in faster agglomerate expansion.

Figure 6.5(b) shows the apparent diffusivity, calculated by comparing the fittings shown in Figure 6.4(b) and 6.4(d) with the theoretical expression (6.12), as a function of the number of droplets N_d. As expected from the results for agglomerate radius expansion in 6.4, for a constant initial volume fraction ϕ_0, the apparent diffusivity increases with the number of droplets inside the agglomerate. Moreover, the effective diffusivity substantially increases with the initial volume fraction ϕ_0. One consequence of an increasing diffusivity and constant Péclet number is that the effective interface permeability of the agglomerate decreases with the increase in number of droplets.

In practical applications, the initial microstructure of the double emulsions is not usually monodisperse, but instead displays a certain degree of polydispersity. Hence, it

is important to verify whether polydispersity plays an important role in the swelling of the agglomerate. A simple way to assess the effects of polydispersity in our model is to, instead of considering an initially monodisperse configuration, draw the initial target radii for the saltwater droplets from a given probability distribution function. A good candidate for such a function is a log-normal distribution, which is classically used to describe lot of situations involving size distributions of emulsions, foams, and pores in porous materials (Stevenson et al., 2010; Henrique et al., 2022). The average saltwater droplet radius for the log-normal distribution is chosen to be $\langle a_s \rangle = (\phi_0/N_d)^{1/3}$. To quantify the polydispersity of saltwater droplets inside the agglomerate, we define a polydispersity index PDI as the ratio between the standard deviation σ and mean $\langle a_s \rangle$ of the log-normal distribution. In dimensionless form, we have

$$\mathrm{PDI} = \frac{\sigma}{\langle a_s \rangle} = \sigma \left(\frac{N_d}{\phi_0} \right)^{1/3}. \tag{6.13}$$

To guarantee that the number of droplets and initial volume fraction are kept constant, we only sample the first $N_d - 1$ droplet radii from the random distribution, with the last droplet having the necessary radius to guarantee the volume fraction is equal to ϕ_0. For cases where the first $N_d - n$ droplets exceed the target volume fraction ϕ_0 for $n \geqslant 1$, we make the radii of the last n droplets uniform with radius

$$a_i = \left(\frac{\phi_0 - \sum_{k=1}^{N_d - n - 1} a_k^3}{n} \right)^{1/3} \tag{6.14}$$

for i ranging from $N_d - n$ to N_d. An example of initial polydisperse configuration generated by this method is shown in Figure 6.2(b) for $N_d = 50$.

After the generation of initial configuration, all the other simulation steps are the same as described in Sections 6.2 and 6.3. We now proceed to analyze the effects of polydispersity in agglomerate swelling. Figure 6.6 shows numerical simulations for the comparison of radial expansion between different agglomerates for different polidispersity indices PDI, initial volume fraction ϕ_0 and number of droplets N_d. From the results, we see that, for a

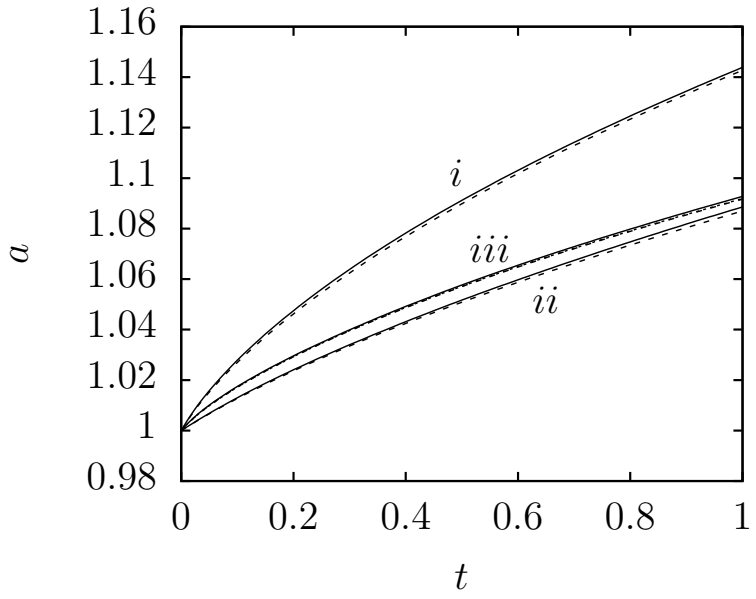

Figure 6.6: Numerical results for radius expansion versus time for an initially polydisperse agglomerate. The initial radii for the saltwater droplets were drawn from a log-normal distribution with mean $(\phi_0/N_d)^{1/3}$. The results are for (i) $\phi_0 = 0.2$, $N_d = 500$ ($\langle a_s \rangle$ = 0.074), (ii) $\phi_0 = 0.2$, $N_d = 50$ ($\langle a_s \rangle$ = 0.159), (iii) $\phi_0 = 0.1$, $N_d = 500$ ($\langle a_s \rangle$ = 0.058), and polydispersity indices PDI = 0 (solid curves), 0.1 (long-dashed curves), and 0.15 (short-dashed curve for (iii)).

same volume fraction and N_d (or, alternatively, average radius), the effect of polydispersity is practically unnoticeable, both in the average results and standard deviation. This result is compatible with the experiments in DeIuliis et al. (2021) for cylindrical rivulets, where, for the same volume fraction and salt concentration, the results for radial evolution for different agglomerates are similar to each other. Of course, in the experiments performed in DeIuliis et al. (2021, 2022), polydispersity plays a role in the sense it is a key factor to achieve larger volume fractions (e.g., up to 95%) of the saltwater phase, and, as shown by our model, the initial saltwater volume fraction results in faster swelling.

6.5 Concluding remarks

We proposed a simple model for the swelling of high-concentration, double emulsion droplets in W/O/W emulsions where the osmotic influx is driven by the presence of salt in the internal water phase. The model consists of spherical salt-water droplets

encapsulated in a larger, spherical oil droplet. As the permeation of water through the oil films inside the agglomerate structure occurs much slower than the diffusion of salt in the aqueous phase, the mass transport inside the agglomerate is mainly determined by the water permeation between neighboring droplets. To account for effects of agglomerate microstructure in the internal mass transport inside the agglomerate, we average our results over an ensemble of microstrucutures, which are randomly generated by a swelling Monte-Carlo algorithm, the latter which is also used to evolve the microstructure in time. Analyzing the average salt concentration profile, we see that, for a fixed initial volume fraction and a high number N_d of small droplets inside of the agglomerate, we observe a typical diffusive-like behavior, such as the concentration profiles predicted by our diffusion-limited swelling model, including the concentration plateau near the center of the agglomerate combined with concentration decrease near the interface, similar to the behavior predicted by the boundary-layer theory for high Péclet numbers at short times. The results for radial expansion of the spherical agglomerate present a similar behavior to the one observed experimentally by DeIuliis et al. (2021, 2022) and by the high-Péclet-number regime in the effective diffusion model from Roure and Davis (2021b). By comparing the radial expansion curves to the universal boundary-layer curve predicted in Roure and Davis (2021b), we were able to obtain effective diffusivities and Péclet numbers. The range of the apparent Péclet numbers obtained from our model were in accordance to both the high Péclet number assumption and the values calculated from experimental data using the same fitting procedure. Increasing the initial volume fraction decreases the Péclet number, resulting in substantially higher swelling rates. Moreover, for the same volume fraction, smaller droplets lead to a more efficient mass transfer and faster swelling. We also performed simulations for initially polydisperse configurations by drawing the initial particle radii from a log-normal distribution. For the same volume fraction, initial average saltwater droplet radius, and lower degrees of polydispersity, there were no significant differences in average swelling behavior when compared to initially

monodisperse configurations. Of course, polydisperse configurations can affect the mass transfer by other means, such as allowing the system to reach high volume fractions.

Part III

Droplets in microchannels

CHAPTER 7

NUMERICAL SIMULATION OF DEFORMABLE DROPLETS IN COMPLEX-SHAPED MICROCHANNELS

This work has been submitted to *Physics of Fluids* with co-authors Alexander Z. Zinchenko and Robert H. Davis and it is currently under review

Synopsis

In this chapter, we develop a boundary-integral method to simulate the motion of drops in microchannels of finite depth with flat walls and fixed depth but otherwise arbitrary geometries. To reduce computational time, we use a moving frame, which follows the droplet throughout its motion, such that the droplet effects are restricted to the moving frame. We provide a full description of the method, including our algorithm used for channel meshing, which is a combination of Monte-Carlo techniques and Delaunay triangulation. Our method is able to simulate drop motion in various geometries, including the main ones that appear in drop-based microfluidics. For regular geometries of uniform cross-section, the infinite-depth limit is approached only slowly with increasing depth, though we show much faster convergence by scaling with maximum versus average velocities. For non-regular channel geometries, features such as different branch heights can affect drop partitioning, as the flow rate required to make a droplet go through a smaller branch of a channel is larger than the one required for making the same droplet go through a smaller branch, in contrast to the symmetrical behavior usually found in regular geometries. Moreover, non-regular geometries also present challenges when comparing the results for deep and infinite-depth channels. A simplified approach is also developed to probe inertial effects on drop motion. To this end, the full Navier-Stokes equations are first solved for the entire channel, and the tabulated solution is then used as a boundary condition at the moving-frame surface for the Stokes flow inside the moving frame. We find that, for moderate Reynolds numbers up to $Re = 5$, inertial effects on the undisturbed flow are

small even for a more complex, irregular geometry, meaning that inertial contributions arise only from the transience of drop motion and are likely small.

7.1 Introduction

The motion of deformable drops in microchannels has a wide range of applications, ranging from drug targeting (Fontana et al., 2016) to micro-chemical reactors (Liu et al., 2020) and generation of emulsions with low polydispersity in drop-based microfluidics (Tan and Lee, 2005). As drop microfluidic applications become more sophisticated, fundamental understanding of the physics of drop motion in bounded domains plays an important role in designing such systems. Owing to the small channel size, the Reynolds number in microfluidic channels is often small, with viscous effects dominating over inertia.

A commonly-used approach to analyze drop motion and fluid flow at low Reynolds numbers is the use of boundary-integral methods (Pozrikidis, 1992), firstly introduced by Rallison and Acrivos (1978). This family of methods consists of reducing the problem of solving the system of partial differential equations, which would often require a discretization of the whole fluid domain, to solving a system of boundary-integral equations, in which only the domain's boundary is discretized. Boundary-integral methods have been extensively used in the literature to investigate the motion of drops in many different contexts, such as shear flows (Loewenberg and Hinch, 1996, 1997; Rother and Davis, 2001; Oliveira and Cunha, 2015), sedimentation/buoyancy (Rother et al., 1997; Zinchenko et al., 1997), motion of emulsions through granular materials (Zinchenko and Davis, 2008), squeezing through interparticle constrictions (Zinchenko and Davis, 2013; Gissinger et al., 2021a), and flow in microchannels (Navarro et al., 2020; Lyu et al., 2021; Kadivar, 2018; Nagel et al., 2014). Regarding the motion of droplets in microchannels, much of the work done has focused on two-dimensional problems (Pozrikidis, 2012; Cunha et al., 2018; Kadivar, 2018), three-dimensional droplets in infinite-depth channels (Navarro et al., 2020), or

channels with circular cross sections (Coulliette and Pozrikidis, 1998; Hodges et al., 2004; Lyu et al., 2021). However, given recent advances in drop microfluidics, numerical and experimental studies have recently considered the motion of drops in rectangular, straight channels (Wang and Dimitrakopoulos, 2012; Horwitz et al., 2014; Rao and Wong, 2018; Luo et al., 2019; Li et al., 2020). As microfluidic devices are often of complex shapes with bifurcations, it is important to be able to numerically simulate the drop motion in such geometries.

To investigate the motion of a drop in a channel, one needs to take into account the influence of the whole channel boundary on the drop, which can be computationally expensive if the channel is much larger than the droplet. To overcome such issues, an economical, "Moving-Frame" (MF) version of the boundary-integral method was previously introduced to simulate the motion of a three-dimensional rigid particle in arbitrary microchannels of infinite depth (Zinchenko et al., 2012). Subsequently, this method was extended to study the motion of a three-dimensional deformable drop in a channel of infinite depth with bifurcations (Navarro et al., 2020). In this approach, the boundary-integral equations are solved at each time step within a moving frame, which follows the particle/drop throughout its trajectory. This frame is much larger than the particle/drop size but can still be made much smaller than the entire channel size with acceptable accuracy, resulting in much faster simulations. However, the assumption of an infinite channel depth is often too restrictive for practical channels, where the presence of a front and back walls can lead to significant changes in the physics of the problem.

In the present work, the MF boundary-integral method is developed for finite-depth channels with piecewise flat walls and fixed depth but otherwise arbitrary profile and bifurcations, and it is applied to deformable drop motion through such channels. The difficulty of dynamical meshing of the front and back panels of the evolving moving frame is overcome by a novel algorithm, which is a combination of Monte Carlo techniques and a two-dimensional version of the Voronoi tessellation algorithm presented in Tanemura

et al. (1983) to efficiently triangulate these panels at each time step with high resolution. We use our code to investigate drop motion in a variety of channel geometries. We compare the results to infinite-depth results obtained by the algorithm of Navarro et al. (2020), discussing in what situations the comparison between the two codes is possible and how to find the equivalent problem for an infinite-depth channel in general geometries. In bifurcating channels with branches of different heights, the convergence of outlet flow rates when the channel depth goes to infinity is approached very slowly. A simplified approach is also used to probe inertial effects (previously neglected in the zero-Reynolds-number analysis) on drop motion in bifurcating channels of finite depth. To this end, the full set of Navier-Stokes equations is first solved for the entire channel without the drop, and the tabulated solution is then used as the boundary condition on the MF boundary for the Stokes flow with the drop inside the MF.

7.2 Boundary-integral formulation

In the present work, we investigate the motion of a neutrally-buoyant drop in a three-dimensional microchannel using a moving-frame, boundary-integral (MFBI) method. The moving-frame approach is based on the observation that effects of the freely-suspended drop on the surrounding fluid flow vanish rapidly away from the drop. Thus, instead of solving for the drop and external flow in the whole channel at each time step, which would require a large amount of computational time, we solve the problem in a smaller, but still sufficiently large region around the droplet, which we call the moving frame. The boundary conditions on the moving-frame are given by the undisturbed flow, which can be determined by solving (once) for this flow inside the whole channel in the absence of the droplet. An illustration of the problem is shown in Figure 7.1. Each channel geometry considered in this work has constant cross sections in the $z = \mathrm{const.}$ planes and is formed by multiple rectangular side panels and two front ($z = W/2$) and back ($z = -W/2$) panels separated by a constant distance W, which we call the channel depth. This channel may

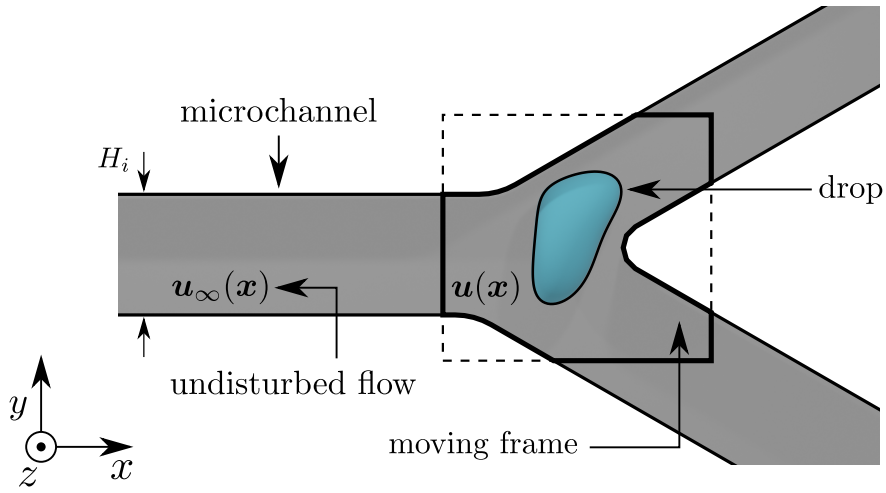

Figure 7.1: Moving-frame approach for the motion of a drop in a microchannel. The channel profile consists of straight segments; sharp corners are beveled, when necessary, by the addition of extra segments. The previously-solved undisturbed background flow is used as the boundary condition for a moving frame that follows the droplet throughout its motion. The moving frame includes the solid (not dashed) surfaces of the box shown above, as well as the channel walls within the box. The channel has front and back panels parallel to the plane of the figure.

have multiple branches with the height of branch i denoted as H_i. For a channel formed by m side panels (including inlets and outlets), the position vectors $\mathbf{x}_{i \pmod m}$ and $\mathbf{x}_{i+1 \pmod m}$ represent, respectively, the initial and final positions of a certain panel at the center plane $z = 0$, labeled counterclockwise. For simplicity, we focus on situations where the droplet is (and remains) centered at this center plane for the whole simulation. When necessary to alleviate simulations, a sharp corner is smoothed by a sufficient number of very small straight segments (as shown in Figure 7.1).

The moving-frame approach can drastically decrease the number of surface elements necessary for the boundary-integral calculation of the velocity at the drop interface, especially in cases where the drop length is much smaller than the channel overall size (this limitation does not preclude the drop from being comparable in size with the narrowest channel throats). Below, we present the theoretical formulation and the boundary-integral equations used in our simulations.

7.2.1 Solution for the undisturbed flow inside the channel

As previously discussed, the first step in the MF method is to compute the undisturbed flow $\mathbf{u}_\infty$ in the entire microchannel (*i.e.*, in the absence of the droplet). To this end, in the context of low-Reynolds-number hydrodynamics, we represent this flow inside the channel by a double-layer distribution:

$$\mathbf{u}_\infty(\mathbf{y}) = 2\int_{S_{ch}} \mathbf{n}(\mathbf{x}) \cdot \boldsymbol{\tau}(\mathbf{x}-\mathbf{y}) \cdot \mathbf{q}_\infty(\mathbf{x}) dS_\mathbf{x}, \tag{7.1}$$

where S_{ch} is the channel surface (including front, back, and all side panels), $\mathbf{n}$ is the external unit normal vector to S_{ch}, $\boldsymbol{\tau}$ is the fundamental stresslet, given by

$$\boldsymbol{\tau}(\mathbf{r}) = \frac{3}{4\pi}\frac{\mathbf{rrr}}{r^5}, \tag{7.2}$$

and $\mathbf{q}_\infty$ is a potential density to be determined. The boundary conditions for $\mathbf{u}_\infty$ are no-slip on all channel walls and prescribed velocity distributions (see below) at all inlet and outlet pannels. The standard limit of (7.1) as $\mathbf{y}$ goes to a point at the channel's boundary results in the integral equation for $\mathbf{q}_\infty$:

$$\mathbf{q}_\infty(\mathbf{y}) = \mathbf{u}_\infty(\mathbf{y}) - 2\int_{S_{ch}} \mathbf{n}(\mathbf{x}) \cdot \boldsymbol{\tau}(\mathbf{x}-\mathbf{y}) \cdot \mathbf{q}_\infty(\mathbf{x}) dS_\mathbf{x} \qquad \text{for } \mathbf{y} \in S_{ch}. \tag{7.3}$$

Here, the integral over S_{ch} should be understood in the sense of a principal-value integral. Solution of equation (7.3) gives the potential density $\mathbf{q}_\infty$ at every point of S_{ch}, which can then be used to calculate the undisturbed velocity field $\mathbf{u}_\infty$ at any point inside the channel according to (7.1). As can be seen by the existence of eigenfunctions $\mathbf{q}_\infty(\mathbf{x}) \propto \mathbf{n}(\mathbf{x})$ for the adjoint homogeneous problem of (7.3) (Kim and Karrila, 2013; Pozrikidis, 1992), the solution for $\mathbf{q}_\infty$ is not unique. Although this ambiguity does not affect the flow field (7.1) inside the channel, it needs to be removed for the numerical solution of (7.3) by imposing the condition of zero flux of $\mathbf{q}_\infty$. Such a constraint is achieved by adding the flux term to equation (7.3):

$$\mathbf{q}_\infty(\mathbf{y}) = \mathbf{u}_\infty(\mathbf{y}) - 2\int_{S_{ch}} \mathbf{n}(\mathbf{x}) \cdot \boldsymbol{\tau}(\mathbf{x}-\mathbf{y}) \cdot \mathbf{q}_\infty(\mathbf{x}) dS_x - \frac{\mathbf{n}(\mathbf{y})}{S_{ch}} \int_{S_{ch}} \mathbf{n}(\mathbf{x}) \cdot \mathbf{q}_\infty(\mathbf{x}) dS_x. \quad (7.4)$$

Here, in contrast to Navarro et al. (2020), we did not perform a full deflation of the problem. However, for our numerical solutions, this partial deflation is sufficient to obtain convergent iterations in a biconjugate-gradient scheme.

As the boundary condition for $\mathbf{u}_\infty$ on the inlets and outlets (assumed to be perpendicular to the corresponding channel branches), it is most natural to use the fully-developed, unidirectional pressure-driven flow in a long duct with rectangular cross section provided by Boussinesq (1868). Namely, the velocity $\mathbf{u}^{(i)} = u_n^{(i)}\mathbf{n}$ at the end of a branch i is given by

$$u_n^{(i)} = \frac{G_i H_i^2}{\mu}\left[\frac{y_i}{2H_i}\left(1-\frac{y_i}{H_i}\right) - 4\sum_{k=1}^{\infty} \frac{\sinh\left(\beta_k^i\,(W/2+z_i)\right) + \sinh\left(\beta_k^i(W/2-z_i)\right)}{(H_i\beta_k^i)^3 \sinh\left(\beta_k^i W\right)} \sin\left(\beta_k^i y_i\right)\right], \quad (7.5)$$

where μ is the viscosity of the background fluid, $\beta_k^i = (2k-1)\,\pi/H_i$, $z_i = z$ and $y_i = \mathbf{t}\cdot(\mathbf{x}-\mathbf{x}_i)$ (where $\mathbf{t} = \boldsymbol{e}_z \times \mathbf{n}$) are the intrinsic Cartesian coordinates in the input/output panel ($|z_i| \leqslant W/2$, $0 \leqslant y_i \leqslant H_i$), $\mathbf{n}$ is the external normal vector at the branch end, H_i is the inlet/outlet height of branch H_i (see Figure 7.1), and G_i is the pressure gradient, which is linearly related to the volumetric flow rate Q_i through the panel by

$$Q_i = \frac{G_i H_i^4}{\mu}\left[\frac{W}{12H_i} - 16\sum_{n=1}^{\infty} \frac{\cosh\left(\beta_n^i W\right)-1}{(H_i\beta_n^i)^5 \sinh\left(\beta_n^i W\right)}\right]. \quad (7.6)$$

This relationship may be used in (7.5) to obtain the Boussinesq velocity profile at each inlet and outlet in terms of the corresponding flow rate Q_i in place of the pressure gradient G_i. One way to make the solution unique is to specify all the flow rates Q_i (with zero total sum, assuming positive sign of Q_i for outlets and negative for inlet panels). Note that, for a particular channel and stationary flow rates Q_i, the boundary-integral problem (7.4)

has to be solved only once for all drop motion simulations. The same is obviously true for unsteady flow rates of the form $Q_i = f(t)Q_i^0$ with constant Q_i^0, in the Stokes regime.

Moreover, to find the undisturbed flow $\mathbf{u}_\infty(\mathbf{y})$ with prescribed, generally time-dependent, input/output fluxes $Q_i(t)$ (totaling to zero), the solution of equation (7.1) can be rapidly obtained through a limited database of precalculated solutions with only one inlet and one outlet panels and unit fluxes. For example, for four fluxes $Q_1, \ldots, Q_4$, one can write

$$\begin{bmatrix} Q_1 \\ Q_2 \\ Q_2 \\ Q_4 \end{bmatrix} = Q_1 \begin{bmatrix} 1 \\ 0 \\ 0 \\ -1 \end{bmatrix} + Q_2 \begin{bmatrix} 0 \\ 1 \\ 0 \\ -1 \end{bmatrix} + Q_3 \begin{bmatrix} 0 \\ 0 \\ 1 \\ -1 \end{bmatrix}. \tag{7.7}$$

Hence, by the linearity of Stokes flows, the undisturbed background flow is given by a linear combination $\mathbf{u}_\infty(\mathbf{y}) = Q_1\mathbf{u}_\infty^{(1)}(\mathbf{y}) + Q_2\mathbf{u}_\infty^{(2)}(\mathbf{y}) + Q_3\mathbf{u}_\infty^{(3)}(\mathbf{y})$ of the flow modes induced by the flow-rate configurations on the RHS of equation (7.7). Using this strategy, it is possible to change the fluxes dynamically and independently with time, allowing our MF boundary-integral simulations to tackle problems involving drop manipulation and the implementation of features such as a feedback controller in microfluidic systems. The control and manipulation of drop shapes and position in a microfluidic channel is the subject of an upcoming work.

Alongside with Q_i, it is also useful (see Section 7.6) to operate with the average velocity $U^B_{av,i} = Q_i/(H_i W)$, the maximum velocity (by magnitude) $U^B_{max,i}$ on the inlet/outlet (achieved at $y_i = H_i/2$ and $z_i = 0$), and the centerline flow rates Q_i^{cl} (obtained by integrating u_n^i over $0 \leqslant y_i \leqslant H_i$ at $z = 0$). All these quantities can be computed by (7.5) and (7.6) once Q_i are given.

7.2.2 Velocity at drop interface

The boundary-integral equations used to calculate the fluid velocity $\mathbf{u}$ at the interface S_d of a drop in a moving frame are the same as in Navarro et al. (2020) (see Appendix A for a brief derivation). This set of equations is given by

$$\begin{aligned}\mathbf{u}(\mathbf{y}) = \frac{2}{\lambda+1}\left[\mathbf{u}_\infty(\mathbf{y}) + 2\int_{S_\infty} \mathbf{n}(\mathbf{x})\cdot\boldsymbol{\tau}(\mathbf{x}-\mathbf{y})\cdot\mathbf{q}(\mathbf{x})\ dS_\mathbf{x} + \mathbf{F}(\mathbf{y})\right] \\ + 2\frac{(\lambda-1)}{(1+\lambda)}\int_{S_d} \mathbf{n}(\mathbf{x})\cdot\boldsymbol{\tau}(\mathbf{x}-\mathbf{y})\cdot\mathbf{u}(\mathbf{x})\ dS_\mathbf{x},\end{aligned} \tag{7.8}$$

for $\mathbf{y}$ on the drop surface S_d, and

$$\begin{aligned}\mathbf{q}(\mathbf{y}) = &-2\int_{S_\infty} \mathbf{n}(\mathbf{x})\cdot\boldsymbol{\tau}(\mathbf{x}-\mathbf{y})\cdot\mathbf{q}(\mathbf{x})\ dS_\mathbf{x} - \mathbf{F}(\mathbf{y}) \\ &-(\lambda-1)\int_{S_d} \mathbf{n}(\mathbf{x})\cdot\boldsymbol{\tau}(\mathbf{x}-\mathbf{y})\cdot\mathbf{u}(\mathbf{x})\ dS_\mathbf{x} - \frac{\mathbf{n}(\mathbf{y})}{|S_\infty|}\int_{S_\infty} \mathbf{n}(\mathbf{x})\cdot\mathbf{q}(\mathbf{x})dS_\mathbf{x},\end{aligned} \tag{7.9}$$

for $\mathbf{y}$ on the moving-frame surface S_∞. Here, $\mathbf{q}(\mathbf{y})$ is the double-layer potential density on S_∞. The non-homogeneous term $\mathbf{F}(\mathbf{y})$ is given by

$$\mathbf{F}(\mathbf{y}) = \frac{1}{\mu}\int_{S_d} 2\sigma\kappa(\mathbf{x})\mathbf{G}(\mathbf{x}-\mathbf{y})\cdot\mathbf{n}(\mathbf{x})\ dS_\mathbf{x}, \tag{7.10}$$

where $\mathbf{G}(\mathbf{r}) = -\left(\mathbf{I}/r + \mathbf{r}\mathbf{r}/r^3\right)/(8\pi)$ is the free-space Green's function for Stokes flow, $\lambda = \mu_d/\mu$ is the ratio between the viscosities of the drop and surrounding fluid, σ is the interfacial tension, and κ is the mean curvature, which was numerically calculated (together with the normal vectors $\mathbf{n}(\mathbf{x})$) by using the best-paraboloid-spline method described in Zinchenko and Davis (2000). A simpler, best-paraboloid method Zinchenko et al. (1997) would give comparable accuracy for $\kappa(\mathbf{x})$, but less-accurate normals $\mathbf{n}(\mathbf{x})$.

The boundary-integral equations (8.1) and (8.2) are solved simultaneously, yielding the velocity $\mathbf{u}(\mathbf{y})$ at the drop surface. The MF contour (marked bold in Figure 7.1) is generally obtained from the intersection of a square (dashed line) centered at the drop center (with square sides parallel to the fixed coordinate axes x and y) and the channel profile in the $z = 0$ plane. This contour (dynamically constructed as in Zinchenko et al. (2012) and Navarro et al. (2020)) is then extended in the $z-$direction to the full channel depth (i.e., $|z| \leqslant W/2$) to form the side surface of S_∞. The interior of the MF contour, translated to $z = \pm W/2$, also forms the front and back panels of the MF, to complement the side surface to the full closed surface S_∞ around the drop. As in Figure 7.1, the MF (computational

domain) in our simulations is typically much smaller than the whole channel size in the $z = 0$ plane, resulting in a substantial decrease in the number of boundary elements on S_∞ when compared to the whole channel S_{ch}. Still, the presence of the front and back panels of the MF, with their non-negligible contribution to the boundary integrals in (8.1) and (8.2), combined with necessary dynamic meshing (see Section 7.3), is a considerable complication (both in terms of coding and computational effort) compared to simulations of particle/drop motion in an infinite-depth channel (Zinchenko et al., 2012; Navarro et al., 2020). For our drops, not much thinner in the $z-$direction than the channel depth, it would be hardly beneficial to crop the MF in this direction, and so we opted to use the full channel depth for S_∞.

The governing equations are made non-dimensional by using the channel inlet height H as the length scale, and the inlet entrance velocity $U^B_{av} \equiv |Q|/(HW)$ to scale $\mathbf{u}(\mathbf{x})$ and $\mathbf{q}(\mathbf{x})$. Here, H is equal to H_i for the main inlet branch (see Figure 7.1) and Q is the inlet flow rate for this branch. This non-dimensionalization procedure keeps equations (8.1) and (8.2) unaltered, while the non-dimensional form of $\mathbf{F}(\mathbf{y})$ becomes

$$\mathbf{F}(\mathbf{y}) = \frac{2}{Ca}\int_{S_d} \kappa(\mathbf{x})\mathbf{G}(\mathbf{x}-\mathbf{y})\cdot\mathbf{n}(\mathbf{x})\, dS_{\mathbf{x}}, \tag{7.11}$$

where $Ca = \mu U^B_{av}/\sigma$ is the capillary number, which measures the ratio between flow and interfacial-tension effects.

7.3 Numerical method

Our numerical techniques for the undisturbed flow solution (Section 7.2.1) and the MF solution (Section 7.2.2) have much in common, regarding how the double-layer boundary integral contributions (7.1) and (7.4) from the entire channel surface S_{ch} and contributions (8.1) and (8.2) from the MF boundary S_∞ are computed. The first principal step is to alleviate singularities in these integrals stemming from $|\boldsymbol{\tau}(\mathbf{r})| \sim r^{-2}$ at $r \to 0$. Although there is no self contribution from a flat panel of S_{ch} (or S_∞) containing the observation point

$\mathbf{y}$, difficulties arise with a near-singular contribution from a neighboring panel (if $\mathbf{y}$ is close to the ridge between the panels), and also for $\mathbf{y}$ inside S_{ch} (or S_∞) but close to it. Due to the presence of sharp (or nearly sharp) corners in the channel/MF geometries, standard (near-)singularity subtraction using the whole integration surface (S_{ch} or S_∞) performs poorly. Instead, we follow the approach of Zinchenko et al. (2012) to desingularize the contribution of each panel S_{ch}^j of S_{ch} (or S_∞^j of S_∞) separately. As an example, for S_∞^j, the following identity is used:

$$\int_{S_\infty^j} \mathbf{q}(\mathbf{x}) \cdot \boldsymbol{\tau}(\mathbf{r}) \cdot \mathbf{n}(\mathbf{x}) dS_\mathbf{x} = \int_{S_\infty^j} [\mathbf{q}(\mathbf{x}) - \mathbf{q}^*] \cdot \boldsymbol{\tau}(\mathbf{r}) \cdot \mathbf{n}(\mathbf{x}) dS_\mathbf{x} + \\ + \frac{1}{4\pi} \left[\oint_{\Gamma_\infty^j} \frac{(\mathbf{q}^* \cdot \mathbf{r})(\mathbf{r} \times d\mathbf{r})}{r^3} + \omega \mathbf{q}^* \right]. \tag{7.12}$$

Here, $\mathbf{r} = \mathbf{x} - \mathbf{y}$ and $\mathbf{q}^* = \mathbf{q}(\mathbf{x}^*)$ is the value of $\mathbf{q}(\mathbf{x})$ at the collocation point $\mathbf{x}^* \in S_\infty^j$ that is nearest to $\mathbf{y}$. The subtraction of $\mathbf{q}^*$ sufficiently alleviates singular behavior of $\boldsymbol{\tau}$ to make the first RHS integral in (7.12) amenable to numerical integration (see below). In the added-back term (i.e., the second line of (7.12)), the area integration over S_∞^j is transformed into a contour integral over the perimeter Γ_∞^j of S_∞^j, using the technique presented in Bazhlekov et al. (2004). For our contours Γ_∞^j (or, alternatively, Γ_{ch}^j) consisting of straight segments, these integrals are handled analytically, as detailed in Zinchenko and Davis (2021). Finally, the solid angle ω, at which the flat panel S_∞^j is seen from the observation point $\mathbf{y}$, also allows for analytical treatment by projecting $\mathbf{y}$ on the plane of S_∞^j, connecting the projection point to the contour vertices and calculating ω as the algebraic sum of the resulting spherical triangle areas. This whole approach works for the rectangular side panels, as well as for the polygonal front/back panels (regardless of convexity), not considered in Zinchenko et al. (2012) nor in Navarro et al. (2020).

To compute the desingualized integral in (7.12) over the rectangular side panels S_∞^j, we use a fine, non-adaptive mesh of points along the MF contour, matching the corners and with almost uniform density. This mesh is extended in the $z-$direction ($|z| \leqslant W/2$) with fine resolution to discretize the side surface of S_∞ into rectangular boundary elements.

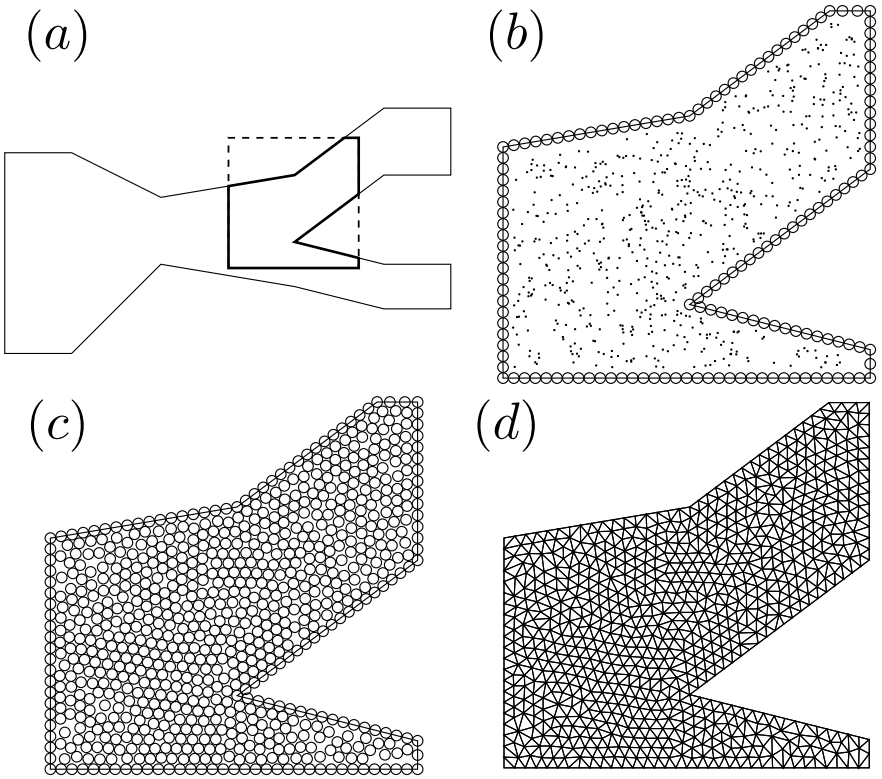

Figure 7.2: Meshing procedure of the front and back walls of a complex geometry. (a) shows the whole channel geometry with the MF contour inside the dashed perimeter. The closeups represent (b) the boundary mesh nodes (with circles of target radius a_t on the MF contour) and the seed distribution of internal nodes prior to equilibration, (c) the dense packing of disks of target radius a_t covering the MF front/back panel, obtained after equilibration of internal nodes, and (d) the constrained Delaunay triangulation of the MF front/back panel, using the disk centers from (c) as mesh nodes.

The midpoints of these elements serve as collocation points for the integral equation (8.2) and are used in the simplest, second-order Euler integration over the elements.

It is more difficult to efficiently compute the regularized integrals in (7.12) over the front and back panels of the MF as they have more complex shapes. To this end, we use non-adaptive, corner- and boundary-fitted unstructured triangulations of the front and back panel, dynamically constructed at each time step (see Figure 7.2). As an auxiliary construction, the panel domain is covered with a prescribed number N_{vfr} of non-overlapping disks at near-maximum packing density, to ensure nearly uniform distances between neighboring disk centers throughout the domain. The disk centers then serve as N_{vfr} nodes for the mesh triangles. The target disk radius a_t is estimated a priori, with sufficient

accuracy, from N_{vfr} and the panel area. The algorithm starts by placing non-overlapping disks of radius a_t in the panel corners, then, uniformly, along the MF contour edges, to form boundary nodes. The remaining nodes are first randomly generated inside the panel domain, with statistically uniform distribution and sufficient clearance from the boundary nodes (see Figure 7.2(b)). These internal modes are considered as centers of disks of initially zero radius. The internal disk system is then subjected to stochastic mixing (i.e., equilibration), with gradual increase in the disk radius, thus going through a polydisperse stage, until all disks reach the target radius a_t (Figure 7.2(c)). The following step is to connect all boundary and internal points by unconstrained Delaunay triangulation and remove redundant triangles to obtain a suitable boundary-fitted panel triangulation (Figure 7.2(d)). The detailed description of this meshing technique is given in Appendix B.

The idea of using dense disk arrangements as a base for domain triangulation is not new, of course, and it was used in the 'bubble mesh' algorithms (Shimada and Gossard, 1995; Yamakawa and Shimada, 2003; Chung and Kim, 2003; Kim et al., 2003). However, to our knowledge, the present in-house algorithm is unique in how this disk arrangement is generated, inspired by Monte-Carlo techniques from statistical physics for dense molecular systems (Metropolis et al., 1953; MacKeown, 2001) and more recent stochastic algorithms (Zinchenko and Davis, 2013, 2021) for dense packing of particles in constricted geometries. In contrast to bubble-mesh methods or other Delaunay-based meshing algorithms (Frey and George, 2007) used in open-source applications like GMSH (Geuzaine and Remacle, 2009), our algorithm has a very simple, physically-motivated logic, straightforward to implement regardless of the domain convexity, and (unlike other methods) it gives us strict control over the number N_{vfr} of mesh nodes. This latter point is the primary reason for creating the meshing algorithm, as our boundary-integral code was optimized by memory allocation for a pre-calculated number of nodes. The implementation of an adaptive version (allowing for variable, prescribed node density) of the algorithm would

be nearly as simple. Although our meshing method is not as fast as some available open-source tools (Geuzaine and Remacle, 2009), it still provides sufficient mesh quality (see Figure 7.2) and is fast enough not to slow down appreciably the whole simulation of the drop dynamics (see Appendix B). An even faster, but still extremely simple MF meshing method (with the number of mesh nodes allowed to slightly fluctuate near the target N_{vfr}) is also described in Appendix B.

Figure 7.2 shows an example of meshing for a complex channel geometry with $N_{vfr} = 800$ mesh nodes in the front or back panel of the MF. This reduced number of nodes was chosen to improve visualization; for simulations, we use more refined meshes with $N_{vfr} = 4K - 8K$ (in contrast to $N_{vfr} \sim 16K$ for the whole channel shown in Figure 7.2(a)). The proof-of-concept geometry in Figure 7.2 was chosen to demonstrate the performance of the meshing algorithm for geometries with lack of symmetry, as well as the presence of sharp and obtuse corners. As can be seen in Figure 7.2, the meshing algorithm works well even for such complex geometries.

The internal triangular mesh nodes are used to collocate the coupled integral equations (8.1) and (8.2) for the front/back MF panels. However, to avoid difficulties, the boundary mesh nodes, i.e., those that lie on the ridges between front/back and side panels of S_∞, are excluded from collocation and the solution. The reason is that the solution $\mathbf{q}(\mathbf{y})$ is not smooth across the ridges. Instead, for every mesh triangle touching the ridge in one or two vertices, the triangle center of mass is used as a collocation point. Accordingly, the contribution of such a triangle to the surface integral in (7.12) is approximated as the integrand value at the triangle center times the triangle area ΔS_i. For any strictly internal triangle, the integrand average over the triangle vertices times ΔS_i is used instead.

The singular and near-singular behavior of the integrands in the drop-surface contributions (i.e., over S_d) was alleviated in a standard way (Loewenberg and Hinch, 1996) by subtracting $\mathbf{u}(\mathbf{x}^*)$ from $\mathbf{u}(\mathbf{x})$ in (8.1) and (8.2), and subtracting $\kappa(\mathbf{x}^*)$ from $\kappa(\mathbf{x})$ in (7.10), where $\mathbf{x}^*$ is the mesh node on S_d that is nearest to the observation point $\mathbf{y}$. This subtraction

does not completely eliminate the near-singular behavior of the double-layer integrand in (8.2), when $\mathbf{y}$ is slightly off the integration surface S_d, but it was sufficient in the present simulations. An unstructured, curvature-adaptive triangulation is used to discretize the drop surface, with a standard trapezoidal rule to compute the regularized boundary-integral contributions in (8.1)-(7.10) and triangle vertices (i.e., mesh nodes) as collocation points. At $t = 0$, the initial spherical shape is triangulated starting from either a regular icosahedron or dodecahedron followed by a series of refinements (e.g., Zinchenko et al. (1997)). For the simulations in this chapter, we typically used 8640 triangular elements for the drop triangulation. For simulations involving the geometry shown in Figure 7.2(a), the total number of channel collocation points ranges from 65K (for low channel depths) to 130K (for deep channels), with 32K points for the front and back panels and $33K - 98K$ points on the side panels (versus $\sim 6K - 18K$ on the MF side panels). Note that the number of effective collocation points in the channel is effectively half of these values due to the symmetry of the problem with respect to the $z = 0$ plane.

The discretized forms of the second-kind integral equations (8.1) and (8.2) are solved at each time step for $\mathbf{u}$ and $\mathbf{q}$ by biconjugate-gradient iterations; the solution for the surface velocity $\mathbf{u}$ is used to advance the drop shape. As in Navarro et al. (2020) (and detailed in Zinchenko and Davis (2013)), the drop mesh quality is maintained in the dynamical simulation by a combination of passive mesh stabilization, active mesh restructuring by minimization of a potential 'mesh energy', and node reconnection by edge swapping.

7.4 Benchmark case: straight square channels

A simple benchmark case to compare/validate our numerical solver is the motion of a single droplet in an infinitely-long straight channel with a square cross-section. This problem has been recently investigated by Wang and Dimitrakopoulos (2012) using a Spectral Boundary-Element (SBE) method and by Horwitz et al. (2014) using a Lattice-Boltzmann (LB) scheme. For this problem, our method becomes simpler in the sense

that we are not required to solve for the undisturbed flow $\mathbf{u}^{\infty}$, as the latter is given by equations (7.5) and (7.6). Figure 7.3(a) shows examples of cases of droplets moving through a straight channel with rectangular cross-section.

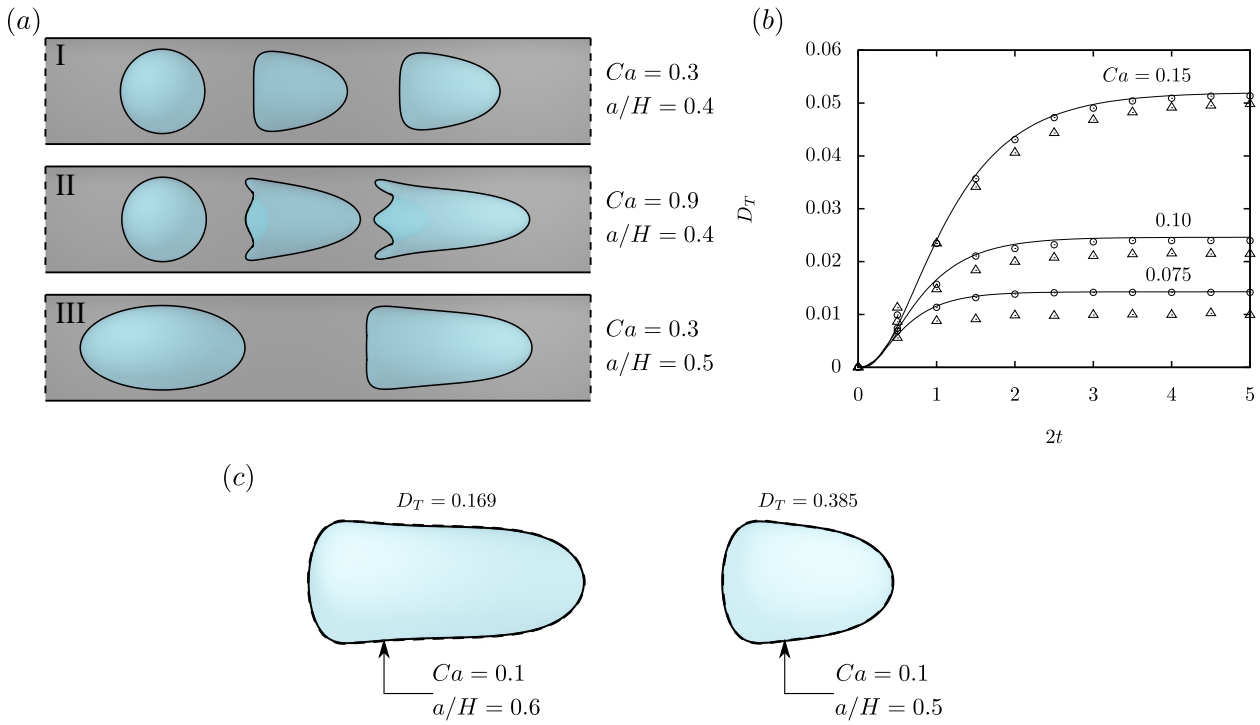

Figure 7.3: Numerical results for droplets going through a straight channel with a square cross-section. Figure (a) shows our results for $\lambda = 1$ and different values for Ca and drop radius a. Figure (b) shows our results (continuous lines) for the Taylor deformation parameter for a droplet with $a = 0.4H$, $\lambda = 2.04$ and different values of capillary numbers, compared with the results obtained by Wang and Dimitrakopoulos (2012) ($\circ$) and Horwitz et al. (2014) ($\triangle$). Figure (c) shows comparison between our simulations (solid contours) and the results by Wang and Dimitrakopoulos (2012) (dashed contours) for the steady shapes of tightly-squeezing droplets with $\lambda = 2.04$.

Depending on the values of physical and geometric parameters, the droplet can either reach a steady configuration with a steady-state translation velocity (e.g., result I in Figure 7.3(a)), or form tails that can eventually pinch off and break up, producing satellite droplets (e.g., result II in Figure 7.3(a)). This last situation happens for more deformable droplets (i.e., high Ca, larger droplets, and high viscosity ratios). The four-tail structure observed in Figure 7.3(a)) II and the formation of satellite droplets has been recently explored experimentally by Wang et al. (2021).

Moreover, in many applications and experiments, such as those in (Wang et al., 2021), the droplet volume is such that the equivalent spherical droplet would not fit in the channel. However, it is also of our interest to investigate the motion of such large droplets in channels, which can be done by using an artificial initial condition where the droplet starts as an ellipsoid of the same corresponding volume, as shown in Figure 7.3(a) III.

We now compare the results for the transient Taylor deformation parameter $D_T(t)$ of the droplet from our straight-channel simulations to those in (Wang and Dimitrakopoulos, 2012) and (Horwitz et al., 2014). The results in (Horwitz et al., 2014) were obtained for $Re = 2$ by the lattice-Boltzmann method. The comparison for the Taylor deformation parameter between the three different numerical schemes is shown in Figure 7.3(b). Our results closely match those obtained by the SBE method in (Wang and Dimitrakopoulos, 2012), while the LB results show smaller deformations. Note that, as indicated by other simulations for droplets with surfactants (so not quantitatively comparable) in square channels Luo et al. (2018, 2019), results for $Re < 5$ are minimally affected by the Reynolds number, suggesting that the discrepancies from the Lattice-Boltzmann simulations observed in Figure 7.3(b) come from numerical inaccuracy of the LB simulations for low Reynolds/capillary numbers rather than from inertia. Furthermore, we have also compared our method to more critical cases investigated in Wang and Dimitrakopoulos (2012) for tightly-squeezing droplets; this comparison is shown in Figure 7.3(c), with excellent agreement between the drop steady shapes. For the case of $Ca = 0.1$ and $a/H = 0.6$, we can also compare the drop steady-state average velocity, defined as

$$\mathbf{U}_d^{ss} = \lim_{t\to\infty} \mathbf{U}_d = \lim_{t\to\infty} \frac{1}{V} \int_{V_d} \mathbf{u}\, dV, \tag{7.13}$$

which is ≈ 1.42 in our simulations and ≈ 1.41 in Wang and Dimitrakopoulos (2012). A significant advantage of the present algorithm over the prior simulations (Wang and Dimitrakopoulos, 2012; Horwitz et al., 2014) is that it is not limited to simple, straight channel geometries, as shown below.

7.5 Drop motion in complex microfluidic channels

In complex microfluidic channels, the bulk flow rates of different branches can be determined individually by performing a circuit analysis in the channel (Kirby, 2010). Hence, when designing drop-microfluidic applications, it is of utmost importance to analyze the drop dynamics within the individual complex geometries and junctions that appear in different parts of the network. To this end, the moving-frame, boundary-integral algorithm developed in this work allows us to simulate drop motion in many types of complex geometries, including geometries that often appear in microfluidic channels, such as T-junctions, Y-junctions, U-turns and straight sections. To demonstrate the ability of the code to handle such complex geometries, Figure 7.4 shows examples of numerical results from simulations for a droplet moving through three distinct complex geometries.

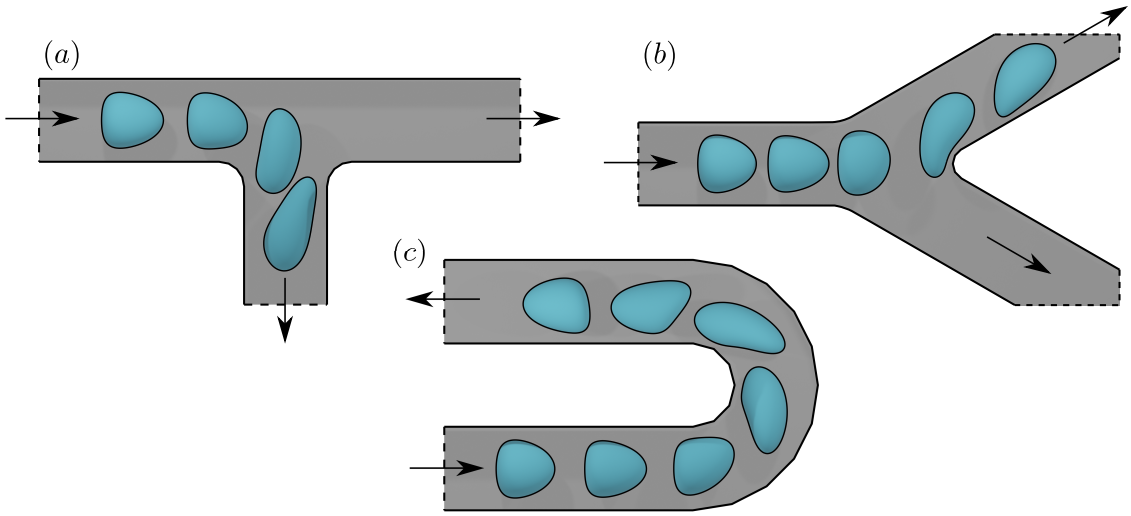

Figure 7.4: Sample numerical simulations of a deformable drop moving through different geometries using the moving-frame, boundary-integral method developed in this work; (a), (b), and (c) show the motion of a droplet in a T-junction, a Y-shaped bifurcation, and a U-turn, respectively. The arrows show the direction of the flow.

To demonstrate that our numerical method can be used to describe the motion of drops in flat-walled channels of complex geometries, we first focus on the problem of a drop moving through the bifurcating channel with the proof-of-concept geometry shown in Figure 7.2. The geometry of the problem, as well as the direction of the inlet and outlet

flow rates Q, Q_1, and Q_2, are shown in Figure 7.5, which also shows numerical results for the motion of a droplet in such channel. Note that $|Q| = |Q_1| + |Q_2|$ due to mass conservation and constant density. For the simulation of the initially spherical droplet with radius a in the channel shown in Figure 7.5(a), we set $|Q_1| = 0.7\,|Q|$. As Q_1 is much larger than Q_2, the drop goes through the upper branch of the channel. One of the most notable features about the drop motion is the formation of a two-tail structure at the back of the drop. This double-tail formation, which can lead to drop breakup and formation of satellite droplets, is produced by the hydrodynamic interaction between the drop and channel boundaries. Namely, the portion of the droplet located near the center of the channel moves with a velocity substantially higher than the portions close to the boundaries, which tend to move slowly because of the non-slip boundary condition at the channel boundary. It is noted that, for the same channel geometry, this particular tail geometry would not be observed in infinite-depth simulations, as these tails are formed by the interaction with the front and back panels, which are absent in such simulations. However, tail formations in the xy plane could still be observed due to interaction of the droplet with the other boundaries (Navarro et al., 2020).

We can further explore the motion of droplets in this geometry by changing the parameter values, such as the dimensionless depth of the channel W/H, ratio between flow rates, capillary number, viscosity ratio, initial position, and drop size. Figure 7.6 shows numerical results for drop motion in our proof-of-concept geometry and distinct geometrical and physical configurations. In Figure 7.6(a), we use the same flow-rate ratios and initial drop position used in Figure 7.5. However, the capillary number is set to $Ca = 0.267$ and the aspect ratio is given by $W/H = 1$. In this case, the two tails observed in Figure 7.5 for $W/H = 0.34$ are no longer present, and we instead observe the formation of a short double-tail structure in the xy plane, caused by the interaction of the drop with the boundaries of the upper branch of the channel.

As we are considering a bifurcating channel, one important parameter to be measured

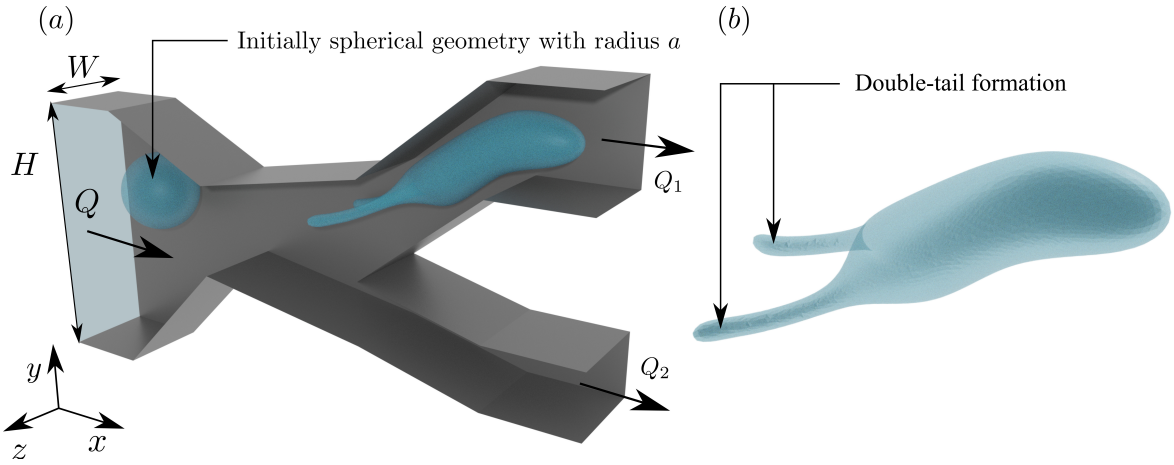

Figure 7.5: Drop motion through our proof-of-concept bifurcating channel. Figure (a) shows the geometrical parameters of the problem; it also includes the initial and final configurations of the drop obtained via numerical simulation for $W/H = 0.34$, $2a/H = 0.3$, $Ca = 0.3$, $\lambda = 1$, and $|Q_1| = 0.7\,|Q|$. The closeup in (b) shows the final configuration of the drop, highlighting the double-tail formation caused by hydrodynamic interaction between the drop and the channel walls.

is the critical value of Q_1 (or, alternatively, Q_2) for which the droplet will pass through the bottom branch instead of breaking up. Figure 7.6(b) shows the drop motion for the same physical and geometrical parameters as 7.6(a), for $|Q_1| = 0.1\,|Q|$. As shown by the results, this situation leads to the breakup of the droplet caused by its collision with the sharp corner. In fact, even simulations for $|Q_2| = 0.95\,|Q|$ resulted in a similar breakup scenario for a droplet with the same starting position. Hence, in the present geometry, even a very high bottom-to-top flow-rate ratio is not enough to make the droplet pass through the bottom branch. This hindrance is partially caused by the presence of a sharp corner and can be mitigated by beveling the corner. Figure 7.6(c) shows that, for a smoothed corner, subdivided in four smaller segments, the droplet is goes through the bottom branch of the channel for $|Q_2| = 0.9\,|Q|$.

However, even with the beveled corner, the flow-rate conditions for the droplet to go through the top branch are not symmetric, in contrast to results for regular geometries such as T bifurcations with the same branch heights (Navarro et al., 2020). This asymmetry can be seen in Figure 7.6(d), which shows the drop moving through the channel with

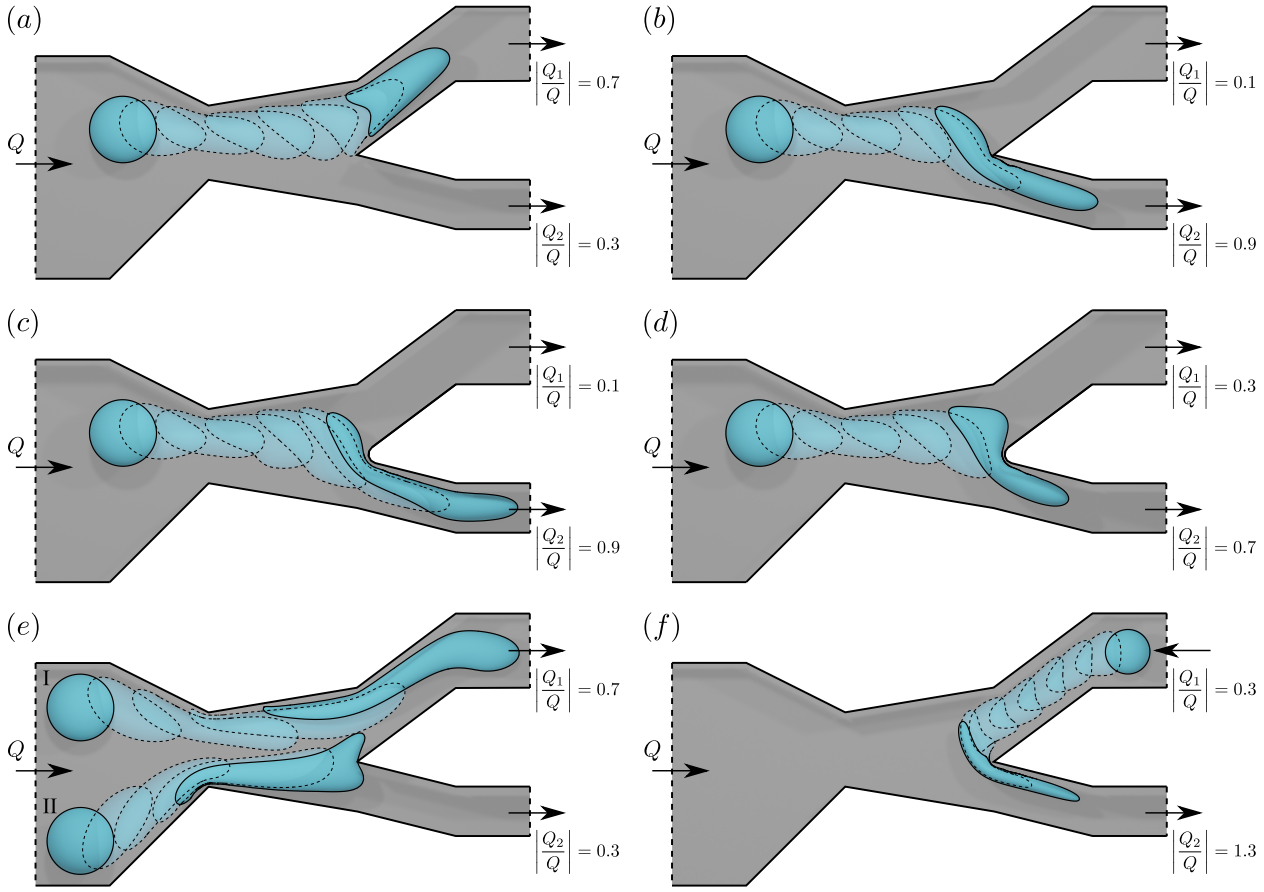

Figure 7.6: Sample simulations of droplets moving through our proof-of-concept geometry with $\lambda = 1$, $2a/H = 0.3$ and $(a-e)$ $Ca = 0.267$, $W/H = 1$ or (f) $Ca = 0.281$, $W/H = 0.5$. The flow-rate ratio for each simulation is indicated in the figure panel for that case. The starting and ending configurations of the droplets are represented by the solid lines and opaque shapes, whereas the intermediate configurations are represented by dashed contours and transparent shapes. The droplets in $(a-d)$ have the same starting position. The sharp corner is replaced by the smoothed geometries in (c) and (d) to avoid problems with drop collision. Figure (e) displays the motion of a drop with two distinct starting positions for the same flow-rate ratio, showing the effect of initial position on drop motion.

$|Q_2| = 0.7\,|Q|$. In contrast to the simulation for $|Q_1| = 0.7\,|Q|$, for which the droplet simply goes through the upper branch, the drop in 7.6(d) collides with the corner, leading to a breakup condition. The reason behind this behavior is a combination of the general asymmetric geometry of the channel, the fact that the bottom branch is smaller than the top one, and the drop's initial position. In fact, for this same starting configuration in 7.6(a) and 7.6(b), we see that there is little difference in the drop motion up to the point where

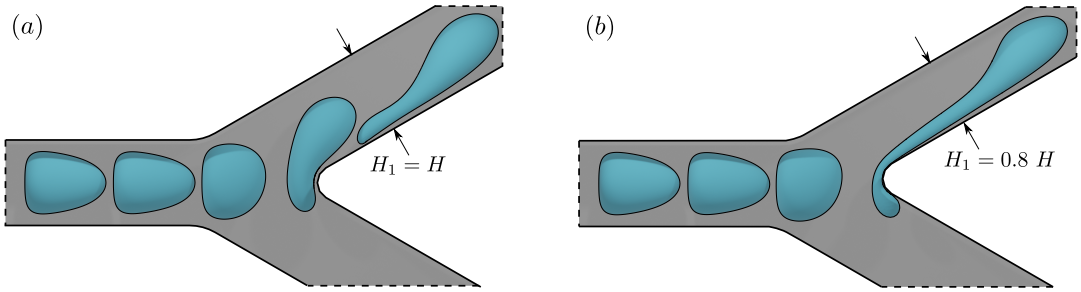

Figure 7.7: Consecutive shapes of a droplet moving through a smoothed Y-shaped channel for $Ca = 0.3$, $\lambda = 1$, $W/H = 1$, $2a/H = 0.8$, and $|Q_1| = 0.675\ |Q|$ for (a) $H_1/H = 1.0$ and (b) $H_1/H = 0.8$. Both inlet and lower branches have the height H. The drop-sorting symmetry usually found on Y-shaped bifurcations is broken in (b) due to different branch heights as, for the same flow-rate ratios, the droplet tends to break instead of going through the upper branch of the channel.

the droplet reaches the middle portion of the channel, where it starts to turn towards the bottom channel in Figure 7.6(b). However, it is possible to make the droplet go through the bottom channel more easily by changing its starting position.

To illustrate the impact of branch size in drop partitioning, we recall that, as previously mentioned, in regular geometries such as T- and Y-shaped junctions, the partitioning for moderate capillary numbers occurs in an almost symmetrical way with respect to the flow-rate ratios (even for non-symmetrical geometries such as T-junctions), as seen in Navarro et al. (2020). However, this symmetry can be broken if the channel branches are not of the same size. To demonstrate this symmetry breaking, Figure 7.7 shows numerical results from simulations of a droplet moving through (a) a regular Y-junction and (b) an irregular Y-junction with top branch size $H_1/H = 0.8$. For the same flow-rate ratios and physical parameters, the droplet in (a) goes through the upper branch of the channel, whereas the droplet in (b) breaks up before branching, indicating that the smaller size of the top branch results in a larger threshold flow rate for which the droplet will completely move through the upper branch.

Moreover, we also observe that the drop behavior is strongly dependent on the initial position of the drop. This behavior is expected when portions of the channel are much larger than the droplet, as observed in Navarro et al. (2021). Figure 7.6(e) shows the

motion of a drop in the channel with the same configuration and physical parameters from 7.6(a) at two distinct starting positions, represented in the figure by I and II. We see that, even though the flow rate through the top branch of the channel is much higher than through the bottom one, droplets starting near the bottom collide with the corner instead of going through the top branch. In fact, for this configuration, even a droplet starting at the center of the channel will collide with the corner instead of going through the top branch. Moreover, it is also noted that droplets moving near the channel walls undergo a larger deformation.

Instead of a bifurcating flow rate, we can also consider the case where we have two different inlet flow rates and one single outlet one. Figure 7.6(f) shows a simulation for $W/H = 0.5$ and $Ca = 0.281$ where the top flow rate Q_1 is now an inlet flow rate with magnitude $|Q_1| = 0.3\,|Q|$. In this situation, the droplet tends to exit through the bottom channel. It is noted that, because of the abruptness of the trajectory caused by the presence of the sharp corner, the droplet undergoes a rapid large deformation.

Besides geometrical parameters, the changes in physical parameters such as capillary number and viscosity ratio substantially affect drop dynamics. Hence, in the last portion of this section, we show some of the effects of viscosity ratio an capillary number for the same initial condition used in Figure 7.6(a). These results are shown in Figure 7.8.

The results in Figure 7.8(a) indicate that, like the results in (Navarro et al., 2020) for T-shaped bifurcations, besides the capillary number increasing drop deformation, it also affects drop sorting. However, as we are not dealing with symmetric configurations/geometries, the geometric parameters of the problem also play a significant role in how Ca influences the dynamics. Namely, in (Navarro et al., 2020) for channels of infinite depth, the increase of capillary number increased the breakup range of flow-rate configurations. In contrast, in our results for channels of finite depth, we see that the higher capillary number combined with a more upwards initial position of the droplet resulted in a smaller interaction between the droplet and the sharp corner that may potentially

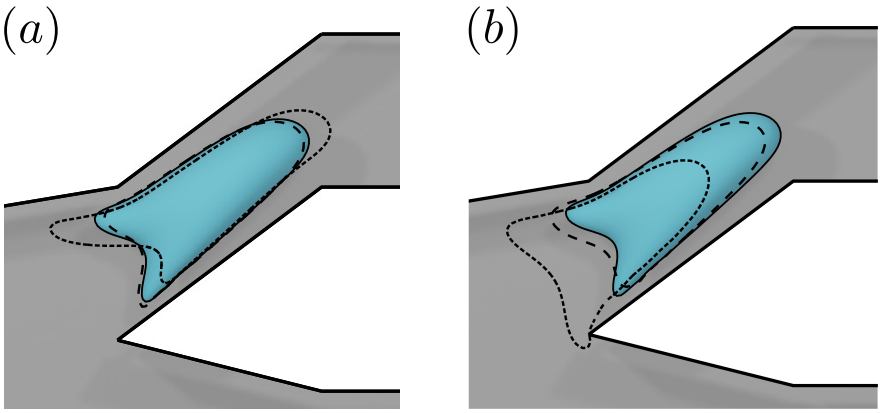

Figure 7.8: Numerical simulations of droplets moving through our proof-of-concept geometry with the same initial conditions and flow rates as Figure 7.6(a) and (a) $\lambda = 1$ and $Ca = 0.239$ (long-dashed contour), 0.267 (solid contour and shape), and 0.477 (short-dashed contour) and (b) $Ca = 0.267$ and $\lambda = 0.5$ (short-dashed contour), 1 (solid contour and shape), and 2 (long-dashed contour).

lead to breakup. In contrast, for viscosity ratio (Figure 7.8(b)), we observe a similar trend to the results in Navarro et al. (2020), where a smaller viscosity ratio $\lambda = 0.5$ results in a direct collision between the drop lower tail and the sharp corner, which leads to breakup.

7.6 Infinite-depth limit

An important question concerning finite-depth simulations is how well the results match the ones obtained by infinite-depth simulations, such as those in Navarro et al. (2020), in the limit $W/H_i \gg 1$, and at what channel aspect ratios W/H_i such an approximation is valid. With this knowledge, it would be beneficial to use the infinite-depth formulation in the appropriate range, since it is easier to implement and requires substantially less computational times due to a smaller number of boundary elements in the absence of front and back channel/moving-frame walls.

In the infinite-depth simulations, the linear flow rates Q_i^P (i.e., flow rate per unit depth) through each input/output channel branch are specified, with the corresponding planar Poiseuille flow as the input/output boundary condition for the fluid velocity (Navarro et al., 2020). Instead, in the present finite-depth channel simulations, we specify volumetric

flow rates Q_i^B through each inlet/outlet branch and use the corresponding Boussinesq solution for the flow in a rectangular duct as a boundary condition in the inlet/outlet. The sum of Q_i^B, as well as Q_i^P, over all input/output branches must total to zero for mass conservation and the solutions to exist.

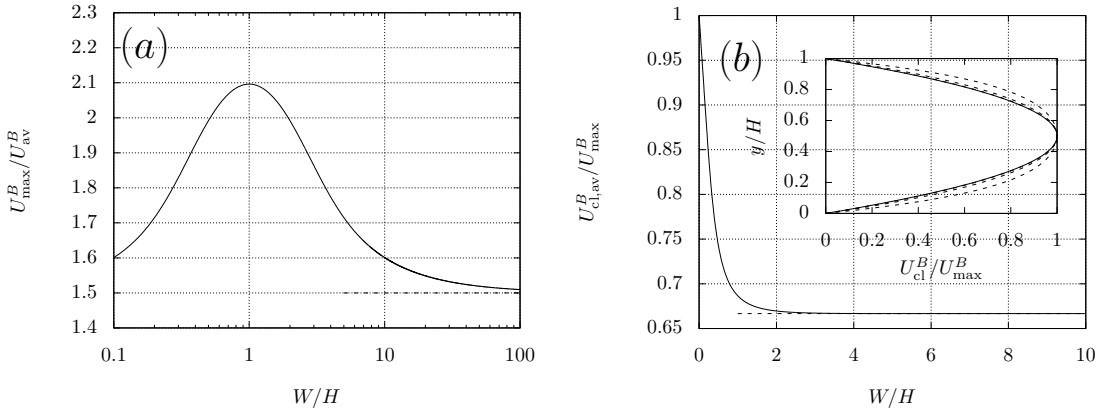

Figure 7.9: Behavior of inlet flow, given by Boussinesq's solution, with increasing aspect ratio. Figure (a) shows the slow convergence of the maximum velocity when keeping the average velocity constant. The dashed line in (a) represents the Poiseuille limit, where the ratio between the maximum and average entrance velocity is 1.5. Figure (b) shows the limiting behavior of the average centerplane velocity versus aspect ratio; the dashed straight line represents the Poiseuille limit of 2/3. The inset in (b) shows different centerplane velocity profiles for (from out to in) $W/H = 0.5$, 1.0, and 2.0, represented by the dashed curves; the solid curve represents the Poiseuille profile, which essentially coincides with the results for $W/H = 2.0$.

The most straightforward way, legitimate for channels of arbitrary geometry, to compare the finite- and infinite-depth simulations would be to match Q_i^B/W with Q_i^P (i.e., to match the average velocities in each input/output branch between the two simulations). In this manner, however, the infinite-depth limit in the drop behavior is approached very slowly, in the sense that a good agreement between the finite- and infinite-depth simulations for channels with arbitrary geometries would only occur for very large values of W/H. The reason is that, for a drop moving with its center in the channel midplane $z = 0$ (the case considered herein), the drop behavior is more affected by the Boussinesq input/output flow near $z = 0$ than by the average input/output velocities in the ducts, as the latter are reduced by the no-slip condition on the front and back panels and slow flow

near the corners. In Figure 7.9a, the ratio U^B_{max}/U^B_{av} between the maximum and average Boussinesq flow velocities in a generic rectangular duct is shown as a function of the duct depth-to-height aspect ratio W/H; indeed it requires at least $W/H > \mathcal{O}(100)$ to approach the theoretical limit of 1.5 for U_{max}/U_{av}, due to slowly-decaying end effects at $z \approx \pm W/2$. To rectify this situation, we consider the channel midplane, $z = 0$, which is parallel to the front and back panels and midway between them. Figure 7.9b shows the effect of the duct aspect ratio W/H on the Boussinesq velocity averaged only over the centerline $0 \leqslant y \leqslant H$, $z = 0$, scaled with U^B_{max} for this W/H. The inset in Figure 7.9(b) shows the corresponding Boussinesq velocity distribution along this centerline, also normalized by U^B_{max} . In contrast to Figure 7.9(a), the scaled centerline Boussinesq velocity converges much faster to its Poiseuille limit (i.e., $W/H \to \infty$), with good agreement observed for $W/H > 2$. On these grounds, to compare the finite- and infinite-depth channel simulations, it would be much better to match the maximum velocities $U^B_{max,i}$ with $U^P_{max,i}$ in every input/output branch i, i.e., to set

$$Q^P_i = \frac{2}{3}\frac{U^B_{max,i}}{U^B_{av,i}}\frac{Q^B_i}{W} \tag{7.14}$$

as the mapping between the linear and volumetric flow rates in the two simulations. For specific channel geometries, where all input/output branches have the same height $H_i = H$, rule (7.14) results in the same split ratios for the flow rates in both finite- and infinite-depth simulations. However, since the ratio $U^B_{max,i}/U^B_{av,i}$ depends on the panel aspect ratio W/H_i (Figure 7.9(a)), rule (7.14) has to be modified to account for the more general geometries, where the branch heights can be different from each other, as the infinite-depth flow rates prescribed in (7.14) may break mass continuity; this situation is discussed later.

To illustrate the application of rule (7.14), Figure 7.10 shows a direct comparison between a finite-depth simulation for drop motion in a T-junction with equal branch heights H_i and its infinite depth counterpart, obtained by the algorithm from Navarro et al. (2020). Since both finite- and infinite-depth simulations have matching U_{max} at the

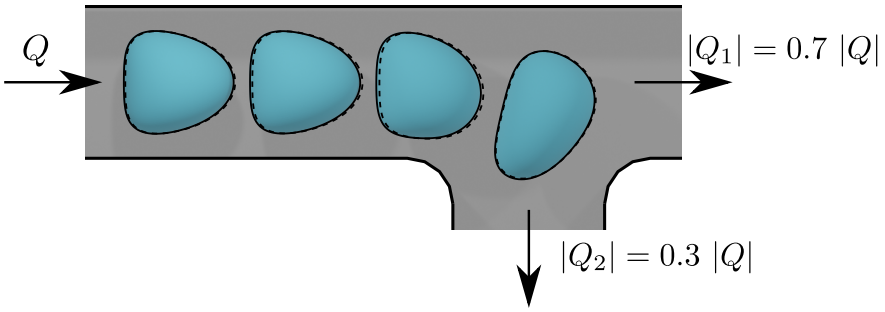

Figure 7.10: Direct comparison between drop shapes from finite- and infinite-depth simulations in a T-shaped junction for $2a/H = 0.7$, $\lambda = 1$, $Ca^* = 0.561$, and $|Q_1| = 0.7\ |Q|$. The solid lines represent the drop contours for $W/H = 2$, whereas the dashed lines are the shapes at the same times for the limit $W/H \to \infty$.

entrance, we use a modified capillary number $Ca^* = \mu U_{max}/\sigma = 0.561$ and time scale H/U_{max} for non-dimensionalization in both simulations. In the results shown in Figure 7.10, the drop starts with the same initial spherical shape and location near the inlet. Even for a moderate aspect ratio of $W/H = 2$, there is excellent agreement between the finite-depth results (represented by the filled solid contours) and the infinite-depth ones (dashed contours).

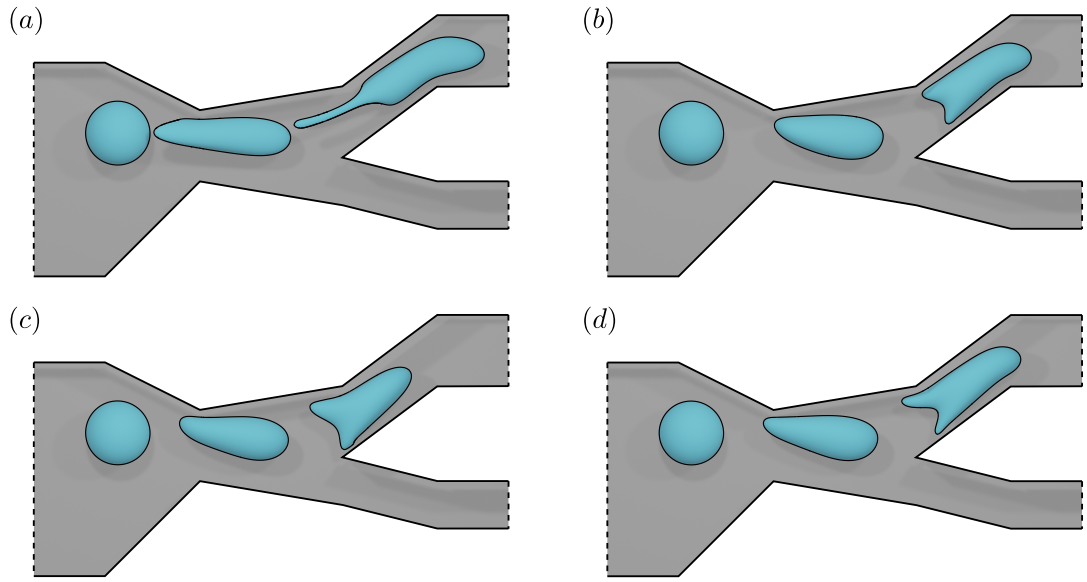

Figure 7.11: Motion of a single drop with initial radius $2a/H = 0.3$ in our proof-of-concept channel for different aspect ratios (a) $W/H = 0.34$, (b) $W/H = 0.5$, (c) $W/H = 3.0$, and (d) $W/H = \infty$, for $Ca^* = 0.561$, $\lambda = 1.0$, and a fixed $|Q_1| = 0.7\ |Q|$.

For a general channel geometry with unequal branch heights H_i, one way of mapping

between the finite-depth and infinite-depth simulations would be to match U^B_{max} and U^P_{max} by the rule (7.14) in only one, arbitrarily-chosen branch with $H_i = H$ (e.g., the entrance, in what follows) and forcefully keep the split ratios Q^P_j/Q^P in the other input/output branches j the same as Q^B_j/Q^B to preserve mass conservation for the infinite-depth channel setup. Figure 7.11 shows the corresponding results for a droplet moving in the proof-of-concept geometry shown in Figure 7.5 for different values of the aspect ratio. The drop snapshots in panels $7.11(b-d)$ are at the same non-dimensional times $t^* = tU_{max}/H$. As previously pointed out, as W increases, the long double-tail structure highlighted in Figure 7.5 and seen from the side in Figure 7.11 diminishes and eventually gives place to two smaller tails in the xy plane, indicating a decrease in the interaction between the drop and front and back panels when $W \gg a$. However, in contrast to the simulations for a regular T-junction, there is a notable disagreement between drop motion for a moderate aspect ratio $W/H = 3.0$ and $W/H = \infty$, even though the channel depth is much larger than the drop diameter. Moreover, in Figure $7.11(c)$, besides a slower drop motion, we also observe a distinct deformation in the bottom tail caused by a stronger interaction between the droplet and the corner. This difference occurs because of the changes in maximum velocities in the top and bottom branches, which lead to substantially different flow configurations near the midplane $z = 0$.

The results in Figure 7.11 indicate that, for general channel geometries, the limit $W \to \infty$ while keeping the same flow-rate split ratio is only approached for very high values of W/H. To better understand the reason behind such a slow approach for irregular channel geometries, we first consider a much simpler problem of a droplet going through a constriction. Figure 7.12 shows results from both finite- and infinite-depth simulations of a droplet moving through a constriction for the same maximum velocity at the entrance and $Ca^* = 0.561$. As expected, in the left portion of the channel, there is an excellent match of shapes and drop positions between the infinite- and finite-depth simulations, as can be seen qualitatively in Figure $7.12(a)$ and quantitatively in Figure $7.12(b)$. The latter shows

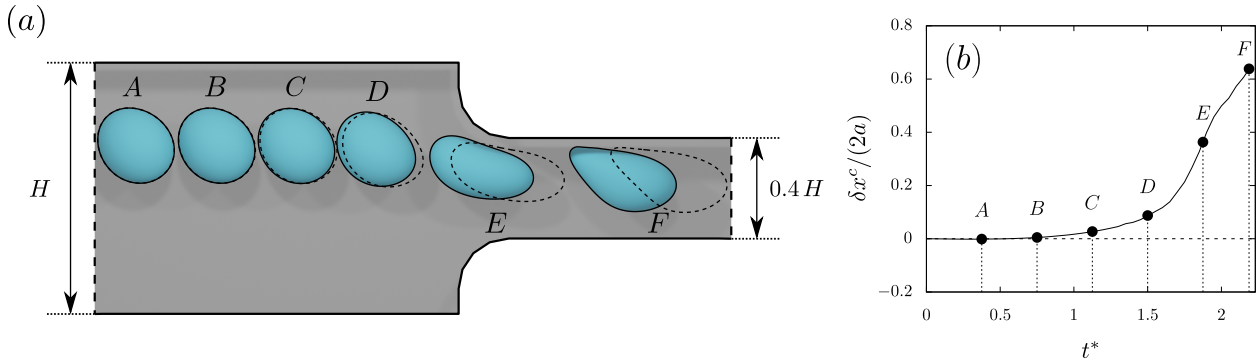

Figure 7.12: Numerical comparison between finite- and infinite-depth simulations of a droplet moving through a narrow constriction for $Ca^* = 0.561$, $\lambda = 1$, and $2a = 0.3$ H. The figures show (a) different drop configurations from finite-depth simulations (solid shapes with solid contours) for $W/H = 3$ and infinite-depth simulations (dashed contours) and (b) the x component of the center-to-center distance δx^c between the droplets.

the first component (i.e., along the channel) of the center-to-center distance δx^c between the droplets in the infinite-depth and finite-depth simulations. The droplet center was calculated as a surface centroid. However, in the right portion of the channel, the droplet in the infinite-depth simulation moves substantially faster than its finite-depth counterpart, presenting displacements of the same order of magnitude as the drop diameter.

The difference in drop velocity between finite- and infinite-depth simulations can be understood by analyzing the ratio $U^B_{max,c}/U^P_{max,c}$ between the maximum fluid velocity at the constriction outlet for the finite- and infinite-depth cases. For the case where the maximum fluid velocity $U^B_{max} = U^P_{max}$ at the inlet is kept the same, this ratio can be expressed as a function of the inlet aspect ratio W/H and the throat height ratio H_c/H. This relationship, which is non-monotonic, is shown in Figure 7.13(b). We see that the maximum outlet flow velocity for $W/H = 3.0$ is about 10% slower than the infinite-depth case, which explains the faster droplet in Figure 7.12. The non-monotonicity of $U^B_{max,c}/U^P_{max,c}$ can qualitatively explain the behavior of even large, tightly-squeezing droplets going through the constriction for different channel aspect ratios W/H (Figure 7.13). As an example, Figure 7.13(c) shows results for the average velocity (defined as in Equation (7.13)) of tightly-squeezing droplets of $2a/H = 0.6$ going through the channel

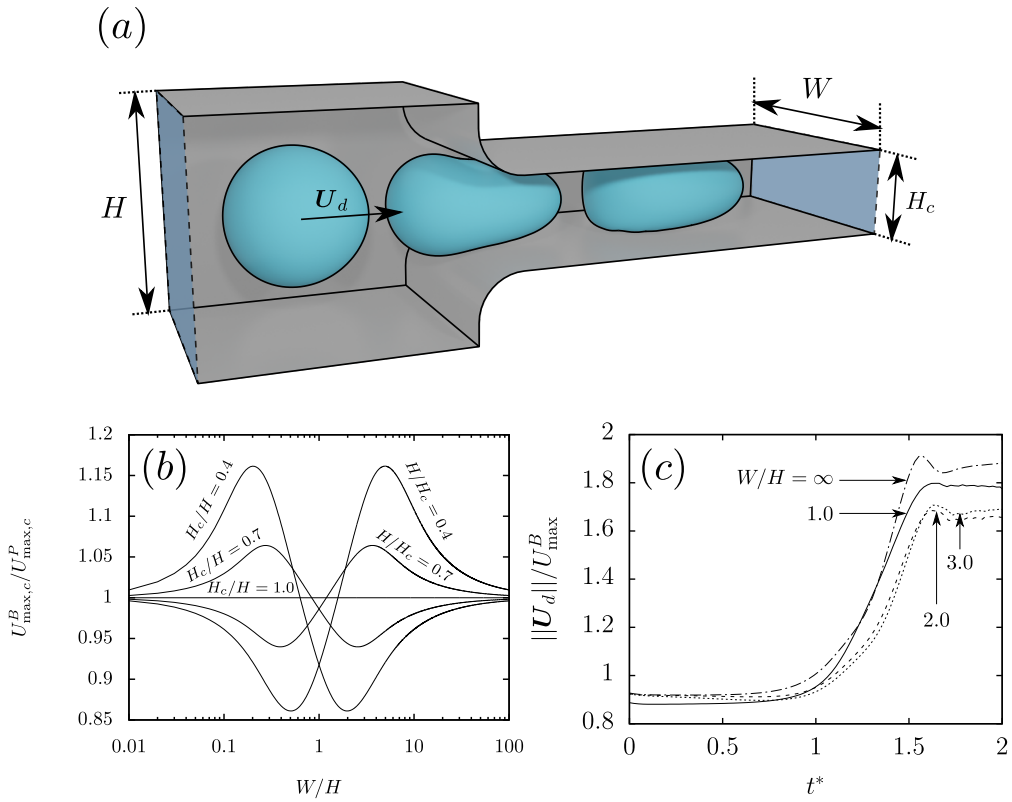

Figure 7.13: (a) Numerical results for a tightly-squeezing droplet going through the constriction geometry introduced in Figure 7.12 for $2a/H = 0.6$, $W/H = 1$, $H_c/H = 0.4$, $\lambda = 1$ and $Ca^* = 0.1$, (b) the ratio between the outlet Boussinesq and Poiseuille maximum velocities versus aspect ratio W/H for different throat height ratios H_c/H, and (c) the average droplet velocity versus time as the droplet goes through the constriction for $Ca^* = 0.1$, $\lambda = 1$, $H_c/H = 0.4$, and $W/H = 1$ (solid curve, represented in (a)), 2 (long-dashed curve), 3 (short-dashed curve), and ∞ (dot-dashed curve).

constriction for several aspect ratios. From the results, there is a clear correlation between the drop velocities inside the constriction (i.e., larger times in Figure 7.13(c)) and the results for the maximum outlet velocities in Figure 7.13(b) for $H_c/H = 0.4$. One interesting case is the one for $W/H = 1.0$. In this case, the droplet starts moving slower than in the cases with higher aspect ratios because of a strong interaction with the front and back panels. However, as the droplet approaches the constriction, it reaches a higher velocity than in $W/H = 2$ and 3 (although still slower than the infinite-depth case).

For complex bifurcating channels such as in Figure 7.11, besides the difference in overall velocity, we also observe a substantial deviation between drop shapes and splitting

in finite- vs infinite-depth channels. The main reason behind such discrepancy is the inability to use the rule (7.14) for geometries with different branch heights, resulting in different fluid velocities at each inlet/outlet, affecting the general flow configuration. Thus, for a better comparison between finite- and infinite-depth simulations for more general channel geometries, we need to choose appropriate flow rates such that the infinite-depth fluid flow has a similar behavior to the flow near the midplane $x = 0$ from the finite-depth simulations. As discussed above in this section, for general geometries, the flow rates in equation (7.14) do not generally satisfy mass continuity, except for very specific cases. A simple way to adapt expression (7.14) for general geometries is to pick the set of flow rates $\tilde{Q}_i^P$ for an infinite-depth simulation that is closest to Q_i^P predicted by (7.14) but satisfying mass conservation. Namely, the set of $\tilde{Q}_i^P$ is required to minimize $\sum_i (\tilde{Q}_i^P - Q_i^P)^2$ constrained to $\sum_i \tilde{Q}_i^P = 0$. This procedure yields

$$\tilde{Q}_i^P = Q_i^P - \frac{1}{n} \sum_{k=1}^{n} Q_k^P, \tag{7.15}$$

where n is the total number of inlet/outlet branches.

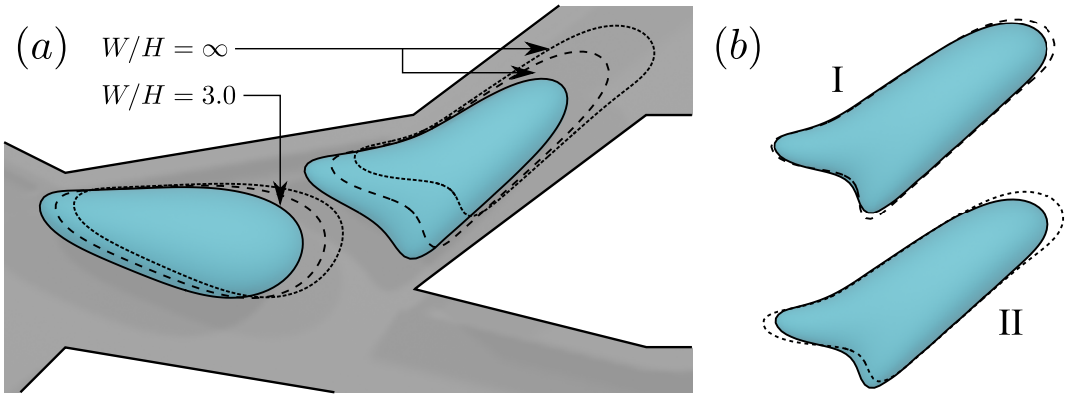

Figure 7.14: Comparison between drop shapes from finite- and infinite-depth simulations for $Ca^* = 0.561$, $\lambda = 1.0$, and $|Q_1| = 0.75\,|Q|$. The drop shapes in (a) are compared at the same time. The solid lines represent the drop contours for $W/H = 3$, whereas the short- and long-dashed lines are the shapes at the same times for the limit $W/H \to \infty$ for the direct comparison and using the least-squares flow-rate mapping (7.15), respectively. In (b), a comparison is made between the shapes at the same drop center position (but different times).

To illustrate the application of equation (7.15), Figure 7.14 shows a comparison between

a finite-depth simulation and its equivalent infinite-depth case, with and without the least-squares flow-rate mapping (7.15). The modified Ca^* and non-dimensionalization for this infinite-depth problem is still based on U^B_{max} at the entrance (not $\tilde{U}^P_{max}$). The solid drop contours represent the droplet snapshots in the finite-depth problem ($W/H = 3.0$). The long-dashed lines are for the drop snapshots at the same times as in the equivalent finite-depth simulation with appropriate flow rates obtained by using equation (7.15). The short-dashed contours are for the infinite-depth simulation with exact maximum-velocity matching in the inlet and matching all the split ratios Q^P_j/Q to Q^B_j/Q. Although, as expected, none of the infinite-depth simulations perfectly matches the finite-depth results at the same times, the results from the infinite-depth simulations with flow rates determined by (7.14) and (7.15) present a better agreement compared with the results using matched maximum velocities at the entrance and flow-rate split ratios. Moreover, Figure 7.14(b) shows the comparison between drop shapes at the same x position in the channel. The drop shapes produced by using the least-squares flow-rate mapping (I) also present a better agreement with the finite depth simulations if compared at the same channel positions, in contrast to the alternative mapping (II), which produces a larger upper-tail and larger deformation.

The results shown in Figure 7.14 indicate that, although not perfect, the least-squares flow-rate compatibility condition (7.15) provides an overall better correspondence between the finite- and infinite depth simulations, especially when comparing the evolution of droplet geometry. However, for certain cases, especially near critical conditions, the small discrepancies between drop shape in the finite- and infinite-depth simulations can result in significant changes in drop behavior. To demonstrate this fact, we go back to the results from Figure 7.11, where, for $W/H = 3.0$, we noticed a pronounced deformation in the bottom tail of the droplet due to interaction with the corner. Figure 7.15 shows the comparison between this case with its infinite-depth counterpart using the least-squares flow-rate condition (7.15). Like Figures 7.12(c) and 7.14(b), the comparison

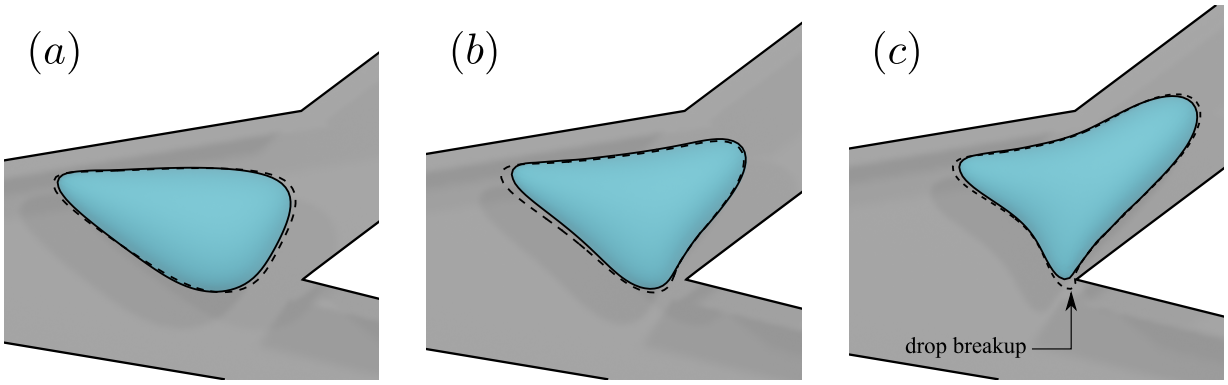

Figure 7.15: Comparison between drop shapes from finite- and infinite-depth simulations for $Ca^* = 0.561$, $\lambda = 1.0$, $W/H = 3$, and $|Q_1| = 0.7\,|Q|$ at the same center $x-$positions (and different times). The solid lines represent the drop contours for the finite-depth simulation, whereas the dashed lines are the shapes at the same time for the limit $W/H \to \infty$. The infinite-depth flow rates were determined by equation (7.15). For these conditions, the drop in the finite-depth simulation goes through the upper branch, whereas its infinite-depth counterpart collides with the corner, which leads to the breakup of the drop.

between shapes is not done at the same time, but at the same drop center position. From the simulation results, we see that both cases present similar drop configurations up to the location in the channel where the tail of the droplet in the infinite-depth channel collides with the sharp corner, leading to drop breakup. Hence, although the infinite-depth simulations described in Navarro et al. (2020) may provide a good approximation for certain cases where $W \gg H$, especially for more uniform geometries, our results indicate that one must be careful when using these simulations for more general channel geometries, as the flow in the channel can be heavily influenced by the presence of the front/back panels for moderate values of channel depth.

7.7 Estimation of inertial effects

So far, all of our results neglected the presence of inertial effects in the fluid, which is often a good approximation for microfluidic applications. However, in some cases, moderate-Reynolds-number conditions can produce changes in drop motion. According to the simulation results reported in (Luo et al., 2018), the influence of inertial effects on drop motion is small for Reynolds numbers $Re < 10$. However, these results were

for a drop moving through a straight channel with rectangular cross section, where the steady-state solution of the Navier-Stokes equations for a single-phase fluid is the same as the Boussinesq solution for Stokes flow. For such cases, the inertial effects appear as a consequence of the transient drop motion. However, for more general geometries, additional inertial effects coming from the different background flows might appear.

To fully account for inertial effects on drop motion, the full Navier-Stokes equations must be solved numerically in the whole domain, including the droplet, as done in previous works for straight and regular geometries (Sarrazin et al., 2006; Carlson et al., 2010; Horwitz et al., 2014). However, to estimate the effect of non-zero Reynolds numbers on the background flow, we instead solve the full set of Navier-Stokes equations numerically for the single-phase, undisturbed flow. Then, following the approach in Navarro et al. (2020), this steady-state solution for the background flow is used as a boundary condition for the Stokes flow on the moving frame to probe the effects of inertia on the drop deformation and motion. While this approach is approximate, it is expected to be rigorous for sufficiently small drops, such that the droplet Reynolds number is small. To this end, we developed a full Navier-Stokes solver for the fluid flow inside complex channels with finite depth in the absence of droplets.

The simple Navier-Stokes solver in Navarro et al. (2020), based on a finite-difference scheme and streamfunction/vorticity formulation, was specific for geometries for geometries such as a T-junction of infinite depth without corner smoothing. In contrast, no such limitations are imposed on the present three-dimensional, in-house solver, based on the meshing techniques from section 7.3 and Appendix B.

The solution algorithm for the single-phase flow is as follows. The Navier-Stokes equations for an incompressible flow,

$$\frac{\partial \mathbf{u}}{\partial t} = -\mathbf{u}\cdot\nabla\mathbf{u} - \frac{1}{Re}\nabla p + \frac{1}{Re}\nabla^2\mathbf{u}, \quad \nabla\cdot\mathbf{u} = 0, \tag{7.16}$$

are made non-dimensional using the channel average entrance velocity and entrance

height as the velocity and length scales, respectively. Accordingly, the Reynolds number in (7.16) is based on these scales.

Let $\mathbf{u}(\mathbf{x}, t_k) \equiv \mathbf{u}_k(\mathbf{x})$ and $p(\mathbf{x}, t_k) \equiv p_k(\mathbf{x})$ at a time moment $t_k = k\Delta t$. Applying a split-time-step scheme, we define an intermediate field $\mathbf{u}^*$, such that

$$\mathbf{u}^* = \mathbf{u}_k + \Delta t \left(-\mathbf{u}_k \cdot \nabla \mathbf{u}_k + \frac{1}{Re} \nabla^2 \mathbf{u}_k \right). \tag{7.17}$$

The velocity field at time t_{k+1} is then given by

$$\mathbf{u}_{k+1} = \mathbf{u}^* - \frac{\Delta t}{Re} \nabla p_k. \tag{7.18}$$

Equation (7.18), together with the zero-divergence constraint for the velocity field results in a Poisson equation for the pressure, given by

$$\nabla^2 p_k = \frac{Re}{\Delta t} \nabla \cdot \mathbf{u}^* \tag{7.19}$$

with Neumann boundary conditions

$$\nabla p_k \cdot \mathbf{n}|_S = \nabla^2 u_k^{\perp}|_S, \tag{7.20}$$

where $u^{\perp} = \mathbf{u} \cdot \mathbf{n}$ denotes the velocity component perpendicular to the boundary. The calculation of the boundary conditions at the auxiliary boundary points (see Appendix C) is made by decomposing $\nabla^2 u^{\perp}|_S$ into tangential and normal parts. The tangential term is then calculated from the boundary conditions, whereas the normal term is approximated by a finite difference and the fact that $\partial u^{\perp}/\partial n|_S = 0$ for all panels.

For the spatial discretization, we use the mesh of triangle vertices for front/back panels of the entire channel (see Section 7.3 and B) naturally extended to 3D along the z direction. Numerically, the spatial derivatives in equations (7.17) and (7.19) are calculated by using a least-squares quadratic fitting scheme. Details of the numerical procedure for calculating the derivatives, as well as solving the Poisson equation for pressure using this least-squares scheme, are found in Appendix C.

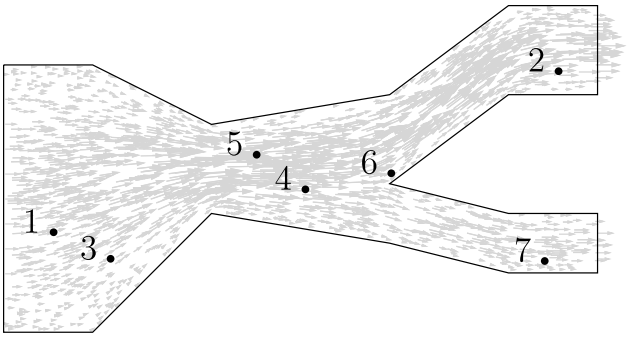

Figure 7.16: Sample points in the channel used for comparison of the Least-Squares Navier-Stokes solver and the boundary-integral method.

To validate the Navier-Stokes solver, we compare its steady-state results for the limit $Re \to 0$ with the flow found by the boundary-integral method (which is formally restricted to $Re = 0$). For the channel profile, we again consider our proof-of-concept geometry shown in Figure 7.2 with aspect ratio $W/H = 1.0$ and split ratio $Q_1/Q = 0.7$. A comparison between the two numerical solutions is shown in Table 7.1 at the points displayed in Figure 7.16. Both the Navier-Stokes and BI solvers used 16K vertices in the xy plane and 80 steps in the z direction. The results in Table 7.1 show a very good agreement, with a discrepancy (relative to $\|\mathbf{u}\|$) below 1% for most points, between the Navier-Stokes solver and the boundary integral method. The largest relative error occurs when the velocity magnitude is small (e.g., at point 3).

We now probe the inertial effects of the steady-state background flow on the droplet dynamics. To this end, we interpolate the precalculated steady-state Navier-Stokes solution for $\mathbf{u}_\infty$ to define the velocity boundary condition at the MF. This interpolation is performed by using the velocity and its gradient (calculated as described in Appendix C) at the nearest grid point $\mathbf{x}_0$ (found by using a linked-list structure). Namely, we have

$$\mathbf{u}_\infty(\mathbf{x}) \approx \mathbf{u}_\infty(\mathbf{x}_0) + (\mathbf{x} - \mathbf{x}_0) \cdot \nabla \mathbf{u}_\infty|_{\mathbf{x}_0}. \tag{7.21}$$

Figure 7.17 shows the numerical results for a droplet moving through the proof-of-concept geometry using an inertial background flow as the boundary condition for the

Table 7.1: Comparison between the solution for the steady-state, undisturbed flow in the channel represented in Figure 7.16 obtained by the full Navier-Stokes solver (at $Re = 0$) and the boundary-integral scheme. The xy position of the probe points is shown in Figure 7.16. All the probe points are located at a nondimensional distance 0.27 from the center plane $z = 0$.

Position	(LS)		(BI)		Rel. Error (%)
	u_x	u_y	u_x	u_y	
1	1.454	0.388	1.469	0.395	1.1
2	2.787	0.056	2.802	0.054	0.5
3	0.874	0.541	0.891	0.552	2.0
4	3.244	-0.120	3.274	-0.119	0.9
5	3.981	0.186	4.018	0.189	0.9
6	1.010	0.749	1.015	0.758	0.8
7	1.446	-0.005	1.457	-0.005	0.8

moving frame. The drop shapes are shown at the same times for different Reynolds numbers. The numerical results indicate that, for $Re = 1$ and $Re = 5$, the inertial effects in the ambient flow have almost no effect on drop motion, as indicated by the droplet shapes almost coinciding with the solution for $Re = 0$ for such cases. This result suggests that the inertial effects at this lower range of Reynolds numbers will arise only from the transient drop motion, as seen in the case of straight channels and regular geometries (Luo et al., 2018). These effects are expected to be small, as well.

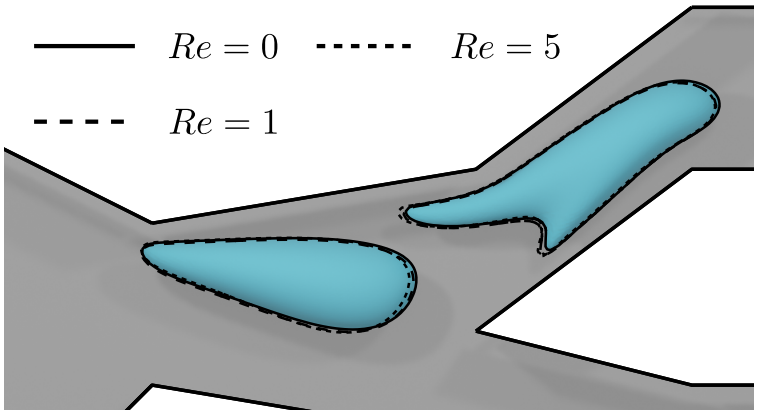

Figure 7.17: Numerical simulation of a droplet moving through the proof-of-concept geometry for $Ca = 0.3$, $\lambda = 1$, $W/H = 1.0$, and $|Q_1| = 0.7\,|Q|$ using an inertial background flow as the boundary condition for the moving frame for different Reynolds numbers $Re = 0$, 1, and 5 at the same time moments.

7.8 Concluding remarks

In this work, we developed a novel boundary-integral framework to simulate the motion of droplets in three-dimensional, complex geometries composed of multiple flat panels. Specifically, we focused on geometries with constant cross sections in the $z = const.$ planes, as these are common in microfluidic applications. Our method uses (i) a moving frame that follows the droplet throughout the channel, reducing the computational time, and (ii) a new meshing algorithm that combines Monte-Carlo-based techniques and Delaunay triangulation to deal with the channel front and back panels.

As an application of our method, we investigated how geometrical parameters like channel depth, drop position, and non-uniform branch heights, influence the motion of a single droplet in a complex-shaped bifurcating channel. In contrast to infinite-depth simulations, the interaction between the droplet and the channel front and back panels causes the formation of extra tail structures that can eventually pinch off and break up, forming satellite droplets. The differences between finite- and infinite-depth simulations become even more distinct when we consider irregular channel geometries (i.e., geometries that are not a simple combination of equal-sized straight branches).

To better understand the effects of the front and back panels on drop motion, we compared the results from our method to infinite-depth simulations performed using the algorithm described in Navarro et al. (2020). For regular geometries, such as straight channels or T-junctions with straight branches of equal heights, we can map the finite-depth problem to an infinite-depth one with the same maximum velocities in all channel inlets/outlets. In these instances, we observe an excellent agreement between finite- and infinite-depth simulations even for moderate channel aspect ratios $W/H = 2.0$ when the channel depth is much larger than the droplet diameter. However, for more complex geometries, a frame-to-frame comparison may only be possible for prohibitively large aspect ratios. This issue is present even for non-bifurcating geometries, such as a straight channel with a constriction, as the presence of the front and back panels strongly influences

the flow at the center plane. One implication of this result is that experimental results for deep, irregular channels cannot be readily compared to infinite-depth simulations.

For complex-shaped bifurcating channels, comparing finite- and infinite-depth simulations becomes even more complicated, as one also needs to match the flow-splitting behavior for both simulations. In these cases, if we use the same flow-rate ratios from the finite-depth simulation, even drop shapes at the same center $x-$position show substantial discrepancies. A better mapping between the finite- and infinite-depth problems is made by using a least-squares rule based on the maximum inlet/outlet velocities at all branches.

Furthermore, as a preliminary investigation of inertial effects, we solved the Navier-Stokes equations for the background channel flow and used the solution as a boundary condition for the moving-frame boundary-integral simulations. For moderate Reynolds numbers up to $Re = 5$, we found that fluid inertia does not play a significant role in the steady-state solution of the Navier-Stokes equations. Thus, we expect inertial effects to arise only from the presence of the drop and its transient motion. Although a full investigation of the inertial effects on drop motion requires the solution of the full Navier-Stokes equations, including the droplet, we expect such inertial effects to be small for this range of Reynolds numbers, as in the case for regular geometries.

CHAPTER 8

DYNAMICS AND ACTIVE MIXING OF A DROPLET IN A STOKES TRAP

"We adore chaos because we love to produce order."

M.C. Escher

Particle trapping and manipulation have a wide range of applications in biotechnology and engineering. Recently, a flow-based, particle-trapping mechanism called the Stokes trap was developed to allow for trapping and control of small particles in the intersection of multiple branches in a microfluidic channel. The motion of such particles can then be controlled by changing the flow rates in the branches. For deformable particles and vesicles, this mechanism can also be used to perform rheological experiments to determine the viscoelastic response of an emulsion or cell suspension. In this chapter, we show that, besides these applications, the various flow modes produced by the Stokes trap can also be used to manipulate drop shapes and induce active mixing inside droplets. To this end, we analyze the dynamics of a droplet in a Stokes trap through boundary-integral simulations. We also explore the dynamic response of drop shape with respect to distinct external flow modes, which allow us to perform numerical relaxation experiments such as step strain and oscillatory extension. A linear controller is used to manipulate drop position, and the drop deformation is characterized by a decomposition of the shape into spherical harmonics. For droplets with small deformation (e.g., small radii and/or capillary number), we observe a linear superposition of harmonics that can be used to manipulate drop shape. We also investigate how the different flow modes may be combined to induce mixing inside the droplets. The transient combination of modes produces an effective chaotic mixing inside the droplet, which can be further enhanced by changing parameters such as viscosity ratio and flow frequency.

8.1 Introduction

The field of microfluidics has been widely explored in recent years due to its various applications such as drug targeting (Fontana et al., 2016), micro-chemical reactors (Liu et al., 2020), and cell sorting (Shields IV et al., 2015). More specifically, some of these applications include the control of small particles or droplets in a microchannel by external inputs such as sound waves (Zhang et al., 2020; Lee et al., 2023), electromagnetic fields (Spellings et al., 2015; Brooks et al., 2018; Lee et al., 2019), chemical fields (Raj et al., 2023; Ganguly and Gupta, 2023), or hydrodynamic forces.

Hydrodynamic manipulation and trapping of particles and droplets has been investigated for many decades. One example of an early work is the paper by G.I. Taylor (Taylor, 1934), in which he introduces the "four-roll mill" experiment, which was originally designed to experimentally investigate droplet dynamics and deformation under extensional-flow conditions. A computer-controlled version of a four-roll mill was later developed by Bentley and Leal (1986), allowing for the trapping of a droplet at the center of the extensional flow for an extended time. More recently, with the rise of microfluidics, several works developed microfluidic analogues of the four-roll-mill experiment (Hudson et al., 2004; Lee et al., 2007; Shenoy et al., 2019). In such cases, instead of four rolls, the particles are constrained within the intersection of four branches of a microfluidic channel. The flow inside the intersection is then controlled by changing the flux at each branch of the channel. This type of mechanism, as well as its generalization for multiple branches, is called a Stokes trap. In such devices, the motion of particles can be controlled by changing the flow rates in the branches, allowing for precise trajectory control of small particles, even in the Brownian range (Shenoy et al., 2019). These systems can be used for different applications, including the trapping and control of small particles and extensional-flow experiments with vesicles (Hsiao et al., 2017; Kumar et al., 2020a,c,b; Kumar and Schroeder, 2021; Lin et al., 2021).

Although several works regarding particle control in Stokes traps have been reported

in the literature, one simplifying assumption typically made is that the trapped particles are very small, and, hence, move with the velocity of the external flow field, which is approximated by a superposition of Hele-Shaw sources. Such a model allows for the implementation of model predictive control (MPC) of the system, which can be used to control the trajectory of two different particles at the same time with a six-branch Stokes trap. This approximation, of course, ceases to be valid for large droplets/vesicles, where the length of the drop is comparable to the intersection length. Besides the size, the dynamics of the problem is strongly affected by changes in shape, especially when the droplets/vesicles present large deformations. Although some recent works tackled the deformation of vesicles (Kumar et al., 2020a,b; Kumar and Schroeder, 2021; Lin et al., 2021) and control of small droplets using a Stokes trap (Narayan et al., 2020a,b), the complex dynamics of drop deformation and response to different flow modes have not been extensively examined. However, recently, the work by Razzaghi and Ramachandran (2023) has experimentally shown that richer flow modes produced by hydrodynamic traps, such as a quadratic flow, can result in more interesting drop shapes.

In this work, we analyze the motion and deformation of a droplet in a 6-branch Stokes trap. The droplet dynamics are computed using boundary-integral simulations with dynamically-changing fluxes. A simple proportional control is implemented to keep the droplet at the center of the channel. The six channel branches enable us to examine the effects similar to classical deformation modes, such as pure-extension, simple-shear, and the six-fold extensional flow, allowing us to perform different numerical experiments. We also analyze how the combination of these modes affect the drop shape, which is analyzed via a spherical-harmonic decomposition. Moreover, we explore the influence of physical parameters such as capillary number and viscosity ratio on drop dynamics. In addition, we investigate how the different flow modes and their combination affect mixing inside the droplets, which can be useful in applications such as microfluidic reactors. To this end, we follow the mixing number analysis procedure used in papers such as Stone

and Stone (2005) and Muradoglu and Stone (2005), extending the backward Poincaré cell method Wang et al. (2001) to three-dimensional, continuously-deforming droplets. We also investigate how drop deformation may cause an extra contribution to mixing due to the breaking of kinematic reversibility.

8.2 Boundary-integral formulation

In this work, we investigate the dynamics of a single Newtonian droplet in the intersecting region between six symmetrically-distributed branches of a three-dimensional microfluidic channel with finite depth. We consider the droplet to be neutrally buoyant and with its center of mass positioned at the center plane of the microfluidic channel. We also consider the system to be in a creeping-flow regime, which is a reasonable assumption for most microfluidic systems.

To model the branch intersection, we consider a hexagonal prism as our computational domain. The problem geometry, as well as a sample simulation of a deformable droplet in such geometry, can be seen in Figure 8.1. In this geometry, the parallel top and bottom hexagonal panels correspond to the rigid, impenetrable walls of the microfluidic channel, whereas the six rectangular side panels correspond to the connections of the inlet/outlet branches with the intersection region. The flow rates at each branch, labeled Q_i can be changed with time almost independently, with the only constraint being mass conservation. We place the origin of the coordinate system at the geometric center of the intersection, as indicated in Figure 8.1(b).

As boundary conditions, we consider that the flow velocity at the branches is given by Boussinesq's solution for a rectangular channel and that there is no slip at the channel's top and bottom panels. The volumetric flow rate at each branch is prescribed and can be dynamically changed. The non-dimensionalization of the problem is made by using the inlet height H as the length scale, and $U_{av}^{B} \equiv |Q|/(HW)$ to scale the velocity and density potentials, where Q is the characteristic volumetric flow rate and W is the width of the

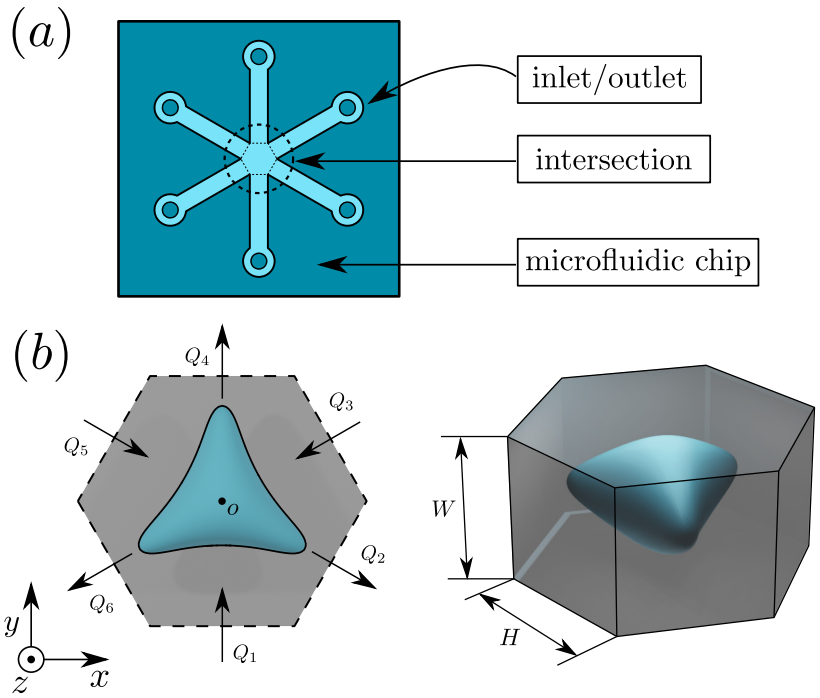

Figure 8.1: Geometry used for the numerical simulations of a droplet in a Stokes trap. The computational domain shown in (b) is a hexagonal prism corresponding to the intersecting region of the multiple rectangular channel branches, illustrated in (a). The origin of the coordinate system, denoted as O in (b), is placed at the geometric center of the hexagonal prism. The flow velocity at each rectangular panel is given by a Boussinesq velocity profile with prescribed fluxes Q_i, which can be dynamically changed.

microfluidic channel.

As we consider the creeping-flow regime, the velocity on the drop interface is given by the solution of the following set of non-dimensional boundary-integral equations (Roure et al., 2023):

$$\mathbf{u}(\mathbf{y}) = \frac{2}{\lambda+1}\left[2\int_{S_\infty} \mathbf{n}(\mathbf{x})\cdot\boldsymbol{\tau}(\mathbf{x}-\mathbf{y})\cdot\mathbf{q}(\mathbf{x})\,dS_\mathbf{x} + \mathbf{F}(\mathbf{y})\right] + 2\frac{(\lambda-1)}{(1+\lambda)}\int_{S_d} \mathbf{n}(\mathbf{x})\cdot\boldsymbol{\tau}(\mathbf{x}-\mathbf{y})\cdot\mathbf{u}(\mathbf{x})\,dS_\mathbf{x}, \tag{8.1}$$

for $\mathbf{y}$ on the drop surface S_d and

$$\begin{aligned}\mathbf{q}(\mathbf{y}) = \mathbf{u}^\infty(\mathbf{y}) &- 2\int_{S_\infty} \mathbf{n}(\mathbf{x})\cdot\boldsymbol{\tau}(\mathbf{x}-\mathbf{y})\cdot\mathbf{q}(\mathbf{x})\,dS_\mathbf{x} - \mathbf{F}(\mathbf{y}) \\ &- (\lambda-1)\int_{S_d} \mathbf{n}(\mathbf{x})\cdot\boldsymbol{\tau}(\mathbf{x}-\mathbf{y})\cdot\mathbf{u}(\mathbf{x})\,dS_\mathbf{x} - \frac{\mathbf{n}(\mathbf{y})}{|S_\infty|}\int_{S_\infty} \mathbf{n}(\mathbf{x})\cdot\mathbf{q}(\mathbf{x})dS_\mathbf{x}\end{aligned} \tag{8.2}$$

for $\mathbf{y}$ on the channel surface S_∞. Here, $\lambda = \mu_d/\mu$ is the ratio between the drop viscosity and the viscosity of the surrounding fluid, $\mathbf{n}$ is the outward unit normal vector, $\boldsymbol{\tau}(\mathbf{r}) = 3\mathbf{rrr}/(4\pi r^5)$ is the fundamental stresslet, $\mathbf{q}$ is a potential density (to be found) defined on the surfaces of the channel, and

$$\mathbf{F}(\mathbf{y}) = \frac{2}{Ca}\int_{S_a} \kappa(\mathbf{x})\mathbf{G}(\mathbf{x}-\mathbf{y})\cdot\mathbf{n}(\mathbf{x})\, dS_x \tag{8.3}$$

for a neutrally-buoyant droplet, where $Ca = \mu U_{av}^B/\sigma$ is the capillary number, which measures the ratio between flow and interfacial-tension effects, κ is the mean curvature, σ is the interfacial tension, and $\mathbf{G}(\mathbf{r}) = -(\mathbf{I}/r + \mathbf{rr}/r^3)/(8\pi)$ is the Green's function for Stokes flow. Also note that, in contrast to our prior work, the potential density $\mathbf{q}$ also includes the undisturbed flow representation, in a way that the undisturbed velocity $\mathbf{u}^\infty$ appears in the boundary-integral equation on the channel boundary, where the velocity is known from the boundary conditions.

The two boundary-integral equations (8.1) and (8.2) are solved simultaneously by discretizing both the drop and channel interfaces and solving the resulting finite system of linear equations using biconjugate-gradient iterations (see Roure et al. (2023) for more details about the numerical method). The discretization of the drop interface, which we consider to always start in a spherical configuration with radius a, follows the icosahedron/dodecahedron approach from Zinchenko et al. (1997). The triangulation of the channel uses a combination of Monte-Carlo methods for disk packing and Delaunay triangulation shown in Roure et al. (2023). The calculation of the mean curvature and the outward normal vector $\mathbf{n}$ is done by using the best-paraboloid-spline method described in Zinchenko and Davis (2000). Further details about the boundary-integral formulation and the numerical methods can be found in our previous work (Roure et al., 2023).

For the mixing investigation presented in Section 8.4, we also need to calculate the velocity inside the droplets. To this end, we use a generalized double-layer representation for the velocity field inside the droplet (Pozrikidis, 1992; Kim and Karrila, 2013):

$$\mathbf{u}^{(i)}(\mathbf{y}) = 2\int_{S_d} \mathbf{n}(\mathbf{x}) \cdot \boldsymbol{\tau}(\mathbf{x}-\mathbf{y}) \cdot \mathbf{Q}(\mathbf{x}) dS_x, \tag{8.4}$$

where $\mathbf{Q}$ is a potential density that can be calculated by solving the semi-deflated boundary integral equation:

$$\mathbf{u}(\mathbf{y}) = 2\int_{S_d} \mathbf{n}(\mathbf{x}) \cdot \boldsymbol{\tau}(\mathbf{x}-\mathbf{y}) \cdot \mathbf{Q}(\mathbf{x}) dS_x + \mathbf{Q}(\mathbf{y}) + \frac{\mathbf{n}(\mathbf{y})}{S_d}\int_{S_d} \mathbf{Q}(\mathbf{x}) \cdot \mathbf{n}(\mathbf{x}) dS_x, \ \mathbf{y} \in S_d. \tag{8.5}$$

Note that equation (8.5) has the same form as the boundary-integral equation for the undisturbed channel flow in Roure et al. (2023). Here, the surface velocity is given by the solution of the first boundary-integral problem (i.e., equations (8.1) and (8.2)). Equation (8.5) is discretized using a linear quadrature (Zinchenko et al., 1997) and solved numerically using the method of generalized minimal residuals (GMRES). For the evaluation of the double-layer integrals in (8.4) and (8.5), we use the standard singularity/near-singularity subtraction from Loewenberg and Hinch (1996).

8.3 Flow modes and drop deformation

Many works in the literature analyze drop and vesicle behavior under simple-shear and extensional flows (e.g., Zinchenko et al. (1997); Loewenberg and Hinch (1996, 1997); Oliveira and Cunha (2015)). More recently, the four-branch Stokes trap has been used to perform extensional-flow experiments with vesicles Kumar et al. (2020a). In the six-branch Stokes trap, the higher number of degrees of freedom allows us not only to locally reproduce a pure-extensional flow but also other "classical" flow modes such as extensional and quadratic flows by manipulating the flow rates Q_i in the branches. As an example, Figure 8.2 shows some of these different flow modes and the deformation response of a droplet to each one.

The three flow modes represented by (a), (b), and (c) in Figure 8.2 are given, respectively, by

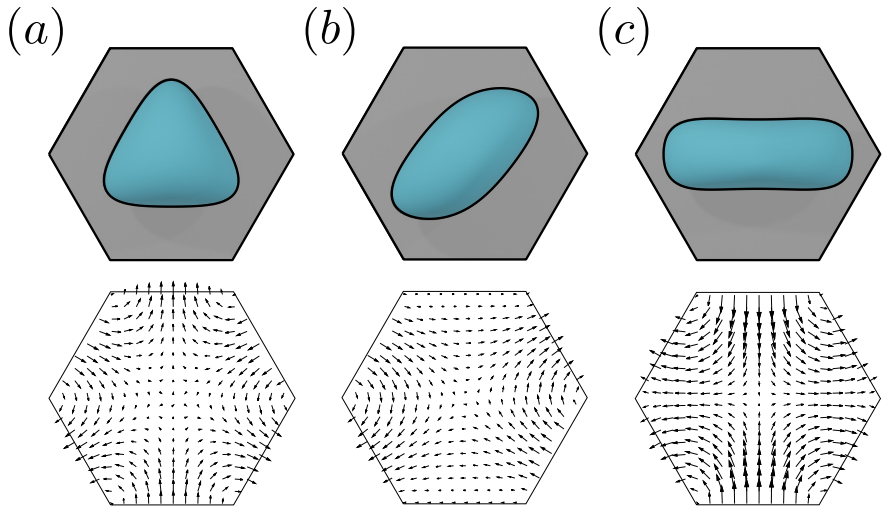

Figure 8.2: Different drop deformation modes produced by the Stokes trap. The undisturbed flow for each mode is shown on the bottom, whereas the shape responses are shown on top. The simulations consider $W = 1$, $a = 0.5$, $Ca = 0.1$, $\lambda = 1$, and (a) $\mathbf{Q} = \mathbf{Q}_{tri}$, (b) $\mathbf{Q} = \mathbf{Q}_{sh}$, and (c) $\mathbf{Q} = \mathbf{Q}_{ext}$.

$$\mathbf{Q}_{tri} = (1, -1, 1, -1, 1, -1), \tag{8.6}$$

$$\mathbf{Q}_{sh} = (0, 1, -1, 0, 1, -1), \tag{8.7}$$

and $$\mathbf{Q}_{ext} = (2, -1, -1, 2, -1, -1). \tag{8.8}$$

We call these modes (a) tri-axial extension, (b) shear, and (c) extension, respectively. Note that the extensional mode can be obtained by a "symmetrization" of the shear mode. Namely, $\mathbf{Q}_{ext} = \mathcal{S}\mathbf{Q}_{sh} - \mathcal{S}^2\mathbf{Q}_{sh}$, where $\mathcal{S}$ is the shift operator, defined by

$$\mathcal{S}(\mathbf{Q})_i = \begin{cases} Q_{i+1} & \text{for } i < 6 \\ Q_1 & \text{for } i = 6 \end{cases} \tag{8.9}$$

The shift operator corresponds to a 60° rotation of a given flow configuration. By symmetry, we have $\mathcal{S}^2\mathbf{Q}_{tri} = \mathbf{Q}_{tri}$ and $\mathcal{S}^3\mathbf{Q}_{sh} = \mathbf{Q}_{sh}$.

The simulations in Figure 8.2 were performed by considering an initially spherical droplet of radius $a = 0.5H$ starting at the center of the channel. For less deformable droplets (e.g., small Ca ad λ), the drop shape will eventually reach an equilibrium shape.

However, in both experiments and numerical simulations, this equilibrium point might be unstable, meaning that small changes in the drop initial position may lead to the drop escaping the Stokes trap; this situation is shown in Figure 8.3(b). To overcome this issue, we introduce a simple linear feedback controller to keep the droplet at the center of the channel. To control drop translation, it is useful to know how to induce drop translation in the x and y axes individually, as these translation modes can combine linearly for Stokes flow to induce translation in any arbitrary direction in the xy plane. One way that these modes can be achieved is shown in Figure 8.3(a). Considering the translation flow modes

$$\mathbf{Q}_h = (0, -1, -1, 0, 1, 1) \tag{8.10}$$

$$\text{and} \qquad \mathbf{Q}_v = (1, 0, 0, -1, 0, 0), \tag{8.11}$$

the controlled flow rates are given by

$$\mathbf{Q} = \mathbf{Q}_0 - [\alpha\mathbf{Q}_h \ \beta\mathbf{Q}_v] \begin{bmatrix} x_c \\ y_c \end{bmatrix}, \tag{8.12}$$

where $\mathbf{Q}_0$ is the applied flux configuration in the absence of control, $[\alpha\mathbf{Q}_h \ \beta\mathbf{Q}_v]$ is a block matrix whose columns are given by $\alpha\mathbf{Q}_h$ and $\beta\mathbf{Q}_v$, and $\mathbf{x}_c = (x_c, y_c, z_c)$ is the surface centroid, given by

$$\mathbf{x}_c = \frac{1}{S_d} \int_{S_d} \mathbf{x} dS, \tag{8.13}$$

with α and β being constants related to the strength of the control. When the droplet is not centered in the Stokes trap, the flux correction in equation (8.12) adds a counter flux contribution, proportional to the droplet displacement from the center of the channel, which moves the droplet towards the intersection center by combining the translation modes seen in Figure 8.3.

For general applications, one has to be careful to chose the constants α and β, as strong additional fluxes may lead to drop breakup and weak additional fluxes might not be strong enough to counteract the flux $\mathbf{Q}_0$, leading to a small region of effectiveness of the control

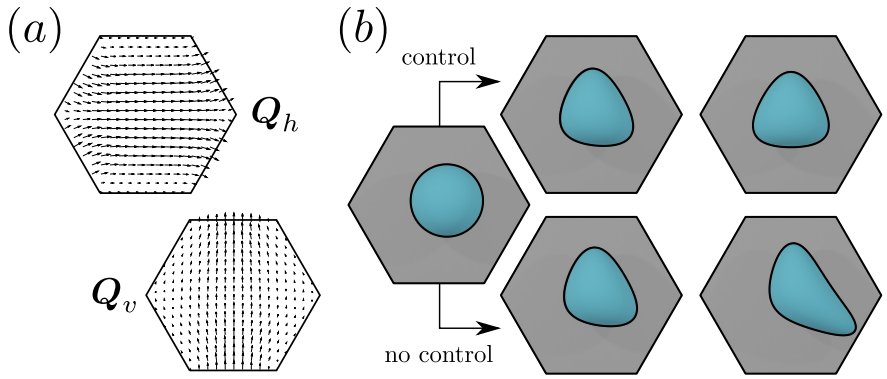

Figure 8.3: Application of the linear feedback control. Figure (a) shows the horizontal and vertical flow modes used for the control implementation. Figure (b) shows the drop behavior in the presence (top) and absence (bottom) of control in numerical simulations for $a = 0.4$, $Ca = 0.1$, $\lambda = 1$, and starting center position $\mathbf{x}_c = (0.1\cos(0.5), 0.1\sin(0.5), 0)$, for $t = 0$ (left), 0.25 (middle), 1.5 (bottom right), and steady state (top right).

algorithm near the center of the intersection region. For the purpose of the simulations in this chapter, the values $\alpha = \beta = 1$ have been found to perform well. It is also noted that, if the origin is not an equilibrium point for the flux configuration $\mathbf{Q}_0$ or if one wants the drop center to be positioned at a different target position, an integral component should be added to (8.12). To illustrate the effectiveness of the simple proportional control algorithm, Figure 8.3(b) shows the effect of the controller on the motion of a droplet starting off-center. In the absence of a controller, the droplet tends to escape the channel, as shown in the bottom case in Figure 8.3(b). The extension in this regime can also lead to drop breakup. In contrast, when the controller is turned on (top case in Figure 8.3), the additional fluxes move the drop to the center of the channel, keeping its position and shape stable.

8.3.1 Characterizing drop deformation via spherical harmonics

Often in the literature, drop deformation is characterized by parameters such as the Taylor deformation, which measures the deviation of a drop from its spherical equilibrium shape. From Figure 8.2, it is clear that the different drop shapes induced by the distinct flow modes show substantial variation. Hence, to properly describe drop deformation, we need a more

precise way to characterize the deformed drop shape. One way to do this, valid for star-shaped drop geometries, is to decompose the shape of the droplet in spherical harmonics. To this end, consider the shape of the droplet described by the function $r(\theta, \varphi)$, where r is the spherical radial coordinate and φ and θ are the azimuthal and polar angles, respectively. This function can be decomposed as:

$$r(\theta, \varphi) = \sum_{\ell,m} c_{\ell m} Y_\ell^m(\theta, \varphi), \tag{8.14}$$

where $Y_\ell^m(\theta, \varphi)$ are the normalized spherical harmonics and

$$c_{\ell m} = \int_{S^2} r(\theta, \varphi) \tilde{Y}_\ell^m(\theta, \varphi) d\Omega, \tag{8.15}$$

where S^2 is the unit sphere and tilde denotes complex conjugation. Numerical implementation of equation (8.15) consists of first projecting the drop mesh on the unit sphere and using a linear quadrature (Zinchenko et al., 1997).

As an example of harmonic decomposition, we examine the case of a droplet undergoing a tri-axial extensional flow previously shown in Figure 8.2. Figure 8.4 shows numerical results for (a) the harmonic decomposition of drop shape in a tri-axial extensional flow mode and (b) reconstruction of drop shape by using the first few harmonics. As the tri-extensional flow is locally quadratic, we expect the main excited harmonic to be Y_{33}, as in the regime of small deformations. Indeed, as shown in Figure 8.4(a), besides Y_{00}, the largest harmonic in the spectrum is Y_{33}, followed by Y_{66}. All other harmonics are substantially smaller, which is supported by the fact that we can reconstruct the drop shape with good accuracy by using only three harmonics, as shown in Figure 8.4(b).

The results shown in Figure 8.4 indicate that a good parameter to measure drop deformation in a tri-axial extensional flow is the imaginary part of c_{33}. Hence, we can perform numerical experiments with our trapped droplet. One possible example of such a numerical experiment is an oscillatory flow of the form

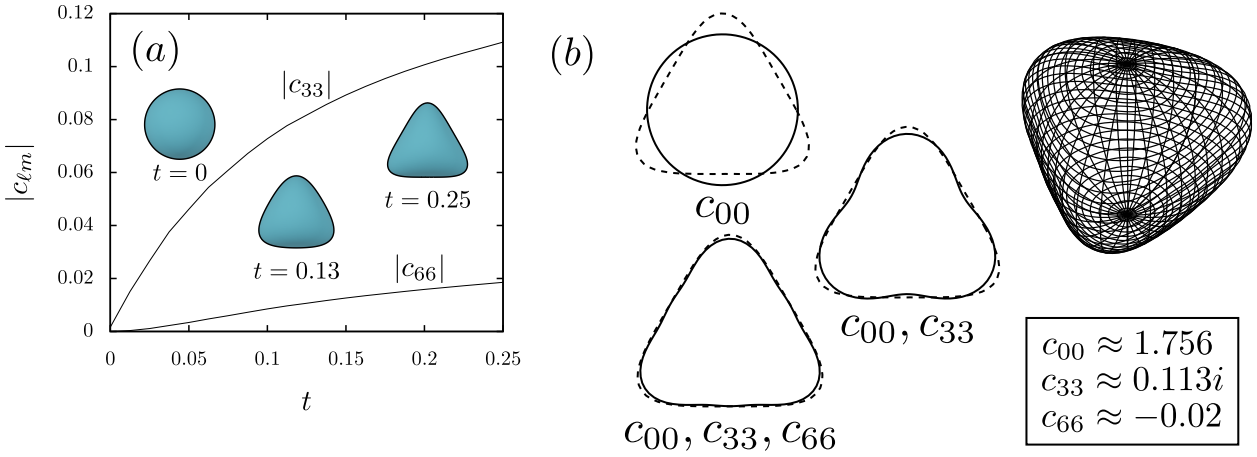

Figure 8.4: Harmonic decomposition of the shape of a droplet in a Stokes trap undergoing a tri-axial extensional flow for $Ca = 0.1$, $\lambda = 1$, $W = 1$, and $a = 0.5$. The results show (a) the evolution of the Y_{33} and Y_{66} harmonics with time as the drop extends and (b) the reconstruction of drop shape from the three main harmonics for $t = 0.25$. The dashed shapes in (b) are the numerical drop shape, whereas the solid lines are the harmonic approximations. The meshed geometry in (b) is a three-dimensional visualization of the harmonic reconstruction using the main three modes.

$$\mathbf{Q}_0(t) = \mathbf{Q}_{tri}\cos(\omega t), \tag{8.16}$$

where ω is the inlet frequency. Figure 8.5 shows the response of c_{33}, normalized by the drop radius a, to the oscillatory tri-extensional flow for $Ca = 0.1$, $\lambda = 1$, $W = 1$, and $\omega = 3$ for different values of drop radius a.

As expected, larger droplets are more deformable, which results in a larger values of $\mathrm{Im}(c_{33})/a$. Moreover, for droplets with radii $a = 0.4$ or less (Fig. 8.5(a)), besides an initial transient regime, the harmonic response presents a sinusoidal behavior slightly out of phase with the flux, which is expected given the elastic character of the interfacial tension. We also note that drop size slightly affects the phase of drop oscillation. However, for $a = 0.5$, we observe non-sinusoidal oscillations, as shown in Figure 8.5(b). Note that the oscillations in Figure 8.5(b) have different amplitudes, indicating a larger time for the droplet oscillation to reach a steady behavior.

We can also use our method to simulate the stretching and relaxation behavior of

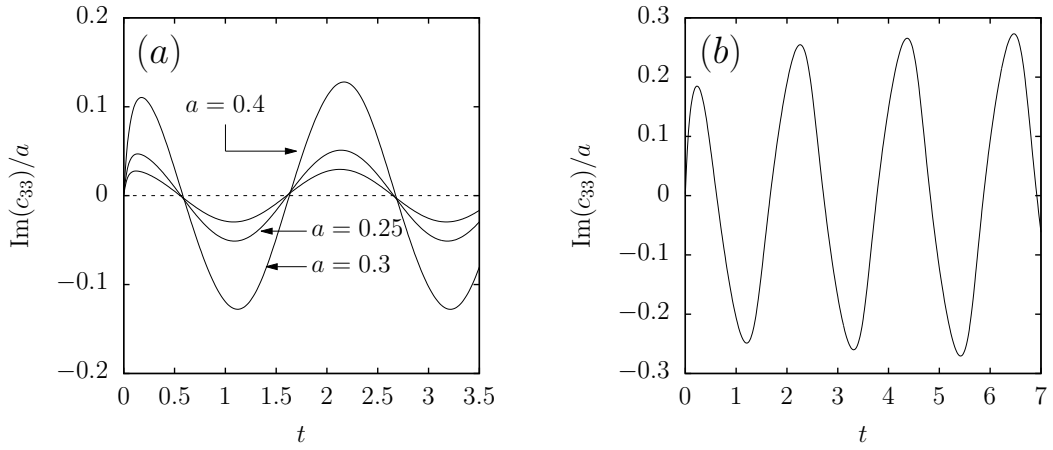

Figure 8.5: Numerical results for the imaginary part of the harmonic amplitude c_{33}, normalized by the drop radius, versus time for a droplet undergoing an oscillatory tri-axial extensional flow $\mathbf{Q}_0 = \mathbf{Q}_{\mathrm{tri}} \cos(\omega t)$. The results consider $Ca = 0.1$, $\lambda = 1$, $W = 1$, $\omega = 3$, and (a) $a = 0.25$, 0.3, 0.4, and (b) $a = 0.5$.

a droplet under step-strain conditions, similar to the vesicle experiments performed in Kumar et al. (2020b). Besides, the decomposition in spherical harmonics allows us to quantify drop deformation for both regular extensional ($\mathbf{Q}_{ext}$) and tri-extensional ($\mathbf{Q}_{\mathrm{tri}}$) flow modes.

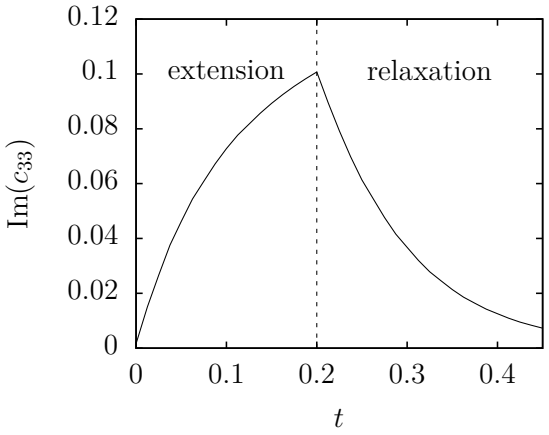

Figure 8.6: Numerical results for the Y_{33} harmonic response of a droplet undergoing a step tri-axial strain with $Ca = 0.1$, $\lambda = 1$ $a = 0.5$, $W = 1$, and $\mathbf{Q}_0 = \mathbf{Q}_{\mathrm{tri}}$ for $t \leqslant 0.2$ and $\mathbf{Q} = \mathbf{0}$ for $t > 0.2$.

To illustrate this type of step-strain numerical experiment, Figure 8.6 shows numerical

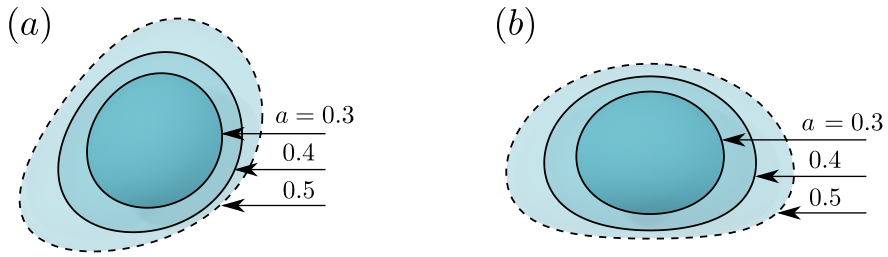

Figure 8.7: Numerical results for drop shapes resulting from combination of (a) tri-extensional + shear and (b) tri-extensional + extensional flow modes for $Ca = 0.05$, $\lambda = 1$, $W = 1$, and different drop radii. The solid contours represent steady shapes, whereas the dashed contours, corresponding to (a) $t = 0.925$ and (b) $t = 0.35$, eventually escape the intersection, possibly leading to breakup.

results for a droplet undergoing a step-strain, tri-axial extension for $Ca = 0.1$, $\lambda = 1$, $W = 1$, and $a = 0.5$. The flow configuration is given by $\mathbf{Q}_{tri}$ for $t \leqslant 0.2$ and $\mathbf{0}$ for $t > 0.2$. For $t \leqslant 0.2$, the drop experiences a tri-axial extension that is characterized by an increase in the Y_{33} harmonic, as shown in Figure 8.4. As the external flow stops, the droplet shape relaxes towards its initial spherical configuration.

8.3.2 Mode combination and shape manipulation

As shown in the previous section, subjecting the droplet to different flow modes in the Stokes trap may excite specific harmonics on the drop interface; a feature that can be used for shape manipulation. These modes can also be combined together to produce more complex drop shapes. To illustrate this observation, Figure 8.7 shows numerical simulations for droplets undergoing a combination of (a) shear + tri-axial extension and (b) extension + tri-axial extension for $Ca = 0.05$, $\lambda = 1$, and different drop radii a.

The results shown in Figure 8.7 show that the combination of different flow modes can result in asymmetric drop shapes such as the ones shown in Figure 8.7(a), while the droplet is kept at the center of the channel by the controller. This asymmetry is even more pronounced for larger droplets. However, above a certain radius threshold, the droplet becomes too elongated, escaping the intersection, possibly leading to breakup.

For small radii a, for which the droplet undergoes small deformations, we observe a

Table 8.1: Numerical results for the steady-state harmonic decomposition of different simple and combined flow modes for $Ca = 0.05$, $\lambda = 1$, and $W = 1$. The results are rounded to three decimal places.

a	Mode	c_{20}	c_{22}	c_{44}	c_{33}	c_{66}
0.3	$\mathbf{Q}_{tri}/2$	0.000	0.000	0.000	0.005i	0.000
	$\mathbf{Q}_{ext}/2$	−0.002	0.035	0.001	0.000	0.000
	$\mathbf{Q}_{sh}/2$	−0.001	−0.020i	−0.001 − 0.001i	0.000	0.000
	$(\mathbf{Q}_{tri} + \mathbf{Q}_{ext})/2$	−0.002	0.036	0.001	0.005i	0.000
	$(\mathbf{Q}_{tri} + \mathbf{Q}_{sh})/2$	−0.001	0.001 − 0.021i	−0.001 − 0.001i	0.005i	0.000
0.4	$\mathbf{Q}_{tri}/2$	−0.001	0.000	0.000	0.012i	0.000
	$\mathbf{Q}_{ext}/2$	−0.009	0.078	0.004	0.000	0.000
	$\mathbf{Q}_{sh}/2$	−0.003	0.001 − 0.044i	−0.002 − 0.002i	0.000	0.000
	$(\mathbf{Q}_{tri} + \mathbf{Q}_{ext})/2$	−0.010	0.081	0.005	0.013i	−0.001
	$(\mathbf{Q}_{tri} + \mathbf{Q}_{sh})/2$	−0.004	0.005 − 0.049i	−0.003 − 0.002i	0.013i	−0.001

linear deformation regime, where the harmonics superpose linearly. This linear superposition for small droplets is shown in Table 8.1, which shows numerical results for the main spherical harmonics present in the steady shapes previously shown in Figure 8.7 with additional results from numerical simulation using the isolated "half modes" $\mathbf{Q}_{tri}/2$, $\mathbf{Q}_{ext}/2$, and $\mathbf{Q}_{sh}/2$. The numerical results show that, for small droplets (e.g., $a = 0.3$), the harmonic spectrum of the final shape due to a combined mode seems to be given by a linear superposition of the isolated modes, as expected from the theory of small deformations (Leal, 2007). In contrast, like in the case for the oscillatory flow, we start to observe a non-linear behavior for large droplets, which is characterized by the lack of linear harmonic superposition and the presence of extra harmonics. As an example, we can start to see some small discrepancies for $a = 0.4$ between the final harmonics and the ones from the isolated modes. For $a = 0.5$, like in the harmonic response to the oscillatory flow presented in Section 8.3.1, linearity is no longer observed.

8.3.3 A hydrodynamic "three-phase rotor"

Drop rotation often plays an important role in improving the chaotic mixing inside the droplets (Stone et al., 1991), which is crucial for applications in drop-based microreactors.

It is known from the literature that droplets undergoing a simple shear flow display a tumbling motion for high viscosity ratios (Bilby and Kolbuszewski, 1977; Wetzel and Tucker, 2001; Oliveira and Cunha, 2015). In contrast, droplets with low viscosity ratios reach a steady-state deformation, where they present a "tank-treading" motion (Kennedy et al., 1994). Whereas a four-roll mill can produce rotational flow, it is difficult, and possibly not feasible, to produce a flow that is locally rotational at the center of a Stokes trap. For example, the model used by Shenoy et al. (2019) represents the external flow inside a Stokes trap as a superposition of potential sources, which is irrotational. In fact, the mode shown in Figure 8.2(b), which we labeled as "shear", is locally an extensional flow.

However, the Stokes trap allows us to generate a rotating extensional external flow by combining the three different possible modes for the "shear" mode, $\mathbf{Q}_{sh}$, $\mathcal{S}\mathbf{Q}_{sh}$, and $\mathcal{S}^2\mathbf{Q}_{sh}$, off phase by $2\pi/3$, in the following form:

$$\mathbf{Q}_{rotor} = \frac{1}{3}\left[\mathbf{Q}_{sh}\cos(\omega t) + \mathcal{S}\mathbf{Q}_{sh}\cos(\omega t + 2\pi/3) + \mathcal{S}^2\mathbf{Q}_{sh}\cos(\omega t + 4\pi/3)\right]. \quad (8.17)$$

Note, for example, that for $t = \pi/2$, $\mathbf{Q}_{rotor} \propto \mathbf{Q}_{ext}$. Numerical results for a single droplet in a stokes trap undergoing the external flow produced by the flux configuration described in (8.17) with $\omega = 3$ are shown in Figure 8.8. The droplet starts with a spherical shape and undergoes a transient extension regime until it reaches a periodic rotation similar to the wobbling motion observed in high-viscosity-ratio droplets undergoing a simple shear flow.

One interesting feature of this type of flow is that, at each time step, the external flow acts similarly to an extensional flow. As the internal flow inside a droplet undergoing an external extensional flow has four circulation regions, a continuously-rotating extensional flow will continuously change these invariant mixing regions, making it possible to observe effective mixing inside the droplet. In the following sections, we investigate how this rotating flow mode may be used to produce active mixing inside the droplet.

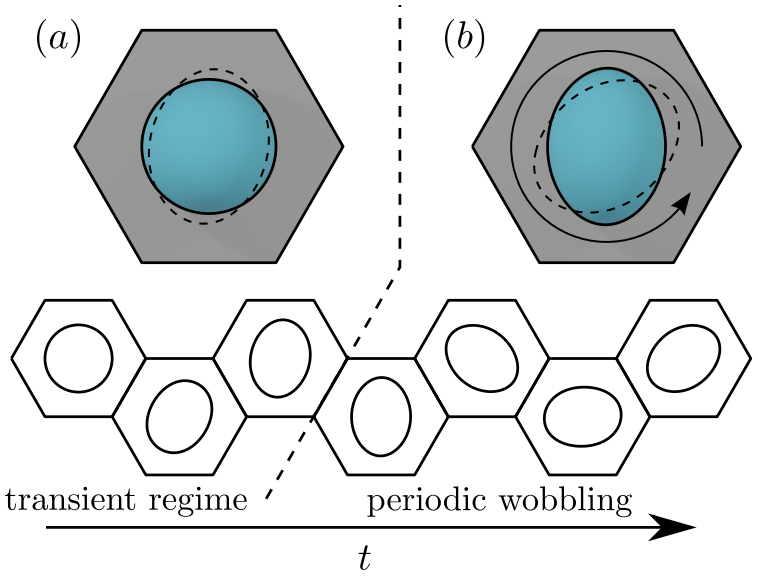

Figure 8.8: Numerical results for a droplet undergoing a three-phase extensional flow for $Ca = 0.1$, $\lambda = 1$, $a = 0.4$, $W = 1$, and $\omega = 3$. The motion of the drop is comprised of a short transient regime, shown in (a), where the droplet transitions from a spherical to an ovoid shape, and a periodic wobbling regime, shown in (b). The timeline at the bottom displays the full motion of the droplet. The solid drop shape for each part represents the first drop configuration for that part, whereas the dashed shape corresponds to the last configuration displayed on the timeline for that part.

8.4 Chaotic mixing inside droplets

Besides influencing drop shape and deformation, the different flow modes investigated in the first portion of this chapter also affect the internal circulation inside the droplet. In this section, we investigate how these induced internal flows influence mixing inside the droplets.

Due to the large number of microfluidic applications, chaotic mixing inside droplets has been extensively investigated in the literature, both theoretically and experimentally (Sarrazin et al., 2006; Blanchette, 2010; Zhao et al., 2015; Chen et al., 2018). For example, chaotic mixing inside spherical droplets induced by linear external flows was investigated by Stone et al. (1991), inducing chaos by applying external, non-aligned extensional an rotation flows. For quadratic flows, even earlier results by Bajer and Moffatt (1990) show a stretch-twist-fold chaotic dynamics. Later, Stone and Stone (2005) investigated a

transient combination of shear and uniform flows to emulate the conditions in a typical microfluidic serpentine mixer. This work was also extended to direct numerical simulations of deformable two-dimensional droplets in a serpentine channel Muradoglu and Stone (2005) using a finite-volume/front-tracking scheme. The characterization of mixing inside droplets in different microfluidic channels is still being explored (Fu et al., 2019; Cao et al., 2021; Belousov et al., 2021). Recently, Gissinger et al. (2021b) used boundary-integral simulations to investigate the mixing inside a droplet trapped in constrictions formed by rigid particles and fibers. Beyond the context of microchannels, the work by Watanabe et al. (2018) also explored active mixing inside droplets in an acoustic trap.

Here, similarly to the previous work by Gissinger et al. (2021b), we use boundary-integral simulations to investigate the mixing dynamics inside the droplet. One of the advantages of boundary-integral methods for mixing simulations is that the velocity of the fluid at any point inside the droplet can be determined by the numerical evaluation of (8.4), without requiring any interpolation. In contrast to the problem considered in Gissinger et al. (2021b), our droplet undergoes continuous deformation, not being confined to a steady state. To illustrate the velocity calculation inside the droplets for deformable droplets, Figure 8.9(a) shows the short-time evolution of streamlines inside an initially spherical droplet. It reveals the formation of six circulation regions at the midplane $z = 0$ inside a droplet undergoing a tri-axial extensional flow. At $t = 0$, the flow inside the droplet resembles the undisturbed external flow shown in Figure 8.2(a). As the droplet deforms, we start to see six saddle-like fixed points moving from the drop center towards its boundary, giving rise to the six circulation regions. For droplets with small deformations (e.g., $Ca \to 0$), this formation happens almost instantly. These circulation regions are very similar to the ones observed inside a spherical droplet subjected to an external quadratic flow.

One of the possible ways to characterize mixing inside droplets, introduced by Stone and Stone (2005), is the mixing number. To illustrate the definition of the mixing number,

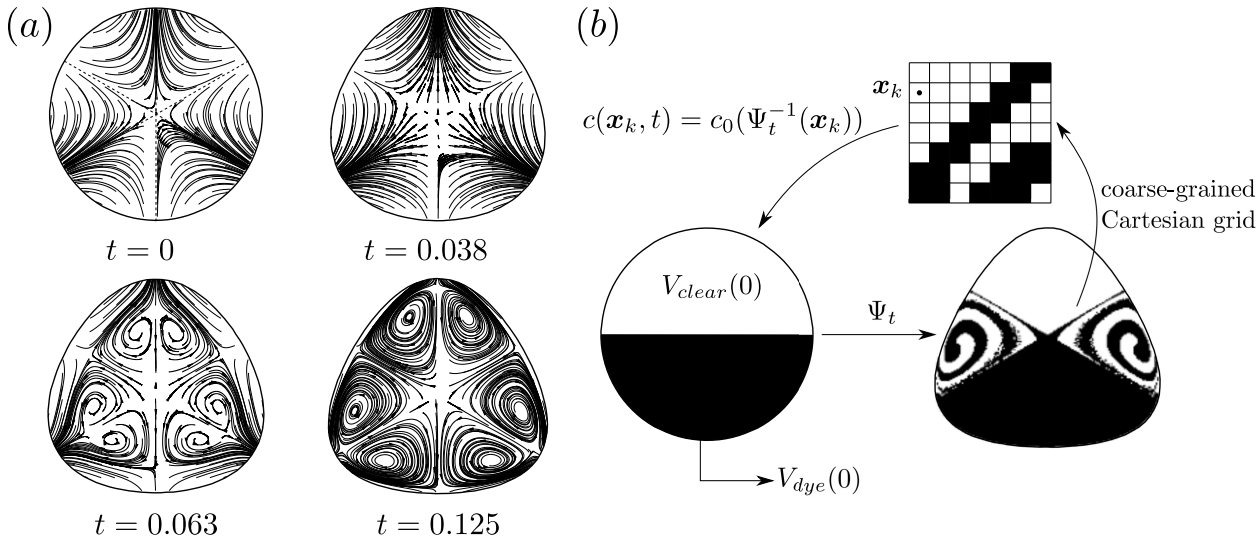

Figure 8.9: Flow inside a spherical droplet subject to an external tri-axial extensional flow with $Ca = 0.1$, $\lambda = 1$, $a = 0.4$, and $W = 1$. Figure (a) shows the transient formation of six circulation regions inside the droplet. Figure (b) illustrates the details of the mixing simulations, including the the regions V_{dye} (in black) and V_{clear} (in white) used in the calculation of the mixing number. The final configuration is calculated by backtracing the centers of cells in a Cartesian grid to their initial positions.

we focus on the classical example of an initially spherical droplet with passive dye completely filling one of its hemispheres. This problem is illustrated in Figure 8.9(b). As time passes, the dye is advected with the same velocity as the flow inside the droplet. As the dye is not diffused, the sets V_{dye}, consisting of the dyed points and V_{clear}, consisting of the clear points are disjoint. The mixing number is a measure of closeness between the two disjoint sets. In our specific case, we define it in the following grid-indifferent form:

$$m(t) = \frac{1}{a^2 V_d}\left[\int_{V_{dye}} d^2(\mathbf{x}, V_{clear})dV + \int_{V_{clear}} d^2(\mathbf{x}, V_{dye})dV\right], \tag{8.18}$$

where $d^2(\mathbf{x}, A) = \inf_{\mathbf{y}\in A} d^2(\mathbf{x}, \mathbf{y})$ is the square of the distance between the point $\mathbf{x}$ and the set A. The normalization factor a^2 is used to make the mixing number non-dimensional and to avoid an extra drop-size dependency in $m(t)$. If the system is well mixed, the two sets become strongly intertwined and the mixing number approaches zero, hence providing an inverse measure of mixing between the two sets.

In practical applications, as the non-linear dynamics of the system must be solved

numerically, the implementation of (8.18) is performed in a coarser domain given by a Cartesian grid formed by cubic cells of the same volume. Under these circumstances, the mixing number is given by

$$m(t) \approx \frac{1}{a^2 N_g} \sum_{k=1}^{N_g} d^2(\mathbf{x}_k, \mathrm{Opp}(\mathbf{x}_k)), \tag{8.19}$$

which is the same expression presented in Stone and Stone (2005). Here, the summation is over the grid cells, N_g is the total number of cells, $\mathbf{x}_k$ is the midpoint of a cell k, and

$$\mathrm{Opp}(\mathbf{x}) = \begin{cases} V_{dye} & \text{if } \mathbf{x} \in V_{clear}, \\ V_{clear} & \text{if } \mathbf{x} \in V_{dye}, \end{cases} \tag{8.20}$$

where V_{dye} and V_{clear} are the coarse-grained versions of their continuous counterparts. For a two-dimensional system, the definition of the mixing number (8.18) would be similar, but with areas instead of volumes. Its numerical counterpart (8.19), however, would remain unaltered, with the exception that the Cartesian grid would now be two-dimensional.

The regions V_{dye} and V_{clear} are determined by tracing the center points of each cell to its starting position and using the initial condition for dye concentration (see Figure 8.9(b)). This method is referred to as the backward Poincaré cell method (Wang et al., 2001) and has been used in previous works to obtain graphical representations for the chaotic mixing inside droplets. For incompressible flows, such a method yields more accurate results for the mixing number when compared to forward propagation, as it consists in a direct discretization of the final concentration profile obtained by the method of characteristics for the advective transport equation (Roure and Davis, 2021a). Namely, if the dye concentration $c(\mathbf{x}, t)$ undergoes a purely-advective transport, with $\partial c/\partial t + \mathbf{u} \cdot \nabla c = 0$ with initial condition $c_0(\mathbf{x})$, the concentration at a time t is given by $c_0(\Psi_t^{-1}(\mathbf{x}))$, where Ψ_t is the time evolution of the dynamical system from a starting position at $t = 0$. Note that forward propagation is still necessary to calculate quantities such as the mixing entropy (Muradoglu and Stone, 2005), which we do not explore in this work.

For calculation of both regular and backward trajectories, we use a second-order Runge-Kutta scheme. The drop velocity for each time step is calculated by the numerical evaluation of (8.4). To this end, the drop shapes and potential densities for the relevant time steps are pre-calculated and stored by solving the boundary-integral problem. To keep track of the points inside the droplet, we use an indicator function

$$I(\mathbf{y}) = \frac{1}{4\pi}\int_{S_d} \frac{\mathbf{n}(\mathbf{x})\cdot(\mathbf{x}-\mathbf{y})}{||\mathbf{x}-\mathbf{y}||^3} dS_x, \tag{8.21}$$

which is 1 for $\mathbf{y} \in V_d$ and 0 for $\mathbf{y} \notin V_d$. The implementation of (8.21) is made by using the fact that the contribution from each mesh triangle to the integral in (8.21) is the observational solid angle from the point $\mathbf{y}$.

8.4.1 Mixing in deformable droplets

We now investigate of how different flow modes may influence the mixing inside deformable droplets. As we are considering the droplet to be neutrally buoyant and centered at $z = 0$, the plane $z = 0$ is a two-dimensional invariant manifold for all the flow modes considered in this chapter. As the mixing in this two-dimensional submanifold often correlates with overall three-dimensional mixing inside the droplet (Stone and Stone, 2005), we focus our mixing analysis on the cross section $z = 0$.

One of the main consequences of drop deformation is the breaking of the kinematic reversibility usually present in Stokes flows, which may improve the mixing inside the droplet for specific cases. To illustrate the effects of irreversibility, we return to the oscillatory flow problem discussed in section 8.3.1. For a perfectly spherical droplet (e.g., $Ca = 0$), the linearity of Stokes equations implies that an oscillatory flow mode would not produce any type of effective mixing inside the droplet. Instead, all points would return to their initial position after one period. In contrast, for a deformable droplet, this kinematic symmetry is broken by the drop deformation, meaning that a given material point inside the droplet will display non-periodic dynamics, as illustrated in Figure 8.10(a).

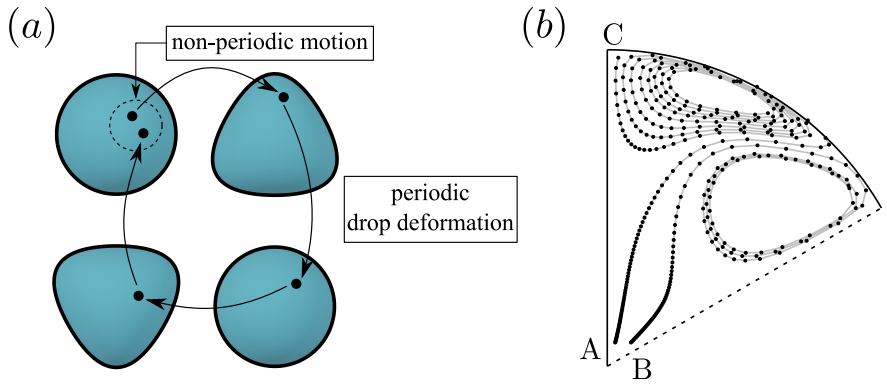

Figure 8.10: Symmetry breaking of kinematic reversibility caused by drop deformation. Figure (a) shows a droplet with $a = 0.4$, $\lambda = 1$, and $Ca = 0.1$ undergoing a periodic deformation caused by an external oscillatory tri-axial extension flow. After one period, the material point presents a displacement from its initial position. Figure (b) shows a Poincaré section at $z = 0$ for three initial positions (A, B, C).

To better visualize the global effects of this symmetry breaking for the oscillatory tri-axial extension flow mode, Figure 8.10(b) shows a Poincaré section for three different starting points inside the droplet at the $z = 0$ plane and $t = 1.625$, where the droplet shape is approximately spherical and the drop displays a periodic motion. Each point in the discrete trajectories shown in Figure 8.10 corresponds to the material particle position after one period of oscillation. The results in Figure 8.10(b) show the existence of non-periodic orbits, which are caused by drop deformation.

From Figure 8.10, we see that near the center of the droplet (i.e., away from the surface), the symmetry breaking is small, as indicated by the points very close to each other. In contrast, near the surface, we observe a more noticeable deviation from periodicity, as indicated by the presence of two attractor-like structures. Due to the nature of our numerical method, it is hard to tell precisely if the Poincaré map is spiraling down to an attractor or if the structure consists of quasi-periodic orbits, with the latter being the most likely alternative due to surface incompressibility at the $z = 0$ plane. In both cases, the breaking of periodicity is clear.

Although the breaking of the kinematic reversibility due to drop deformation may potentially improve mixing locally, it alone does not guarantee a full mixing inside the

droplet, especially in the plane $z = 0$. For example, for the tri-axial extension mode, like in the problem of a spherical droplet under a quadratic flow, the internal dynamics is constrained to the six symmetry quadrants inside the droplet. One way to overcome this issue and to induce a more effective mixing even in the midplane $z = 0$ is to use a time-dependent combination of flow modes, which is, in fact, the main strategy used in traditional microfluidic mixers. One such alternative would be the previously-discussed three-phase mode $\mathbf{Q}_{\text{rotor}}$ discussed in Section 8.3.3. Figure 8.11 shows numerical simulations of mixing inside a droplet undergoing a three-phase extensional external flow mode for $a = 0.4$, $Ca = 0.1$, and $W = 1$ for different times and different values of viscosity ratio and frequencies. The number below each droplet is the mixing number $m(t)$, calculated using equation (8.19).

Like in the example shown in Figure 8.9(b), the droplet starts with black points in the lower region and white points in the upper region. The final configuration of the points is calculated by using the backward Poincaré cell method described in this section. One immediate result, expected from the results found in Stone and Stone (2005), is that mixing is more effective for less-viscous droplets. This result is indicated by the very small mixing numbers and happens because the lower viscosity of the droplet results in a faster internal advection.

Another important factor in the mixing induced by the three-phase extensional flow is the frequency of the flow. Namely, for high frequencies such as $\omega = 6$, we observe very little overall mixing. However, for low frequencies (e.g., $\omega = 1.5$), we observe a more effective mixing even for $\lambda = 1$. The reason behind the better mixing effectiveness is similar to the increase in effectiveness caused by lowering the viscosity ratio: the interplay between internal circulation and drop rotation. For high values of ω, the droplet rotates much faster than the time it takes for the internal flow to advect the passive dye. For lower values of ω, internal advection happens faster than rotation, allowing for a more effective mixing in a shorter time. Of course, for $\omega = 0$, the inner flow becomes steady,

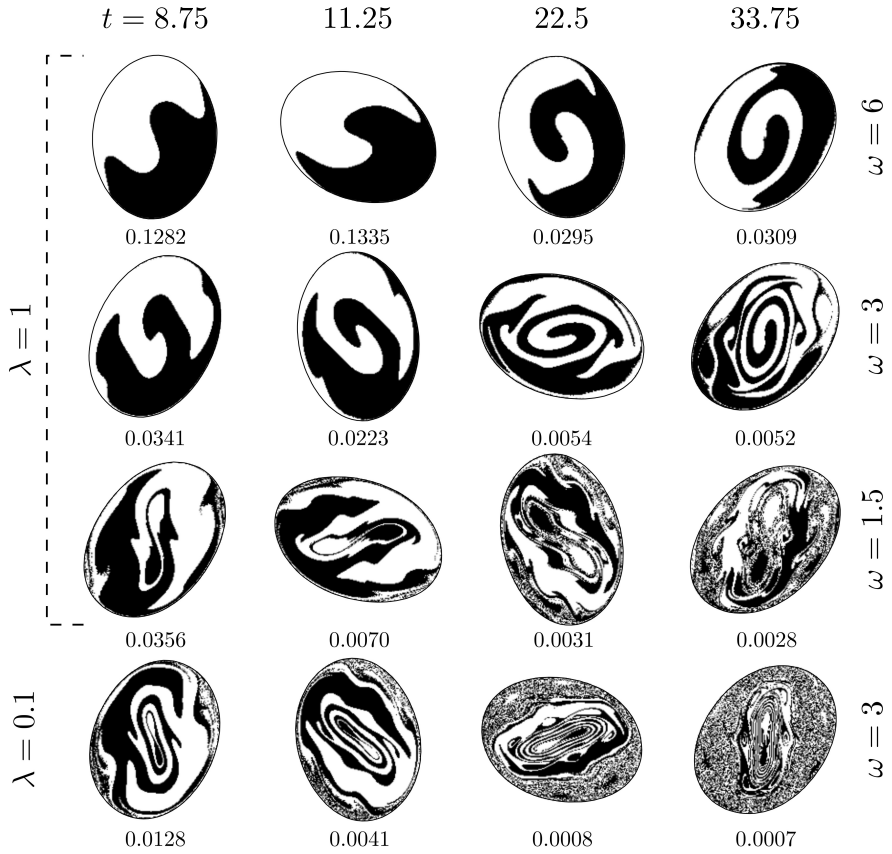

Figure 8.11: Numerical simulations of mixing inside a droplet undergoing a three-phase extensional flow for $a = 0.4$, $Ca = 0.1$, $W = 1$ at different times for distinct values of viscosity ratio and frequency ω. The results are for the midplane $z = 0$. The number below each droplet is the mixing number $m(t)$, calculated using equation (8.19). Droplets with a lower viscosity ratio present a better mixing, which is indicated by a smaller mixing number.

meaning that an effective mixing in the $z = 0$ plane is impossible. Hence, there should be an optimal value of ω to promote mixing.

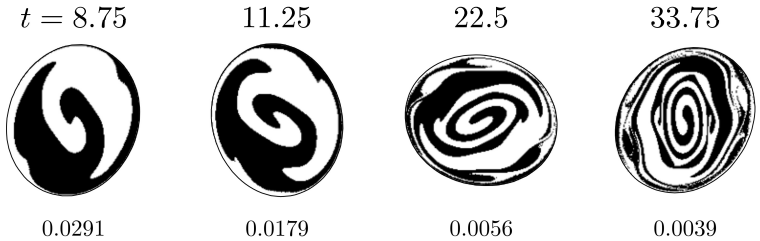

Figure 8.12: Numerical simulations of mixing inside a droplet undergoing a three-phase extensional flow for $a = 0.4$, $Ca = 0.05$, $W = 1$, $\omega = 3$, and $\lambda = 1$ at different times. The results are for the midplane $z = 0$. The number below each droplet is the mixing number $m(t)$, calculated using equation (8.19).

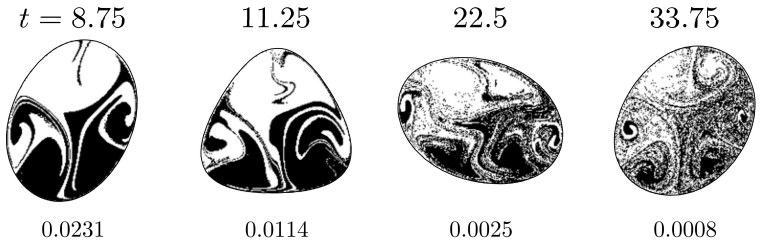

Figure 8.13: Numerical simulation of mixing inside a droplet for an external flow alternating between three-phase extension and tri-axial extension modes for $Ca = 0.1$, $\lambda = 1$, $W = 1$, and $\omega = 3$ for the midplane $z = 0$. The number below each droplet is the mixing number $m(t)$, calculated using equation (8.19).

As mentioned in the beginning of this section, drop deformation often plays an important role in mixing. Although our results from Figure 8.10 indicate that drop deformation can potentially aid mixing inside the droplet by breaking the kinematic reversibility of Stokes flow, earlier results by Muradoglu and Stone (2005) show an opposite trend. In fact, in our system, we also observe situations where drop deformation slows down mixing. As an example, Figure 8.12 shows the results for numerical mixing simulations of a droplet subject to a three-phase extensional flow with $\omega = 3$, $\lambda = 1$, $W = 1$, $a = 0.4$, and $Ca = 0.05$. Comparing the mixing numbers with the result shown in the second row of Figure 8.11, we see that, like the results in Muradoglu and Stone (2005), a smaller Ca results in a better mixing; although the difference between the two cases is less pronounced in our system. This result is characterized by the lower mixing numbers at most time steps. Similarly to the effect of frequency on mixing, this improvement on mixing for less-deformable droplets can be physically explained by an interplay between surface deformation velocity and inner advection. For higher values of Ca, drop deformation happens faster than inner advection, resulting in a less effective mixing. Hence, although drop deformation breaks the kinematic reversibility of the Stokes flow inside the droplet, larger deformations can decrease mixing, as previously observed for passive mixers in Muradoglu and Stone (2005).

Another way to combine the different modes to enhance active mixing is to alternate between different modes, like is usually done in passive mixing (e.g., serpentine chan-

nels) and in the investigation in Stone and Stone (2005), where a spherical droplet was subjected to alternating uniform and shear flows. In our system, one possibility is to alternate between three-phase extension mode and the tri-axial extension. To illustrate this improvement, Figure 8.13 shows numerical results for the mixing inside a droplet for $Ca = 0.1$, $\lambda = 1$, $\omega = 3$ and external flow given by

$$\mathbf{Q}_0(t) = \begin{cases} \mathbf{Q}_{rotor} & \text{for } t \leqslant 2\pi/\omega \pmod{4\pi/\omega}, \\ \mathbf{Q}_{tri} & \text{for } t > 2\pi/\omega \pmod{4\pi/\omega}. \end{cases} \tag{8.22}$$

The results shown in Figure 8.13 indicate that, even for viscosity ratios of $\mathcal{O}(1)$, it is possible to get a more efective mixing by alternating between equal periods of the two flow modes.

8.5 Concluding remarks

In this chapter, we investigated the motion of a droplet inside a six-branch Stokes trap. We identified different flow modes related to both translation and stretching. The different translating flow modes allow for the implementation of a linear control for drop position, whereas the deformation modes allow for manipulation of drop shape. Different flow modes can be used to perturb specific harmonics, and a combination of these flow modes can produce non-symmetrical drop shapes — a feature that can be useful in manufacturing processes. This complex drop deformation can be quantified by a decomposition into spherical harmonics, which allow us to observe the drop response to oscillatory and step-strain flow modes.

For small-deformation regimes such as droplets with small radii, we observed a linear response of drop deformation to the applied flow field, characterized by a harmonic response to oscillatory flows and linear mode superposition at small radii. When the droplets present a large deformation, this linearity is broken, which can be seen by non-harmonic (and non-periodic) responses to oscillatory flows and the presence of different harmonics when combining modes. The linear mode superposition found for small

droplets opens the possibility of using the Stokes trap, or other hydrodynamic traps, to generate specific drop shapes. However, a different branch configuration would be required to manipulate higher-order harmonics.

Moreover, we found that the combination of the different flow modes can be used to perform active mixing inside the droplet. As an example, we obtained numerical results for mixing inside a droplet under a transient three-phase extensional flow. Like previous results in the literature, droplets with small viscosity ratio present more effective mixing. However, it is possible to obtain a more efficient mixing inside more viscous droplets with $\lambda = 1$ by lowering the rotation frequency and/or alternating between different flow modes. Our results indicate that a Stokes trap, like other particle trapping systems like acoustic traps, can be used as an active mixer in microfluidic applications.

Part IV

Conclusion

CHAPTER 9

CONCLUDING REMARKS AND FUTURE WORK

In this work, we investigated the motion of droplets and particles moving in fluids in the low-Reynolds number regime. Our research was centered around two primary objectives: the numerical simulation of droplet-based microfluidics and investigating the mechanisms driving particle agglomeration by swelling emulsion binders. In the following sections, we present our final remarks on each of these topics and explore potential directions for future investigations.

9.1 Particle capture by swelling droplets

Particle capture by small, salt-water drops, each covered with a thin permeable film, was analyzed by solving the two-sphere mobility equations for the drop-particle relative trajectories in an extensional flow field. The collision efficiency between particles and droplets was calculated by using an extension of classical collision theory to systems with moving interfaces, where the pair distribution function does not reach a steady state. Osmotic flow into the drops is characterized by an engulfment parameter (ratio of permeate flow to imposed external flow), while effective salt diffusion inside the drop is characterized by

a Péclet number (ratio of osmotic flow to diffusive flux). Our theoretical analysis gave us new insights regarding the physics involved in the capture of small particles during the process of fast agglomeration by emulsion binders (van Netten et al., 2017). Our results indicate that increasing the engulfment parameter increases the particle-drop collision efficiency, especially for very small particles, which tend to flow on streamlines around non-expanding drops rather than collide with them. Increasing the Péclet number decreases the collision efficiency, however, as the slower diffusion of salt from the drop center to its edge leads to a diffusion boundary-layer of declining salt concentration near the inner edge of the drop interface and a reduced driving force for osmotic flow and drop expansion. Nevertheless, this effect is relatively weak, as even for very slow droplet swelling, the engulfment mechanism substantially improves particle collision, especially for very small particles, where even a small amount of engulfment can provide a substantial relative increase in the collision efficiency over that without engulfment.

Besides decreasing the imposed shear rate $\dot{\gamma}$ (which would reduce the base collision rate proportionately) or increasing the initial salt concentration, engulfment-dominated capture can be improved by using drops with smaller radius a_i, as smaller drops have less diffusional resistance and, hence, faster swelling and higher collision efficiencies. Moreover, the particle-to-drop size ratio is increased for smaller drops, which further increases the collision rate. Thus, smaller drops are recommended where feasible. Regardless, the simulations show that fast agglomeration is a suitable alternative for froth flotation of even very small particles, as long as modest engulfment due to osmotic flow into expanding drops is present.

One important direction for future work is the development of a comprehensive kinetic model for particle capture. The development of such a model would involve considering additional factors, such as the surface coverage of droplets by small particles, as well as exploring different capture modes, such as the binding of larger particles by small droplets. A "full" kinetic model that incorporates these aspects would provide a more

complete understanding of particle-capture processes.

9.2 Modeling the swelling of droplets and double emulsions

In Chapters 4 and 6, we modeled the osmotic-driven swelling of single droplets and droplet agglomerates. Although prior studies have considered the important problem of modeling drop swelling (Mezzenga et al., 2004; Leal-Calderon et al., 2012; Wan and Zhang, 2002; Yan and Pal, 2001; Roure and Davis, 2021a; DeIuliis et al., 2021), Chapter 4 presents the first quantitative model that describes both osmotic permeation into the swelling droplet and the salt counterdiffusion from the droplet interior to the diluted region where the fresh permeate has entered. In contrast to other similar diffusion-expansion models, such as the ones found in works concerning evaporation (Frank, 1950; Tredenick et al., 2021; Font, 2018; Sobac et al., 2015), our model involves a non-linear boundary condition to describe the balance of permeation and diffusion at the moving interface which is similar to the moving-boundary conditions in the so-called Stefan problems with kinetic undercooling (Cohen and Erneux, 1988; Evans and King, 2000; Back et al., 2014; McCue et al., 2011). This non-linearity leads to multiple time scales and a challenging solution. In this work, we have presented asymptotic and numerical solutions for the moving-boundary problem that governs the system, as well as the inclusion of interfacial-tension effects, which impose a finite limit to drop expansion. We also compared our theoretical results to previously-performed experiments (DeIuliis et al., 2021).

As hypothesized, the presence of salt-diffusion resistance inside the droplet slows down drop expansion considerably. Moreover, in the regime of slow diffusion (*i.e.*, large Péclet numbers), as are typical of the experiments considered (DeIuliis et al., 2021), the diffusion effects are constrained to a boundary-layer region located adjacent to the drop interface. In this regime, we obtained a similarity solution, valid for short times, for the concentration profile in the boundary layer. We also developed an asymptotic expres-

sion for the boundary-expansion thickness in the regime of small values of the re-scaled time. This novel theoretical prediction is also observed in the numerical results for very large Péclet numbers. These numerical results match those predicted by the similarity solution, except near the drop interface at very short times, which is, instead, described by our asymptotic analysis for small times. In this boundary-layer regime, the re-scaled expansion thickness displays a 'universal' behavior (*i.e.*, independent of Pe) when plotted as a function of the re-scaled time variable, a feature that is also verified by the numerical simulations and experiments (DeIuliis et al., 2021).

The comparison with the experimental data from DeIuliis et al. (2021) shows a remarkable similarity between our boundary-layer theory and the experimental results. In particular, after a very short initial transient, both theory and experiment exhibit a linear relationship between the increase of drop radius and the square root of time, with a slope directly proportional to the square root of the effective diffusivity within the water-in-oil-in-water emulsion.

We have also considered the effects of interfacial tension on drop expansion by balancing osmotic and interfacial-tension effects. Such effects have been considered by prior works on swelling kinetics, such as Mezzenga et al. (2004), but in the absence of internal diffusion. In this case, the presence of interfacial tension imposes an upper limit to the drop radius. As shown by our simulations, internal diffusion may still play a fundamental role in such cases by slowing down drop expansion, especially for large Péclet numbers. This key finding represents an improvement in the present work compared to prior studies of emulsion swelling (Mezzenga et al., 2004; Leal-Calderon et al., 2012; Wan and Zhang, 2002; Yan and Pal, 2001; Roure and Davis, 2021a; DeIuliis et al., 2021).

Besides the model for the diffusion-limited swelling of a single droplet, we have also proposed a simple model for the swelling of high-concentration, double-emulsion droplets in W/O/W emulsions. The model consists of spherical salt-water droplets encapsulated in a larger, spherical oil droplet. As the permeation of water through the oil films inside the

agglomerate structure occurs much slower than the diffusion of salt in the aqueous phase, the mass transport inside the agglomerate is mainly determined by the water permeation between neighboring droplets. To account for effects of agglomerate microstructure in the internal mass transport inside the agglomerate, we average our results over an ensemble of microstrucutures, which are randomly generated by a swelling Monte-Carlo algorithm, the latter which is also used to evolve the microstructure in time. Analyzing the average salt concentration profile, we see that, for a fixed initial volume fraction and a high number N_d of small droplets inside the agglomerate (i.e., small droplet to agglomerate size ratio), we observe a typical diffusive-like behavior, such as the concentration profiles predicted by our diffusion-limited swelling model, including the concentration plateau near the center of the agglomerate combined with concentration decrease near the interface, similar to the behavior predicted by the boundary-layer theory for high Péclet numbers at short times. The results for radial expansion of the spherical agglomerate present a similar behavior to the one observed experimentally by DeIuliis et al. (2021, 2022) and by the high-Péclet-number regime in the effective diffusion model from Roure and Davis (2021b). By comparing the radial expansion curves to the universal boundary-layer curve predicted in Roure and Davis (2021b), we were able to obtain effective diffusivities and Péclet numbers. The Péclet numbers obtained were in accordance to both the high Péclet number assumption and the ones calculated from experimental data using the same procedure, suggesting that, although simple, this model can give us some insight regarding such systems.

There are multiple possible directions for future works on this project. One possible direction is the implementation of interfacial-tension effects in the agglomerate model. As seen in the single droplet model, the inclusion of interfacial tension leads to interesting behaviors such as the possibility of de-swelling due to the interface "elasticity". For the permeation network model, this could result in an effective elastic structure, due to the chain behavior, which would make the analogy between our problem and the

swelling of hydrogels even more evident. Another possibility of future work would be the development of a more detailed model for the physics inside the agglomerate, including the droplet dynamics and the presence of polymers inside the oil phase. In the experiments performed by DeIuliis et al. (2021), the swelling behavior for short times coincided with our predictions for large Péclet numbers. However, for larger times, there is a transition to another regime where the droplet expansion also presents a behavior proportional to $t^{1/2}$, but with a lower apparent diffusivity. We believe this behavior may be caused by the presence of polymers in the oil phase, which can form structures such as micelles that can locally change the permeability of water. Hence, such a model could give us more insights regarding this "phase transition".

9.3 Numerical simulations of droplets in microfluidic channels

We developed a novel boundary-integral framework to simulate the motion of droplets in three-dimensional, complex geometries composed of multiple flat panels. Specifically, we focused on geometries with constant cross sections in the $z = const.$ planes, as these are common in microfluidic applications. Our method uses (i) a moving frame that follows the droplet throughout the channel, reducing the computational time, and (ii) a new meshing algorithm that combines Monte-Carlo-based techniques and Delauney triangulation to deal with the channel front and back panels.

As a first application of our method, in Chapter 7 we investigated how geometrical parameters like channel depth, drop position, and non-uniform branch heights, influence the motion of a single droplet in a complex-shaped bifurcating channel. In contrast to infinite-depth simulations, the interaction between the droplet and the channel front and back panels causes the formation of extra tail structures that can eventually pinch off and break up, forming satellite droplets. The differences between finite- and infinite-depth simulations become even more distinct when we consider irregular channel geometries

(i.e., geometries that are not a simple combination of equal-sized straight branches).

To better understand the effects of the front and back panels on drop motion, we compared the results from our method to infinite-depth simulations performed using the algorithm described in Navarro et al. (2020). For regular geometries, such as straight channels or T-junctions with straight branches of equal heights, we can map the finite-depth problem to an infinite-depth one with the same maximum velocities in all channel inlets/outlets. In these instances, we observe an excellent agreement between finite- and infinite-depth simulations even for moderate channel aspect ratios $W/H = 2.0$ when the channel depth is much larger than the droplet diameter. However, for more complex geometries, a frame-to-frame comparison may only be possible for prohibitively large aspect ratios. This issue is present even for non-bifurcating geometries, such as a straight channel with a constriction, as the presence of the front and back panels strongly influences the flow at the center plane. One implication of this result is that experimental results for deep, irregular channels cannot be readily compared to infinite-depth simulations.

For complex-shaped bifurcating channels, comparing finite- and infinite-depth simulations becomes even more complicated, as one also needs to match the flow-splitting behavior for both simulations. In these cases, if we use the same flow-rate ratios from the finite-depth simulation, even drop shapes at the same center $x-$position show substantial discrepancies. A better mapping between the finite- and infinite-depth problems is made by using a least-squares rule based on the maximum inlet/outlet velocities at all branches.

As a preliminary investigation of inertial effects, we solved the Navier-Stokes equations for the background channel flow and used the solution as a boundary condition for the moving-frame boundary-integral simulations. For moderate Reynolds numbers up to $Re = 5$, we found that fluid inertia does not play a significant role in the steady-state solution of the Navier-Stokes equations. Thus, we expect inertial effects to arise only from the presence of the drop and its transient motion. Although a full investigation of the inertial effects on drop motion requires the solution of the full Navier-Stokes equations,

including the droplet, we expect such inertial effects to be small for this range of Reynolds numbers, as in the case for regular geometries.

We also investigated the dynamics of a droplet inside a six-branch hydrodynamic trap. Different flow modes can be used to perturb specific harmonics, and a combination of these flow modes can produce non-symmetrical drop shapes — a feature that can be useful in manufacturing processes. This complex drop deformation can be quantified by a decomposition into spherical harmonics, which allow us to observe the drop response to oscillatory and step-strain flow modes.

For small- to moderate-deformation regimes such as droplets with small radii, we observed a linear response of drop deformation to the applied flow field, characterized by a harmonic response to oscillatory flows and linear mode superposition at small radii. When the droplets present a large deformation, this linearity is broken, which can be seen by non-harmonic (and non-periodic) responses to oscillatory flows and the presence of different harmonics when combining modes. The linear mode superposition found for small droplets opens the possibility of using the Stokes trap, or other hydrodynamic traps, to generate specific drop shapes. However, a different branch configuration would be required to manipulate higher-order harmonics.

Moreover, we found that the combination of the different flow modes can be used to perform active mixing inside the droplet. As an example, we obtained numerical results for mixing inside a droplet under a transient three-phase extensional flow. Like previous results in the literature, droplets with small viscosity ratio present more effective mixing. However, it is possible to obtain a more efficient mixing inside more viscous droplets with $\lambda = 1$ by lowering the rotation frequency and/or alternating between different flow modes. Our results indicate that a Stokes trap, like other particle trapping systems like acoustic traps, can be used as an active mixer in microfluidic applications.

There are several possible future directions for this project. One such possibility would be to include surfactant dynamics to address how it affects droplet splitting and sorting

in different channel geometries. This would also open a possibility for the investigation of deformable active droplets inside channels. In Chapter 7, we briefly mentioned how to dynamically and independently change the fluxes while still using the moving-frame approach, meaning that we can extend our trajectory control presented in for a droplet in a hydrodynamic trap to more complex-shaped microchannels. This advancement would be particularly valuable in applications such as drug delivery, where precise control over droplet or particle positioning is essential. Another important extension of the work would be to use the moving-frame technique for multiple droplets. In this case, when droplets approach one another, the moving frames would merge into a larger moving frame. For the specific problem of droplet dynamics in hydrodynamic traps, two different possibilities for future work would be to see how additional branches could be used to produce finer shape control and the possibility of using non-symmetric hydrodynamic traps for shape manipulation.

Currently, ongoing experiments are being conducted in our research group to analyze droplet motion in small channels. As prototypes for microfluidic systems, we have opted to utilize slightly larger channels in the millimeter scale. To maintain dynamical similarity, highly viscous fluids and slow flow rates are employed. The choice of using larger channels provides easier manufacturing and visualization. Notably, the larger size of these systems eliminates the need for microscopic visualization. This experimental setup can be applied for further validation of our numerical simulation results and for prototyping of microfluidic systems. Presently, the experiments focus on droplet motion through straight channels with rectangular cross-sections. However, we have plans to expand these investigations to encompass more complex channel geometries.

Part V

Bibliography

BIBLIOGRAPHY

S. G. Ahmed. An approximate method for oxygen diffusion in a sphere with simultaneous absorption. *International Journal of Numerical Methods for Heat & Fluid Flow*, 1999.

C. Amatore, O. V. Klymenko, A. I. Oleinick, and I. Svir. Diffusion with moving boundary on spherical surfaces. *ChemPhysChem*, 10(9-10):1593–1602, 2009.

G. Astaluta and G. Sarti. A class of mathematical models for sorption of swelling solvents in glassy polymers. *Polymer Engineering & Science*, 18(5):388–395, 1978.

G. Astarita and S. Joshi. Sample-dimension effects in the sorption of solvents in polymers—a mathematical model. *Journal of Membrane Science*, 4:165–182, 1978.

R. Asthana and S. N. Tewari. The engulfment of foreign particles by a freezing interface. *Journal of materials science*, 28(20):5414–5425, 1993.

J. M. Back, S. W. McCue, M. H.-N. Hsieh, and T. J. Moroney. The effect of surface tension and kinetic undercooling on a radially-symmetric melting problem. *Applied Mathematics and Computation*, 229:41–52, 2014.

J. Bahtz, D. Z. Gunes, A. Syrbe, N. Mosca, P. Fischer, and E. J. Windhab. Quantification of spontaneous w/o emulsification and its impact on the swelling kinetics of multiple w/o/w emulsions. *Langmuir*, 32(23):5787–5795, 2016.

K. Bajer and H. Moffatt. On a class of steady confined Stokes flows with chaotic streamlines. *Journal of Fluid Mechanics*, 212:337–363, 1990.

G. Barnocky and R. H. Davis. The lubrication force between spherical drops, bubbles and rigid particles in a viscous fluid. *International Journal of Multiphase Flow*, 15(4):627–638, 1989.

G. K. Batchelor and J. T. Green. The determination of the bulk stress in a suspension of spherical particles to order c^2. *Journal of Fluid Mechanics*, 56(03):401–427, 1972a.

G. K. Batchelor and J. T. Green. The hydrodynamic interaction of two small freely-moving spheres in a linear flow field. *Journal of Fluid Mechanics*, 56(2):375–400, 1972b.

S. Baysinger and R. Davis. Particle interactions with permeable drops in shear flow. *Powder Technology*, 383:410–417, 2021.

I. B. Bazhlekov, P. D. Anderson, and H. E. Meijer. Nonsingular boundary integral method for deformable drops in viscous flows. *Physics of Fluids*, 16(4):1064–1081, 2004.

K. Belousov, N. Filatov, I. Kukhtevich, V. Kantsler, A. Evstrapov, and A. Bukatin. An asymmetric flow-focusing droplet generator promotes rapid mixing of reagents. *Scientific Reports*, 11(1):1–10, 2021.

B. Bentley and L. G. Leal. An experimental investigation of drop deformation and breakup in steady, two-dimensional linear flows. *Journal of Fluid Mechanics*, 167:241–283, 1986.

T. Bertrand, J. Peixinho, S. Mukhopadhyay, and C. W. MacMinn. Dynamics of swelling and drying in a spherical gel. *Physical Review Applied*, 6(6):064010, 2016.

B. A. Bilby and M. Kolbuszewski. The finite deformation of an inhomogeneity in two-dimensional slow viscous incompressible flow. *Proceedings of the Royal Society of London. A. Mathematical and Physical Sciences*, 355(1682):335–353, 1977.

G. Birkhoff, R. S. Margulies, and W. A. Horning. Spherical bubble growth. *The Physics of Fluids*, 1(3):201–204, 1958.

F. Blanc, E. Lemaire, A. Meunier, and F. Peters. Microstructure in sheared non-brownian concentrated suspensions. *Journal of rheology*, 57(1):273–292, 2013.

F. Blanchette. Simulation of mixing within drops due to surface tension variations. *Physical Review Letters*, 105(7):074501, 2010. ISSN 0031-9007, 1079-7114. doi: 10.1103/PhysRevLett.105.074501.

J. Boussinesq. Mémoire sur l'influence des frottements dans les mouvements réguliers des fluids. *Journal de mathématiques pures et appliquées*, 13(2):377–424, 1868.

J. F. Brady and J. F. Morris. Microstructure of strongly sheared suspensions and its impact on rheology and diffusion. *Journal of Fluid Mechanics*, 348:103–139, 1997.

A. M. Brooks, S. Sabrina, and K. J. Bishop. Shape-directed dynamics of active colloids powered by induced-charge electrophoresis. *Proceedings of the national academy of sciences*, 115(6):E1090–E1099, 2018.

X. Cao, B. Zhou, C. Yu, and X. Liu. Droplet-based mixing characteristics in bumpy serpentine microchannel. *Chemical Engineering and Processing-Process Intensification*, 159: 108246, 2021.

C. Capes and R. Germain. Selective oil agglomeration in fine coal beneficiation. In *Physical cleaning of coal*, pages 293–351. Marcel Dekker New York, 1982.

A. Carlson, M. Do-Quang, and G. Amberg. Droplet dynamics in a bifurcating channel. *International Journal of Multiphase Flow*, 36(5):397–405, 2010.

C. Chen, Y. Zhao, J. Wang, P. Zhu, Y. Tian, M. Xu, L. Wang, and X. Huang. Passive mixing inside microdroplets. *Micromachines*, 9(4):160, 2018.

S. W. Chung and S. J. Kim. A remeshing algorithm based on bubble packing method and its application to large deformation problems. *Finite elements in analysis and design*, 39 (4):301–324, 2003.

D. S. Cohen and T. Erneux. Free boundary problems in controlled release pharmaceuticals. i: Diffusion in glassy polymers. *SIAM Journal on Applied Mathematics*, 48(6):1451–1465, 1988.

C. Coulliette and C. Pozrikidis. Motion of an array of drops through a cylindrical tube. *Journal of Fluid Mechanics*, 358:1–28, 1998.

J. Crank. *Free and Moving Boundary Problems*. Oxford University Press, 1987.

L. Cunha, I. Siqueira, E. Albuquerque, and T. Oliveira. Flow of emulsion drops through a constricted microcapillary channel. *International Journal of Multiphase Flow*, 103:141–150, 2018.

P. Cvitanovic, R. Artuso, R. Mainieri, G. Tanner, G. Vattay, N. Whelan, and A. Wirzba. Chaos: classical and quantum. *ChaosBook. org (Niels Bohr Institute, Copenhagen 2005)*, 69: 25, 2005.

R. H. Davis. The rate of coagulation of a dilute polydisperse system of sedimenting spheres. *Journal of Fluid Mechanics*, 145:179–199, 1984.

R. H. Davis and A. Z. Zinchenko. Particle collection by permeable drops. *Physical Review Fluids*, 3(11):113601, 2018.

G. DeIuliis, G. Sahasrabudhe, R. H. Davis, and K. P. Galvin. Water transport by osmosis through a high-internal-phase, water-in-oil emulsion. *Chemical Engineering Science*, 232: 116348, 2021.

G. DeIuliis, G. Sahasrabudhe, R. Davis, J. White, and K. Galvin. Effects of emulsifier

concentration in a high-internal-phase, w/o emulsion binder on particle agglomeration. *Chemical Engineering Science*, 248:117098, 2022.

M. Doi. *Soft Matter Physics*. Oxford University Press, 2013.

V. Eisinaite, P. D. Estrada, K. Schroën, C. Berton-Carabin, and D. Leskauskaite. Tayloring w/o/w emulsion composition for effective encapsulation: The role of pgpr in water transfer-induced swelling. *Food Research International*, 106:722–728, 2018.

M. El-Hachem, S. W. McCue, and M. J. Simpson. A sharp-front moving boundary model for malignant invasion. *Physica D: Nonlinear Phenomena*, 412:132639, 2020.

J. Evans and J. King. Asymptotic results for the stefan problem with kinetic undercooling. *The Quarterly Journal of Mechanics and Applied Mathematics*, 53(3):449–473, 2000.

G. S. Ezra. On the statistical mechanics of non-hamiltonian systems: the generalized liouville equation, entropy, and time-dependent metrics. *Journal of Mathematical Chemistry*, 35(1):29–53, 2004.

A. Florence and D. Whitehill. The formulation and stability of multiple emulsions. *International Journal of Pharmaceutics*, 11(4):277–308, 1982.

F. Font. A one-phase stefan problem with size-dependent thermal conductivity. *Applied Mathematical Modelling*, 63:172–178, 2018.

F. Fontana, M. P. Ferreira, A. Correia, J. Hirvonen, and H. A. Santos. Microfluidics as a cutting-edge technique for drug delivery applications. *Journal of Drug Delivery Science and Technology*, 34:76–87, 2016.

F. C. Frank. Radially symmetric phase growth controlled by diffusion. *Proceedings of the Royal Society of London. Series A. Mathematical and Physical Sciences*, 201(1067):586–599, 1950.

P. J. Frey and P.-L. George. *Mesh generation: application to finite elements*. Iste, 2007.

Y. Fu, H. Wang, X. Zhang, L. Bai, Y. Jin, and Y. Cheng. Numerical simulation of liquid mixing inside soft droplets with periodic deformation by a lattice boltzmann method. *Journal of the Taiwan Institute of Chemical Engineers*, 98:37–44, 2019.

F. Gadala-Maria and A. Acrivos. Shear-induced structure in a concentrated suspension of solid spheres. *Journal of Rheology*, 24(6):799–814, 1980.

K. P. Galvin and K. van Netten. A new method for ultra-fast concentration of hydrophobic particles. *Chemical Engineering Science*, 158:439–444, 2017.

A. Ganguly and A. Gupta. Going in circles: Slender body analysis of a self-propelling bent rod. *Physical Review Fluids*, 8(1):014103, 2023.

C. Geuzaine and J.-F. Remacle. Gmsh: A 3-d finite element mesh generator with built-in pre-and post-processing facilities. *International journal for numerical methods in engineering*, 79(11):1309–1331, 2009.

J. R. Gissinger, A. Z. Zinchenko, and R. H. Davis. Drops with insoluble surfactant squeezing through interparticle constrictions. *Journal of Fluid Mechanics*, 878:324–355, 2019.

J. R. Gissinger, A. Z. Zinchenko, and R. H. Davis. Drop squeezing between arbitrary smooth obstacles. *Journal of Fluid Mechanics*, 908, 2021a.

J. R. Gissinger, A. Z. Zinchenko, and R. H. Davis. Internal circulation and mixing within tight-squeezing deformable droplets. *Physical Review E*, 103(4):043106, 2021b.

H. C. Hamaker. The london—van der waals attraction between spherical particles. *Physica*, 4(10):1058–1072, 1937.

K. Han, C. W. Shields IV, N. M. Diwakar, B. Bharti, G. P. López, and O. D. Velev. Sequence-encoded colloidal origami and microbot assemblies from patchy magnetic cubes. *Science advances*, 3(8):e1701108, 2017.

F. Henrique, P. J. Zuk, and A. Gupta. Charging dynamics of electrical double layers inside a cylindrical pore: predicting the effects of arbitrary pore size. *Soft Matter*, 18(1):198–213, 2022.

R. W. Hockney and J. W. Eastwood. *Computer Simulation Using Particles*. CRC Press, 2021.

S. Hodges, O. Jensen, and J. Rallison. The motion of a viscous drop through a cylindrical tube. *Journal of Fluid Mechanics*, 501:279–301, 2004.

H. Holback, Y. Yeo, and K. Park. Hydrogel swelling behavior and its biomedical applications. In *Biomedical hydrogels*, pages 3–24. Elsevier, 2011.

J. Horwitz, P. Kumar, and S. Vanka. Three-dimensional deformation of a spherical droplet in a square duct flow at moderate reynolds numbers. *International Journal of Multiphase Flow*, 67:10–24, 2014.

K.-W. Hsiao, J. Dinic, Y. Ren, V. Sharma, and C. M. Schroeder. Passive non-linear microrheology for determining extensional viscosity. *Physics of Fluids*, 29(12):121603, 2017.

S. Hudson, F. Phelan Jr, M. Handler, J. Cabral, K. Migler, and E. Amis. Microfluidic analog of the four-roll mill. *Applied Physics Letters*, 85(2):335–337, 2004.

S. K. Jena, T. Srivastava, S. S. Bahga, and S. Kondaraju. Effect of channel width on droplet generation inside t-junction microchannel. *Physics of Fluids*, 35(2), 2023.

J. W. Joyce and R. N. Gottron. *Fluidics: basic components and applications*. US Army Electronics Research and Development Command, Harry Diamond Laboratories, 1979.

E. Kadivar. Modeling droplet deformation through converging–diverging microchannels at low reynolds number. *Acta Mechanica*, 229(10):4239–4250, 2018.

M. R. Kennedy, C. Pozrikidis, and R. Skalak. Motion and deformation of liquid drops, and the rheology of dilute emulsions in simple shear flow. *Computers & fluids*, 23(2):251–278, 1994.

B. Khadem and N. Sheibat-Othman. Modeling droplets swelling and escape in double emulsions using population balance equations. *Chemical Engineering Journal*, 382:122824, 2020.

J.-H. Kim, H.-G. Kim, B.-C. Lee, and S. Im. Adaptive mesh generation by bubble packing method. *Structural Engineering and Mechanics*, 15(1):135–150, 2003.

S. Kim. The completed double layer biem: A boundary integral method for complex microstructures in a viscous fluid. In *Boundary Element Methods: Fundamentals and Applications*, pages 167–175. Springer, 1992.

S. Kim and S. J. Karrila. *Microhydrodynamics: principles and selected applications*. Courier Corporation, 2013.

B. J. Kirby. *Micro- and Nanoscale Fluid Mechanics: Transport in Microfluidic Devices*. Cambridge university press, 2010.

J. A. Kitchener. The froth flotation process: past, present and future-in brief. In *The Scientific Basis of Flotation*, pages 3–51. Springer, 1984.

D. Kumar and C. M. Schroeder. Nonlinear transient and steady state stretching of deflated vesicles in flow. *Langmuir*, 37(48):13976–13984, 2021.

D. Kumar, C. M. Richter, and C. M. Schroeder. Conformational dynamics and phase behavior of lipid vesicles in a precisely controlled extensional flow. *Soft Matter*, 16(2): 337–347, 2020a.

D. Kumar, C. M. Richter, and C. M. Schroeder. Double-mode relaxation of highly deformed anisotropic vesicles. *Physical Review E*, 102(1):010605, 2020b.

D. Kumar, A. Shenoy, J. Deutsch, and C. M. Schroeder. Automation and flow control for particle manipulation. *Current Opinion in Chemical Engineering*, 29:1–8, 2020c.

L. G. Leal. *Advanced transport phenomena: fluid mechanics and convective transport processes*, volume 7. Cambridge University Press, 2007.

F. Leal-Calderon, S. Homer, A. Goh, and L. Lundin. W/o/w emulsions with high internal droplet volume fraction. *Food Hydrocolloids*, 27(1):30–41, 2012.

J. G. Lee, A. M. Brooks, W. A. Shelton, K. J. Bishop, and B. Bharti. Directed propulsion of spherical particles along three dimensional helical trajectories. *Nature communications*, 10(1):2575, 2019.

J. G. Lee, R. R. Raj, C. P. Thome, N. B. Day, P. Martinez, N. Bottenus, A. Gupta, and C. Wyatt Shields IV. Bubble-based microrobots with rapid circular motions for epithelial pinning and drug delivery. *Small*, page 2300409, 2023.

J. S. Lee, R. Dylla-Spears, N. P. Teclemariam, and S. J. Muller. Microfluidic four-roll mill for all flow types. *Applied physics letters*, 90(7):074103, 2007.

J. Leja. *Surface Chemistry of Froth Flotation*. Springer Science & Business Media, 2012.

M. Li, Z. Liu, Y. Pang, C. Yan, J. Wang, S. Zhao, and Q. Zhou. Flow topology and its transformation inside droplets traveling in rectangular microchannels. *Physics of Fluids*, 32(5):052009, 2020.

C. Lin, D. Kumar, C. M. Richter, S. Wang, C. M. Schroeder, and V. Narsimhan. Vesicle dynamics in large amplitude oscillatory extensional flow. *Journal of Fluid Mechanics*, 929: A43, 2021.

L. Liu, N. Xiang, and Z. Ni. Droplet-based microreactor for the production of micro/nano-materials. *Electrophoresis*, 41(10-11):833–851, 2020.

M. Loewenberg and R. H. Davis. Flotation rates of fine, spherical particles and droplets. *Chemical Engineering Science*, 49(23):3923–3941, 1994.

M. Loewenberg and E. Hinch. Numerical simulation of a concentrated emulsion in shear flow. *Journal of Fluid Mechanics*, 321:395–419, 1996.

M. Loewenberg and E. J. Hinch. Collision of two deformable drops in shear flow. *Journal of Fluid Mechanics*, 338:299–315, 1997.

Z. Y. Luo, X. L. Shang, and B. F. Bai. Marangoni effect on the motion of a droplet covered with insoluble surfactant in a square microchannel. *Physics of Fluids*, 30(7):077101, 2018.

Z. Y. Luo, X. L. Shang, and B. F. Bai. Effect of soluble surfactant on the motion of a confined droplet in a square microchannel. *Physics of Fluids*, 31(11):117104, 2019.

J. Lyu, P. G. Chen, G. Boedec, M. Leonetti, and M. Jaeger. An isogeometric boundary element method for soft particles flowing in microfluidic channels. *Computers & Fluids*, 214:104786, 2021.

P. K. MacKeown. *Stochastic Simulation in Physics*. Springer-Verlag, 2001.

G. Marti-Mestres and F. Nielloud. Emulsions in health care applications—an overview. *Journal of Dispersion Science and Technology*, 23(1-3):419–439, 2002.

S. Matsumoto, T. Inoue, M. Kohda, and K. Ikura. Water permeability of oil layers in w/o/w emulsions under osmotic pressure gradients. *Journal of Colloid and Interface Science*, 77 (2):555–563, 1980.

S. W. McCue, B. Wu, and J. M. Hill. Classical two-phase stefan problem for spheres. *Proceedings of the Royal Society A: Mathematical, Physical and Engineering Sciences*, 464 (2096):2055–2076, 2008.

S. W. McCue, M. Hsieh, T. J. Moroney, and M. I. Nelson. Asymptotic and numerical results for a model of solvent-dependent drug diffusion through polymeric spheres. *SIAM Journal on Applied Mathematics*, 71(6):2287–2311, 2011.

V. P. Mehrotra, K. V. S. Sastry, and B. W. Morey. Review of oil agglomeration techniques for processing of fine coals. *International Journal of Mineral Processing*, 11(3):175–201, 1983.

N. Metropolis, A. W. Rosenbluth, M. N. Rosenbluth, A. H. Teller, and E. Teller. Equation of state calculations by fast computing machines. *The journal of chemical physics*, 21(6): 1087–1092, 1953.

R. Mezzenga, B. M. Folmer, and E. Hughes. Design of double emulsions by osmotic pressure tailoring. *Langmuir*, 20(9):3574–3582, 2004.

T. Miettinen, J. Ralston, and D. Fornasiero. The limits of fine particle flotation. *Minerals Engineering*, 23(5):420–437, 2010.

J. F. Morris and B. Katyal. Microstructure from simulated brownian suspension flows at large shear rate. *Physics of Fluids*, 14(6):1920–1937, 2002.

S. Mukherjee and D. M. Stefanescu. Liquid convection effects on the pushing-engulfment transition of insoluble particles by a solidifying interface: Part i. analytical calculation of the lift forces. *Metallurgical and Materials Transactions A*, 35(2):613, 2004.

S. Mukhopadhyay, S. Ghosh, and V. A. Juvekar. Mathematical model for swelling in a liquid emulsion membrane system. *Desalination*, 232(1-3):110–127, 2008.

M. Muradoglu and H. A. Stone. Mixing in a drop moving through a serpentine channel: A computational study. *Physics of Fluids*, 17(7):073305, 2005.

T. G. Myers, M. G. Hennessy, and M. Calvo-Schwarzwälder. The stefan problem with variable thermophysical properties and phase change temperature. *International Journal of Heat and Mass Transfer*, 149:118975, 2020.

M. Nagel, P.-T. Brun, and F. Gallaire. A numerical study of droplet trapping in microfluidic devices. *Physics of Fluids*, 26(3):032002, 2014.

S. Narayan, I. Makhnenko, D. B. Moravec, B. G. Hauser, A. J. Dallas, and C. S. Dutcher. Insights into the microscale coalescence behavior of surfactant-stabilized droplets using a microfluidic hydrodynamic trap. *Langmuir*, 36(33):9827–9842, 2020a.

S. Narayan, D. B. Moravec, A. J. Dallas, and C. S. Dutcher. Droplet shape relaxation in a four-channel microfluidic hydrodynamic trap. *Physical Review Fluids*, 5(11):113603, 2020b.

R. Navarro, A. Z. Zinchenko, and R. H. Davis. Boundary-integral study of a freely suspended drop in a t-shaped microchannel. *International Journal of Multiphase Flow*, 130: 103379, 2020.

R. Navarro, A. Maristany, and R. H. Davis. Simulation of drop motion and breakup in narrow pores. *Chemical Engineering Science*, 229:116057, 2021.

T. Oliveira and F. Cunha. Emulsion rheology for steady and oscillatory shear flows at moderate and high viscosity ratio. *Rheologica Acta*, 54(11):951–971, 2015.

S. N. Omenyi and A. W. Neumann. Thermodynamic aspects of particle engulfment by solidifying melts. *Journal of Applied Physics*, 47(9):3956–3962, 1976.

A. Pawlik, P. W. Cox, and I. T. Norton. Food grade duplex emulsions designed and stabilised with different osmotic pressures. *Journal of Colloid and Interface Science*, 352(1): 59–67, 2010.

C. M. Phan, A. V. Nguyen, J. D. Miller, G. M. Evans, and G. J. Jameson. Investigations of bubble–particle interactions. *International Journal of Mineral Processing*, 72(1-4):239–254, 2003.

C. Pozrikidis. *Boundary Integral and Singularity Methods for Linearized Viscous Flow*. Cambridge university press, 1992.

C. Pozrikidis. Passage of a liquid drop through a bifurcation. *Engineering Analysis with Boundary Elements*, 36(2):93–103, 2012.

R. R. Raj, C. W. Shields, and A. Gupta. Two-dimensional diffusiophoretic colloidal banding: Optimizing the spatial and temporal design of solute sinks and sources. *Soft Matter*, 2023.

J. R. Rajian, M. L. Fabiilli, J. B. Fowlkes, P. L. Carson, and X. Wang. Drug delivery monitoring by photoacoustic tomography with an icg encapsulated double emulsion. *Optics express*, 19(15):14335–14347, 2011.

J. Rallison and A. Acrivos. A numerical study of the deformation and burst of a viscous drop in an extensional flow. *Journal of Fluid Mechanics*, 89(1):191–200, 1978.

S. S. Rao and H. Wong. The motion of long drops in rectangular microchannels at low capillary numbers. *Journal of Fluid Mechanics*, 852:60–104, 2018.

A. Razzaghi and A. Ramachandran. Deformation of a hele–shaw drop undergoing quadratic flow. *Physics of Fluids*, 35(7), 2023.

R. B. Reboucas and M. Loewenberg. Collision rates of permeable particles in creeping flows. *Physics of Fluids*, 33(8):083322, 2021.

M. Rother, J. Stark, and R. Davis. Gravitational collision efficiencies of small viscous drops at finite stokes numbers and low reynolds numbers. *International Journal of Multiphase Flow*, 146:103876, 2022.

M. A. Rother and R. H. Davis. The effect of slight deformation on droplet coalescence in linear flows. *Physics of Fluids*, 13(5):1178–1190, 2001.

M. A. Rother, A. Z. Zinchenko, and R. H. Davis. Buoyancy-driven coalescence of slightly deformable drops. *Journal of Fluid Mechanics*, 346:117–148, 1997.

G. Roure, A. Z. Zinchenko, and R. H. Davis. Numerical simulation of deformable droplets in three-dimensional, complex-shaped microchannels. *Physics of Fluids (under review)*, 2023.

G. A. Roure and F. R. Cunha. Hydrodynamic dispersion and aggregation induced by shear in non-brownian magnetic suspensions. *Physics of Fluids*, 30(12):122002, 2018.

G. A. Roure and R. H. Davis. Modelling of particle capture by expanding droplets. *Journal of Fluid Mechanics*, 912:A11, 2021a.

G. A. Roure and R. H. Davis. Diffusion-limited osmotic swelling of droplets. *Physics of Fluids*, 33(11):117109, 2021b.

G. A. Roure, J. Trost, and R. H. Davis. Particle capture by expanding droplets: effects of inner diffusion. *Journal of Fluid Mechanics*, 948:A36, 2022.

S. Safran. *Statistical Thermodynamics of Surfaces, Interfaces, and Membranes*. CRC Press, 2018.

G. Sahasrabudhe, G. DeIuliis, J. Davy, and K. Galvin. Selective and ultrafast agglomeration of chalcopyrite by a water in oil emulsion binder. *Minerals Engineering*, 167:106900, 2021.

M. Sandri. Numerical calculation of lyapunov exponents. *Mathematica Journal*, 6(3):78–84, 1996.

F. Sarrazin, K. Loubiere, L. Prat, C. Gourdon, T. Bonometti, and J. Magnaudet. Experimental and numerical study of droplets hydrodynamics in microchannels. *AIChE Journal*, 52(12):4061–4070, 2006.

A. Shenoy, D. Kumar, S. Hilgenfeldt, and C. M. Schroeder. Flow topology during multiplexed particle manipulation using a stokes trap. *Physical Review Applied*, 12(5):054010, 2019.

C. W. Shields IV, C. D. Reyes, and G. P. López. Microfluidic cell sorting: a review of the advances in the separation of cells from debulking to rare cell isolation. *Lab on a Chip*, 15(5):1230–1249, 2015.

K. Shimada and D. C. Gossard. Bubble mesh: automated triangular meshing of non-manifold geometry by sphere packing. In *Proceedings of the third ACM symposium on Solid modeling and applications*, pages 409–419, 1995.

A. F. Sirianni, C. E. Capes, and J. E. Puddington. Recent experience with the spherical agglomeration process. *The Canadian Journal of Chemical Engineering*, 47(2):166–170, 1969.

B. Sobac, P. Talbot, B. Haut, A. Rednikov, and P. Colinet. A comprehensive analysis of the evaporation of a liquid spherical drop. *Journal of colloid and interface science*, 438:306–317, 2015.

M. Spellings, M. Engel, D. Klotsa, S. Sabrina, A. M. Drews, N. H. Nguyen, K. J. Bishop, and S. C. Glotzer. Shape control and compartmentalization in active colloidal cells. *Proceedings of the National Academy of Sciences*, 112(34):E4642–E4650, 2015.

D. M. Stefanescu, F. R. Juretzko, A. Catalina, B. Dhindaw, S. Sen, and P. A. Curreri. Particle engulfment and pushing by solidifying interfaces: Part ii. microgravity experiments and theoretical analysis. *Metallurgical and Materials Transactions A*, 29(6):1697–1706, 1998.

P. Stevenson, A. J. Sederman, M. D. Mantle, X. Li, and L. F. Gladden. Measurement of bubble size distribution in a gas–liquid foam using pulsed-field gradient nuclear magnetic resonance. *Journal of colloid and interface science*, 352(1):114–120, 2010.

H. A. Stone, A. Nadim, and S. H. Strogatz. Chaotic streamlines inside drops immersed in steady stokes flows. *Journal of Fluid Mechanics*, 232:629–646, 1991.

Z. Stone and H. A. Stone. Imaging and quantifying mixing in a model droplet micromixer. *Physics of Fluids*, 17(6):063103, 2005.

A. Suea-Ngam, P. D. Howes, M. Srisa-Art, and A. J. DeMello. Droplet microfluidics: from proof-of-concept to real-world utility? *Chemical communications*, 55(67):9895–9903, 2019.

Y.-C. Tan and A. P. Lee. Microfluidic separation of satellite droplets as the basis of a monodispersed micron and submicron emulsification system. *Lab on a Chip*, 5(10): 1178–1183, 2005.

M. Tanemura, T. Ogawa, and N. Ogita. A new algorithm for three-dimensional voronoi tessellation. *Journal of Computational Physics*, 51(2):191–207, 1983.

G. I. Taylor. The formation of emulsions in definable fields of flow. *Proceedings of the Royal Society of London. Series A, containing papers of a mathematical and physical character*, 146 (858):501–523, 1934.

S. Tonini and G. Cossali. Effect of moving boundaries on the modeling of heat and mass transfer from an evaporating spherical drop. *Physics of Fluids*, 33(7):077117, 2021.

E. C. Tredenick, W. A. Forster, R. Pethiyagoda, R. M. van Leeuwen, and S. W. McCue. Evaporating droplets on inclined plant leaves and synthetic surfaces: experiments and mathematical models. *Journal of Colloid and Interface Science*, 592:329–341, 2021.

M. Tuckerman, C. Mundy, and G. Martyna. On the classical statistical mechanics of non-hamiltonian systems. *EPL (Europhysics Letters)*, 45(2):149, 1999.

K. van Netten, R. Moreno-Atanasio, and K. P. Galvin. Fine particle beneficiation through selective agglomeration with an emulsion binder. *Industrial & Engineering Chemistry Research*, 53(40):15747–15754, 2014.

K. van Netten, R. Moreno-Atanasio, and K. P. Galvin. Selective agglomeration of fine coal using a water-in-oil emulsion. *Chemical Engineering Research and Design*, 110:54–61, 2016.

K. van Netten, D. J. Borrow, and K. P. Galvin. Fast agglomeration of ultrafine hydrophobic

particles using a high-internal-phase emulsion binder comprising permeable hydrophobic films. *Industrial & Engineering Chemistry Research*, 56(38):10658–10666, 2017.

Y. Wan and X. Zhang. Swelling determination of w/o/w emulsion liquid membranes. *Journal of Membrane Science*, 196(2):185–201, 2002.

G. Wang, C. Zhu, T. Fu, and Y. Ma. Formation mechanism and criterion of tail satellite droplets for moving droplet in microchannel. *Chemical Engineering Science*, 238:116607, 2021.

L. Wang, Y. Fan, and Y. Chen. Animation of chaotic mixing by a backward poincaré cell-map method. *International Journal of Bifurcation and Chaos*, 11(07):1953–1960, 2001.

W. Wang, C. Ji, F. Lin, X. Wei, and J. Zou. Formation of water in oil in water particles by drop impact on an oil layer. *Physics of Fluids*, 31(3):037107, 2019.

Y. Wang and P. Dimitrakopoulos. Low-Reynolds-number droplet motion in a square microfluidic channel. *Theoretical and Computational Fluid Dynamics*, 26:361–379, 2012.

A. Watanabe, K. Hasegawa, and Y. Abe. Contactless fluid manipulation in air: Droplet coalescence and active mixing by acoustic levitation. *Scientific reports*, 8(1):10221, 2018.

E. D. Wetzel and C. L. Tucker. Droplet deformation in dispersions with unequal viscosities and zero interfacial tension. *Journal of Fluid Mechanics*, 426:199–228, 2001.

B. A. Wills and T. Napier-Munn. *Froth Flotation in Mineral Processing Technology: An Introduction to the Practical Aspects of Ore Treatment and Mineral*. Elsevier Science & Technology Books, 2006.

H. J. Wilson. An analytic form for the pair distribution function and rheology of a dilute suspension of rough spheres in plane strain flow. *Journal of Fluid Mechanics*, 534:97–114, 2005.

S. Yamakawa and K. Shimada. Anisotropic tetrahedral meshing via bubble packing and advancing front. *International Journal for Numerical Methods in Engineering*, 57(13):1923–1942, 2003.

J. Yan and R. Pal. Osmotic swelling behavior of globules of w/o/w emulsion liquid membranes. *Journal of Membrane Science*, 190(1):79–91, 2001.

R. Yoon and G. Luttrell. The effect of bubble size on fine particle flotation. *Mineral Procesing and Extractive Metallurgy Review*, 5(1-4):101–122, 1989.

G. Youngren and A. Acrivos. Stokes flow past a particle of arbitrary shape: a numerical method of solution. *Journal of fluid Mechanics*, 69(2):377–403, 1975.

G. R. Zeichner and W. R. Schowalter. Use of trajectory analysis to study stability of colloidal dispersions in flow fields. *AIChE Journal*, 23(3):243–254, 1977.

P. Zhang, H. Bachman, A. Ozcelik, and T. J. Huang. Acoustic microfluidics. *Annual Review of Analytical Chemistry*, 13:17–43, 2020.

S. Zhao, A. Riaud, G. Luo, Y. Jin, and Y. Cheng. Simulation of liquid mixing inside micro-droplets by a lattice boltzmann method. *Chemical Engineering Science*, 131:118–128, 2015.

A. Z. Zinchenko. Effective conductivity of loaded granular materials by numerical simulation. *Philosophical Transactions of the Royal Society of London. Series A: Mathematical, Physical and Engineering Sciences*, 356(1749):2953–2998, 1998.

A. Z. Zinchenko and R. H. Davis. An efficient algorithm for hydrodynamical interaction of many deformable drops. *Journal of Computational Physics*, 157(2):539–587, 2000.

A. Z. Zinchenko and R. H. Davis. Algorithm for direct numerical simulation of emulsion flow through a granular material. *Journal of Computational Physics*, 227(16):7841–7888, 2008.

A. Z. Zinchenko and R. H. Davis. Emulsion flow through a packed bed with multiple drop breakup. *Journal of Fluid Mechanics*, 725:611–663, 2013.

A. Z. Zinchenko and R. H. Davis. Algorithm for flow of highly-concentrated emulsions through a narrow constriction. *Journal of Computational Physics*, 438:110363, 2021.

A. Z. Zinchenko, M. A. Rother, and R. H. Davis. A novel boundary-integral algorithm for viscous interaction of deformable drops. *Physics of Fluids*, 9(6):1493–1511, 1997.

A. Z. Zinchenko, J. F. Ashley, and R. H. Davis. A moving-frame boundary-integral method for particle transport in microchannels of complex shape. *Physics of Fluids*, 24(4):043302, 2012.

Part VI

Appendices

APPENDIX A

DERIVATION OF THE BI EQUATIONS

Below, we provide a short derivation of the boundary-integral equations (8.2) and (8.1), used to calculate the velocity at the interface of a drop in a moving frame. Applying Green's third identity in the region outside the droplet (but inside the MF) to the fluid velocity perturbation $\Delta\mathbf{u} = \mathbf{u} - \mathbf{u}_\infty$, we obtain in that region:

$$\begin{aligned}\Delta\mathbf{u}(\mathbf{y}) = &-\frac{1}{\mu}\int_{S_\infty} \mathbf{G}(\mathbf{x}-\mathbf{y})\cdot\Delta\mathbf{f}(\mathbf{x})\,dS_\mathbf{x} + \int_{S_\infty} \mathbf{n}(\mathbf{x})\cdot\boldsymbol{\tau}(\mathbf{x}-\mathbf{y})\cdot\Delta\mathbf{u}(\mathbf{x})\,dS_\mathbf{x} \\ &+\frac{1}{\mu}\int_{S_d} \mathbf{G}(\mathbf{x}-\mathbf{y})\cdot\Delta\mathbf{f}(\mathbf{x})\,dS_\mathbf{x} - \int_{S_d} \mathbf{n}(\mathbf{x})\cdot\boldsymbol{\tau}(\mathbf{x}-\mathbf{y})\cdot\Delta\mathbf{u}(\mathbf{x})\,dS_\mathbf{x},\end{aligned} \tag{A.1}$$

where $\Delta\mathbf{f} = \mathbf{f} - \mathbf{f}_\infty = \mathbf{n}\cdot(\mathbf{T} - \mathbf{T}_\infty)$ is the traction perturbation due to the presence of the drop (with $\mathbf{T}$ being the stress tensor). By the boundary conditions on the MF, the second integral in (A.1) vanishes. Moreover, the contributions from $\mathbf{u}_\infty$ and $\mathbf{f}_\infty$ to the last two integrals in (A.1) vanish, given that, by direct application of the reciprocal theorem,

$$\frac{1}{\mu}\int_{S_d} \mathbf{G}(\mathbf{x}-\mathbf{y})\cdot\mathbf{f}_\infty(\mathbf{x})\,dS_\mathbf{x} - \int_{S_d} \mathbf{n}(\mathbf{x})\cdot\boldsymbol{\tau}(\mathbf{x}-\mathbf{y})\cdot\mathbf{u}_\infty(\mathbf{x})\,dS_\mathbf{x} = 0. \tag{A.2}$$

Furthermore, applying the reciprocal theorem to the flow generated by a point force and the flow inside the droplet, in combination with (A.1) and using continuity of the velocity field at the interface, we have (Rallison and Acrivos, 1978):

$$\begin{aligned}\mathbf{u}(\mathbf{y}) = \mathbf{u}_\infty(\mathbf{y}) - \frac{1}{\mu}\int_{S_\infty} \mathbf{G}(\mathbf{x}-\mathbf{y})\cdot\Delta\mathbf{f}(\mathbf{x})\ dS_\mathbf{x} + \frac{1}{\mu}\int_{S_d} \mathbf{G}(\mathbf{x}-\mathbf{y})\cdot[\![\mathbf{f}(\mathbf{x})]\!]\ dS_\mathbf{x} \\ + (\lambda-1)\int_{S_d} \mathbf{n}(\mathbf{x})\cdot\boldsymbol{\tau}(\mathbf{x}-\mathbf{y})\cdot\mathbf{u}(\mathbf{x})\ dS_\mathbf{x},\end{aligned} \tag{A.3}$$

where λ is the viscosity ratio, and $[\![\mathbf{f}]\!] = 2\sigma\kappa\mathbf{n}$ is the traction jump at the interface, given by the Young-Laplace law. As the flow contribution due to the first integral in the RHS of equation (A.3) has zero flux through S_∞, we can represent it inside S_∞ (e.g., Pozrikidis (1992)) by a double-layer distribution,

$$-\frac{1}{\mu}\int_{S_\infty} \mathbf{G}(\mathbf{x}-\mathbf{y})\cdot\Delta\mathbf{f}(\mathbf{x})\ dS_\mathbf{x} = 2\int_{S_\infty} \boldsymbol{\tau}(\mathbf{x}-\mathbf{y})\cdot\mathbf{q}(\mathbf{x})\ dS_\mathbf{x}, \tag{A.4}$$

and rewrite equation (A.3) as

$$\begin{aligned}\mathbf{u}(\mathbf{y}) = \mathbf{u}_\infty(\mathbf{y}) + 2\int_{S_\infty} \mathbf{n}(\mathbf{x})\cdot\boldsymbol{\tau}(\mathbf{x}-\mathbf{y})\cdot\mathbf{q}(\mathbf{x})\ dS_\mathbf{x} + \mathbf{F}(\mathbf{y}) \\ + (\lambda-1)\int_{S_d} \mathbf{n}(\mathbf{x})\cdot\boldsymbol{\tau}(\mathbf{x}-\mathbf{y})\cdot\mathbf{u}(\mathbf{x})\ dS_\mathbf{x},\end{aligned} \tag{A.5}$$

where $\mathbf{F}(\mathbf{y})$ is the non-homogeneous term (7.10).

Taking the limits of equation (A.5) where $\mathbf{y}$ approaches the drop surface S_d (from outside) or the MF surface S_∞ (from inside), we obtain coupled boundary-integral equations for the drop-interface velocity $\mathbf{u}$, given by (8.1), and the potential density $\mathbf{q}$,

$$\mathbf{q}(\mathbf{y}) = -2\int_{S_\infty} \mathbf{n}(\mathbf{x})\cdot\boldsymbol{\tau}(\mathbf{x}-\mathbf{y})\cdot\mathbf{q}(\mathbf{x})\ dS_\mathbf{x} - \mathbf{F}(\mathbf{y}) - (\lambda-1)\int_{S_d} \mathbf{n}(\mathbf{x})\cdot\boldsymbol{\tau}(\mathbf{x}-\mathbf{y})\cdot\mathbf{u}(\mathbf{x})\ dS_\mathbf{x}. \tag{A.6}$$

As in Section 7.2.1, the extra flux term added in (8.2) simply selects a unique solution of the system (8.1) and (A.6); namely, the one with zero flux of $\mathbf{q}$ through S_∞.

APPENDIX B

DYNAMIC, BOUNDARY-FITTED TRIANGULATION OF FRONT/BACK PANELS

Here, we present the details of the meshing algorithms outlined in Section 7.3. We use the same simple in-house algorithm to triangulate the front/back panels of the whole channel (in the solution for $\mathbf{u}_\infty$) and of the moving frame (MF); specifically, the triangulation of the moving frame is described below. In the latter case, the meshing efficiency is paramount, since this procedure, with typically a large, prescribed number $N_{vfr} = 8K - 16K$ of mesh nodes on the front/back panel, is applied at each time step, and it should not slow down appreciably the time marching.

Mathematically, the 2D domain to be meshed is an arbitrary polygon, which may or may not be convex, with straight edges. The mesh should be boundary-fitted, meaning that every contour corner must be a mesh node (except in rare, extreme cases discussed below), and the mesh edges must lie along the polygon contour.

Adaptive front/back triangulations (with substantially variable mesh density across the domain) are not needed in our case, and so, the simplest, non-adaptive version is described below. In this case, the target uniform half-distance a_t between the neighbouring

mesh nodes is easily estimated from

$$a_t = [c_{2d} S/(\pi N_{vfr})]^{1/2}, \tag{B.1}$$

where S is the polygon area and c_{2d} is the maximum area fraction that non-overlapping disks of equal radii can occupy. Instead of the theoretical $c_{2d} = \pi/(2\sqrt{3}) \approx 0.907$ for hexagonal packing in unbounded space, we use $c_{2d} \approx 0.8$ to make meshing always robust in our problem. Variations of c_{2d} between 0.8 and 0.9 had very minor effect on meshing quality.

First, disks of radius a_t centered in the polygon corners are successively installed. If a contour segment $[j, j+1]$ is too short to accommodate the next disk without overlapping the previous one, then the corner $\mathbf{x}_{j+1}$ is skipped. With our high resolutions (i.e., $a_t \ll 1$), these very rare events did not affect either robustness or accuracy of the simulations. Additional non-overlapping, equally-spaced disks of radius a_t are then installed with maximum density on each polygon edge; overlapping with the corner disks is also not allowed. The centers of these contour disks, together with those of the corner disks, constitute N_b boundary mesh nodes (unchanged during the further steps of the process).

The remaining $N_{vfr} - N_b$ mesh nodes are generated inside the polygon by a Monte-Carlo method. This part of our simple meshing scheme is entirely different from the 'bubble mesh' algorithms (Shimada and Gossard, 1995; Yamakawa and Shimada, 2003; Chung and Kim, 2003; Kim et al., 2003). Instead, it is more in the spirit of statistical physics algorithms widely used to calculate the equilibrium thermodynamical properties of dense molecular systems (Metropolis et al., 1953; MacKeown, 2001) and more recent swelling algorithms (Zinchenko and Davis, 2013, 2021) for dense packing of disks (and spheres) in constricted geometries. First, the polygon is tightly embedded in a square $\mathcal{D}$, and a sufficient number of random points, with statistical uniform distribution in $\mathcal{D}$, is generated until we accumulate the required number $N_{vfr} - N_b$ of points which (i) lie inside the polygon and (ii) are well-separated from all the boundary mesh nodes with at

least $2a_t$ clearance. To sort out such points, the indicator function is used,

$$I(\mathbf{y}) = \frac{1}{2\pi} \oint_C \frac{\mathbf{r} \cdot \mathbf{n}}{r^2} dS_x, \qquad \mathbf{r} = \mathbf{x} - \mathbf{y}, \tag{B.2}$$

which is 0 for $\mathbf{y}$ outside, and 1 for $\mathbf{y}$ inside the polygon contour C; $\mathbf{n}$ is the external unit normal to C lying in the contour plane. It is advantageous that the contribution of each contour segment to the integral in (B.2) is $\pm$ the observation angle from $\mathbf{y}$; hence, the integral is handled analytically, which makes this initial generation of internal mesh nodes quite fast. It is generally better to build $\mathcal{D}$ as a square (not a rectangle) to make the distribution of initial nodes more isotropic and thereby accelerate their subsequent equilibration.

Each internal node, as constructed above, becomes a center of a disk with an initially zero radius. The system is then subject to stochastic mixing, one randomly-chosen internal node j at a time, with gradual increase in the disk radius a_j. A random displacement of the node j (and its related disk) is accepted if (a) it leaves the node j inside the polygon (which is verified by the indicator function (B.2)) and (b) does not lead to disk overlap with any other disks, internal or boundary. The random displacement vector is uniformly generated in a small square $[-\delta, \delta]^2$, with $\delta \sim (0.04-0.06)a_t$ to make the portion of accepted displacements around 50%, in line with statistical physics recommendations. After each successful displacement, the disk radius is increased by half of the geometrically-allowed increment, but not to exceed a_t. Thus, with a suitable a_t, the system of internal disks goes through a polydisperse stage, until all a_j reach the same target radius a_t. The algorithm is greatly accelerated by the usual tool of the chaining mesh/linked-list structure (Hockney and Eastwood, 2021) to limit calculation of internode distances to close pairs. Another way to speed up the front/back panel meshing in our dynamic simulations stems from the observation that the MF contour changes little between two successive time steps. Accordingly, many of the equilibrated internal nodes plus the boundary nodes from the preceding time step can be used in the initial construction of the internal nodes set for the

current time step (instead of doing it from scratch, as described above). This optimization reduces the meshing CPU time in about half, to ≈ 13 sec for $N_{vfr} = 8K$, and to just ≈ 3 sec for cruder $N_{vfr} = 4K$ on a single core of a PC with 4.5 GHz clock speed. In comparison, the BI solver for a single time step for $N_{vfr} = 4K$ can range from 4 sec for a droplet with $\lambda = 1$ away from the channel walls to a few minutes when the droplet is either near a corner, in tightly-squeezing simulations such as the ones shown in Figure 7.13, or for very deep channels.

The disk centers from the equilibrated dense packing (Fig. 7.2(c)) are then connected by the Delauney mesh. The 2D version of the unconstrained Delauney triangulation algorithm (Tanemura et al., 1983) used herein is highly efficient, but it naturally produces many irrelevant mesh triangles which need to be discarded to obtain the MF panel meshing. A simple rule, provided by A. Maristani in a personal communication, worked surprisingly well in all the present simulations; the rule is to discard all Delauney triangles with centers of mass outside of the MF contour. Figure 7.2(d) demonstrates the result.

In addition to the above meshing scheme (i.e., 'random packing'), an alternative mixed scheme, still extremely simple, was developed to make meshing practically uniform in the bulk and reduce the meshing CPU cost. In the mixed version, the boundary modes (constructed in the same way described above) are complemented by a hexagonal mesh of points $(m_1 h + m_2 h/2, m_2 h\sqrt{3}/2)$ (with integer m_1, m_2 and mesh size $h = 2a_t$) inside the MF, keeping only the nodes which have, at least $\approx 2a_t$ clearance from all the boundary nodes. All the internal disks for the hexagonal mesh are then assigned an initially zero radius and subject to stochastic mixing with gradual increase in disk radius (as before), until the target radius a_t is reached for all the disks. In the mixed version of the algorithm, we can afford larger target area fraction $c_{2d} \approx 0.9$ in (B.1), and we use smaller random displacements (e.g., $\delta = 0.01a_t$). Since the internal nodes are almost equilibrated from the start, the Monte-Carlo stage is now very short, and the internal node arrangement remains practically uniform during mixing. It remains, as before, to connect all the nodes

by the Delaunay mesh and remove the redundant triangles. Figure B.1 demonstrates the result. This mixed scheme requires about the same or less CPU time to create a mesh as the optimized version of the random-packing algorithm but has the drawback of not giving an exact, reproducible number of nodes. In the mixed version, the attained number of mesh nodes (boundary and internal) is usually very close, to a few percent, to the target N_{vfr}.

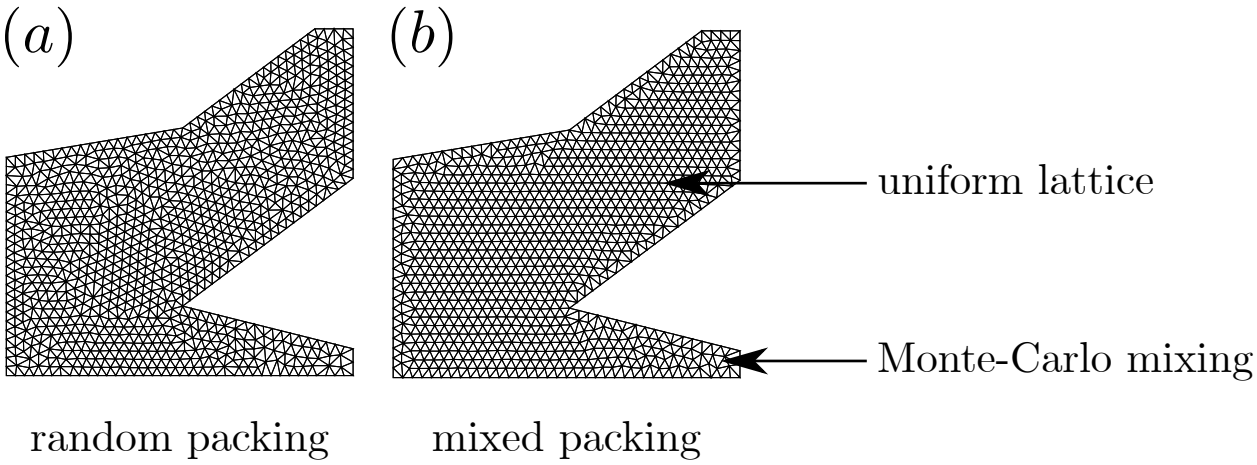

Figure B.1: Comparison between the simple application of our meshing algorithm using (a) a pure random packing for initial point distribution and (b) a hybrid accelerated method combining an initially uniform lattice of packed points inside the MF boundary with subsequent, but limited Monte-Carlo mixing. The number of vertices for each mesh is (a) $N_{vfr} = 1000$ and (b) $N_{vfr} = 1003$.

APPENDIX C

LEAST-SQUARES POISSON SOLVER

Below, we describe the method used to solve the Poisson equation for the pressure (7.19) with pure Neumann boundary conditions in complex geometries with constant cross sections in the z direction. For generality, we consider the problem $\nabla^2\phi = f(\boldsymbol{x})$, with Dirichlet or Neumann boundary conditions prescribed at different sections of the boundary. For the numerical solution of the problem, we use a least-square scheme, which basically consists of using a second-degree polynomial fitting to approximate the first- and second-order derivatives of a function at a certain point. Methods of this kind have been used previously in the literature for time evolution problems, such as surfactant transport on droplet interfaces (Gissinger et al., 2019). However, the application of such methods for bounded, time-independent problems require further details, which are provided in this appendix.

We start by describing the two-dimensional version of the algorithm and then generalize it to geometries with constant cross sections in the z direction. For the discretization of the field, we use the mesh constructed for the front and back panels of the channel for the boundary-integral algorithm (Section 7.3). To calculate derivatives in the inner points of the mesh (i.e., not on the boundary), we take one of such points, $\boldsymbol{x}_0$, and its surrounding neighbors, and use them to fit a second-order polynomial of the form

$$\phi(\mathbf{x}) \approx \phi(\mathbf{x}_0) + \mathbf{A} \cdot \delta\mathbf{x} + \mathbf{B} : \delta\mathbf{x}\delta\mathbf{x}, \tag{C.1}$$

where $\delta\mathbf{x} = \mathbf{x} - \mathbf{x}_0$, and $\mathbf{A}$ and $\mathbf{B}$ are, respectively, a constant vector and a constant second order tensor, to be determined by the least-squares fitting. For a two-dimensional function, the least-squares fitting requires at least five neighbor points, which is guaranteed by the meshing algorithm. The xy derivatives are then approximated by

$$\nabla\phi \approx \boldsymbol{A} \tag{C.2}$$

$$\text{and} \qquad \nabla\nabla\phi \approx 2\mathbf{B}. \tag{C.3}$$

The numerical Laplacian $\nabla^2\phi \approx 2\mathrm{Tr}(\mathbf{B})$ is a linear operator on the finite-dimensional, discretized solution space. Thus, we have converted the PDE into a system of linear algebraic equations that can be solved iteratively by the method of generalized minimal residuals (GMRES).

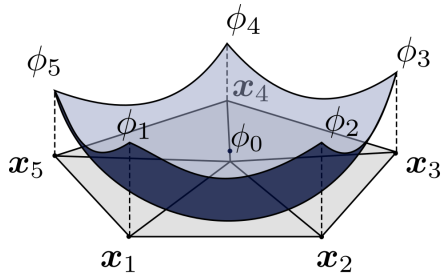

$$\phi(\boldsymbol{x}) \approx \phi(\boldsymbol{x}_0) + \boldsymbol{A} \cdot \delta\boldsymbol{x} + \boldsymbol{B} : \delta\boldsymbol{x}\delta\boldsymbol{x}$$

$$\nabla^2\phi \approx 2Tr(\boldsymbol{B})$$

Figure C.1: Local least-squares approximation for the field ϕ by a paraboloid. The fit parameters can be used to calculate the partial derivatives at the center point.

The implementation of the algorithm is straightforward for Dirichlet boundary conditions. However, for Neumann boundary conditions, which is our case of interest for the Navier-Stokes solver, some extra details concerning the boundaries have to be addressed. In finite-difference schemes, a commonly-used technique to deal with Neumann boundary conditions is to introduce virtual points outside the computation domain. However, calculating the Laplacian at the boundary via a least-squares fitting is not efficient,

even with the introduction of such virtual points. To overcome this issue, we introduce auxiliary points at the boundary by projecting the boundary-neighboring points to the boundary itself (e.g., points i and ii in Figure C.2). The value of ϕ in these auxiliary points is calculated by using the Neumann boundary conditions. These points can then be used to calculate the value of the field at boundary points (e.g., points 1, 2, and 3 in Figure C.2) by interpolation or extrapolation. To avoid double valuedness of the function at corners between two Neumann edges, we average the results obtained from the two adjacent edges. Furthermore, for purely-Neumann boundary conditions, we also impose a zero-mean condition to the field (i.e., $\sum_k \phi_k = 0$), to avoid problems with the multiplicity of solutions.

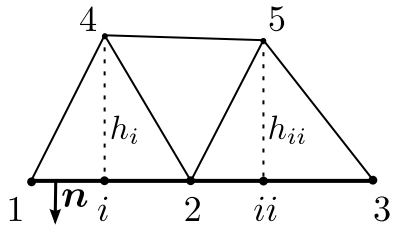

$$\phi_i \approx \phi_4 + \left.\frac{\partial \phi}{\partial n}\right|_i h_i$$

Figure C.2: Sketch of the auxiliary boundary points (e.g., i and ii) used to calculate the values of the field at the boundary points at each numerical iteration.

For three-dimensional geometries with constant cross sections in the z direction, we use a combination between the previously-described least-square scheme for the xy plane and a finite-difference scheme for the $z-$direction, where the $z-$derivatives are approximated by central finite differences. The solution of the system is still performed using GMRES. For the calculation of mixed derivatives, which might be important in some applications, we first calculate the derivatives in the xy directions using a least-square fitting and then perform the z differentiation using central finite differences.